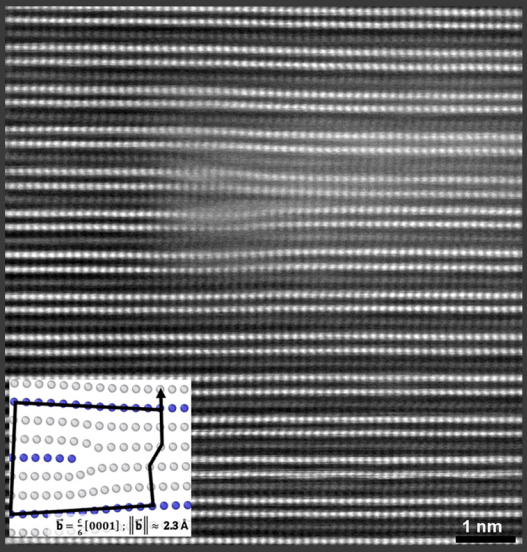

New Research Progress in Ti_2AlCN MAX Phases and Their Reinforced Magnesium Composites

Wenbo Yu

New Research Progress in Ti_2AlCN MAX Phases and Their Reinforced Magnesium Composites

New Research Progress in Ti_2AlCN MAX Phases and Their Reinforced Magnesium Composites

By

Wenbo Yu

Cambridge Scholars Publishing

New Research Progress in Ti_2AlCN MAX Phases and Their Reinforced Magnesium Composites

By Wenbo Yu

This book first published 2022

Cambridge Scholars Publishing

Lady Stephenson Library, Newcastle upon Tyne, NE6 2PA, UK

British Library Cataloguing in Publication Data
A catalogue record for this book is available from the British Library

ISBN (10): 1-5275-8318-X
ISBN (13): 978-1-5275-8318-4

The people who get on in this world are the people who get up and look for circumstances they want, and if they cannot find them, make them.
——Bernard Shaw

CONTENTS

Preface xi

Chapter 1 1
Introduction
1.1. Introduction of MAX phases 1
1.1.1. History, definition and interest 1
1.1.2. Crystallographic structure and electronic structure of MAX phases 3
1.2. MAX phase solid solutions 7
1.2.1. Substitution at M, A and X positions 7
1.3. Physical properties of MAX phases 13
1.3.1 Hardness measured by microindentation and nanoindentation tests 13
1.3.2. Electronic transport properties in the framework of the two-band model 18
1.3.3. Solid solution and vacancy effects on the transport properties 19
1.4. MAX reinforced Mg composites 21
1.5. Proposed further study 24
References 24

Chapter 2 34
Synthesis and microstructural characterization of $Ti_2Al(C_xN_y)$ ($x+y\leq1$) solid solutions and related end-members
2.1. Introduction 34
2.2. Optimization of Ti_2AlCx ($x<1$) MAX synthesis 38
2.2.1. The chemical composition obtained from 2Ti:1.1Al:1C 38
2.2.2. The effects of sintering condition and powder composition. 39
2.3. Synthesis and microstructural characteristics of Ti_2AlN_y ($y\leq1$) MAX phase 44
2.3.1. The effect of the reactant powder mixture composition 44
2.3.2. The effect of N content on Ti_2AlN lattice parameters 48
2.4. Synthesis and microstructural characteristics of $Ti_2Al(C_xN_y)$ solid solutions 51
2.4.1. Stoichiometric $Ti_2Al(C_xN_{1-x})$ solid solutions 51

2.5. Substoichiometric $Ti_2Al(C_xN_y)$ solid solutions (x+y<1) 53
2.5.1. Hypothesis 53
2.5.2. Microstructural characterization and discussion 54
2.6. Summary and conclusions 58
References 58

Chapter 3 62
Solid solution and vacancy effects in mechanical and physical properties of $Ti_2Al(C_xN_y)$ solid solutions
3.1 Introduction 62
3.2. Mechanical properties of $Ti_2Al(C_xN_y)$ solid solutions 63
3.2.1. Elastic modulus and intrinsic hardness of polycrystalline $Ti_2AlC_{0.45}N_{0.45}$ 63
3.2.2. Solid solution effect on the hardness and elastic modulus of $Ti_2Al(C_xN_y)$ MAX phases. 65
3.2.3. Vacancy effects on the hardness and elastic modulus of $Ti_2Al(C_xN_y)$ MAX phases 66
3.2.4. Vacancy effects on electronic localization and Density of states 67
3.3. Transport properties of $Ti_2Al(C_xN_y)$ solid solutions 71
3.3.1. Electronic structure and local order 71
3.3.2. Resistivity vs temperature measurements 76
3.3.3. Effect of solid solution on the resistivity of stoichiometric $Ti_2AlC_xN_{1-x}$ MAX phases 80
3.4. Conclusions 82
References 83

Chapter 4 87
Anisotropic transport properties of Ti_2AlC and Ti_3SiC_2
4.1 Introduction 87
4.1.1. Electronic transport properties in the framework of the two-band model 87
4.1.2 Contradiction in transport properties 89
4.2. Ti_2AlC transport properties anisotropy 90
4.2.1. Hall effect 90
4.2.2 Resistivity vs temperature measurements 94
4.2.3. Discussion and summary 99
4.3. Ti_3SiC_2 transport properties anisotropy 100
4.3.1. Resistivity and Hall coefficient measurements 100
4.3.2. Magnetoresistance measurements 105
4.3.3. Summary and conclusions 109
References 110

Chapter 5 115
Grain size effect on oxidation behavior of Ti_2AlC and atomic level reaction behavior between Ti_2AlC and Cu
5.1. Grain size effect in Ti_2AlC oxidation behavior 115
5.1.1. Introduction 115
5.1.2. Microstructure of FG and CG-Ti_2AlC bulks 116
5.1.3. Oxidation behavior and phase evolution 118
5.1.4. FIB-TEM investigations 124
5.1.5. The oxidation mechanism at the atomic level 127
5.2. Reaction behavior with Cu at the atomic level 128
5.2.1. Introduction 128
5.2.2. Diffusion and distribution of Cu and Al atoms 129
5.2.3. The formation of Ti_2C platelets 132
5.3. Conclusions 136
References 137

Chapter 6 142
Mechanical properties of Mg composites reinforced by Ti_2AlC and Ti_3SiC_2
6.1. Introduction 142
6.2. As-cast Ti_2AlC/Mg and Ti_3SiC_2/Mg composites 143
6.2.1. Microstructural characterization 143
6.2.2. Different tensile fracture between Ti_2AlC/Mg and Ti_3SiC_2/Mg 146
6.2.3. Effects of A-site atoms in Ti_2AlC and Ti_3SiC_2 reinforced Mg composites 150
6.2.4. In situ tensile fracture behavior of as-cast Ti_2AlC/Mg 153
6.2.5 Summary 157
6.3. Hot extruded Ti_2AlC/Mg composites 158
6.3.1. Microstructural characterization 158
6.3.2. Tensile properties 160
6.3.3. Compressive properties 163
6.3.4. Electrical resistivity 166
6.4. Summary 168
References 168

Chapter 7 173
Damping behavior and tribological properties of Ti_2AlC/Mg composites
7.1. Introduction 173
7.2. Damping capacity 174
7.2.1. Strain amplitude dependence of damping capacities 174

7.2.2. Temperature dependence of damping capacities 176
7.2.3. Dynamic Young's modulus 177
7.2.4. Damping mechanisms 179
7.2.5. Conclusions 184
7.3. Tribological properties 184
7.3.1. Wear rate 184
7.3.2. Worn surfaces and debris 186
7.3.3. The effect of Ti_2AlC orientation 193
7.3.4. Conclusions 195
7.4. Application of MAX/Mg composites 196
References 197

PREFACE

$M_{n+1}AX_n$ phases (M: transition metal, A: IIIA or IVA group element, and X: either carbon or nitrogen) are a class of ternary nitrides and carbides (n = 1 to 3), which possess both metal and ceramic-like properties. While they show the machinability, thermal shock resistance and electrical and thermal conductivity of metals, their high stiffness and corrosion and oxidation resistances are similar to those of ceramics. Up to now, more than 70 MAX phases have been synthesized. These phases have a hexagonal crystal structure that consists of edge-sharing $[M_6X]$ octahedrons interleaved with A layers; they are thus considered nanolaminated-layered materials. Strong M-X bonds and weaker M-A bonds associated with the nanolayered nature of the structure endow these solids with their unique combination of metal and ceramic properties. Furthermore, MAX phase solid solutions can be formed on any of the three sub-lattices: the M, A and X sites. This extra degree of freedom implies that the chemical/physical properties of the MAX phases may be modified and optimized by the replacement of various elements in the structure. Hence, MAX phases and MAX phase solid solutions have aroused great interest among scientists in physics, chemistry, and materials science.

Even if the stoichiometry of the $M_{n+1}AX_n$ compounds is generally assumed to be 2:1:1; 3:1:2 and 4:1:3 for n = 1, 2 or 3 respectively, differences from this "ideal" stoichiometry can exist and can strongly influence the physical properties. In other words, it would be of interest to know, not only the microstructure, but also the exact stoichiometry of the MAX phase compounds when comparing properties of MAX phases samples. As a result, one can think that the physical and chemical properties of MAX phases may be tuned by playing with substitution and vacancy content.

$Ti_2Al(C_xN_{1-x})$ compounds are one of the most important examples of MAX phase solid solutions on the X site. Since Ti-N and Ti-C have similar chemical bonding characteristics, resembling those of binaries TiC and TiN compounds, it is thus possible to form a wide range of $Ti_2Al(C_xN_{1-x})$ solid solutions with different physical properties. Indeed, the titanium-based compounds have been intensively investigated for high-temperature ohmic contacts on wide gap semiconductors. As a prerequisite

to their application for electrical contacts, the electronic properties of MAX phases, especially their anisotropic transport properties, and their modifications resulting from solid solution and/or vacancy effects have to be properly studied and understood.

Although intensively studied, the anisotropy of the MAX phase transport properties remains a complex issue since the majority of transport experiments were performed on polycrystalline samples, thereby averaging the basal plane and c-axis transport properties. To circumvent this point, several alternative approaches have been investigated, such as the probe of single grain plasmon excitation using electron energy-loss spectroscopy (EELS), the comparison between data obtained on (000l)-oriented thin films and bulk polycrystalline samples, or the comparison between thin films with different grain populations. In the two latter cases, the conductivity anisotropy is evidenced since the (000l)-oriented thin film room temperature (RT) resistivity and electron-phonon interactions are different from either the data recorded on the polycrystalline sample or the thin film exhibiting a different grain population.

In applications where high-temperature oxidation resistance in air is required, the oxidation kinetics of Ti_2AlC and Ti_3AlC_2 have been investigated. Their weight gain vs. time data is documented by cubic and parabolic models in air in the range of 800 to 1300 °C, as presented. Until now, there have been few reports to clarify these two mechanisms.

As a response to the increasing demand for new materials, tailored property composites are highly promising. One example is a composite of copper and MAX phases. In the framework of MAX-Cu composites, Ti-based MAX phases including Ti_3AlC_2, Ti_2AlC and Ti_2AlN have been used. It was reported that the de-intercalation of Al along basal planes induces the formation of Ti_xC platelets in Ti_3AlC_2-reinforced Cu composites. However, a comprehensively atomic-scale evolution during the diffusion of Cu in the Ti_2AlC MAX phase has not been investigated.

Among all structural materials, Mg alloys are regarded as the most attractive candidates for the reduction of vehicle weights, owing to their low density. However, the disadvantages of their poor stiffness and elevated temperature tensile strength restrict their wide utilization for applications. Hence, the development of new magnesium-based materials such as magnesium-based composites combining good mechanical properties, excellent tribological performance and a high damping capacity has become a hot research topic in recent years.

In such a context, this book is divided into seven chapters. Chapter 1 is a general introduction of MAX phases. It also describes lattice and electronic structures of the main MAX phases, and experimental and

theoretical research work on synthesis, mechanical and transport properties of the Ti-Al-C-N system. In addition, the vacancy effect and anisotropic transport properties of MAX phases are described.

Chapter 2 is devoted to the synthesis and microstructural characterization of highly pure and dense stoichiometric and substoichiometric $Ti_2Al(C_xN_y)$ solid solutions and related Ti_2AlC_x and Ti_2AlN_y end-members.

Chapter 3 deals with the mechanical and transport properties with respect to the vacancy content and solid solution effects in the Ti-Al-C-N system.

Chapter 4 is devoted to the anisotropic transport properties of Ti_2AlC and Ti_3SiC_2. Chapter 5 is about the grain size effect in the oxidation behavior of Ti_2AlC and the atomic level reaction behavior between Ti_2AlC and Cu.

Chapter 6 and Chapter 7 deal with the mechanical properties, damping behavior and tribological properties of Mg composites reinforced by Ti_2AlC and Ti_3SiC_2 MAX phases. Some of the potential applications for these composites are introduced.

As is always the case, there have been many people who have influenced the work concerned in this thesis. I am especially, deeply grateful to my Ph.D. supervisors, Sylvain Dubois and Véronique Gauthier-Brunet, and my master's supervisor, Shibo Li. It is certainly through their guidance, understanding, patience, and encouragement that I started to work on Ti_2AlCN. With their guidance, I grow not only as an experimentalist but also as an instructor and an independent thinker. I would like to give my thanks to Profs. Thierry Cabioc'h and Vincent Mauchamp. Thanks for use of the Rietveld refinement and theoretical explanation by ab initio calculations. Thanks to Prof Shoumei Xiong I had the inspiration for the introduction of MAX phases into a Mg matrix and fortunately was financed by the National Science Foundation of China and the State Key Lab of Advanced Metals and Materials.

I am also delighted to work with my collaborators Maxime Vallet, Antoine Guitton, Julien Guénolé and Weiwei Sun who made an everlasting impression on me with their talents and personalities. In addition, I am deeply appreciative of my student Chaosheng Ma due to his effortless corrections of the format of this manuscript.

Moreover, I am heartily thankful to Yang Zhou, Cuiwei Li and Zhengying Huang for their infinite help, not only with scientific problems, but also with personal ones. It is always wonderful to pass agreeable moments with them in the same office.

Last but not least, I am grateful for the support of the National Natural Science Foundation of China (No. 52175284 and 51701010), the State

Key Lab of Advanced Metals and Materials (No. 2021-ZD08), and the Pre-Research Program in National 14 th Five-Year Plan (No. 80923010304).

CHAPTER 1

INTRODUCTION

1.1. Introduction of MAX phases

1.1.1. History, definition and interest

In the 1960s, Hans Nowotny's group in Vienna discovered more than 100 new carbides and nitrides, accomplishing a gargantuan body of work[1]. Among these carbide and nitride phases were the so-called "Hägg phases" or "H phases" and their relatives Ti_3SiC_2 and Ti_3GeC_2. H phases are constituted of M_2X units (where M is a transition metal, and X is C and/or N) separated by the pure planes of an A-element (A being mostly an element of column IIIA or IVA of the periodic table); their chemical formula is M_2AX. The structures of Ti_3SiC_2 and Ti_3GeC_2 are similar to those of H phases—consisting of alternating pure Si or Ge planes and Ti_3C_2 units[1]. In the 1970s, a Russian group published work on the synthesis of Ti_2AlN and Ti_2AlC phases[2, 3], however, this work is unrecognized. This Russian group announced that the micro-hardness of these materials is in the range 21-24 GPa [2, 3], which is not compatible with the values admitted recently (3-12 GPa, see Table 1-7)[4]. Despite the impressive accomplishment of Novotny's group, these phases remained largely unexplored until the 1990s, when several researchers began to take a renewed interest in the H phases. The breakthrough contribution that triggered a renaissance came in the mid-1990s, when M. W. Barsoum and T. El-Raghy synthesized relatively pure-phase samples of Ti_3SiC_2[5] and revealed a material with a unique combination of metallic and ceramic properties. Like metals, Ti_3SiC_2 exhibits high electrical and thermal conductivities, and it is machinable. Moreover, it appears, like ceramics, to be extremely resistant to oxidation and thermal shock. Barsoum et al. demonstrated that Ti_3SiC_2 has a high yield point and presents plasticity behavior at 1300 °C. Furthermore, it is a self-lubricant. When M. W. Barsoum et al. later discovered Ti_4AlN_3[6], it became clear that these phases share a basic structure that gives them similar properties. This achievement led to the introduction of the "$M_{n+1}AX_n$ phases" (n = 1, 2, or

3) or “MAX phases” nomenclature, where M is a transition metal, A is an A-group element, and X is C and/or N (see Fig. 1-1).[7]

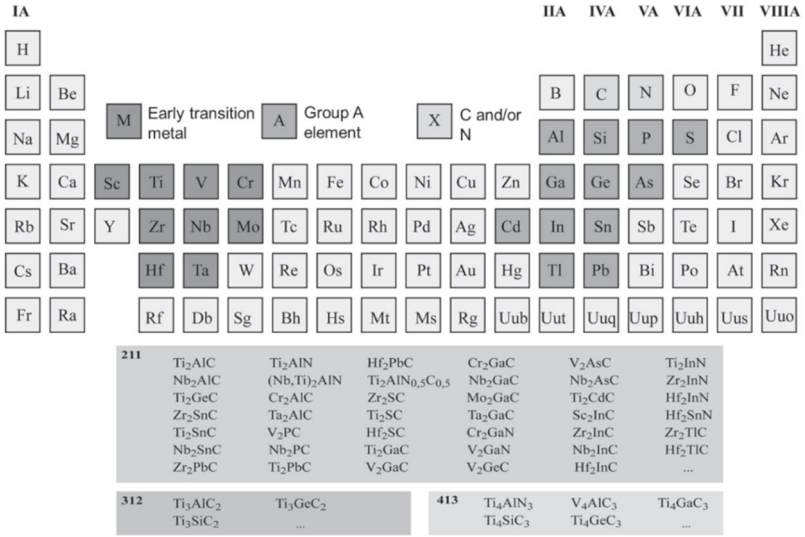

Fig. 1-1: Location of the elements of $M_{n+1}AX_n$ ternary nitrides and carbides in the periodic table[7].

From their lamellar structure, MAX phases are characterized by the exceptionally robust M-X bonds interleaved with the relatively weak M-A bonds. Therefore, MAX phases exhibit a combination of the merits of both metals and ceramics. Like ceramics, they are resistant to chemical attack, are oxidation resistant, quite stiff, and have relatively low thermal expansion coefficients[4, 8, 9]. Like metals, they are resistant to thermal shock, thermally and electrically conductive, damage tolerant and deform plastically at elevated temperatures[4, 8, 9]. Plastic deformation occurs via kink and shear band formation (see Fig. 1-2)[10-12]. Kink bands show almost no cracks at their boundaries (Fig. 1-2a) and the kink bands in $Cr_2Al(Si)C$ can even bend to 180° without fracture[13]. In the hexagonal structure of the MAX phases, dislocation slip is supposed to occur only in the basal planes. As dislocations are thought to be confined to basal planes[10, 14], they arrange themselves either in arrays in the basal plane or in walls perpendicular to basal planes [10]. Two dislocation walls of opposite Burgers vector form a kink band.

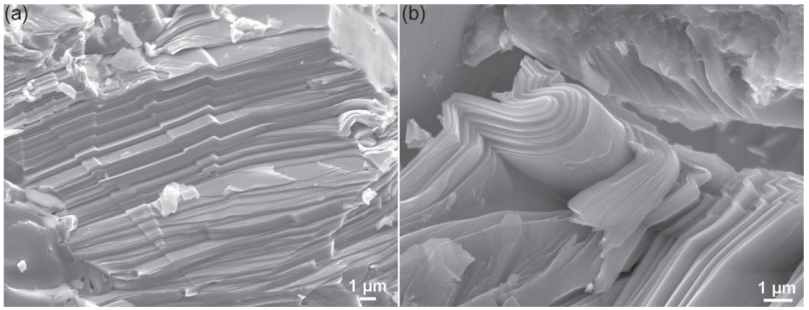

Fig. 1-2: SEM micrographs of the damage modes observed in the fracture surface of Cr_2AlSiC: (a–b) morphologies of kink bands[13].

Fig. 1-3 presents the potential applications for the MAX phases[15], including heating elements (a and b), gas burner nozzles in corrosive environments (c), high-temperature bearings (d), diamond/Ti_3SiC_2 composites for dry drilling of concrete (developed with Hilti Corp.) (e), examples of very thin walled parts manufactured by slip casting (f and g).

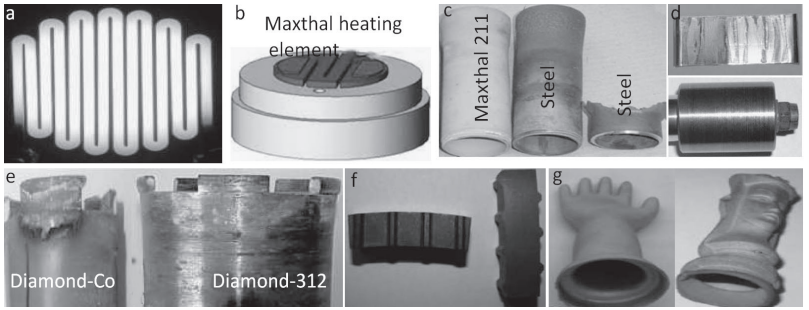

Fig. 1-3: Example of potential MAX phases applications courtesy of Kantal Corp. and 3-ONE-2[15].

1.1.2. Crystallographic structure and electronic structure of MAX phases

Crystallographic structure

The MAX phases are layered materials that crystallize in the hexagonal $P6_3/mmc$ space group. The unit cells of M_2AX, M_3AX_2 and M_4AX_3 phases are given in Fig. 1-4. One can notice that each structure consists of

alternate near-close-packed edge-sharing octahedral [M_6X] interleaved with layers of pure A elements. The main difference, among the structures of the so-called 211, 312 and 413 phases, is the number of M layers in between every two A layers. As can be seen in Fig. 1-4, two M layers exist in between two A layers in the 211 phases, and three M layers and four M layers in between two A layers in the 312 and 413 families, respectively.

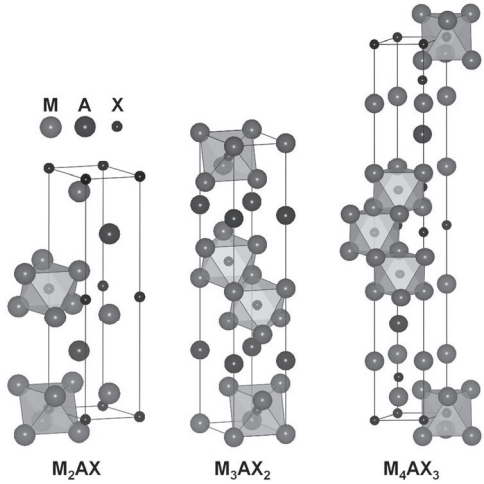

Fig. 1-4: The unit cells of the MAX phases for (a) 211, (b) 312 and (c) 413 classes.

Electronic structure of Ti_2AlC and Ti_2AlN

The electronic structure of a large number of MAX phases has been calculated (for 211 see [16-18], for 312 see [19-21] and for 413 see [22, 23]) through Density Functional Theory (DFT). In this section, we will focus on the electronic band structure, Total Density of States (TDOS) and Partial Density of States (PDOS) of one 413 phase (Ti_4AlN_3), one 312 phase (Ti_3SiC_2) and the two 211 phases investigated in this thesis (Ti_2AlC and Ti_2AlN). All of the reports indicate that there is no gap between the valence band and the conduction band. As a result, MAX phases should present metal-like conductivity, as indeed is demonstrated experimentally. At the Fermi level, the TDOS is mainly dominated by M 3d states, suggesting that the 3d states of the M element dominate the MAX phase's electronic conductivity. One can also notice that, for all MAX phases, the band structure shows strong anisotropic features. In Ti_3SiC_2, Ti_2AlN and Ti_2AlC, the bands are much less dispersive along the c-axis (i.e., along the Γ-A, H-K and M-L directions) than along the basal plane (i.e., along the Γ-

K and Γ-M directions). The Fermi velocity ($\partial E/\partial k$) should be higher along the basal plane than along the c-axis which would also result in very different conductivities in the basal plane and out of the basal plane. Finally, the strong ionic-covalent bonds between M and X and relatively weak ionic-covalent bonds between M and A formed in the (M_{II}-X-M_I-A) or (M_{II}-X-M_I-X-M_{II}-A) or (M_{II}-X-M_I-X-M_{II}-X-M_I-A) unit chains are responsible for the MAX phase high modulus and strength.

For example, the electronic band structure and the TDOS of Ti_2AlC and Ti_2AlN MAX phases, calculated by Hug et al. [24] in the frame of full-potential linearized augmented plane-waves formalism and tested using the generalized gradient approximation for the influence of the exchange and correlation potential, are shown respectively in Figs. 1-5 and 1-6. Minimization of the total energy with respect to the unit cell volume was adopted; the volume deviation was less than 1% between calculation and experiment. The electronic band structures are similar to the ones calculated by Zhou et al.[18]. In Fig. 1-5, it is clear that the bands are much less dispersive along the c-axis (i.e., along the Γ-A, H-K and M-L directions) than along the basal plane (i.e., along the Γ-K and Γ-M directions). This suggests that the electronic properties of Ti_2AlC and Ti_2AlN are anisotropic. The Fermi velocity ($\partial E/\partial k$) should be higher along the basal plane than along the c-axis.

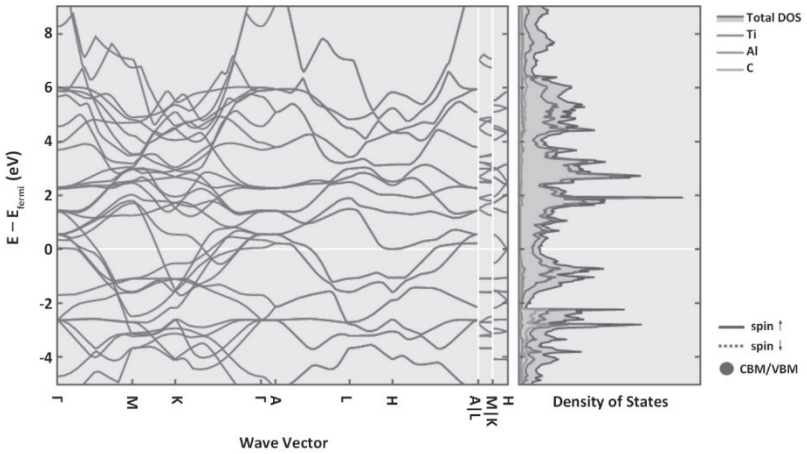

Fig. 1-5: The electronic band structure of Ti_2AlC MAX phases, TDOS and partial density of states of Ti_2AlC MAX phases.

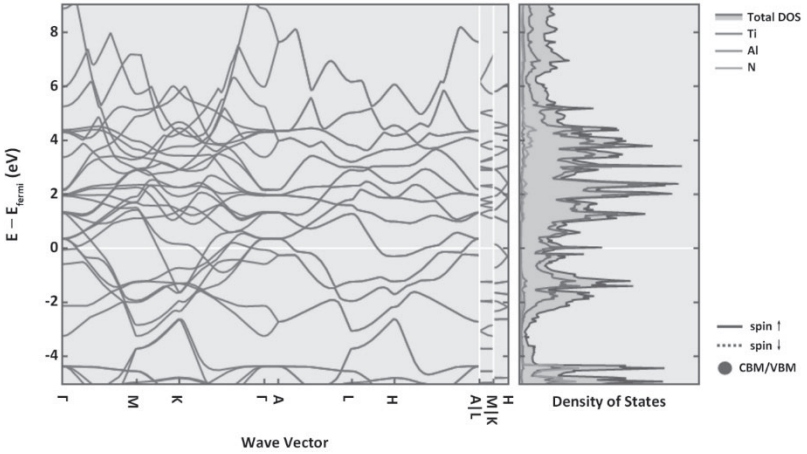

Fig. 1-6: The electronic band structure of Ti_2AlN MAX phases, TDOS and partial density of states of Ti_2AlN MAX phases.

Fig. 1-5 and Fig. 1-6 show the TDOS of the Ti_2AlC (a) and Ti_2AlN (b) MAX phases. Far from the Fermi level (E_F), the deep states are separated from the others by a gap of about 2 eV in the case of Ti_2AlC (-11.5 to -9.5 eV) and about 6.67 eV in the case of Ti_2AlN (-15.2 to -8.4 eV). The gap width is more or less important according to the composition of the MAX phase [24-26]. The bands continue from -8eV to the conduction band. There is no gap at the Fermi level which indicates that Ti_2AlC and Ti_2AlN have a metallic character as indeed has been demonstrated experimentally[27]. From the PDOS of Ti_2AlC and Ti_2AlN, one can notice that the PDOS of the two compounds is dominated, at the Fermi level, by the Ti-d states[24]. For Ti_2AlC and Ti_2AlN, the chemical bonding is dominated by strong hybridizations of Ti-d and Al-p states just below the Fermi level and of Ti p and N s (C s) states. The main difference in the electronic structure of these two compounds is related to the energy level of the hybridized states, such as Ti d –X p, X s. The N s (-15.9 to -15.1eV) and Ti d –N p (-6.7 to -4.2 eV) states are located at a lower energy level, compared to that of C s (-11.2 to -9.5 eV) and Ti d –C p (-5.2 to -2.1 eV) states. The gap difference has been attributed to the stronger electronegativity of N than C[24]. The charge transfers from the Al atom to Ti and N atoms in Ti_2AlN are much higher than the ones from the Al atom to Ti and C atoms in Ti_2AlC. As a result, stronger Ti-X bonds and Ti d-Al p bonds are expected in Ti_2AlN[24]. These calculations also predict that the electronic conductivity should be higher in Ti_2AlN than in Ti_2AlC, which is consistent with

experimental results[28].

Therefore, ionic-covalent Ti d-C/N p bonds are much stronger than ionic-covalent Ti d-Al p bonds. Thus, strong hybridization of Ti d-C/N p states is mainly responsible for the Ti_2AlC and Ti_2AlN high modulus and strength. The metal-like behavior of the Ti_2AlN and Ti_2AlC electronic transport properties results from the Ti d states.

1.2. MAX phase solid solutions

1.2.1. Substitution at M, A and X positions

It is worth noting that, in MAX phases, M, A and X elements either belong to the same group or are close to each other. As a consequence, the chemical and physical properties of the elements of each site are quite similar. One thus expects MAX phases to form a large number of isostructural solid solutions. In this section, some of the solid solutions reported in the literature will be described, as a function of the substitution site, in terms of synthesis techniques, microstructural characteristics and physical properties. As the MAX phase solid solutions synthesized in this manuscript are focused on substitution at the X site, an exhaustive discussion of the literature results will only be reported on these solid solutions.

Substitution at M site

Table 1-1 summarizes the synthesis conditions and some microstructural characteristics of different $(M_xM'_{1-x})_{n+1}AX_n$ solid solutions. $(Ti_{0.5}Zr_{0.5})_2InC$[29], $(Ti_{0.5}Nb_{0.5})_2AlC$[30], $(Ti_xV_{1-x})_2AlC$[31] and $(Cr_{0.5}V_{0.5})_2AlC$[32] can be synthesized by different techniques, such as Hot Isostatic Pressing (HIPing), and Hot Pressing (HPing), in the temperature range 1180-1600 °C. Most of the initial reactant mixtures contain the elements which constitute the final MAX phase solid solution (except for $(Ti_{0.5}Nb_{0.5})_2AlC$[30] which has been prepared from Al_4C_3). Some impurities such as MC binary carbides[29, 30], oxide of the A-element[30, 32] and MM' intermetallics[30] are detected in the final products.

In 2003, ab initio total energy calculations of the solubility of the M element within $(M_xM'_{2-x})AlC$ solid solutions (M and M'=Ti, V, Cr) have been performed by Sun et al.[33]. These results suggest that solubility is expected in the case of $(Cr_{1-x}V_x)_2AlC$ and $(Ti_{1-x}V_x)_2AlC$. Sun et al. have also predicted a strengthening effect (i.e., the bulk modulus is above the value given by a pure rule of mixture) in the $(M_xM'_{2-x})AlC$ (M and M' = Ti, V, Cr) system. These results have also been refined by Wang and Zhou

who have investigated the elastic stiffness and band structures of $(M_x,M'_{2-x})AlC$ solid solutions (M and M' = Ti, V, Cr) by means of the ab initio pseudo-potential total energy calculation method[34].

Table 1-1: Synthesis conditions and microstructural characteristics of some $(M_xM'_{1-x})_{n+1}AX_n$ solid solutions.

Processing methods	Nominal composition	Synthesis conditions	Phase composition Lattice parameters (Å)	Microstructure	Ref.
HIPing	Ti:Zr:In:C	PSing 650 °C/10 h/vacuum + HIP 1300 °C/12 h/70 MPa	$(Ti_{0.5}Zr_{0.5})_2InC$ (95 vol.%) TiC_x and ZrC_x (5 vol.%)	GS: 20-30 µm	[29]
	Ti:Nb:Al:C	1600 °C/8 h/100 MPa	$(Ti_{0.5}Nb_{0.5})_2AlC$ (98 vol.%) Al_2O_3 and Nb-Ti (2 vol.%) a=3.077 c=13.79	GS: 45 µm	[30]
	Ti:V:Al:C	1600 °C/8 h/70 MPa	$(Ti_{0.5}V_{0.5})_2AlC$ Al_2O_3 (2 vol.%)	GS: 25 µm	[35]
HPing	Ti:V:Al:C	1450 °C/1 h/20 MPa	$(Ti_xV_{1-x})_2AlC$ (x=0.05-0.2) Single phase *a* and *c* change linearly with x	GS: 39 µm in diameter and 19µm in thickness (all samples)	[31]
	Cr:V:Al:C	1180°C/8h/1.5GPa	$(Cr_{0.5}V_{0.5})_2AlC$ and $(Cr_{0.5}V_{0.5})C$ a=2.9773 c=12.0619	GS: 4-5µm	[32]
	Ti:Nb:Al:C	1450°C/24h/100 MPa	$(Ti_{0.5}Nb_{0.5})_2AlC$ Al_2O_3 and Nb-Ti (2 vol.%)	GS: 15µm Hv=5.8GPa	[30]

Substitution at the A-site

Table 1-2 lists the synthesis techniques and some microstructural characteristics of $M_{n+1}[A_{1-x}A'_x]C_n$ solid solutions. As is the case for $(M_xM'_{1-x})_{n+1}AX_n$ solid solutions, different techniques such as HIPing, HPing and Pressureless Sintering (PSing) have been used to synthesize $Ti_3(Al_xSn_{1-x})C_2$[34, 36], $Ti_3(Al_xSi_{1-x})C_2$[37, 38], $Ti_3(Si_xGe_{1-x})C_2$[39, 40], $Cr_2(Al_{0.96}Si_{0.13})C$[41] and $Cr_2(Al_xGe_{1-x})C$[42] in the temperature range 1200 - 1600 °C. Some impurities such as MC binary carbides[39, 40], oxide of the A-element[41] and MA intermetallics[41] were detected in the final products.

Wang et al.[43] and Xu et al.[44] predicted, through a plan-wave pseudo-potential method based on DFT, that lattice parameters of $Ti_3(Si_{1-x}Al_x)C_2$ would follow Vegard's law with increasing Al content. This result was partially proven by Zhou et al.[37] by investigating $Ti_3(Si_{1-x}Al_x)C_2$ ($x \leq 0.25$) solid solutions. Indeed, the *c*-lattice parameter decreases with increasing Si content whereas the *a*-lattice parameter remains almost unchanged. Recently, a set of $Ti_3(Al_xSn_{1-x})C_2$ solid solutions has been successfully synthesized by Dubois et al.[34, 36] through HIPing process at the PPRIME Institute. It has been demonstrated that $Ti_3(Al_xSn_{1-x})C_2$ are ideal solid solutions obeying Vegard's law since the c/a ratio varies linearly with the Al content. Furthermore, it has been shown that solid solution strengthening is not operative in the Ti-Al-Sn-C system. Elastic modulus is found to increase non-monotonically from Ti_3SnC_2 to Ti_3AlC_2[34]. Similar results (i.e., no solid solution strengthening) have been obtained by Ganguly et al.[39] for the $Ti_3(Si_{(1-x)}Ge_x)C_2$ solid solutions.

Table 1-2: Synthesis conditions and microstructural characteristics of some $M_{n+1}[A_{1-x}A'_x]C_n$ solid solutions (GS: grain size).

Process-ing methods	Nominal composition	Synthesis conditions	Phase composition Lattice parameters (Å)	Micro-structure	Ref.
HIPing	Ti:Sn:Al:C Ti:Sn:Al:C	1200-1500 °C/1-8 h/50 MPa	$Ti_3(Al_xSn_{1-x})C_2$ (Main phase) TiC and $Ti_2(Al_xSn_{1-x})C$ *c/a* changes linearly with x	GS:10-80 µm Solid solution softening	[34, 36]
	3Ti:0.5Ge:0.5Si:2C	1450 °C/8 h/172 MPa	$Ti_3(Si_{0.5}Ge_{0.5})C_2$ (96vol.%) TiC (4 vol.%) a=3.082 c=17.751	GS: 7 ±3 µm	[39, 40]
	3Ti:0.25Ge:0.75Si:2C	1600 °C/8 h/172 MPa	$Ti_3(Si_{0.75}Ge_{0.25})C_2$ (97vol.%) TiC (3 vol.%) a=3.074 c=17.747	GS: 70±56 µm	[39, 40]
HPing	Ti:(1-x)Al:xSi:C (x≤0.25)	1500 °C/1 h/30 MPa	$Ti_3(Al_{1-x}Si_x)C_2$ single phase a is stable *c* changes linearly with x	GS: 20 µm	[37, 38]
	2Cr:1.1Al:0.2Si:C	1450 °C/1 h/30 MPa	$Cr_2(Al_{0.96}Si_{0.13})C$ Minor impurities: Al_2O_3 and Cr_5Si_3	GS: 50 µm	[41]
PSing	Cr:Al:Ge:C	1400°C/4h/Ar	$Cr_2(Al_xGe_{1-x})C$ (x=0,0.25,0.5,0.75,1) *c*-lattice parameter increases with x *a*-lattice parameter decreases with x	Not mention-ed	[42]

Substitutions at X site

Table 1-3 summarizes the synthesis conditions and some microstructural characteristics of $Ti_{n+1}Al(C_xN_{1-x})_n$ solid solutions. As compared to the studies dedicated to solid solutions on the M and A sites, only two elements (C and N) correspond to the X site in MAX phases. Only HIPing and PSing have been used to synthesize $Ti_3Al(C_{0.5}N_{0.5})_2$[45, 46], $Ti_2Al(C_{0.5}N_{0.5})$[45, 47] and $Ti_2Al(C_xN_{(1-x)})_y$ (x = 0; 0.25; 0.5; 0.75; 1 and $0.7 \leq y \leq 1$)[48] in the temperature range 1300-1400 °C. Some impurities such as TiC[45, 46], Ti(C,N)[6], Al_2O_3[45, 47], TiAl[48] intermetallics and the Ti_3AlC_2[48] MAX phase were detected in the final products. It thus appears as a challenge to synthesize highly pure $Ti_2Al(C_xN_y)$ phases.

As MAX carbonitrides, $Ti_2Al(C_xN_{1-x})$ phases are one of the most important examples of MAX phase solid solutions on the X site. Since Ti-N and Ti-C have similar chemical bonding characteristics, resembling those of binaries TiC and TiN compounds[49], it is thus possible to form a wide range of $Ti_2Al(C_xN_{1-x})$ solid solutions with different physical properties. For example, a $Ti_2Al(C_{0.5}N_{0.5})$ solid solution is reported to be significantly harder than either of its end-members Ti_2AlC and Ti_2AlN. Stoichiometric and substoichiometric $Ti_2Al(C_xN_{(1-x)})_y$ solid solutions have been recently synthesized by Cabioc'h et al.[48] with x = 0; 0.25; 0.5; 0.75; 1 and $0.7 \leq y \leq 1$ by reactive PSing for 4 h at 1400 °C. The authors have shown that irrespective of the number of vacancies on the X site, the *a*-lattice parameter obeys Vegard's law whereas the *c*-lattice parameter of the carbonitrides is smaller than that of the end-members.

Table 1-3: Synthesis conditions and microstructural characteristics of some $Ti_{n+1}Al(C_xN_{1-x})_n$ solid solutions (GS: grain size).

Process-ing methods	Nominal composi-tion	Synthesis conditions	Phase composition Lattice parameter(Å)	Micro-structure	Ref.
HIPing	Ti:Al:C:N	1400 °C/10 h/100 MPa	$Ti_3Al(C_{0.5}N_{0.5})_2$ (95vol.%) TiC (2 vol.%) Al_2O_3 (3 vol.%) c/a changes linearly with C content	GS: 25±15 μm	[45, 46]
	Ti:Al:0.5 C:0.5N	1300 °C/15 h/40 MPa	$Ti_2Al(C_{0.5}N_{0.5})$ (96 vol.%) Al_2O_3 and Ti_3P (4 vol.%)	GS: 25 μm Solid solution strengthening	[45, 47]
PSing	Ti:1.1Al: C:N	1400 °C/4 h/ Ar	$(Ti_2AlC_xN_{1-x})_y$ With minor impurities: Ti_3AlC_2,TiAl, Ti(C,N)	GS: 2-10 μm	[48]

In 1999, Barsoum et al. reported[45, 47, 50] the solid solution strengthening effect in the Ti-Al-C-N system using microindentation tests. For the two Ti_2AlC and Ti_2AlN end-members, their hardness values were about 4.5 GPa and 4 GPa, respectively. The $Ti_2AlC_{0.5}N_{0.5}$ solid solution sample had a value of around 5.5 GPa.

In 2007, Radovic[45] reported Poisson's ratio, Young's modulus E, shear modulus G and longitudinal v_l and shear v_s sound velocities of $Ti_2AlC_{0.5}N_{0.5}$ and two Ti_2AlN samples[51, 52] (more details about their microstructural characteristics are given in Table 1-2). The different parameters measured for $Ti_2AlC_{0.5}N_{0.5}$ and for both end-members [45, 51, 53] by Resonant Ultrasound Spectroscopy (RUS)[45] are listed in Table 1-4. It was found that substituting C with N increased E and G in the solid solution. Furthermore, the decrease in v_s for $Ti_{1.93}AlN_{0.975}$ as compared to $Ti_2AlN_{0.996}$ was attributed to the influence of vacancies; this phenomenon was also reported in binary TiX compounds[54]. For example, ab initio

calculations predict that the introduction of 12.5% vacancies in TiN_x reduces its shear modulus from 180 GPa to less than 150 GPa[55], which is in compatible agreement with experimental results[4].

Table 1-4[45]: Summary of Young's modulus E, shear modulus G, longitudinal υ_l and shear υ_s sound velocities measured by RUS.

Sample	Composition	E (GPa)	G (GPa)	υ_l (m/s)	υ_s (m/s)	Reference
Ti_2AlC	Not measured	278	119	8590	5423	[53]
$Ti_2AlC_{0.5}N_{0.5}$	Not measured	290	123	8670	5407	[45]
Ti_2AlN(a)	$Ti_2AlN_{0.996}$	285	120.5	8553	5328	[45, 51]
Ti_2AlN(b)	$Ti_{1.93}AlN_{0.975}$	277	112	8700	5100	[45, 51]

1.3. Physical properties of MAX phases

1.3.1 Hardness measured by microindentation and nanoindentation tests

Table 1-5 summarizes hardness values of selected MAX phases determined either by microindentation or by nanoindentation tests.

The Vicker's hardness values of polycrystalline MAX phases were distributed in the 3-8 GPa range for microindentation tests, which is much lower than the ones obtained by nanoindentation tests (which were in the range 7-12 GPa). Such a difference has been studied by Bei et al. [34]. As an example, Bei et al. measured Ti_3AlC_2 hardness using nanoindentation and microindentation tests; the results are given in Fig. 1-7. Using the nanoindentation test, Ti_3AlC_2 hardness is a function of the indenter penetration depth, which is attributed to an indentation size effect. Such an effect is well fitted by the Nix and Gao model[56] and hardness reaches a limiting value of 11.4±0.7 GPa[34] for penetration depths in the range 200-300 nm. Such a limiting value is defined as the intrinsic hardness of Ti_3AlC_2. For deeper penetration depth (in the range 400-600 nm in Fig. 1-7), nanoindentation and microindentation tests lead to the same hardness

values (about 7 GPa in Fig. 1-7). At deeper penetration depths (in the range 600-1700 nm in Fig. 1-7), hardness values measured by microindentation tests continue to decrease. Considering MAX phase grain size, in the range of 2-100 µm[41, 47, 57, 58] several grains are involved in the deformation process during microindentation or nanoindentation tests performed at large indenter penetration depths [34]. Thus, hardness values determined at high loads (large penetration depths) consist of a mean value that takes into account grain boundaries and also impurities (TiC[59, 60], TiN[6] and oxide TiO_2[61], Al_2O_3[30, 57]). Upon increasing the penetration depth, more and more grain boundaries and impurities have to be taken into account and thus this leads to a decrease of the microindentation hardness values. Finally, one can extract the intrinsic hardness of MAX phases through nanoindentation in order to avoid the influence of second phases, impurities and grain boundaries. Moreover, a local determination of the MAX phase composition and grain size may allow determining the stoichiometry and grain sizes effects on mechanical properties (elastic modulus and hardness).

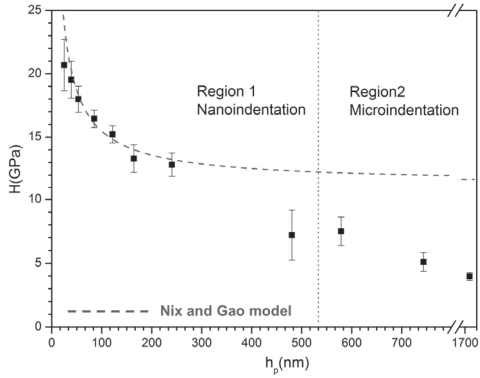

Fig. 1-7[34]: Hardness (squares) of Ti_3AlC_2 as a function of the indenter penetration depth in nanoindentation tests and microindentation tests.

Ti_2AlC hardness values, determined using microindentation tests, were in the range 2.8-5.8 GPa. Such differences in the values may result from grain size and/or carbon stoichiometry. Indeed, Bai et al. have determined, using microindentation tests, that 6 µm grained $Ti_2AlC_{0.69}$ has a hardness value of 5.8 GPa[62]. Yu et al.[41] have measured, using microindentation tests, hardness values of coarse-grained (CG) and fine-grained (FG) Cr_2AlC. A large grain size effect has been evidenced (see Table 1-5). Nevertheless, the reliability of the results is not good considering what has

Table 1-5: Summary of hardness and Young's modulus of selected MAX phases determined by microindentation and nanoindentation tests (L: length of lamella, W: width of lamella). The grain size values are given as average diameters.

	Sample	Grain size (μm)	Phase composition	Load	Hardness (GPa)	Young's modulus (GPa)	Reference
Microindentation	$(Ti_x,V_{1-x})_2AlC$ (x=0.2)	W:19 ± 5 L:39 ± 10	$(Ti_{0.8}V_{0.2})_2AlC$	10 N	3.5-4.5		[31]
	Ti_2AlN	100	10-20 vol.% Al_2O_3, Ti_3P and Ti_4AlN_3	0.5-10 N	4	285	[47]
	$Ti_2AlC_{0.5}N_{0.5}$	25	4 vol.% Al_2O_3 and Ti_3P	0.5-10 N	5.5	290	[47]
	Ti_2AlC	W: 5 L: 20	pure	10N	2.8		[63]
	Ti_2AlC	25	10-15 vol.% Al_2O_3 and Ti_3P	0.5-10 N	4.5		[47]
	Ti_2AlC	W:16 ± 4 L:41 ± 12	Ti_2AlC	10 N	3.5		[31]
	$Ti_2AlC_{0.69}$	6	$Ti_2AlC_{0.69}$ TiAl	50 N	5.8		[62]
	Ti_2AlC	15	pure	10 N	4.2-5.7		[58]
	Cr_2AlC	35	pure	500 N	3.5		[41, 57]
	Cr_2AlC	2	pure	500 N	6.4		
	Ti_2SC	2-4	6 vol.% TiO_2	2-300 N	7-8		[61]
		10-20			6-7		
	Ti_3AlC_2	5	pure	100 N	5.5-6		[60]
	Ti_3AlC_2	35	pure	100 N	3.5-4.5		

Nanoindentation	Ti_3AlC_2	W: 10-40 L: 60-100	pure	1-250 mN	11.4±0.7	260	[34] [64]
	$Ti_3Al_xSn_{(1-x)}C_2$ X=0.25,0.5,0.8		$Ti_3Al_xSn_{(1-x)}C_2$ $Ti_2Al_xSn_{(1-x)}C$ TiC	1-300 mN	7-11	200-250	[36] [34]
	Ti_3SnC_2	W: 3-5 L: 10-15	80.5%Ti_3SnC_2 16.2% TiC 1.1% $FeSn_x$ 2.2% Sn	1-300 mN	9.3	245	[65]

been described previously. It also seems that solid solution hardening can be observed in $Ti_2AlC_xN_{1-x}$ solid solutions. Indeed, Young's modulus and hardness values were higher for $Ti_2AlC_{0.5}N_{0.5}$ than for the end-members. These results are likely to be reliable as Young's modulus is an elastic property that is not affected by penetration depth.

Many of the MAX phases are excellent metal-like electrical conductors [27, 51] [66] [67] [68] [69]. Some of them, such as Ti_3SiC_2, and Ti_3AlC_2, are better conductors than Ti metal itself. Most interestingly, many of the MAX phases whose transport properties have been characterized to date are thought to be compensated conductors. Both electron-like and hole-like states contribute in approximately equal numbers to electrical conductivity. Such a feature has been evidenced by measuring the Hall [51] [70-72] and Seebeck [73] coefficients: the measured coefficients tend to fluctuate around zero and give either slightly positive or slightly negative values. By calculating the components of the thermoelectric tensor of Ti_3SiC_2 in the basal plane and along the c-axis, L. Chaput et al. have demonstrated that they have opposite signs, respectively positive and negative[74]. As a consequence of an almost perfect compensation of both tensor components, the Seebeck coefficient of polycrystalline Ti_3SiC_2 samples, in which the components are averaged, is almost zero. The calculated components of the thermoelectric tensor and its trace are shown in Fig. 1-8. There are nevertheless exceptions. Indeed, transport properties of Ti_4AlN_3 are dominated by hole-like states[75] whereas transport properties of Ti_2SC are dominated by electron-like states[51].

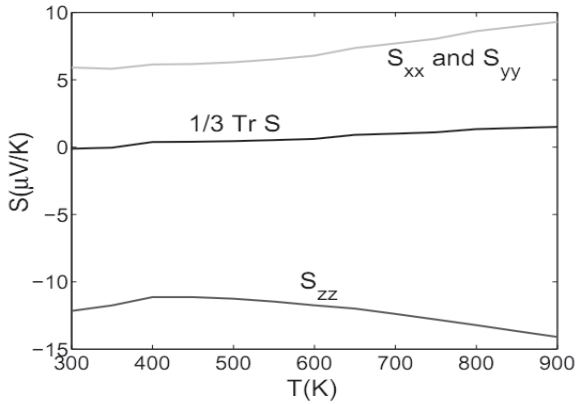

Fig. 1-8[74]: Calculated components of the thermoelectric tensor and its trace as a function of the temperature of the Ti_3SiC_2 MAX phase.

1.3.2. Electronic transport properties in the framework of the two-band model

The combination of small Hall (R_H) and Seebeck coefficients, the linearity of the Hall voltage with magnetic field and finally the parabolic non-saturating magnetoresistance strongly suggest that many of the MAX phases are compensated conductors. In that case, the following equations in the two-band model can be applied:

$$\sigma = \frac{1}{\rho_0} = e(\mu_p p + \mu_n n) \qquad (1-1)$$

$$R_H = \frac{\left(\mu_p^2 p - \mu_n^2 n\right)}{e\left(\mu_p p + \mu_n n\right)^2} \qquad (1-2)$$

$$MR = \frac{\Delta\rho}{\rho_0} = \alpha B^2 = \frac{np\mu_p\mu_n\left(\mu_p + \mu_n\right)^2}{\left(\mu_p p + \mu_n n\right)^2}\ B^2 \qquad (1-3)$$

Where,

e is the electron charge.

σ is the conductivity.

R_H is the Hall coefficient.

n and p are the electron-like and hole-like charge carrier density.

μ_n and μ_p are their respective mobilities.

MR is the magnetoresistance.

The MR is defined as $\Delta\rho/\rho_0 = (\rho_B - \rho_0)/\rho_0$, where ρ_B is the resistivity in the presence of magnetic field B, $\rho_0$is the resistivity in the absence of a magnetic field and α is the magnetoresistance coefficient.

In these equations, n, p, μ_n and $\mu_p$are unknown. Assuming that MAX phases are compensated conductors leads to n = p [1] which allows simplifying equations (1-1) to (1-3) as follows:

$$\sigma = \frac{1}{\rho_0} = ne(\mu_p + \mu_n) \qquad (1-4)$$

$$R_H = \frac{\left(\mu_p - \mu_n\right)}{ne(\mu_p + \mu_n)} = \frac{(1-b)}{ne(1+b)} \qquad (1-5)$$

$$MR = \frac{\Delta\rho}{\rho_0} = \alpha B^2 = \mu_p\mu_n B^2 \qquad (1-6)$$

where b is the ratio μ_n/μ_p.

M. W. Barsoum and co-workers[27, 51, 66, 68, 76, 77] used equation (1-6) to determine electron-like and hole-like mobilities; in a first approximation

[1] M. W. Barsoum et al. assume n = p or $\mu_n = \mu_p$.

they also assumed that $\mu_n = \mu_p$. One can notice that such an assumption implies that RH = 0. Nevertheless, it seems not difficult to adjust μn and μp to yield the correct values and signs for RH. Moreover, the mobility values are relatively close to each other as stated by equation (1-5) and by the low value of the Hall coefficients. In the worst case for which RH is the highest, such as for Ti2SC[78], an exact calculation yields μ_n = 0.017 $m^2V^{-1}s^{-1}$ and μ_p = 0.014 $m^2V^{-1}s^{-1}$ instead of the mean value 0.015 $m^2 V^{-1} s^{-1}$ determined by assuming $\mu_n = \mu_p$ in equation (1-6).

1.3.3. Solid solution and vacancy effects on the transport properties

It has been shown that the electrical resistivity of solid solutions increases compared to that of the related end-members [51, 79]. Such a result has been ascribed to a decrease of the charge carrier mobility which, itself, results from solid solution scattering (i.e., from the scattering of the electrons by substituted atoms). As the conductivity is dominated by the density of states (DOS) at the Fermi level of the d orbitals of the M element, substitution on the different sites (M, A or X) of the MAX phase does not have the same impact on the resistivity.

Substitution on the A-site appears to slightly modify the resistivity. For example, substituting 25% of Si atoms by Al atoms leads to an increase in the room temperature resistivity from 35 to 37 $\mu\Omega \bullet cm^{-1}$[80]. Consistent with the fact that the DOS at the Fermi level is dominated by the d orbitals of the M element, substitution on the M site leads to a large increase in the resistivity in the [Ti-Nb]-Al-C[66] and [Cr-V]-Al-C systems[79]. Transport properties of X site substituted solid solutions has been studied by SE. Lofland et al.[27]. The samples which contained both N and C had higher residual resistivity and lower residual resistivity ratios (RRR = ρ(300K) / ρ(4K)) than the samples which contained only C or N. Such an effect is attributed to solid solution scattering. It is well known that vacancies in corresponding binary carbides and nitrides are potent electron scatterers[81, 82]. A lower concentration of vacancies in the a-sample could explain the difference in residual resistivities (Table 1-6).

By using the two-band model, Scabarozi and co-workers have determined n, p, μ_n, μ_p for the different samples. These different parameters are summarized in Table 1-6.

Table 1-6 clearly indicates that despite wide variations in R_H values (-27 to 90×10^{-11} $m^3 \bullet C^{-1}$), α (0.03 to 690 $\times10^{-5}$ T^{-2}) and mobilities (0.34 to 83 $m^2 V^{-1} s^{-1}$) in the temperature range of 4-300 K, the average and standard deviations in n and p are, respectively, $(0.8 \text{ to } 1.71)\times10^{+27}$ and (1.05 to 0.7)

Table 1-6[27]: Summary of electrical transport parameters as calculated from the RT and 4K resistivity, R_H and α results for the X site substituted solid solutions assuming $\mu_n = \mu_p$.

Composition	Temperature (K)	ρ μΩ cm^{-1}	R_H(10^{-11}) (m^3 C^{-1})	α(T^{-2}) 10^{-5} (m^4 V^{-2} s^{-2})	$\mu_n=\mu_p$ 10^{-3} m^2 V^{-1} s^{-1}	n (10^{27} m^{-3})	p (10^{27}/ m^{-3})	Ref.
Ti_3AlC_2	300 4	35.3 18.1	-1.2 1.0	3.7 11	6.3 10	1.41 1.71	1.4 1.73	[27]
	300	38.7	-1.2	4	μ_n=4.6-4.2 μ_p=5.4-30	1.5-1.6	2-4	[75]
Ti_3AlCN	300 4	40 27	17.4 33	0.65 3.3	2.5 5.7	2.5 1.8	3.5 2	[27]
Ti_2AlC	300 4	36 7.3	-27 -8	2.6 45	5.1 21	1.39 2.1	1.2 1.9	[27]
	300	36	28	20	μ_n=9 μ_p=8.2	1	1	[67]
$Ti_2Al(C_{0.5}N_{0.5})$	300 4	36 12.6	45.6 60	3.5 22	5.9 15	1.1 1.2	1.8 2.4	[27]
Ti_2AlN-a($Ti_2Al_{1.04}N_{0.98}$)	300 4	25 2.9	-3.9 6.1	17 690	12 83	1.02 1.24	1.05 1.3	[27]
Ti_2AlN-b ($Ti_2AlN_{0.95}$)	300 4	34.3 12.3	-7 16	4.8 20	6.3 14	1.46 1.6	1.4 2.0	[27]
$Ti_4AlN_{2.9}$	300 300	26.1 26.1	90 90±5	0.03 0.03	0.55 μ_p=0.34	0.8	3.51 7.0	[75]

$\times 10^{+27}$ m^{-3}. Scabarozi et al. concluded that it seems reasonable to consider that n=p for all compounds investigated. Moreover, the charge carrier density seems to increase slightly going from Ti_2AlN to Ti_2AlC. Such a result is nevertheless in contradiction to the fact that the TDOS of Ti_2AlC

(2.76 eV unit cell^{-1}) is smaller than that of Ti_2AlN (3.9 eV unit cell^{-1})[24]; the charge carrier density is proportional to the cube of the TDOS in a degenerate electron gas.

Wet chemical analysis and electron dispersive spectroscopy were performed on the Ti_2AlN-a and Ti_2AlN-b samples. The authors have shown that the two samples have slightly different stoichiometry, respectively $Ti_2Al_{1.04}N_{0.98}$ and $Ti_2AlN_{0.95}$. Thus, Scabarozi et al.[27] attributed the higher resistivity of the Ti_2AlN-b sample to the presence of vacancies that are known to be potent electron scatters. Indeed, it has been shown that, in binary transition carbides, vacancies contribute to an increase of the residual resistivity and to the charge carrier density[81, 83]. $Ti_4AlN_{2.9}$, with its nitrogen deficiency, has the lowest hole mobility (about 3×10^{-4} $m^2\,V^{-1}\,s^{-1}$) of all MAX phases measured to date. Such a result is in compatible agreement with the fact that vacancies are strong electron scatters. These comments notwithstanding, it is clear that more work is needed in this field in order to get a better understanding of the relationship between stoichiometry and transport properties in these materials. To our knowledge, the experimental results obtained by Scabarozi et al. are the only existing results that look at the relationship between stoichiometry and transport properties.

1.4. MAX reinforced Mg composites

To meet the requirements of reducing the weight of transport vehicles, especially automobiles, the lightest structure magnesium metal is regarded as one of the attractive candidates[84, 85]. Introducing other elements into the Mg alloy by the alloy design method could ameliorate its stiffness and mechanical properties of pure Mg at high temperatures. For example, by adding 4% RE (mischmetal) into Mg alloy to form AE44 alloy (4% Al and 4% RE) [86, 87], the newly formed Al_xRe_y ($Al_{11}Re_3$) phase could stabilize the $Mg_{17}Al_{12}$ phase at high temperatures[88]. However, the stiffness and wear resistance of Mg alloy are still relatively low and the application of Mg alloys into automobile cylinders is still restricted because of the requirements for high stiffness, wear resistance and lubricating capacity at elevated temperatures.

To overcome this restriction, especially to simultaneously enhance the stiffness and superior wear resistance of the Mg alloy, the only effective method is to fabricate magnesium composites through the introduction of ceramic particles into the Mg alloy[89-91]. Until now, the most widely used reinforcements to the Mg matrix are SiC[92, 93], Al_2O_3[88] and graphite particulates[94-96]. SiC and Al_2O_3 particles could strongly ameliorate the

mechanical properties and wear resistance of the matrix[97-99], while the damping and self-lubricating capacities of magnesium composites are reduced[95]. High damping and layered graphite could improve the damping and self-lubricating capacities of magnesium composites[95, 96]. Unfortunately, graphite particulates rapidly degrade when the temperature is above 300 ℃, especially in an oxidizing environment. In addition, the results reported that cracks are generally initiated from the interfacial areas in these composites due to the weak interfacial bonding[88, 92, 93, 96].

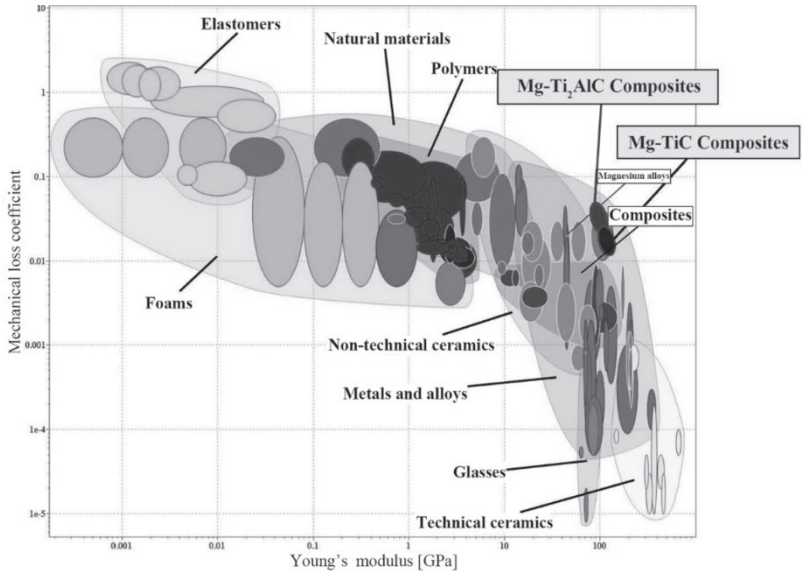

Fig. 1-9: Ashby map showing the log-log relationship between damping and Young's moduli of solids.

Herein, high-temperature-stable reinforcing particles owning desirable wear resistance, self-lubricating capacity and wettability with magnesium are crucially desired in magnesium composites. Recently, Anasori et al. prepared Mg matrix composites with 50% vol. Ti_2AlC content by the infiltration method. Under 250 MPa compressive stress, the volume energy consumption coefficient of Ti_2AlC/Mg composites was 0.34 MJ m^{-3}. In the cyclic loading experiment, a single cycle can absorb 30% of the energy, which is the best composite among all materials[100]. The results show that the excellent mechanical properties of Ti_2AlC Mg matrix composites come from the dispersion strengthening of the Ti_2AlC

reinforced phase, and its excellent damping properties mainly come from the formation and movement of dislocation circles in Ti_2AlC materials and the damping capacity of the Mg matrix. It can be seen from Fig. 1-10 (b) that the damping capacity of Ti_2AlC Mg matrix composites is better than that of TiC-Mg and SiC-Mg matrix composites[100, 101].

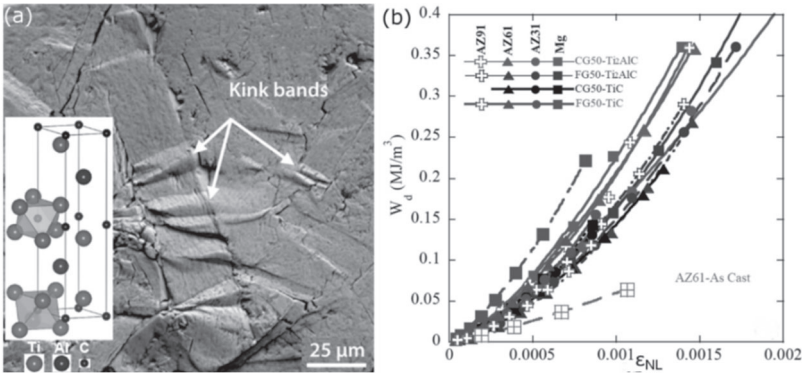

Fig. 1-10: (a) Plastic deformation of Ti_2AlC grain and the cell structure of Ti_2AlC (b) Strain stress curve of Ti_2AlC / Mg matrix composites[100].

Furthermore, measurements of lattice parameters with numerous methods have revealed that MAX phases exhibit elevated high crystalline anisotropy. The c/a ratio is generally higher than 4. MAX phases synthesized by powder metallurgy are polycrystalline bulk samples with random grain orientations[102]. It is commonly observed that during synthesis grains grow in platelet shapes. Because of the high crystalline anisotropy, platelet surfaces are parallel to basal planes. Therefore, projections on the surface are observed as rectangles with a high aspect ratio. This penny-shape causes deviations from Schmid's law[103]. From the view of energy, their plastic deformation behavior is only caused by basal dislocations[104, 105]. Furthermore, their inherent nanolayered structure endows these ternary compounds with a unique combination of metal-like and ceramic-like properties[100, 104, 106]. The MAX phase microstructure results in an exceptional self-lubricating behavior. For example, Ti_2AlC exhibited a low wear rate (1.8×10^{-6} mm Nm^{-1}) during dry sliding against a steel disk[107]. The strong anisotropic mechanical and tribological properties were anticipated in MAX phases[9, 29-31].

1.5. Proposed further study

From the simulation, the weak C-N interactions were not sufficient to result in significant strengthening of $Ti_2AlC_xN_{1-x}$ compounds according to Du et al.[50] and Arroyave[108]. Such a result is nevertheless not compatible with experimental results obtained by Barsoum[47] and Radovic[45]. Therefore, this contradiction needs further work to better understand the role of vacancies on the X site and the effect of solid solutions between C and N.

Understanding the electrical properties of the MAX phases is one of the most important and difficult research challenges in the field. From the experimental side, a reliable determination of the anisotropy in conductivity is needed. In general, a direct measurement of the conductivity along different crystal orientations requires sufficiently large single crystals. Another important contribution would be the synthesis of epitaxial thin films with out-of-plane orientation; this would potentially allow a direct measurement of the anisotropy in the conductivity. Improved understanding of the influence of chemistry (vacancies, substitution) and defects (dislocations) is needed. From the theoretical side, calculations to elucidate the roles of vacancies on the DOS, the role and anisotropy of the electron-phonon coupling are important.

As the configuration of MAX phases is generally characterized with different aspect ratios and the extent of particle loading by the shear mechanism is also dependent on the aspect ratio of the reinforcing particles[6,23-25]. The possible hypothesis is that the mechanical and physical properties of Ti_2AlC-Mg composites should be anisotropic if the Ti_2AlC orientation was textured in the Mg matrix.

References

[1] V.H. Nowotny, Strukturchemie einiger verbindungen der Übergangsmetalle mit den elementen C, Si, Ge, Sn, Progress in Solid State Chemistry 5 (1971) 27-70.

[2] V. Ivchenko, M. Lesnaya, V. Nemchenko, T.Y. Kosolapova, Some physical properties of ternary compounds in the system Ti-Al-C, Powder Metallurgy and Metal Ceramics 15(5) (1976) 367-369.

[3] V. Ivchenko, T.Y. Kosolapova, Abrasive properties of the ternary compounds in the systems Ti-Al-C and Ti-Al-N, Powder Metallurgy and Metal Ceramics 15(8) (1976) 626-628.

[4] M.W. Barsoum, The Mn+1AXn phases: A new class of solids thermodynamically stable nanolaminates, Progress in Solid State

Chemistry 28(1-4) (2000) 201-281.
[5] M.W. Barsoum, T. El ‐ Raghy, Synthesis and characterization of a remarkable ceramic: Ti_3SiC_2, Journal of the American Ceramic Society 79(7) (1996) 1953-1956.
[6] M. Barsoum, T. El-Raghy, A. Procopio, Characterization of Ti_4AlN_3, Metallurgical and Materials Transactions A 31(2) (2000) 333-337.
[7] M.W. Barsoum, The Mn+1AXn phases: A new class of solids: Thermodynamically stable nanolaminates, Progress in Solid State Chemistry 28(1) (2000) 201-281.
[8] Z. Sun, Progress in research and development on MAX phases: a family of layered ternary compounds, International Materials Reviews 56(3) (2011) 143-166.
[9] J. Wang, Y. Zhou, Recent progress in theoretical prediction, preparation, and characterization of layered ternary transition-metal carbides, Annual Review of Materials Research 39 (2009) 415-443.
[10] M. Barsoum, L. Farber, T. El-Raghy, Dislocations, kink bands, and room-temperature plasticity of Ti_3SiC_2, Metallurgical and Materials Transactions A 30(7) (1999) 1727-1738.
[11] M. Barsoum, T. El-Raghy, Room-temperature ductile carbides, Metallurgical and Materials Transactions A 30(2) (1999) 363-369.
[12] M.W. Barsoum, L. Farber, I. Levin, A. Procopio, T. El ‐ Raghy, A. Berner, High ‐ Resolution Transmission Electron Microscopy of Ti_4AlN_3, or $Ti_3Al_2N_2$ Revisited, Journal of the American Ceramic Society 82(9) (1999) 2545-2547.
[13] W. Yu, S. Li, W.G. Sloof, Microstructure and mechanical properties of a $Cr_2Al(Si)C$ solid solution, Materials Science and Engineering: A 527(21) (2010) 5997-6001.
[14] B. Kooi, R. Poppen, N. Carvalho, J.T.M. De Hosson, M. Barsoum, Ti_3SiC_2: A damage tolerant ceramic studied with nano-indentations and transmission electron microscopy, Acta materialia 51(10) (2003) 2859-2872.
[15] M. W.Barsoum, MAX Phases: Properties of machinable ternary carbides and nitrides, Wiley-VCH (2013).
[16] J.M. Schneider, Z. Sun, R. Mertens, F. Uestel, R. Ahuja, Ab initio calculations and experimental determination of the structure of Cr_2AlC, Solid state communications 130(7) (2004) 445-449.
[17] Y. Zhou, H. Dong, X. Wang, S. Chen, Electronic structure of the layered ternary carbides Ti_2SnC and Ti_2GeC, Journal of Physics: Condensed Matter 12(46) (2000) 9617.
[18] Y. Zhou, Z. Sun, Electronic structure and bonding properties of layered machinable Ti_2AlC and Ti_2AlN ceramics, Physical Review B

61(19) (2000) 12570.
[19] Y. Zhou, X. Wang, Z. Sun, S. Chen, Electronic and structural properties of the layered ternary carbide Ti_3AlC_2, Journal of Materials Chemistry 11(9) (2001) 2335-2339.
[20] M. Kanoun, M. Jaouen, Structure of the ternary carbide Ti_3SnC_2 from ab initio calculations, Journal of Physics: Condensed Matter 20(8) (2008) 085211.
[21] R. Ahuja, O. Eriksson, J. Wills, B. Johansson, Electronic structure of Ti_3SiC_2, Applied physics letters 76(16) (2000) 2226-2228.
[22] C. Li, B. Wang, Y. Li, R. Wang, First-principles study of electronic structure, mechanical and optical properties of V_4AlC_3, Journal of Physics D: Applied Physics 42(6) (2009) 065407.
[23] Z. Sun, Y. Zhou, Electronic structure and structural properties of Ti_4AlN_3 investigated by ab initio calculations, Journal of the Physical Society of Japan 71(5) (2002) 1313-1317.
[24] G. Hug, E. Fries, Full-potential electronic structure of Ti_2AlC and Ti_2AlN, Physical Review B 65(11) (2002) 113104.
[25] Y. Zhou, Z. Sun, X. Wang, S. Chen, Ab initio geometry optimization and ground state properties of layered ternary carbides Ti_3MC_2 (M= Al, Si and Ge), Journal of Physics: Condensed Matter 13(44) (2001) 10001.
[26] G. Hug, M. Jaouen, M. Barsoum, X-ray absorption spectroscopy, EELS, and full-potential augmented plane wave study of the electronic structure of Ti_2AlC, Ti_2AlN, Nb_2AlC, and $(Ti_{0.5}Nb_{0.5})_2AlC$, Physical Review B 71(2) (2005) 024105.
[27] S. Lofland, J. Hettinger, K. Harrell, P. Finkel, S. Gupta, M. Barsoum, G. Hug, Elastic and electronic properties of select M2AX phases, Applied physics letters 84(4) (2004) 508-510.
[28] N. Haddad, E. Garcia-Caurel, L. Hultman, M.W. Barsoum, G. Hug, Dielectric properties of TiAlC and TiAlN MAX phases: The conductivity anisotropy, Journal of applied physics 104 (2008) 023531.
[29] S. Gupta, E. Hoffman, M. Barsoum, Synthesis and oxidation of Ti_2InC, Zr_2InC,$(Ti_{0.5}$, $Zr_{0.5})_2InC$ and $(Ti_{0.5}$, $Hf_{0.5})_2InC$ in air, Journal of Alloys and Compounds 426(1-2) (2006) 168-175.
[30] I. Salama, T. El-Raghy, M. Barsoum, Synthesis and mechanical properties of Nb_2AlC and $(Ti, Nb)_2AlC$, Journal of Alloys and Compounds 347(1) (2002) 271-278.
[31] F. Meng, Y. Zhou, J. Wang, Strengthening of Ti_2AlC by substituting Ti with V, Scripta Materialia 53(12) (2005) 1369-1372.
[32] N.A. Phatak, S.K. Saxena, Y. Fei, J. Hu, Synthesis of a new MAX compound $(Cr_{0.5}V_{0.5})_2GeC$ and its compressive behavior up to 49 GPa, Journal of Alloys and Compounds 475(1) (2009) 629-634.

[33] Z. Sun, R. Ahuja, J.M. Schneider, Theoretical investigation of the solubility in ($M_xM'_{2-x}$)AlC (M and M' = Ti, V, Cr), Physical Review B 68(22) (2003) 224112.
[34] G.-P. Bei, Synthesis, Microstructural Characterization and Mechanical Properties of Nanolaminated $Ti_3Al_xSn_{(1-x)}C_2$ MAX Phases, 2011.
[35] S. Gupta, M. Barsoum, Synthesis and Oxidation of V_2AlC and ($Ti_{0.5}$, $V_{0.5}$)$_2$AlC in Air, Journal of The Electrochemical Society 151(2) (2004) D24-D29.
[36] S. Dubois, G.P. Bei, C. Tromas, V. Gauthier‐Brunet, P. Gadaud, Synthesis, Microstructure, and Mechanical Properties of $Ti_3Sn_{(1-x)}Al_xC_2$ MAX Phase Solid Solutions, International Journal of Applied Ceramic Technology 7(6) (2010) 719-729.
[37] Y. Zhou, J. Chen, J. Wang, Strengthening of Ti_3AlC_2 by incorporation of Si to form $Ti_3Al_{1-x}Si_xC_2$ solid solutions, Acta materialia 54(5) (2006) 1317-1322.
[38] J. Chen, Y. Zhou, J. Zhang, Abnormal thermal expansion and thermal stability of $Ti_3A_{1-x}Si_xC_2$ solid solutions, Scripta Materialia 55(8) (2006) 675-678.
[39] A. Ganguly, T. Zhen, M. Barsoum, Synthesis and mechanical properties of Ti_3GeC_2 and $Ti_3(Si_xGe_{1-x})C_2$ (x= 0.5, 0.75) solid solutions, Journal of Alloys and Compounds 376(1-2) (2004) 287-295.
[40] P. Finkel, B. Seaman, K. Harrell, J. Palma, J. Hettinger, S. Lofland, A. Ganguly, M. Barsoum, Z. Sun, S. Li, Electronic, thermal, and elastic properties of $Ti_3Si_{1-x}Ge_xC_2$ solid solutions, Physical Review B 70(8) (2004) 085104.
[41] W. Yu, S. Li, W.G. Sloof, Microstructure and mechanical properties of a $Cr_2Al(Si)C$ solid solution, Materials Science and Engineering: A 527(21) (2010) 5997-6001.
[42] T. Cabioch, P. Eklund, V. Mauchamp, M. Jaouen, M.W. Barsoum, Tailoring of the thermal expansion of $Cr_2(Al_x, Ge_{1-x})C$ phases, Journal of the European Ceramic Society 33(4) (2012) 897–904.
[43] J. Wang, Y. Zhou, First-principles study of equilibrium properties and electronic structure of $Ti_3Si_{0.75}Al_{0.25}C_2$ solid solution, Journal of Physics: Condensed Matter 15(35) (2003) 5959.
[44] X. Xu, E. Wu, X. Du, Y. Tian, J. He, First-principle study of electronic properties of $Ti_3Si_{1-x}Al_xC_2$ solid solutions, Journal of Physics and Chemistry of Solids 69(5) (2008) 1356-1361.
[45] M. Radovic, A. Ganguly, M. Barsoum, Elastic properties and phonon conductivities of $Ti_3Al(C_{0.5},N_{0.5})_2$ and $Ti_2Al(C_{0.5},N_{0.5})$ solid solutions, Journal of Materials Research 23(6) (2008) 1517-1521.

[46] B. Manoun, S. Saxena, G. Hug, A. Ganguly, E. Hoffman, M. Barsoum, Synthesis and compressibility of $Ti_3(Al,Sn_{0.2})C_2$ and $Ti_3Al(C_{0.5},N_{0.5})_2$, Journal of applied physics 101(11) (2007) 113523-113523-7.
[47] M. Barsoum, T. El-Raghy, M. Ali, Processing and Characterization of Ti_2AlC, Ti_2AlN, and $Ti_2AlC_{0.5}N_{0.5}$, Metallurgical and Materials Transactions A 31(7) (2000) 1857-1865.
[48] T. Cabioch, P. Eklund, V. Mauchamp, M. Jaouen, Structural investigation of substoichiometry and solid solution effects in $Ti_2Al(C_x,N_{1-x})(y)$ compounds, Journal of the European Ceramic Society 32(8) (2012) 1803-1811.
[49] V. Ern, A. Switendick, Electronic band structure of TiC, TiN, and TiO, Physical Review 137(6A) (1965) A1927.
[50] Y. Du, Z. Sun, H. Hashimoto, M. Barsoum, Theoretical investigations on the elastic and thermodynamic properties of $Ti_2AlC_{0.5}N_{0.5}$ solid solution, Physics Letters A 374(1) (2009) 78-82.
[51] T. Scabarozi, A. Ganguly, J. Hettinger, S. Lofland, S. Amini, P. Finkel, T. El-Raghy, M. Barsoum, Electronic and thermal properties of TiAl (C, N), TiAl (C, N) and TiAlN, Journal of applied physics 104 (2008) 073713.
[52] A. Mendoza-Galvan, M. Rybka, K. Järrendahl, H. Arwin, M. Magnuson, L. Hultman, M. Barsoum, Spectroscopic ellipsometry study on the dielectric function of bulk Ti_2AlN, Ti_2AlC, Nb_2AlC,$(Ti_{0.5},Nb_{0.5})_2AlC$, and Ti_3GeC_2 MAX-phases, Journal of applied physics 109 (2011) 013530.
[53] J. Hettinger, S. Lofland, P. Finkel, T. Meehan, J. Palma, K. Harrell, S. Gupta, A. Ganguly, T. El-Raghy, M. Barsoum, Electrical transport, thermal transport, and elastic properties of M_2AlC (M= Ti, Cr, Nb, and V), Physical Review B 72(11) (2005) 115120.
[54] W. Lengauer, S. Binder, K. Aigner, P. Ettmayer, A. Guillou, J. Debuigne, G. Groboth, Solid state properties of group IVb carbonitrides, Journal of Alloys and Compounds 217(1) (1995) 137-147.
[55] S.H. Jhi, S.G. Louie, M.L. Cohen, J. Ihm, Vacancy hardening and softening in transition metal carbides and nitrides, Physical Review Letters 86(15) (2001) 3348-3351.
[56] W.D. Nix, H. Gao, Indentation size effects in crystalline materials: a law for strain gradient plasticity, Journal of the Mechanics and Physics of Solids 46(3) (1998) 411-425.
[57] S. Li, W. Yu, H. Zhai, G. Song, W. Sloof, S. Van der Zwaag, Mechanical properties of low temperature synthesized dense and fine-grained Cr_2AlC ceramics, Journal of the European Ceramic Society 31(1) (2011) 217-224.

[58] X.H. Wang, Y.C. Zhou, Microstructure and Properties of Ti_3AlC_2 Preparred by the Solid Liquid Reaction Synthesis and Simultaneous In-situ Hot Pressing Process, Acta Mater. 50 (2002) 3141-3149.
[59] N. Gao, Y. Miyamoto, D. Zhang, Dense Ti_3SiC_2 prepared by reactive HIP, Journal of materials science 34(18) (1999) 4385-4392.
[60] J. H. Han, S. S. Hwang, D. Lee, S. W. Park, Synthesis and mechanical properties of Ti_3AlC_2 by hot pressing TiC_x/Al powder mixture, Journal of the European Ceramic Society 28(5) (2008) 979-988.
[61] S. Amini, M.W. Barsoum, T. El‐Raghy, Synthesis and mechanical properties of fully dense Ti_2SC, Journal of the American Ceramic Society 90(12) (2007) 3953-3958.
[62] Y. Bai, X. He, Y. Li, C. Zhu, S. Zhang, Rapid synthesis of bulk Ti_2AlC by self-propagating high temperature combustion synthesis with a pseudo–hot isostatic pressing process, J. Mater. Res 24(8) (2009) 2528-35.
[63] X. Wang, Y. Zhou, Solid-liquid reaction synthesis and simultaneous densification of polycrystalline Ti_2AlC, Zeitschrift für Metallkunde 93(1) (2002) 66-71.
[64] G. Bei, V. Gauthier‐Brunet, C. Tromas, S. Dubois, Synthesis, Characterization, and Intrinsic Hardness of Layered Nanolaminate Ti_3AlC_2 and $Ti_3Al_{0.8}Sn_{0.2}C_2$ Solid Solution, Journal of the American Ceramic Society 95(1) (2011) 102-107.
[65] C. Tromas, N. Ouabadi, V. Gauthier‐Brunet, M. Jaouen, S. Dubois, Mechanical Properties of Nanolaminate Ti_3SnC_2 Carbide Determined by Nanohardness Cartography, Journal of the American Ceramic Society 93(2) (2010) 330-333.
[66] M.W. Barsoum, I. Salama, T. El-Raghy, J. Golczewski, W.D. Porter, H. Wang, H. Siefert, F. Aldinger, Thermal and electrical properties of Nb_2AlC, $(Ti, Nb)_2AlC$ and Ti_2AlC, Metallurgical and Materials Transactions 33a (2002) 2779.
[67] J.D. Hettinger, S.E. Lofland, P. Finkel, J. Palma, K. Harrell, S. Gupta, A. Ganguly, T. El-Raghy, M.W. Barsoum, Electrical Transpot, Thermal Transport and Elastic Properties of M_2AlC (M = Ti, Cr, Nb and V) Phases, Phys. Rev. B 72 (2005) 115120.
[68] S.E. Lofland, J.D. Hettinger, T. Meehan, A. Bryan, P. Finkel, G. Hug, M.W. Barsoum, Electron-Phonon Coupling in MAX Phase Carbides, Phys. Rev. B 74 (2006) 174501.
[69] C. Hu, L. He, J. Zhang, Y. Bao, J. Wang, M. Li, Y. Zhou, Microstructure and Properties of Bulk Ta_2AlC Ceramic Synthesized by an in situ Reaction/hot Pressing Method, J. Europ. Ceram. Soc. 28 (2008) 1679–1685.

[70] M. Barsoum, H. I. Yoo, I. Polushina, V.Y. Rud, Y.V. Rud, T. El-Raghy, Electrical conductivity, thermopower, and Hall effect of Ti_3AlC_2, Ti_4AlN_3, and Ti_3SiC_2, Physical Review B 62(15) (2000) 10194.
[71] P. Finkel, J. Hettinger, S. Lofland, M. Barsoum, T. El-Raghy, Magnetotransport properties of the ternary carbide Ti_3SiC_2: Hall effect, magnetoresistance, and magnetic susceptibility, Physical Review B 65(3) (2001) 035113.
[72] X. Wang, Y. Zhou, Layered machinable and electrically conductive Ti_2AlC and Ti_3AlC_2 ceramics: a review, Journal of Materials Science & Technology 26(5) (2010) 385-416.
[73] H. Yoo, M. Barsoum, T. El-Raghy, Materials science: Ti_3SiC_2 has negligible thermopower, Nature 407(6804) (2000) 581-582.
[74] L. Chaput, G. Hug, P. Pécheur, H. Scherrer, Anisotropy and thermopower in Ti_3SiC_2, Physical Review B 71(12) (2005) 121104.
[75] P. Finkel, M. Barsoum, J. Hettinger, S. Lofland, H. Yoo, Low-temperature transport properties of nanolaminates Ti_3AlC_2 and Ti_4AlN_3, Physical Review B 67(23) (2003) 235108.
[76] T.H. Scabarozi, P. Eklund, J. Emmerlich, H. Hogberg, T. Meehan, P. Finkel, M.W. Barsoum, J.D. Hettinger, L. Hultman, S.E. Lofland, Weak electronic anisotropy in the layered nanolaminate Ti_2GeC, Solid State Communications 146 (2008) 498-501.
[77] M.W. Barsoum, MAX Phases: Properties of Machinable Ternary Carbides and Nitrides, John Wiley & Sons 2013.
[78] T.H. Scabarozi, S. Amini, P. Finkel, M.W. Barsoum, W.M. Tambussi, J.D. Hettinger, S.E. Lofland, Electrical, Thermal, and Elastic Properties of the MAX Phase Ti_2SC, J. Appl. Phys. 104 (2008) 033502.
[79] T. Scabarozi, S. Benjamin, B. Adamson, J. Applegate, J. Roche, E. Pfeiffer, C. Steinmetz, C. Lunk, M. Barsoum, J. Hettinger, Combinatorial investigation of the stoichiometry, electronic transport and elastic properties of $(Cr_{1-x}V_x)_2GeC$ thin films, Scripta Materialia 66(2) (2012) 85-88.
[80] Y. Zhou, D. Wan, Y. Bao, J. Wang, In Situ Processing and High‐Temperature Properties of Ti_3Si (Al) C_2/SiC Composites, International Journal of Applied Ceramic Technology 3(1) (2006) 47-54.
[81] W.S. Williams, Scattering of electrons by vacancies in nonstoichiometric crystals of titanium carbide, Physical Review 135(2A) (1964) A505.
[82] L.W. Shacklette, W.S. Williams, Scattering of Electrons by Vacancies through an Order‐Disorder Transition in Vanadium Carbide, Journal of applied physics 42(12) (1971) 4698-4703.

[83] V. Lipatnikov, A. Gusev, P. Ettmayer, W. Lengauer, Phase transformations in non-stoichiometric vanadium carbide, Journal of Physics: Condensed Matter 11(1) (1999) 163.
[84] M.O. Pekguleryuz, A.A. Kaya, Creep Resistant Magnesium Alloys for Powertrain Applications, Advanced Engineering Materials 5(12) (2010) 866-878.
[85] B.R. Powell, P.E. Krajewski, A.A. Luo, 4 – Magnesium alloys for lightweight powertrains and automotive structures, Materials Design & Manufacturing for Lightweight Vehicles 80(2) (2010) 114-173.
[86] Y. Xue, M.F. Horstemeyer, D.L. McDowell, H. El Kadir, J. Fan, Microstructure-based multistage fatigue modeling of a cast AE44 magnesium alloy, International Journal of Fatigue 29(4) (2007) 666-676.
[87] S. Zhu, C. Wong, M.J. Styles, T.B. Abbott, J.-F. Nie, M.A. Easton, Revisiting the intermetallic phases in high-pressure die-cast Mg-4Al-4Ce and Mg-4Al-4La alloys, Materials Characterization 156 (2019) 109839.
[88] B. Hu, L.M. Peng, B.R. Powell, M.P. Balough, R.C. Kubic, A.K. Sachdev, Interfacial and fracture behavior of short-fibers reinforced AE44 based magnesium matrix composites, Journal of Alloys and Compounds 504(2) (2010) 527-534.
[89] M. Mondet, E. Barraud, S. Lemonnier, J. Guyon, N. Allain, T. Grosdidier, Microstructure and mechanical properties of AZ91 magnesium alloy developed by Spark Plasma Sintering, Acta Materialia 119 (2016) 55-67.
[90] S.C. Tjong, Recent progress in the development and properties of novel metal matrix nanocomposites reinforced with carbon nanotubes and graphene nanosheets, Materials Science and Engineering: R: Reports 74(10) (2013) 281-350.
[91] X.J. Wang, D.K. Xu, R.Z. Wu, X.B. Chen, Q.M. Peng, L. Jin, Y.C. Xin, Z.Q. Zhang, Y. Liu, X.H. Chen, G. Chen, K.K. Deng, H.Y. Wang, What is going on in magnesium alloys?, Journal of Materials Science & Technology 34(2) (2018) 245-247.
[92] C.J. Wang, K.K. Deng, W. Liang, High temperature damping behavior controlled by submicron SiCp in bimodal size particle reinforced magnesium matrix composite, Materials Science and Engineering a-Structural Materials Properties Microstructure and Processing 668 (2016) 55-58.
[93] K.K. Deng, J.C. Li, K.B. Nie, X.J. Wang, J.F. Fan, High temperature damping behavior of as-deformed Mg matrix influenced by micron and submicron SiCp, Materials Science and Engineering a-Structural Materials Properties Microstructure and Processing 624 (2015) 62-70.

[94] A. Das, S.P. Harimkar, Effect of Graphene Nanoplate and Silicon Carbide Nanoparticle Reinforcement on Mechanical and Tribological Properties of Spark Plasma Sintered Magnesium Matrix Composites, Journal of Materials Science & Technology 30(11) (2014) 1059-1070.
[95] Y.W. Wu, K. Wu, K.B. Nie, K.K. Deng, X.S. Hu, X.J. Wang, M.Y. Zheng, Damping capacities and tensile properties in Grp/AZ91 and SiCp/Grp/AZ91 magnesium matrix composites, Materials Science and Engineering a-Structural Materials Properties Microstructure and Processing 527(29-30) (2010) 7873-7877.
[96] Y.W. Wu, K. Wu, K.K. Deng, K.B. Nie, X.J. Wang, X.S. Hu, M.Y. Zheng, Damping capacities and tensile properties of magnesium matrix composites reinforced by graphite particles, Materials Science and Engineering: A 527(26) (2010) 6816-6821.
[97] S. García-Rodríguez, B. Torres, A. Maroto, A.J. López, E. Otero, J. Rams, Dry sliding wear behavior of globular AZ91 magnesium alloy and AZ91/SiCp composites, Wear 390-391(Supplement C) (2017) 1-10.
[98] S. Shang, K. Deng, K. Nie, J. Li, S. Zhou, F. Xu, J. Fan, Microstructure and mechanical properties of SiCp/Mg-Al-Zn composites containing $Mg_{17}Al_{12}$ phases processed by low-speed extrusion, Materials Science and Engineering: A 610 (2014) 243-249.
[99] P. Poddar, V.C. Srivastava, P.K. De, K.L. Sahoo, Processing and mechanical properties of SiC reinforced cast magnesium matrix composites by stir casting process, Materials Science and Engineering a-Structural Materials Properties Microstructure and Processing 460 (2007) 357-364.
[100] B. Anasori, S. Amini, V. Presser, M.W. Barsoum, Nanocrystalline Mg-Matrix Composites with Ultrahigh Damping Properties, Magnesium Technology 2011 (2011) 463-468.
[101] S. Amini, M.W. Barsoum, On the effect of texture on the mechanical and damping properties of nanocrystalline Mg-matrix composites reinforced with MAX phases, Materials Science and Engineering: A 527(16) (2010) 3707-3718.
[102] W. Yu, M. Vallet, B. Levraut, V. Gauthier-Brunet, S. Dubois, Oxidation mechanisms in bulk Ti_2AlC: influence of the grain size, Journal of the European Ceramic Society (2020).
[103] A. Guitton, S. Van Petegem, C. Tromas, A. Joulain, H. Van Swygenhoven, L. Thilly, Effect of microstructure anisotropy on the deformation of MAX polycrystals studied by in-situ compression combined with neutron diffraction, Applied Physics Letters 104(24) (2014) 201.
[104] A. Guitton, A. Joulain, L. Thilly, C. Tromas, Dislocation analysis of Ti_2AlN deformed at room temperature under confining pressure,

Philosophical Magazine 92(36) (2012) 4536-4546.
[105] A. Guitton, A. Joulain, L. Thilly, C. Tromas, Evidence of dislocation cross-slip in MAX phase deformed at high temperature, Scientific Reports 4 (2014) 6358.
[106] W. Yu, V. Mauchamp, T. Cabioc'h, D. Magne, L. Gence, L. Piraux, V. Gauthier-Brunet, S. Dubois, Solid solution effects in the $Ti_2Al(C_xN_y)$ MAX phases: Synthesis, microstructure, electronic structure and transport properties, Acta Materialia 80 (2014) 421-434.
[107] L. Cai, Z. Huang, W. Hu, S. Hao, H. Zhai, Y. Zhou, Fabrication, mechanical properties, and tribological behaviors of Ti_2AlC and $Ti_2AlSn_{0.2}C$ solid solutions, Journal of Advanced Ceramics 6(2) (2017) 90-99.
[108] R. Arróyave, M. Radovic, Ab initio investigation of Ti_2A (C, N) solid solutions, Physical Review B 84(13) (2011) 134112.

CHAPTER 2

SYNTHESIS AND MICROSTRUCTURAL CHARACTERIZATION OF $Ti_2AL(C_XN_Y)$ ($X+Y\leq1$) SOLID SOLUTIONS AND RELATED END-MEMBERS

2.1. Introduction

Since the pioneering work on the synthesis, in powder form, of Ti_2AlC and Ti_2AlN by Jeitchko and Nowotny in the early 1960s[1], these two MAX phases have been prepared in bulk form through a variety of processing techniques[2-5] including Hot Isostatic Pressing (HIPing), Hot Pressing (HPing), Pressureless Sintering (PSing), Spark Plasma Sintering (SPS) and arc melting methods. As summarized in Table 2-1, normal compositions composed from different initial reactant mixtures, such as $Ti:Al_4C_3:C$[3] [6], $Ti:Al:C$[7] [8], $TiC:Ti:Al:C$[9], and $Ti:TiC:Al$[10] [11] can be used to synthesize Ti_2AlC in the temperature range 1000-1600 °C. $Ti:AlN$[3] / $TiN:Ti:Al$[4, 5, 10] [12] [13] mixtures are used to produce Ti_2AlN in the temperature range 1200-1400 °C.

Table 2-1 shows that using $Ti:Al_4C_3:C$, $Ti:Al:C$, and $Ti:TiC:Al$ as initial reactant powder mixtures leads to the synthesis of non-pure Ti_2AlC bulk samples, regardless of the processing technique and the reaction temperature. The main impurities are Al_2O_3/Ti_3P[2] or TiC[50] in the case of a $Ti:Al_4C_3:C$ initial reactant mixture and Ti_xAl_y[6, 49, 8, 52, 55] in the case of $Ti:Al:C$ and $Ti:TiC:Al$ initial reactant mixtures. However, using $Ti:TiC:Al:C$ as an initial reactant mixture induces the formation of highly pure Ti_2AlC provided that the synthesis temperature is not too high[51]. It can nevertheless be noticed that using too large an excess of Al in the initial reactant mixture leads to the formation of Ti_xAl_y impurities[8]. As a result, it seems that $Ti:TiC:Al:C$ initial reactant mixtures would be the best choice in order to produce highly pure Ti_2AlC bulk samples[51]. Table 2-1 also shows that Ti_2AlC synthesis temperatures range between 1100 °C and 1600 °C. The lowest temperature (1100 °C) is nevertheless used during

SPS experiments. It is well known that SPS experiments allow synthesizing or sintering materials at lower temperatures than more classical processes (HIPing, HPing, etc.). Moreover, Table 2-1 shows that, using the HIPing technique, a synthesis temperature of 1600 °C can lead to the presence of TiC[50] as an impurity, whereas a temperature of 1500 °C can lead to the presence of Ti_3AlC_2[51]. Finally, Ti_2AlC bulk sample can very likely be synthesized by HIPing a Ti:TiC:Al:C initial reactant powder mixture at a synthesis temperature in the range of 1300-1400 °C.

Concerning the synthesis of highly pure Ti_2AlN, it can be noticed from Table 2-1 that the initial reactant powder mixture may also be considered a pertinent parameter. Indeed, using Ti:AlN as initial reactant powder mixture leads to a large amount of impurity (in the range 11-20 vol.% of Ti_4AlN_3, Al_2O_3 and Ti_3P) detected in the final Ti_2AlN bulk sample[3] after HIPing at 1400 °C/40 MPa/48 h. However, using Ti:TiN:Al as initial reactant mixture leads to highly pure Ti_2AlN [4] [5] [12] [13] regardless of the processing technique and the reaction temperature. As a result, it seems that Ti:TiN:Al initial reactant mixtures would be the best choice in order to produce highly pure Ti_2AlN bulk samples. Table 2-1 also shows that Ti_2AlN synthesis temperatures range in between 1200 °C used during SPS[4] and 1400 °C adopted during HIPing[3] and HPing. Finally, Ti_2AlN bulk sample can very likely be synthesized by HIPing a Ti:TiN:Al initial reactant powder mixture at a synthesis temperature in the range of 1300-1400 °C.

Table 2-1: Summary of the different initial reactant mixtures, the different processing techniques that have been used and of some microstructural characteristics of the resulting Ti_2AlC and Ti_2AlN bulk samples. (GS: grain size).

Ti_2AlC					
Processing methods	Nominal composition	Synthesis conditions	Phase composition Ti_2AlC lattice parameters (Å)	Micro-structure	Ref.
HIPing	2Ti:Al:C	1300 °C/40 MPa/30 h	Ti_2AlC (96 vol. %) Al_2O_3, Ti_3P (4 vol. %) a=3.051; c=13.637	Layered structure, GS: 25 µm	[3]
HPing	2Ti:Al:C	1400 °C/30 MPa/1 h	Predominant phase: Ti_2AlC a=3.04; c=13.6	Layered structure, Ti_2AlC formed at TiAl twin boundary	[7]
	2Ti:Al:C	1600 °C/40 MPa/4 h	Ti_2AlC with TiC	Layered structure, 4.11 g cm^{-3}	[6]
	2Ti:Al:C	1400 °C/30 MPa/1 h	Ti_2AlC pure phase 1500°C: Ti_3AlC_2 is formed	GS: 15 µm	[9]
PSing	2Ti:1.1Al:C	1400 °C/4 h/Ar	Ti_2AlC with Ti_xAl_y a=3.0625; c=13.668	GS: 2-10 µm	[10]
SPS	Ti:xAl:C x=(1.1,1.2,1.3)	1100°C/30 MPa/8min / vacuum	Main phases: Ti_2AlC with TiAl when x=1.3 a=3.058; c=13.649	GS: 5 µm in width 20µm in length	[8]
Arc melting	2Ti:Al:C	annealed at 1000 °C/170 h	Ti_2AlC, TiC and $TiAl_3$ a=3.056; c=13.62	Not mentioned	[11]

Ti_2AlN					
HIPing	2Ti:Al:N	1400 °C/40MPa /48 h	Ti_2AlN (80-89 vol. %) Ti_4AlN_3, Al_2O_3, Ti_3P (11-20 vol. %) a=2.9890; c=13.6140	GS: 100 µm	[3]
HPing	2Ti:Al:N	1400 °C/25 MPa/1 h	Single-phased Ti_2AlN a=2.998; c=13.613	GS: 13 µm 4.27 g cm^{-3}	[5]
	2Ti:Al:N	1300 °C/30 MPa/48 h	Single-phased Ti_2AlN	GS: 3-5 µm in width 8-10 µm in length	[12]
	2Ti:Al:N	1400 °C/45 MPa/8 h	$Ti_2Al_{1.04}N_{0.98}$ Wet chemical analysis	Not mentioned	[14]
PSing	Ti_2AlN powders (3-ONE-2, Vorhees)	1500 °C/1 h/Ar	$Ti_2Al_{1.0}N_{0.95}$ Wet chemical analysis	Not mentioned	[15]
	Ti:TiN:1.1Al	1400 °C/4 h/Ar	Ti_2AlN a=2.9890; c=13.6157	GS: 2-10 µm	[10]
SPS	2Ti:Al:N	1000,1100 or 1200 °C/30 MPa/10 min/ vacuum	Pure Ti_2AlN at 1200°C	GS: 8-12 µm in width 20-30 µm in length	[4]
	2Ti:Al:N	1250 °C/30 MPa/10 min/ vacuum	Pure Ti_2AlN	GS: 2-4 µm in width, 5-10 µm in length 4.25-4.34 g cm^{-3}	[13]

2.2. Optimization of Ti_2AlCx (x<1) MAX synthesis

2.2.1. The chemical composition obtained from 2Ti:1.1Al:1C

To synthesize pure Ti_2AlC MAX phase, a nominal composition of 2Ti:1.1Al:1C has been used by HIPing Ti:TiC:1.1Al cold-compacted powders at 1400 °C/80 MPa for 4 h. The powder mixtures used in this study contain an excess of 10 at.% of Al to compensate for the loss of aluminum by preferential out-diffusion during the sintering process. The XRD pattern, obtained in the 8-75° 2θ range and presented in Fig. 2-1, shows that Ti_3AlC_2 and Ti_xAl_y traces are detected in addition to the desired Ti_2AlC MAX phase. From Rietveld refinements of the XRD data, using MAUD software, the 211, 312 and Ti_xAl_y phases volume contents are 83, 16 and 1 vol.% respectively.

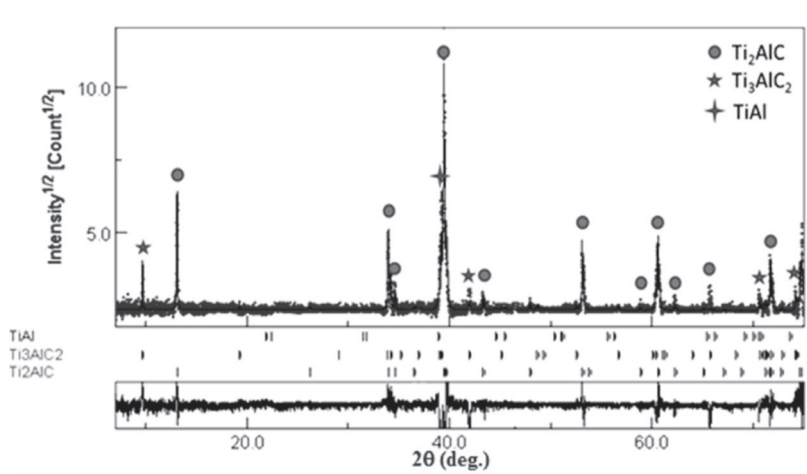

Fig. 2-1: Observed/calculated/difference X-ray diffraction Rietveld plots of the 2Ti:1.1Al:1C mixture HIPed at 1400 °C and 80 MPa for 4 h.

Fig. 2-2 shows a representative SEM micrograph, in back-scattered mode, of the HIPed sample. Wavelength Dispersive x-ray Spectroscopy (WDS) analyses coupled with SEM observations demonstrate that, starting with 2Ti:1.1Al:1C nominal composition, large areas of $Ti_3AlC_{1.81}$ are observed in the $Ti_2AlC_{0.88}$ matrix after HIPing treatment. It is important to note that the uncertainty on the carbon content is considered to be close to 0.02-0.03 using our analysis method. Some Ti_xAl_y and Al_2O_3 are also observed at the grain boundaries.

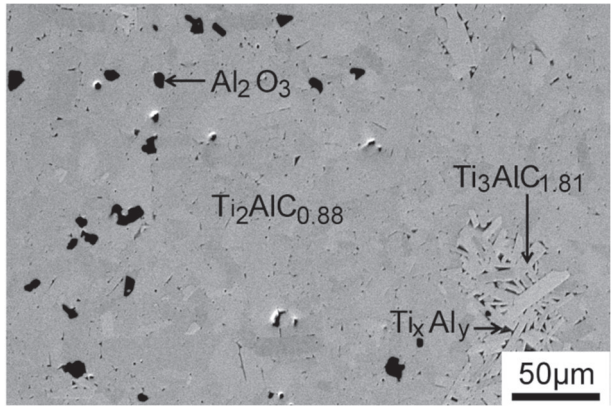

Fig. 2-2: SEM micrograph (back-scattered mode) of the 2Ti:1.1Al:1C mixture HIPed at 1400 °C and 80 MPa for 4h. Chemical composition of the different phases is measured by WDS. $Ti_2AlC_{0.88}$ is marked on the corresponding MAX phase.

2.2.2. The effects of sintering condition and powder composition

In a second step, the effect of sintering temperature and sintering duration on the synthesis of a Ti_2AlC_x MAX phase has been investigated. Various HIPing treatment conditions have been studied, starting with the 2Ti:1.1Al:1C nominal composition: 1400 °C/4 h/80 MPa, 1400 °C/20 h/80 MPa, 1300 °C/4 h/80 MPa. As summarized in Table 2-2, the refining quantitative analysis of XRD patterns (Fig. 2-3) shows that the sintering temperature and duration do not influence the volume content of the different 211, 312 and Ti_xAl_y phases significantly. This suggests that the phase composition is not affected by the soaking temperature and time under this setting pressure (80 MPa). In other words, in order to produce a high-purity Ti_2AlC_x MAX phase, we should consider the effect of the reactant powder mixture composition.

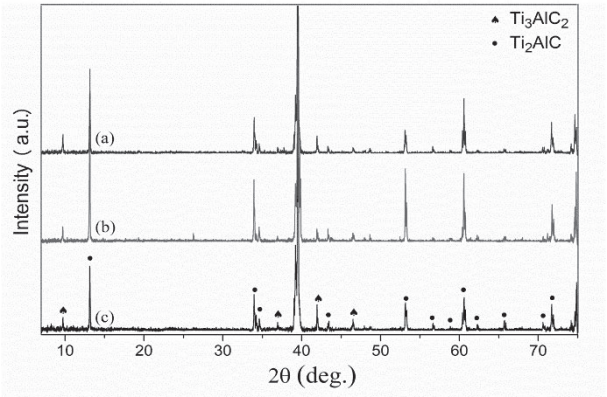

Fig. 2-3: XRD patterns of the 2Ti:1.1Al:C mixture after HIPing at (a)1400 ºC/4 h/80 MPa, (b) 1400 ºC/20 h/80 MPa, (c) 1300 ºC/4 h/80 MPa under Ar atmosphere.

To synthesize pure Ti_2AlC_x MAX phase, different nominal compositions have been investigated: 2Ti:1.1Al:0.9C, 2Ti:1.1Al:0.85C, 2Ti:1.05Al:0.85C, 2Ti:1.05Al:0.80C. Indeed, as it has been previously demonstrated, starting with 2Ti:1.1Al:1C nominal composition, carbon substoichiometry can be achieved to form $Ti_2AlC_{0.88}$ carbide, C deficiency (0.9, 0.85 and 0.8) has been studied. Moreover, the Al content effect (1.1 and 1.05) has been investigated in order to avoid the formation of Ti_xAl_y intermetallic.

Fig. 2-4 shows the XRD patterns of the HIPed end-products sintered at 1400 °C/80 MPa for 4 h. Starting with 2Ti:1.1Al:0.9C (Fig. 2-4 (b)), 2Ti:1.1Al:0.85C (Fig. 2-4 (c)) and 2Ti:1.05Al:0.80C (Fig. 2-4 (e)) nominal compositions, titanium aluminides (TiAl and Ti_3Al) are detected in addition to the desired Ti_2AlC_x MAX phase. Starting with 2Ti:1.05Al:0.85C nominal composition (Fig. 2-4 (d)), only Ti_2AlC_x peaks are observed; no impurities are detected, within the XRD detection limit. The volume content of the different phases, as a function of the starting composition, is measured by performing Rietveld refinement of the XRD data, and is summarized in Table 2-2.

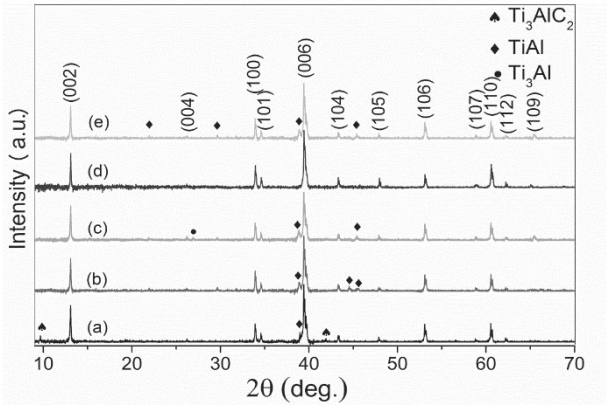

Fig. 2-4: XRD patterns of different mixtures HIPed at 1400 °C and 80 MPa for 4 h. (a) 2Ti:1.1Al:1C, (b) 2Ti:1.1Al:0.9C, (c) 2Ti:1.1Al:0.85C, (d) 2Ti:1.05Al:0.85C, (e) 2Ti:1.05Al:0.80C nominal compositions. The (hkl) indexed peaks correspond to the Ti_2AlC_x MAX phase.

WDS analyses coupled with SEM observations in back-scattered mode demonstrate that, starting with 2Ti:1.05Al:0.85C nominal composition, the resulting $Ti_2AlC_{0.85}$ HIPed sample is single-phased and fully dense (Fig. 2-5). As compared to the Ti_2AlC grains shown in Fig. 2-2 (2Ti:1.1Al:1C mixture HIPed at 1400 °C/4 h/80 MPa), MAX phase lamellae are much more obvious: they have dimensions in the 100-200 µm range in length and 20-50 µm in width. In addition, it has to be noticed that the chemical composition of the end-product, $Ti_2AlC_{0.85}$, is similar to that of the starting powders composition.

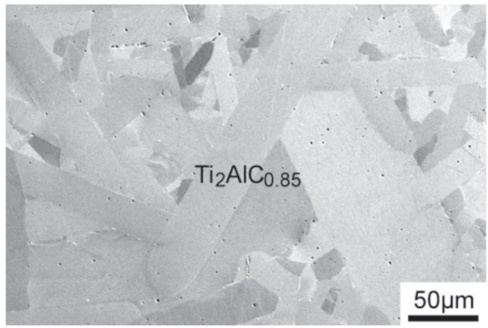

Fig. 2-5: SEM micrograph (back-scattered mode) of $Ti_2AlC_{0.85}$ synthesized from 2Ti:1.05Al:0.85C mixture HIPed at 1400°C and 80MPa for 4 h.

Our result is in contradiction to the work of Cabioc'h et al.[10] who proposed that carbon substoichiometry cannot be achieved in the carbide, using reactive sintering starting from 2Ti:1.1Al:0.7-1C nominal composition. Nevertheless, their results were based on pressureless sintering and the approach developed in their study was only based on XRD data; the carbon amount in the Ti_2AlC_x compounds was not directly measured. Furthermore, the possibility to synthesize substoichiometric Ti_2AlC_x carbide has been mentioned in the literature[16, 17]. Indeed, Guo et al.[17] have successfully synthesized single-phased Ti_2AlC_x ($x<1$) through a combustion synthesis process starting with 2Ti:Al:0.7C powder mixture. The authors have shown that the main combustion product is Ti_3AlC_2 if the molar ratio of the reactant mixture is 2Ti:Al:C. Pietzka et al.[16] have demonstrated, using the wet chemistry method, that Ti_2AlC is carbon deficient with respect to its "ideal" stoichiometry, which is based on the crystal structure formula. At 1300 °C, from the experimental isothermal section of the Ti-Al-C phase diagram and from thermochemical calculations, this phase is reported to be homogeneous at the composition $Ti_2AlC_{0.69}$. The study carried out by Pietzka et al.[16], performed at 1300°C, and the present work resulting from HIPing at 1400 °C/80 MPa indicate that the C substoichiometry may vary with the synthesis conditions. Nevertheless, in most of the studies dedicated to Ti_2AlC synthesis[3, 6-8, 10, 11, 15] the C content is not measured (see Table 2-2). Starting with 2Ti:1-1.2Al:C ratio, the authors consider that the Ti_2AlC final product is stoichiometric.

The lattice parameters of $Ti_2AlC_{0.85}$ measured from Rietveld refinement of the XRD data using MAUD software are a = 3.0607 Å and c = 13.6644 Å. However, there are some discrepancies for the Ti_2AlC a- ($3.04 < a < 3.065$ Å, $a = 3.0525 \pm 0.0125$ Å) and c- ($13.6 < c < 13.71$ Å, $c = 13.655 \pm 0.055$ Å) parameter values reported in the literature (see Table 2-2). Such discrepancies are difficult to understand if one considers Ti_2AlC_x has a narrow range of carbon composition and that vacancy content slightly modifies Lattice Parameter (LP) values. To better estimate the possible influence of residual stress and thermal equilibrium on the LP, $Ti_2AlC_{0.85}$ and other subtoichiometric samples were annealed for one hour at 700 °C (to eliminate residual stresses) and subsequently annealed for 10h at 1300 °C to decrease possible C-N concentration inhomogeneities and to reach equilibrium conditions. Rietveld refinements of the XRD experiments reveal that similar LP are obtained after annealing at 700 °C and 1300 °C, these LP being only slightly different from that obtained directly after the HIPing process. As a result, the presence of residual stress may only partly explain the discrepancy of the Ti_2AlC_x LP's value.

This study demonstrates that, whatever the starting nominal composition of the reactant powder, a single substoichiometric $Ti_2AlC_{0.85}$ can be synthesized in our experimental conditions. This result suggests that $Ti_2AlC_{0.85}$ is a line compound. The synthesized substoichiometric $Ti_2AlC_{0.85}$ is also pure and fully dense at the SEM scale.

Table 2-2: Ti_2AlC processing and microstructural characterization from literature and from the present study.

Nominal composition	Processing	End-product composition	a (Å)	c (Å)	Ref.
Ti_2AlC powder	Pressureless sintering of Ti_2AlC commercial powders in argon	Ti_2AlC*,& (XRD)	3.065±0.004 (a)	13.71±0.03 (a)	[15]
2Ti:1.1Al:C	Pressureless reactive sintering 1400 °C/4 h	Ti_2AlC, Ti_3AlC_2, Ti_xAl_y (XRD)	3.0625(5) (a)	13.668(1) (a)	[10]
2Ti:Al:C	Arc melted + annealing at 1000°C/170 h	Ti_2AlC* (XRD)	3.056(0) (a)	13.62(3) (a)	[11]
2Ti:1.2Al:1C	SPS under vacuum	Ti_2AlC* (XRD, SEM)	3.058±0.002 (a)	13.649±0.002 (a)	[8]
2Ti:Al:C	Hot pressing 1400 °C/1 h/30 MPa	Ti_2AlC* (XRD) +Ti_3AlC_2,TiC (HR-TEM)	3.04 (b)	13.6 (b)	[7]
2Ti:Al:C	Hot pressing 1600 °C/4 h/40 MPa	Ti_2AlC* (XRD+SEM)	Not measured	Not measured	[6]
2Ti:Al:C	HIP 1300 °C/30 h/40 MPa	Ti_2AlC*(XRD) Al_2O_3+Ti_3P (4vol.%, EDS)	3.051 (a)	13.637 (a)	[3]
2Ti:1.05Al: 0.85C	HIP 1400 °C/4 h/80 MPa	$Ti_2AlC_{0.85}$ (XRD, SEM/WDS)	3.0607 (a)	13.6644 (a)	[18]

* C content non-measured, & secondary phases non-determined, (a) determined from refinement of XRD pattern; (b) determined from Selected Area Electron Diffraction.

2.3. Synthesis and microstructural characteristics of Ti_2AlN_y ($y \leq 1$) MAX phase

2.3.1. The effect of the reactant powder mixture composition

Fig. 2-6 (a-e) shows the back-scattered microstructural morphologies of Ti_2AlN_y fabricated by pressureless sintering at 1400 °C for 0.5h from 2Ti:1.05Al:yN (y = 0.85, 0.9, 0.95, 1.0 and 1.05) nominal compositions. We can distinguish that the Ti_2AlN grain size decreased with increasing N content in the starting powders. Starting with 2Ti:1.05Al:0.85N nominal composition (Fig. 2-6 (a)), titanium aluminide (Ti_xAl_y) is detected in addition to the desired Ti_2AlN_y MAX phase. Starting with 2Ti:1.05Al:0.9N (Fig. 2-6 (b)), 2Ti:1.05Al:0.95N (Fig. 2-6 (c)), and 2Ti:1.05Al:1.0N (Fig. 2-6 (d)) nominal compositions, only Ti_2AlN_y is observed; no impurities are detected. Starting with 2Ti:1.05Al:1.05N nominal composition (Fig. 2-6 (e)), SEM observations coupled with EDS analyses confirm that Ti_4AlN_y (Ti/Al = 4), Ti_2AlN_y (Ti/Al = 2) and some Al_2O_3 (white dots) are formed. XRD results confirm the SEM/EDS analyses. Indeed, the XRD pattern shown in Fig. 2-6 (f) demonstrates that only Ti_2AlN_y peaks are detected for N content in the range 0.9-1.0. In addition to Ti_2AlN_y, titanium aluminides (Ti_xAl_y) and Ti_4AlN_y are respectively detected starting with 2Ti:1.05Al:0.85N and 2Ti:1.05Al:1.05N nominal compositions. WDS analyses coupled with SEM observations show that, the Ti, Al and N contents in the Ti_2AlN_y are very close to the ones introduced in the starting powders: $Ti_2Al_{0.99}N_{0.90}$ from 2Ti:1.05Al:0.9N, $Ti_2Al_{0.99}N_{0.95}$ from 2Ti:1.05Al:0.95N, and $Ti_2Al_{0.99}N_{0.99}$ from 2Ti:1.05Al:1.0N except of $Ti_2Al_{0.99}N_{0.87}$ from 2Ti:1.05Al:0.85N and $Ti_2Al_{0.99}N_{1.02}$ from 2Ti:1.05Al:1.05N. This can be ascribed to the formation of titanium aluminides (Ti_xAl_y) and Ti_4AlN_y in the starting powders with nominal ratios of 2Ti:1.05Al:0.85N and 2Ti:1.05Al:1.05N. For all samples, WDS and EDS analyses show that the overall Ti/Al ratio is 2:0.99, very close to 2:1, which indicates the loss of approximately 5 at.% of the aluminum during reactive sintering.

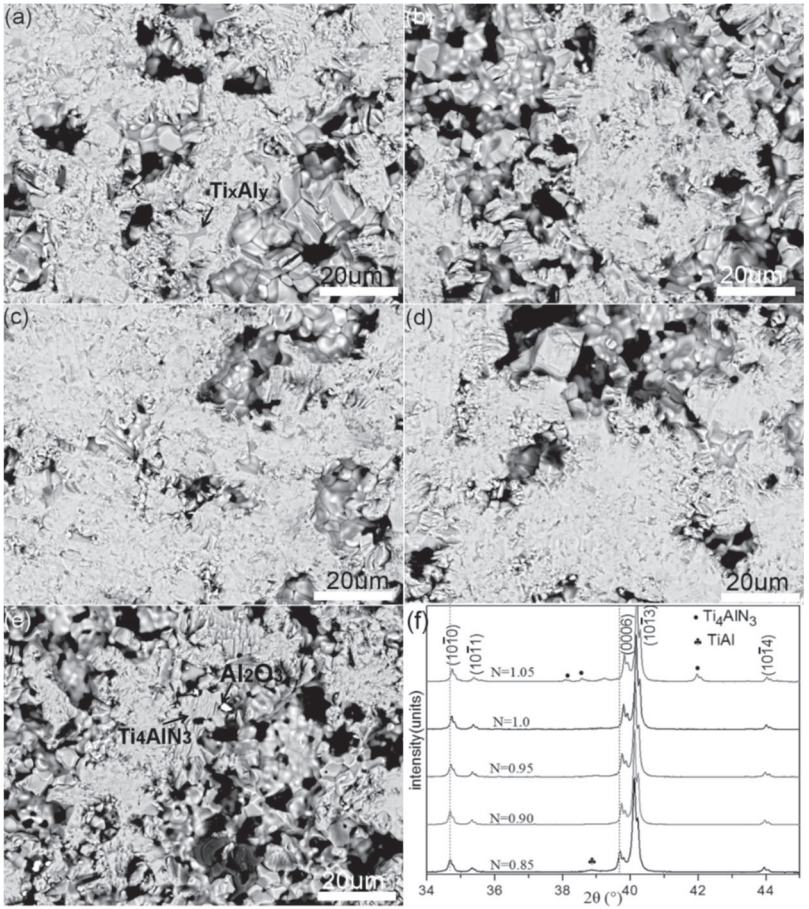

Fig. 2-6: (a-e) Morphologies of Ti_2AlN_y samples produced by pressureless sintering at 1400 °C for 0.5 h from 2Ti:1.05Al:yN (y=0.85, 0.9, 0.95, 1.0 and 1.05) nominal compositions; (f) XRD patterns of different mixtures sintered at 1400 °C for 0.5 h. The (hkml) indexed peaks correspond to the Ti_2AlN_y MAX phase.

Comparing the XRD patterns, the XRD peak corresponding to (0006) planes progressively shifts toward higher 2θ values when N content (y) increases, while the $(10\bar{1}0)$ peak shift is less significant. In reference to the interplanar spacing calculation in hexagonal system shown in equation 2-1, interplanar spacings (d) for (0006) and $(10\bar{1}0)$ planes are $c/8$, and $3a/4$, respectively.

$$d = \frac{1}{\frac{4}{3}\sqrt{\frac{(h^2 + hk + k^2)}{a^2} + \frac{l^2}{c^2}}} \qquad (2-1)$$

Herein, we find that N vacancy has a stronger effect on the *c*-lattice parameter than on *a*.

Fig. 2-7 shows the back-scattered SEM images of the samples HIPed from 2Ti:1.05Al:0.90N (Fig. 2-7 (a)) and 2Ti:1.05Al:1.0N (Fig. 2-7 (b)) starting nominal compositions. SEM observations coupled with WDS analyses confirm that these three samples are predominantly constituted of Ti_2AlN_y (y = 1 starting with 2Ti:1.05Al:1.0N nominal compositions, y = 0.9 starting with 2Ti:1.05Al:0.90N), while some Al_2O_3 (black round-shaped areas) traces are also detected. It can be noticed that the chemical composition of the Ti_2AlN_y end-products is similar to the starting powders composition. The Al_2O_3 content determined by image analysis using the image J software is about 2 vol.% starting with 2Ti:1.05Al:1.0N nominal composition (2Ti:0.05Al:AlN powder reactant mixture), while it is close to 0 starting with 2Ti:1.05Al:0.9N nominal composition (2Ti:0.15Al:0.9AlN powder reactant mixture). The Al_2O_3 content decreases with the decrease of the AlN content in the initial reactant powder mixture. Thus, the presence of alumina likely results from the surface oxidation of AlN starting powders. MAX phase lamellae are much bigger in the $Ti_2AlN_{0.9}$ HIPed samples as compared to the Ti_2AlN sample: indeed, the average dimension of $Ti_2AlN_{0.9}$ grains is in the range of 70-120 µm in length and 10-40 µm in width, as compared to 30-70 µm in length and 20-30 µm width for Ti_2AlN grains.

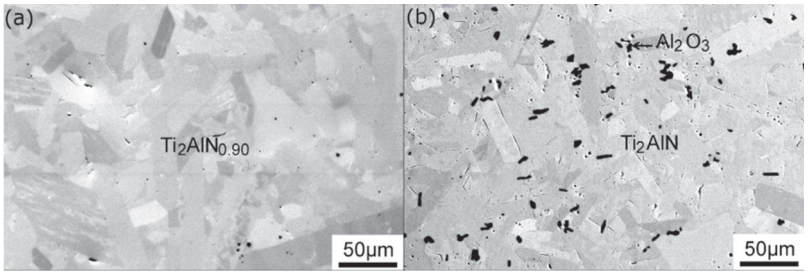

Fig. 2-7: Typical SEM micrographs (back-scattered mode) of different mixtures HIPed at 1400 °C and 80 MPa for 4 h from (a) 2Ti:1.05Al:1.0N, (b) 2Ti:1.05Al:0.90N nominal compositions. Chemical composition is measured by WDS. Ti_2AlN and $Ti_2AlN_{0.9}$ are marked on the corresponding MAX phases.

The synthesis of high-purity Ti_2AlN has been reported in the literature using Hot Pressing (HP) [5, 6, 12] and Spark Plasma Sintering (SPS)[4] methods, while HIPing at 1400 °C/40 MPa/48 h[4] and pressureless reactive sintering at 1400 °C/4 h[10] lead to the formation of secondary phases (see Table 2-3). Starting with 2Ti:1-1.1Al:N nominal composition, the authors consider that the Ti_2AlN end-product is stoichiometric, but they do not evaluate the N content[3, 10].

Table 2-3 Ti_2AlN processing and microstructural characteristics from the literature and from the present study.

Nominal composition	Processing	End-product composition	a (Å)	c (Å)	Ref.
Ti_2AlN powders (3ONE2)	Pressureless sintering 1500 °C/1 h/Ar	$Ti_{1.93}AlN_{0.975}$ wet chemical analysis	Not measured	Not measured	[14] [19]
Ti_2AlN	Pressureless sintering of Ti_2AlN powders	Ti_2AlN*,& (XRD)	2.986±0.003 (a)	13.60±0.02 (a)	[15]
2Ti:1.1Al:N	Pressureless reactive sintering 1400 °C/4 h	Ti_2AlN,Ti_xAl_y (XRD)	2.9891(2) (a)	13.615(1) (a)	[10]
2Ti:Al:N	SPS under vacuum 1200 °C/10 min/30 MPa	Ti_2AlN(XRD) $Ti_2Al_{0.83}N_{1.13}$ (EPMA)	Non-measured	Non-measured	[4]
2Ti:Al:N	Hot pressing 1600°C/4h/ 40MPa	Ti_2AlN* (XRD+SEM)	Not measured	Not measured	[6]
2Ti:Al:N	Hot pressing 1400 °C/25 MPa/1 h	Ti_2AlN* (XRD,SEM)	2.998 (a)	13.613 (a)	[5]

2Ti:Al:N	Hot pressing 1300 °C/2 h/30 MPa	Ti_2AlN (XRD) $Ti_2Al_{0.89}N_{1.06}$ (EPMA)	Not measured	Not measured	[12]
2Ti:Al:N	Hot pressing 1400 °C/8 h/45 MPa	$Ti_2Al_{1.04}N_{0.98}$ wet chemical analysis	Not measured	Not measured	[14]
2Ti:Al:N	HIP 1400 °C/48 h/40 MPa	Ti_2AlN* (XRD) Al_2O_3+Ti_3P+ Ti_4AlN_3 (11-20vol.%, EDS)	2.989 [(a)]	13.614 [(a)]	[3]
2Ti:1.05 Al:0.9N 2Ti:1.05 Al:1N	HIP 1400 °C/4 h/80 MPa	$Ti_2AlN_{0.9}$ (XRD, SEM/WDS) Ti_2AlN (98 vol.%) Al_2O_3 (2 vol.%) (XRD, SEM/WDS)	2.9879 2.9886	13.6302 13.615	[20]

* C content non-measured, & secondary phases non-determined, [(a)] from refinement of XRD pattern.

2.3.2. The effect of N content on Ti_2AlN lattice parameters

The lattice parameters (LPs) of Ti_2AlN_y as a function of N content, measured from Rietveld refinement of the XRD data using MAUD software, and calculated using ab initio calculations, are shown in Fig. 2-8 (a). Similar to the findings by Cabioc'h et al.[21], the volumes of the unit cell remain almost constant independent of y, while different variations for *a* and *c* LPs are clearly found. Experimentally, the lattice contraction of Ti_2AlNy is strongly anisotropic, namely, the *a* parameter slightly increases by about 0.0062 Å while the *c* parameter decreases about 0.0498 Å as the N content increases from 0.87 to 1.02. From Fig. 2-8 (b), the almost linear variation of the *c*/*a* ratio as a function of N content and consistency with the calculations indicates that the N vacancies are primarily randomly distributed. The calculated trends of the LPs reproduce the experimental measurements well. As the *c* parameter is about 4.5 times larger than the *a* parameter in Ti_2AlN MAX phases, as shown in Fig. 2-8 (c), we plotted the relative change changes in *a* and *c* as a function of N content. Both experimental and theoretical calculations indicate that the relative changes

in *c* are about 1.8 times larger than that of *a* as the N content increases from 0.87 to 1.02, which means the effect of N vacancies on Ti_2AlN lattice structure is anisotropic.

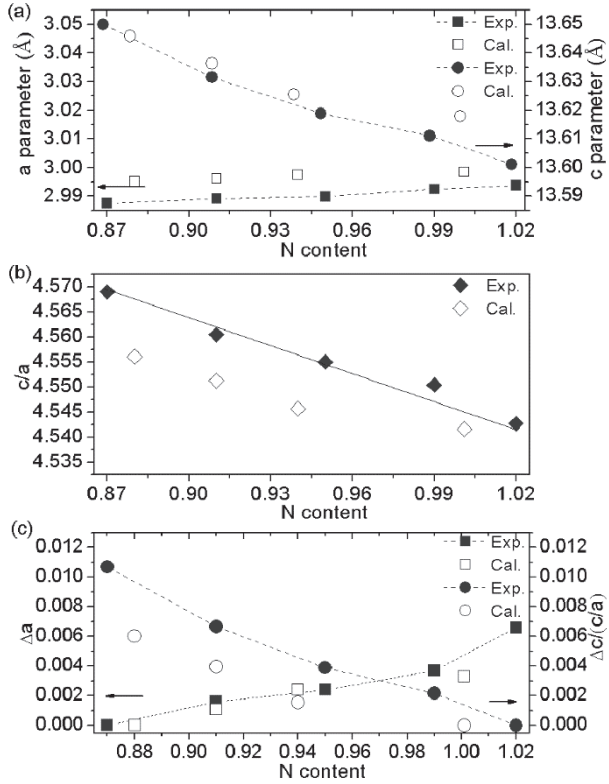

Fig. 2-8. (a) Variation of the *a* and *c* -LPs as a function of nitrogen content in the Ti_2AlN_y compounds from XRD experiments (blue) and ab initio calculations (white). (b) The *c*/*a* ratio versus N content. Error bars for lattice parameters being too small to be clearly observable (uncertainties of 5×10^{-4} Å and 5×10^{-3} Å were typically obtained for *a* and *c* parameters). (c) The relative change changes in *a* and *c* versus N content.

The MAX crystal unit cell, as shown in Fig. 2-9 (a), can be considered to be constituted of $[M_6X]$ octahedrons and $[M_6A]$ trigonal prisms[22, 23] allowing us to describe the "211" MAX phases[24]. A cubic octahedron is the unit block of the binary MX, but the fourfold axis is absent in ternary

MAX that results in a relaxation owing to the lowered symmetry. The parameter O_d, defined as the ratio of the distances between two faces not in the basal planes (d_1) and two opposite faces contained in the basal planes (d_2)[23], can be used to estimate the non-cubic distortion of the octahedron. It is given by:

$$O_d = \frac{d_1}{d_2} = \frac{\sqrt{3}}{2\sqrt{4z_{Ti}^2(\frac{c}{a})^2 + \frac{1}{12}}} \qquad (2-2)$$

The distortion parameter P_d, defined as the ratio of the M-M distance and the M-A distance[22], allows estimation of the distortion of the trigonal prism. It is given, in 211 MAX phases, by:

$$P_d = \frac{1}{\sqrt{(\frac{1}{4} - z_{Ti})^2(\frac{c}{a})^2 + \frac{1}{3}}} \qquad (2-3)$$

For an ideal packing of hard spheres of equal diameter, a ratio for c/a as of $8\times\sqrt{\frac{2}{3}}$ will be satisfied, and for an ideal octahedron (cubic) and trigonal prism, a unity for both O_d and P_d should also be reached. From the position of Ti atoms (z_{Ti}), a and c-lattice parameters measured above, both O_d and P_d were experimentally determined and plotted as a function of the N content in Ti_2AlN_y in Fig. 2-9 (b). Obviously, the relative distortion of the prism is similar to the one of the octahedra whatever the N content in Ti_2AlN_y, and the variations of O_d and P_d are very weakly dependent on the N content, and show the increasing linearly with the N content.

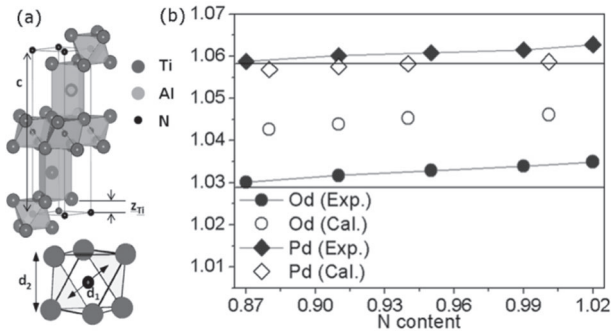

Fig. 2-9: (a) The unit cell of the Ti_2AlN phase with [Ti_6N] octahedrons (red) and [Ti_6Al] trigonal prisms (blue) represented with VESTA [24]. (b) The Octahedron (O_d, circles) and trigonal prism (P_d, squares) distortion parameters versus N content in Ti_2AlN_y.

2.4. Synthesis and microstructural characteristics of $Ti_2Al(C_xN_y)$ solid solutions

2.4.1. Stoichiometric $Ti_2Al(C_xN_{1-x})$ solid solutions

A series of stoichiometric $Ti_2Al(C_xN_{1-x})$ solid solutions has been synthesized using different nominal compositions (2Ti:1.1Al:0.25C:0.75N, 2Ti:1.1Al:0.50C:0.50N and 2Ti:1.1Al:0.75C:0.25N), with reactant powder mixture consisting of Ti, TiC, Al and AlN powders. The HIPing conditions are similar to the ones used previously: 1400 °C/4 h/80 MPa.

Fig. 2-10 (a-c) shows back-scattered SEM micrographs of the samples HIPed at 1400 °C and 80 MPa for 4 h. WDS analyses coupled with SEM observations demonstrate that, starting with 2Ti:1.1Al:xC:(1-x)N nominal composition with x = 0.25 and 0.5, the resulting $Ti_2AlC_{0.23}N_{0.76}$ (Fig. 2-10 (a)) and $Ti_2AlC_{0.49}N_{0.49}$ (Fig. 2-10 (b)) HIPed samples are predominantly single-phased. Starting with reactant mixtures containing higher C content, i.e., x = 0.75, some $Ti_3AlC_{1.48}N_{0.49}$ is detected in addition to $Ti_2AlC_{0.74}N_{0.25}$ (Fig. 2-10 (c)). One can notice that, starting with x = 1, large areas of $Ti_3Al_{0.99}C_{1.81}$ are observed in the $Ti_2AlC_{0.88}$ matrix (see Fig. 2-2). WDS analyses show that the Ti, Al, C and N contents in the $Ti_2Al(C_xN_{1-x})$ solid solutions are very close to the ones introduced in the starting powders. Moreover, for all samples, WDS shows that the overall Ti/Al ratio is very close to 2, which confirms the expected loss of approximately 10 at.% of the aluminum during reactive sintering, by evaporation and/or diffusion into molten glass at high temperatures.

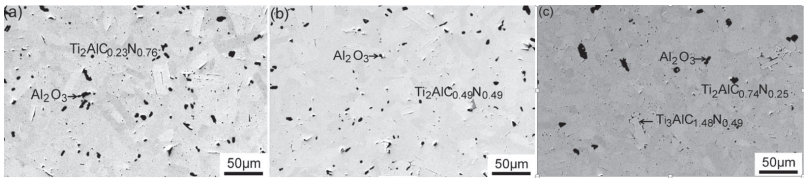

Fig. 2-10: Typical SEM micrographs (back-scattered electrons) of different mixtures HIPed at 1400 °C and 80 MPa for 4h, starting with (a) 2Ti:1.1Al:0.25C:0.75N, (b) 2Ti:1.1Al:0.50C:0.50N, (c) 2Ti:1.1Al:0.75C:0.25N nominal compositions. Chemical compositions are measured by WDS. $Ti_2AlC_{0.23}N_{0.76}$, $Ti_2AlC_{0.49}N_{0.49}$ and $Ti_2AlC_{0.74}N_{0.25}$ are marked on the corresponding MAX phases.

WDS analyses coupled with SEM observations also reveal the presence of Al_2O_3 (round-shaped black areas) in the $Ti_2AlC_{0.23}N_{0.76}$, $Ti_2AlC_{0.49}N_{0.49}$ and $Ti_2AlC_{0.74}N_{0.25}$ solid solutions. Using the image J software, image analysis allows the determination of a volume content of Al_2O_3 in the range 1-2.1 vol.%; such a result is in compatible agreement with the phase composition determined using the Rietveld refinement method. Note that the Al_2O_3 content of the stoichiometric solid solutions increases with the increase of the AlN content in the initial reactant powder mixture. Indeed, it has been previously shown that the Al_2O_3 content of the Ti_2AlN synthesized samples increases with the increase of the AlN content in the initial reactant powder mixture. Finally, the presence of alumina likely results from the surface oxidation of AlN starting powders. About 1-2 vol.% of Ti_xAl_y is also detected in the $Ti_2AlC_{0.74}N_{0.25}$ solid solution using the image J software; such a result is in compatible agreement with Rietveld refinement results.

Fig. 2-11 shows the XRD patterns recorded on different mixtures HIPed at 1400 °C/4 h/80 MPa. $Ti_2Al(C_xN_{1-x})$ is the only phase detected after reactive sintering starting with x = 0.25 and 0.5. One can notice that, starting with x = 0.75, some traces of $Ti_3Al(C_xN_{1-x})$ are detected in addition to the $Ti_2Al(C_xN_{1-x})$ solid solution after HIPing treatment. This secondary phase has also been evidenced by SEM (Fig. 2-10 (c)). Comparing the XRD patterns, a progressive shift of the $Ti_2Al(C_xN_{1-x})$ diffraction peaks toward lower 2θ values is observed when the C content (x) increases. It has been reported that MAX phases easily form solid solutions at M site [11, 25], A-site [26-29], and X site[3]. The C covalent radius (R_C = 0.76 Å) is slightly larger than the one of N (R_N = 0.71 Å)[30]. It may thus be possible for N atoms to be incorporated into the Ti_2AlC unit cell, and to substitute the C atoms to form stoichiometric $Ti_2Al(C_xN_{1-x})$ solid solutions. As a consequence, and assuming that Ti-C or Ti-N bonds show covalent bonding[31], the cell parameters of $Ti_2Al(C_xN_{1-x})$ should decrease compared to the ones of Ti_2AlC; such a hypothesis is in compatible agreement with our results.

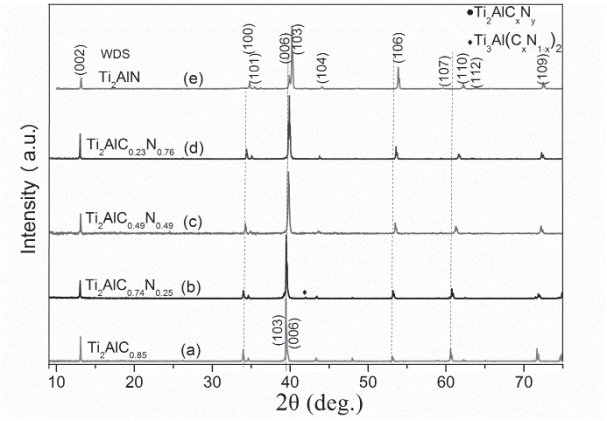

Fig. 2-11: XRD patterns of different mixtures HIPed at 1400 °C and 80 MPa for 4 h. (a) 2Ti:1.05Al:0.85C(b) 2Ti:1.1Al:0.75C:0.75N, (c) 2Ti:1.1Al:0.50C:0.50N, (d) 2Ti:1.1Al:0.25C:0.75N, (e) 2Ti:1.05Al:1.05N nominal compositions. The (hkl) indexed peaks correspond to the $Ti_2Al(C_xN_{1-x})$ solid solution.

2.5. Substoichiometric $Ti_2Al(C_xN_y)$ solid solutions (x+y<1)

2.5.1. Hypothesis

To produce pure substoichiometric $Ti_2Al(CxNy)$ solid solutions with x/y = 3, 1 or 1/3, (2-x)Ti:(1.05-y)Al:xTiC:yAlN starting powders have been used according to the following reaction:

(2-x)Ti + (1.05-y)Al + xTiC + yAlN –> $Ti_2AlCxNy$ (2-4)

Assuming that the vacancy content varies linearly from 0 to 0.15 going from Ti_2AlN to $Ti_2AlC0_{.85}$, x and y can be easily calculated. Indeed, in our synthesis conditions, the range of carbon composition in Ti_2AlC_x samples can be considered as very narrow around x = 0.85, and Ti_2AlN (y = 1) can be obtained as a single phase. Thus, pure $Ti_2Al(C_xN_y)$ solid solutions would only be obtained for a single value of the x/(1-y) = 0.85 ratio. One can also calculate this single value from the $Ti_2AlC0_{.85}$ end-member for which x/(1-y) = 0.85.

Given the values x/y = 3, 1 and 1/3, the subsequent nominal compositions are obtained: **2Ti:1.05Al:0.66C:0.22N** ((2-0.66)Ti:(1.05-0.22)Al:0.66TiC:0.22AlN starting powder mixture), **2Ti:1.05Al:0.46C:0.46N** ((2-0.46)Ti:(1.05-0.46)Al:0.46TiC:0.46AlN starting powder mixture) and **2Ti:1.05Al:0.24C:0.72N** ((2-0.24)Ti:(1.05-0.72)Al:0.24TiC:0.72AlN starting

powder mixture).

2.5.2. Microstructural characterization and discussion

From the XRD patterns shown in Fig. 2-12, $Ti_2Al(C_xN_y)$ is the only phase detected after HIPing treatment at 1400 °C and 80 MPa for 4 h of the different compositions investigated.

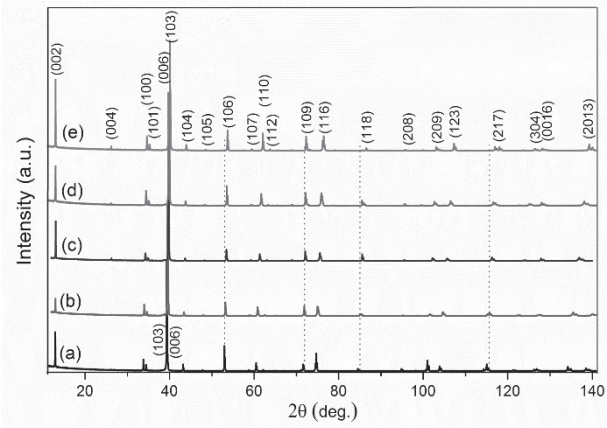

Fig. 2-12: XRD patterns of different mixtures HIPed at 1400 °C and 80 MPa for 4 h. (a) 2Ti:1.05Al:0.85C, (b) 2Ti:1.05Al:0.66C:0.22N, (c) 2Ti:1.05Al:0.46C:0.46N, (d) 2Ti:1.05Al:0.24C:0.72N, (e) 2Ti:1.05Al:1N nominal compositions. The (hkl) indexed peaks correspond to the $Ti_2Al(C_xN_y)$ phase.

Fig. 2-13 (a-c) shows SEM micrographs in back-scattered mode of the different solid solutions resulting from reactive sintering. The average dimensions of the grains are in the range 50-100 µm in length and 20-30 µm in width. The increase in grain size as compared to stoichiometric solid solutions is confirmed whatever the composition investigated. WDS analyses coupled with SEM observations show that, the Ti, Al, C and N contents in the $Ti_2Al(C_xN_y)$ solid solutions are very close, if not identical, to the ones introduced in the starting powders: $Ti_2AlC_{0.23}N_{0.71}$ from 2Ti:1.05Al:0.24C:0.72N, $Ti_2AlC_{0.45}N_{0.45}$ from 2Ti:1.05Al:0.46C:0.46N and $Ti_2AlC_{0.66}N_{0.22}$ from 2Ti:1.05Al:0.66C:0.22N. Moreover, for all samples, WDS analyses show that the overall Ti/Al ratio is 2:1, which indicates the expected loss of 5 at.% of aluminum during reactive sintering. WDS analyses coupled with SEM observations demonstrate that the resulting $Ti_2AlC_{0.66}N_{0.22}$ (Fig. 2-13 (a)) dense HIPed sample is single-phased. Starting with reactant mixtures containing high N content, i.e., y =

0.46 (Fig. 2-13 (b)) and y = 0.72 (Fig. 2-13 (c)), some Al_2O_3 (round-shaped black areas) is detected in dense HIPed samples. The Al_2O_3 content determined by image analysis, using the ImageJ software, is 0.3 and 0.9 vol.% in $Ti_2AlC_{0.45}N_{0.45}$ (Fig. 2-13 (b)) and $Ti_2AlC_{0.23}N_{0.71}$ (Fig. 2-13 (c)) respective solid solutions. The presence of Al_2O_3 likely results from the surface oxidation of AlN starting powders as its content increases with AlN content in the initial reactant powder mixture.

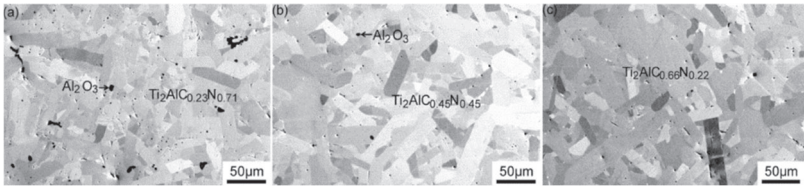

Fig. 2-13: SEM micrographs (back-scattered mode) of different mixtures HIPed at 1400 °C and 80 MPa for 4 h. (a) 2Ti:1.05Al:0.24C:0.72N, (b) 2Ti:1.05Al:0.46C:0.46N, (c) 2Ti:1.05Al:0.66C:0.22N nominal compositions. Chemical composition of the different phases is measured by WDS. $Ti_2AlC_{0.23}N_{0.71}$, $Ti_2AlC_{0.45}N_{0.45}$ and $Ti_2AlC_{0.66}N_{0.22}$ are marked on the corresponding MAX phases.

Comparing the XRD patterns shown in Fig. 2-12, the $Ti_2Al(C_xN_y)$ diffraction peaks are shifted toward higher 2θ values when the N content increases. Such a feature is not true for the (000l) peak family; the substitution of C by N thus mainly influences *a*-lattice parameters. This feature is explained by the variation of the *a* and/or *c*-lattice parameters of the hexagonal MAX phase. Fig. 2-14 gives the variation of the *a*- (Fig. 2-14 (a)) and *c*- (Fig. 2-14 (b)) lattice parameters of the stoichiometric and substoichiometric $Ti_2Al(C_xN_y)$ phase as a function of C content (x), determined by WDS analyses. It is important to notice that, for substoichiometric solid solutions, the vacancy content on the X site increases with the C content (red circles); as a consequence, both C substitution and vacancy contents should be considered to explain the variation of the *a* and *c*-lattice parameters of the $Ti_2Al(C_xN_y)$ solid solutions. Cabioc'h et al. [10] have demonstrated that very slight variations of the *a* and *c*-lattice parameters are observed when the vacancy content increases in $Ti_2Al(C_xN_{1-x})_y$ solid solutions, where x is fixed (0<x<1). For example, *a* and *c*-lattice parameters are (*a*=3.0201Å, *c*=13.618Å) and (*a*=3.0217Å, *c*=13.615Å) respectively for $Ti_2Al(C_{0.51}N_{0.49})_{0.80}$ and $Ti_2Al(C_{0.50}N_{0.50})_{0.88}$ compounds[10]. Such a result is confirmed by our studies. Indeed, whatever the vacancy content, *a*-parameter variation with

carbon content lies on a single line (Fig. 2-14 (a)). Thus, one can conclude that the *a*-lattice parameter variation can be mainly attributed to the substitution effect.

From Fig. 2-14 (a), it can be observed that the *a*-lattice parameter of the carbonitrides increases linearly with the C content; the *a*-lattice parameter of the stoichiometric (black square) and substoichiometric (red circle) solid solutions being larger than that of pure Ti_2AlN nitride (2.9886 Å) but smaller than that of pure $Ti_2AlC_{0.85}$ carbide (3.0607 Å). For stoichiometric and substoichiometric solid solutions, the linear variation of the *a*-lattice parameter with composition is consistent with the formation of a continuous substitutional solid solution in which N and C atoms that substitute for each other and are randomly distributed on the X site; in other words, *a* values obey Vegard's law. Such a linear variation was also observed for TiC_xN_{1-x} carbonitride[30] because of the close relationships between the $M_{n+1}X_n$ layers of the MAX phase and that of the corresponding binary MX compounds. The values of the *a*-lattice parameter obtained in this study for substoichiometric carbonitrides are also in very good agreement with the experimental ones from [10] and the one calculated by using the Cluster Expansion formalism[32].

Fig. 2-14 also shows that the lattice contraction of stoichiometric and substoichiometric $Ti_2Al(C_xN_y)$ solid solutions is strongly anisotropic, namely, much more reduction, going from Ti_2AlC_x to Ti_2AlN, along the *a*-axis than along the *c*-axis. From Fig. 2-14 (b), one can observe that the *c*-lattice parameter does not vary monotonically as a function of the C content in the solid solutions. Arroyave and Radovic have obtained the same kind of variation by investigating the energies of the C-N alloying in the C sublattice using the Cluster Expansion formalism[32]. The deviation from Vegard's law is attributed to the stronger M-X interactions that result from carbon and nitrogen mixing in the X sublattice. For substoichiometric solid solutions, the *c*-lattice parameters of $Ti_2AlC_{0.23}N_{0.71}$ and $Ti_2AlC_{0.45}N_{0.45}$ are smaller than those of both substoichiometric end-members, whereas for $Ti_2AlC_{0.66}N_{0.22}$ the *c*-lattice parameter is between those of both substoichiometric end-members. For stoichiometric solid solutions, the *c*-lattice parameter of $Ti_2AlC_{0.23}N_{0.76}$ is smaller than those of Ti_2AlN, $Ti_2AlC_{0.85}$ and $Ti_2AlC_{0.88}$, whereas for $Ti_2AlC_{0.49}N_{0.49}$ and $Ti_2AlC_{0.74}N_{0.25}$ the *c*-lattice parameter is between those of the previously mentioned end-members.

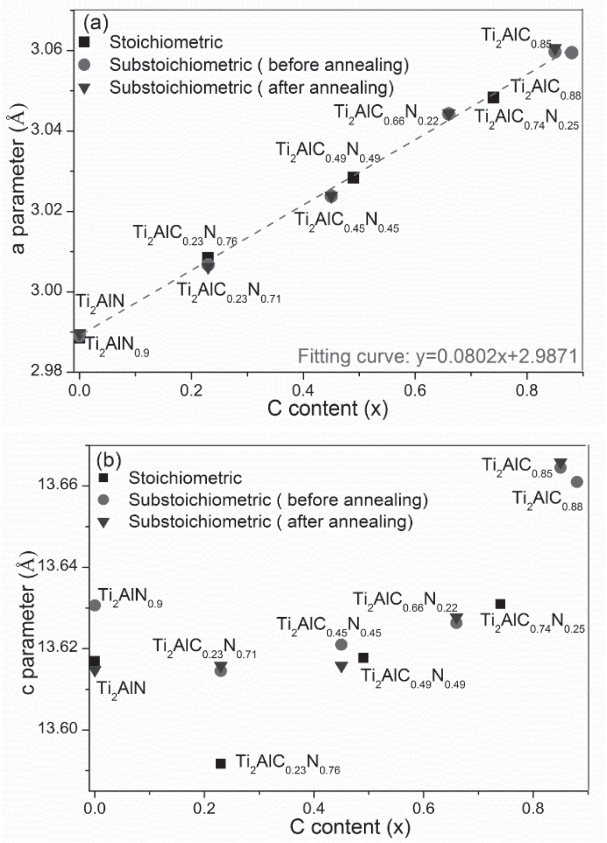

Fig. 2-14: Evolution of the *a*- (a) and *c*- (b) lattice parameters of stoichiometric (black square) and substoichiometric (red circle) $Ti_2Al(C_xN_y)$ solid solutions and related end-members determined from Rietveld refinement of the XRD data using MAUD software. Blue triangles indicate the *a*- and *c*- lattice parameters of substoichiometric samples and Ti_2AlN after annealing.

Assuming that C and N vacancies in substoichiometric $Ti_2Al(C_xN_y)$ carbonitrides solid solution is proportional to the vacancies in the end-members allows synthesizing high-purity and dense $Ti_2AlC_{0.66}N_{0.22}$, $Ti_2AlC_{0.45}N_{0.45}$ and $Ti_2AlC_{0.23}N_{0.71}$ solid solutions using HIPing technique at 1400 °C/80 MPa for 4 h. The lattice contraction in both $Ti_2Al(C_xN_{1-x})$ and $Ti_2AlC_xN_y$ is strongly anisotropic, namely, much more reduction, going from $Ti_2AlC_{0.9}$ to Ti_2AlN, along the a-axis than along the c-axis. The

a-lattice parameter obeys Vegard's law whatever the carbon and nitrogen vacancy content, whereas the *c*- parameter variation is not linear.

2.6. Summary and conclusions

For a high-purity and fully dense $Ti_2AlC_{0.85}$ carbide it was demonstrated that stoichiometric Ti_2AlC cannot be produced in our synthesis conditions since, whatever the nominal composition of the reactant powder investigated, a single substoichiometric $Ti_2AlC_{0.85}$ carbide is obtained.

Ti_2AlN was synthesized with varying N vacancy concentrations by pressureless sintering and Hot Isostatic Pressing. XRD and SEM prove that Ti_2AlN could be synthesized with up to 13% N substoichiometry.

For high-purity and fully dense substoichiometric $Ti_2Al(C_{0.66}N_{0.22})$, $Ti_2Al(C_{0.45}N_{0.45})$ and $Ti_2Al(C_{0.23}N_{0.71})$ solid solutions, it was assumed that the vacancy content on the C site of substoichiometric carbonitrides is proportional to the vacancy content in the C site of the $Ti_2AlC_{0.85}$ end-member.

The lattice contraction of stoichiometric and substoichiometric $Ti_2Al(C_xN_y)$ solid solutions is strongly anisotropic, namely, there is much more reduction, going from $Ti_2AlC_{0.85}$ to Ti_2AlN, along the *a*-axis than along the *c*-axis. The *a*-unit cell parameter obeys Vegard's law whereas the *c*-lattice parameter of the carbonitrides is not linear with C content.

References

[1] H.Nowotny, Structurchemie Einiger Verbindungen der Ubergangsmetalle mit den Elementen C, Si, Ge, Sn, Progress in Solid State Chemistry. 2(9) (1970) 27.

[2] X. Wang, Y. Zhou, Layered machinable and electrically conductive Ti_2AlC and Ti_3AlC_2 ceramics: a review, Journal of Materials Science & Technology 26(5) (2010) 385-416.

[3] M. Barsoum, T. El-Raghy, M. Ali, Processing and Characterization of Ti_2AlC, Ti_2AlN, and $Ti_2AlC_{0.5}N_{0.5}$, Metallurgical and Materials Transactions A 31(7) (2000) 1857-1865.

[4] M. Yan, B. Mei, J. Zhu, C. Tian, P. Wang, Synthesis of high-purity bulk Ti_2AlN by spark plasma sintering (SPS), Ceramics international 34(6) (2008) 1439-1442.

[5] Z. Lin, M. Zhuo, M. Li, J. Wang, Y. Zhou, Synthesis and microstructure of layered-ternary Ti_2AlN ceramic, Scripta Materialia 56(12) (2007) 1115-1118.

[6] M.W. Barsoum, D. Brodkin, T. El-Raghy, Layered machinable ceramics for high temperature applications, Scripta Materialia 36(5) (1997) 535-541.
[7] Z. Lin, M. Zhuo, Y. Zhou, M. Li, J. Wang, Microstructural characterization of layered ternary Ti_2AlC, Acta materialia 54(4) (2006) 1009-1015.
[8] W. Zhou, B. Mei, J. Zhu, X. Hong, Rapid synthesis of Ti_2AlC by spark plasma sintering technique, Materials Letters 59(1) (2005) 131-134.
[9] P. WANG, B.-c. MEI, X.-l. HONG, W.-b. ZHOU, Synthesis of Ti_2AlC by hot pressing and its mechanical and electrical properties, Transactions of Nonferrous Metals Society of China 17(5) (2007) 1001-1004.
[10] T. Cabioch, P. Eklund, V. Mauchamp, M. Jaouen, Structural investigation of substoichiometry and solid solution effects in $Ti_2Al(C_x, N_{1-x})_y$ compounds, Journal of the European Ceramic Society 32(8) (2012) 1803-1811.
[11] J. Schuster, H. Nowotny, C. Vaccaro, The ternary systems: CrAlC, VAlC, and TiAlC and the behavior of H-phases (M_2AlC), Journal of Solid State Chemistry 32(2) (1980) 213-219.
[12] M. Yan, Y.-l. Chen, B.-c. Mei, J.-q. Zhu, Synthesis of high-purity Ti_2AlN ceramic by hot pressing, Transactions of Nonferrous Metals Society of China 18(1) (2008) 82-85.
[13] E. S. Choi, J. Sung, Q.-m. Wang, K.-H. Kim, A. Busnaina, M.C. Kang, Material properties and machining performance of hybrid Ti_2AlN bulk material for micro electrical discharge machining, Transactions of Nonferrous Metals Society of China 22 (2012) s781-s786.
[14] T. Scabarozi, A. Ganguly, J. Hettinger, S. Lofland, S. Amini, P. Finkel, T. El-Raghy, M. Barsoum, Electronic and thermal properties of $Ti_3Al(C_{0.5}, N_{0.5})_2$, $Ti_2Al(C_{0.5}, N_{0.5})$ and Ti_2AlN, Journal of applied physics 104 (2008) 073713.
[15] B. Manoun, F. Zhang, S. Saxena, T. El-Raghy, M. Barsoum, X-ray high-pressure study of Ti_2AlN and Ti_2AlC, Journal of Physics and Chemistry of Solids 67(9-10) (2006) 2091-2094.
[16] M. Pietzka, J. Schuster, Summary of constitutional data on the Al–C–Ti system, Journal of Phase Equilibria 15(4) (1994) 392.
[17] J.-M. Guo, K.-X. Chen, Z.-B. Ge, H.-P. Zhou, X.-S. Ning, Effects of TiC and Ti_3AlC_2 Addition on Combustion Synthesis of Ti_3AlC_2 Powders [J], Journal of Inorganic Materials 1 (2003) 042.
[18] W. Yu, V. Gauthier-Brunet, T. Cabioc'h, S. Dubois, Synthesis and Microstructural Characterization of Substoichiometric $Ti_2Al(C_xN_y)$ Solid Solutions and Related Ti_2AlC_x and Ti_2AlN End-Members, Journal of the American Ceramic Society 97(7) (2014) 2308-2313.

[19] A. Mendoza-Galvan, M. Rybka, K. Järrendahl, H. Arwin, M. Magnuson, L. Hultman, M. Barsoum, Spectroscopic ellipsometry study on the dielectric function of bulk Ti_2AlN, Ti_2AlC, Nb_2AlC, $(Ti_{0.5}, Nb_{0.5})_2AlC$, and Ti_3GeC_2 MAX-phases, Journal of applied physics 109 (2011) 013530.
[20] W. Yu, W. Jia, F. Guo, Z. Ma, P. Zhang, C. Tromas, V. Gauthier-Brunet, P.R.C. Kent, W. Sun, S. Dubois, The correlation between N deficiency and the mechanical properties of the Ti_2AlNy MAX phase, Journal of the European Ceramic Society 40(6) (2020) 2279-2286.
[21] T. Cabioc'h, P. Eklund, V. Mauchamp, M. Jaouen, Structural investigation of substoichiometry and solid solution effects in $Ti_2Al(C_x,N_{1-x})_y$ compounds, Journal of the European Ceramic Society 32(8) (2012) 1803-1811.
[22] G. Hug, Electronic structures of and composition gaps among the ternary carbides Ti_2MC, Physical Review B - Condensed Matter and Materials Physics 74(18) (2006).
[23] G. Hug, M. Jaouen, M.W. Barsoum, X-ray absorption spectroscopy, EELS, and full-potential augmented plane wave study of the electronic structure of Ti_2AlC, Ti_2AlN, Nb_2AlC, and $(Ti_{0.5}Nb_{0.5})_2AlC$, Physical Review B - Condensed Matter and Materials Physics 71(2) (2005) 024105-1-024105-12.
[24] K. Momma, F. Izumi, VESTA: A three-dimensional visualization system for electronic and structural analysis, Journal of Applied Crystallography 41(3) (2008) 653-658.
[25] S. Gupta, E. Hoffman, M. Barsoum, Synthesis and oxidation of Ti_2InC, Zr_2InC, $(Ti_{0.5}, Zr_{0.5})_2InC$ and $(Ti_{0.5}, Hf_{0.5})_2InC$ in air, Journal of Alloys and Compounds 426(1-2) (2006) 168-175.
[26] A. Ganguly, T. Zhen, M. Barsoum, Synthesis and mechanical properties of Ti_3GeC_2 and $Ti_3(Si_xGe_{1-x})C_2$ (x = 0.5, 0.75) solid solutions, Journal of Alloys and Compounds 376(1-2) (2004) 287-295.
[27] Y. Zhou, J. Chen, J. Wang, Strengthening of Ti_3AlC_2 by incorporation of Si to form $Ti_3Al_{1-x}Si_xC_2$ solid solutions, Acta materialia 54(5) (2006) 1317-1322.
[28] P. Finkel, B. Seaman, K. Harrell, J. Palma, J. Hettinger, S. Lofland, A. Ganguly, M. Barsoum, Z. Sun, S. Li, Electronic, thermal, and elastic properties of $Ti_3Si_{1-x}Ge_xC_2$ solid solutions, Physical Review B 70(8) (2004) 085104.
[29] S. Dubois, G.P. Bei, C. Tromas, V. Gauthier-Brunet, P. Gadaud, Synthesis, Microstructure, and Mechanical Properties of $Ti_3Sn_{(1-x)}Al_xC_2$ MAX Phase Solid Solutions, International Journal of Applied Ceramic Technology 7(6) (2010) 719-729.

[30] K. Wokulska, Thermal expansion of whiskers of Ti(C, N) solid solutions, Journal of Alloys and Compounds 264(1) (1998) 223-227.
[31] H.O. Pierson, Handbook of Refractory Carbides & Nitrides: Properties, Characteristics, Processing and Apps, William Andrew1996.
[32] R. Arróyave, M. Radovic, Ab initio investigation of $Ti_2Al(C, N)$ solid solutions, Physical Review B 84(13) (2011) 134112.

CHAPTER 3

SOLID SOLUTION AND VACANCY EFFECTS IN MECHANICAL AND PHYSICAL PROPERTIES OF $Ti_2Al(C_xN_y)$ SOLID SOLUTIONS

3.1 Introduction

The substitution and substoichiometric effects and adjustment of the chemistry of MAX phases allow the modification and, in some cases, improvement of their physical properties. For example, $Ti_2AlC_{0.5}N_{0.5}$ has been reported [2] [5, 6] to be significantly harder than either of its end-members Ti_2AlC and Ti_2AlN, and there may be other ratios of C and N with even better properties. Scarabozi et al. have shown that the $Ti_2AlC_{0.5}N_{0.5}$ solid solution has a higher residual resistivity than the Ti_2AlC and Ti_2AlN end-members[1]. Such a higher residual resistivity has been attributed to scattering by impurities, vacancies or other defects. Results also suggest that vacancies are potent electron scatters as is well established in binary transition carbides[7, 8]; Scabarozi et al. have shown that substoichiometric $Ti_2AlN_{0.95}$ has a higher resistivity than stoichiometric Ti_2AlN[9] which suggests that vacancies are strong electron scatters. As a prerequisite to their application for electrical contacts, MAX phases electronic properties and especially their modifications resulting from solid solution and/or vacancy effects have to be properly studied and understood.

In the first section, nanoindentation is performed to evaluate the intrinsic hardness and the elastic modulus of highly pure $Ti_2Al(C_xN_y)$ substoichiometric solid solutions and their related end-members $Ti_2AlC_{0.85}$ and Ti_2AlN_y (y = 1 and 0.9). The results allow investigating eventual solid solution and vacancy effects on the mechanical properties of the Ti-Al-C-N system.

In the second section, the transport properties of Ti_2AlN_y (y = 1 and 0.9), $Ti_2AlC_{0.85}$ and a $Ti_2Al(C_xN_y)$ solid solutions series (stoichiometric and substoichiometric) were measured and compared. Experimental and theoretical results are discussed, focusing on the substitution and vacancy content effects.

3.2. Mechanical properties of $Ti_2Al(C_xN_y)$ solid solutions

3.2.1. Elastic modulus and intrinsic hardness of polycrystalline $Ti_2AlC_{0.45}N_{0.45}$

Fig. 3-1a shows the indent network performed on the $Ti_2Al(C_{0.45}N_{0.45})$ sample. One hundred and fifty nanoindentation tests were performed with different loads (100, 30, 15, 10, 6, 3, 2 and 1mN) in a regular array with a step size of 50µm. Furthermore, 15 large indents, obtained at 220mN, have been performed along two lines at the border of the array. These two lines allow an easy localization of the indent's network using SEM. For all samples, SEM observations were carried out to remove from the statistics the hardness and elastic modulus values that have been measured on indents that were not localized on a single MAX phase grain. As an example, Fig. 3-1d shows an indent localized in grain boundaries whereas Fig. 3-1 € shows an indent localized in a single grain.

Fig. 3-2 exhibits $Ti_2Al(C_{0.45}N_{0.45})$ hardness and elastic modulus as a function of the penetration depth of the indenter. The standard deviations result from an average of different grain orientations. $Ti_2Al(C_{0.45}N_{0.45})$ nanoindentation modulus remains constant (270±10 GPa) whatever the penetration depth is. Such a result attests that the indenter shape calibration is correct and, consequently, that the Indentation Size Effect (ISE) discussed below is not an artifact due to errors in indenter shape calibration. Indeed, one can notice that hardness values strongly decrease with increasing penetration depth. This variation is attributed to the ISE[10], which has already been reported in the case of Ti_3SnC_2[11], Ti_3AlC_2[12] and $Ti_3(Al_{0.8}Sn_{0.2})C_2$[12] MAX phase materials. The variation of the hardness values is well fitted by the same function as that proposed in the Nix and Gao model[13], where indents located are in a single grain, except for the higher loads (i.e., 100 and 220 mN). From the fit shown in Fig. 3-2, one can deduce that the intrinsic hardness value of $Ti_2Al(C_{0.45}N_{0.45})$ is 10.9 ±0.3 GPa. For the 100 and 220 mN loads, the size of the indents is close to the mean grain size. In that case, as observed by SEM (see Fig. 3-1c), several grains are involved in the deformation process and grain boundaries play an important role in macroscopic deformation, as reported by Tromas et al.[11]. For such high loads, nanoindentation conditions (loads, depth of the indent, number of grains involved in the deformation etc.) are close to those for microindentation and the hardness values are similar to those reported in microindentation experiments[27]. However, the intrinsic hardness values determined here from nanoindentation tests, and corresponding to single grain deformation, are not comparable to those resulting from microindentation tests[39].

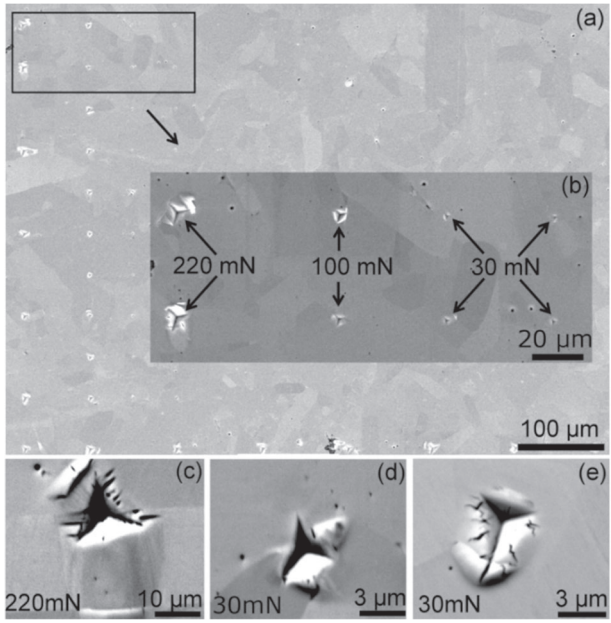

Fig. 3-1: (a) Array of indents performed on $Ti_2Al(C_{0.45}N_{0.45})$ sample. (b) Insert: enlarged SEM image of the area shown in the black rectangle of (a). (c) Indent performed at 220 mN: neighboring grains are involved in the deformation. (d) Indent performed at 30 mN and located on grain boundaries. € Indent performed at 30 mN and located in a single grain.

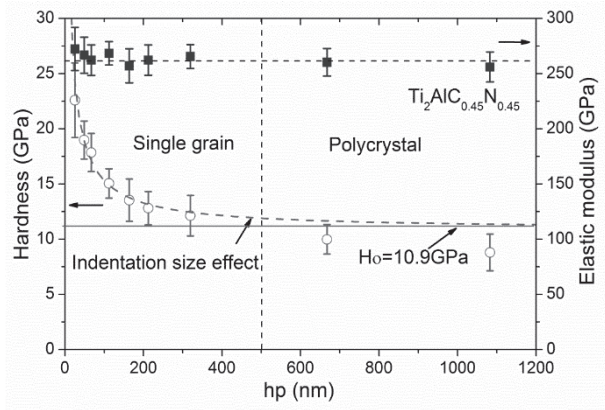

Fig. 3-2**:** $Ti_2Al(C_{0.45}N_{0.45})$ hardness (circles) and nanoindentation modulus (squares) plotted as a function of the indenter penetration depth. Dotted red line fits the ISE using the function proposed in the Nix and Gao model[13].

3.2.2. Solid solution effect on the hardness and elastic modulus of $Ti_2Al(C_xN_y)$ MAX phases.

Fig. 3-3 shows the variation of the intrinsic hardness and elastic modulus as a function of the C content in the substoichiometric solid solutions and related end-members. The decrease of the elastic modulus from Ti_2AlN_y (y=0.9 and 1) to $Ti_2AlC_{0.85}$ is in good qualitative agreement with theoretical calculations performed by Du et al.[6] and Arroyave et al.[14] using the Cluster Expansion method. These authors demonstrate that the elastic properties of the stoichiometric $Ti_2Al(C_{(1-x)}N_x)$ structure more or less closely follow the linear rule of mixing. Furthermore, most of the elastic constants in the system remain more or less constant as the carbon content increases. Moreover, the calculated orbital overlap shows that the Ti3d-N2p bonding orbitals in Ti_2AlN are stronger than the Ti(3d)-C(2p) bonding orbitals in Ti_2AlC[15]. Indeed, Magnusson et al. have shown, by comparing the N K Soft X-ray Emission (SXE) spectrum of Ti_2AlN and the C K SXE spectrum of Ti_2AlC, that the main peak of the former appears at -4.8 eV whereas the peak of the latter appears at -2.9 eV; a shift of -1.9 eV is clearly observed[15]. The peak shift to lower energy, from the Fermi level, indicates stronger interaction and bonding in Ti_2AlN than in Ti_2AlC. However, the strong decrease of elastic modulus in the case of $Ti_2AlC_{0.85}$ should be attributed to the vacancies effect.

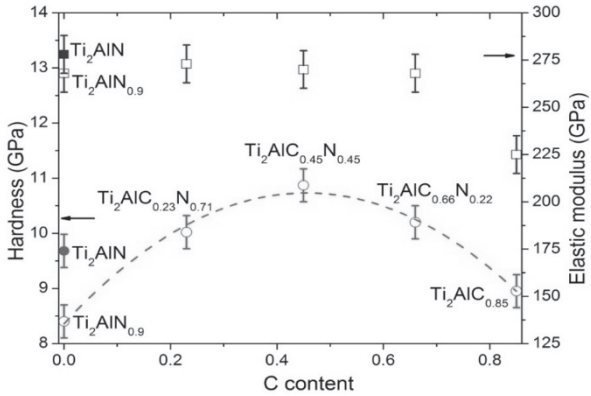

Fig. 3-3**:** Intrinsic hardness (circles) and nanoindentation modulus (squares) versus C content in the $Ti_2Al(C_xN_y)$ system.

Concerning the intrinsic hardness, one can notice that substoichiometric solid solution samples (H_v in the range 10.0-10.9 GPa) have higher

hardness values than their substoichiometric $Ti_2AlC_{0.85}$ (H_v=8.9 GPa) and $Ti_2AlN_{0.9}$ (H_v=8.1 GPa) end-members. Neglecting the slight variation of the vacancy content for these samples, such an effect mainly results from the solid solution strengthening effect.

3.2.3. Vacancy effects on the hardness and elastic modulus of $Ti_2Al(C_xN_y)$ MAX phases

From the fit shown in Fig. 3-4, one can deduce that the intrinsic hardness values of $Ti_2AlN_{0.9}$ and Ti_2AlN are respectively 8.1 and 9.7 GPa. For the 100 mN load, the size of the indents is in the order of the mean grain size. In that case, several grains are involved in the deformation process and grain boundaries play an important role in macroscopic deformation, as reported by Tromas et al. [11]. For such high loads, nanoindentation conditions (loads, depth of the indent, number of grains involved in the deformation etc.) are close to those for microindentation and the hardness values are similar to those reported in microindentation experiments.[16]

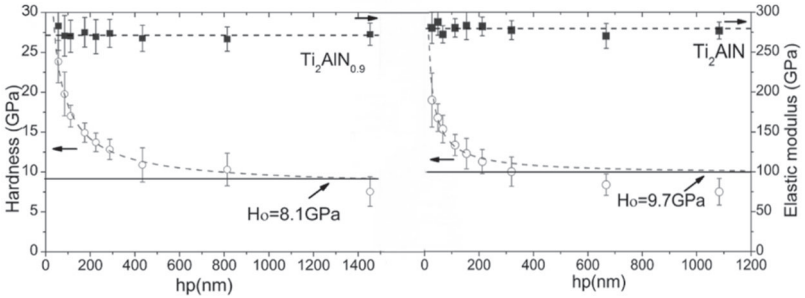

Fig. 3-4: Hardness (circles) and nanoindentation modulus (squares) of Ti_2AlN and $Ti_2AlN_{0.9}$ as a function of the indenter penetration depth.

Up to now, the effect of vacancies on the mechanical properties of MAX phases has not been investigated. The hardness values of TiC_x and TiN_y decrease with increasing vacancy content[17, 18]. In substoichiometric TiN_y, the integrated DOS demonstrates that Ti(3*d*)-N(2*p*) bonding states are reduced in the presence of vacancies, leading to weakened bond strength, shear strength and hardness[19]. Furthermore, it is predicted that the introduction of 12.5% of vacancies in TiN_y significantly reduces its shear stiffness from 190 GPa to less than 150 GPa[18], agreeing well with the experimental results[20]. A similar trend has been measured experimentally

in TiC_x [17]. For the ternary nitride Ti_2AlN, intuitively, the N vacancies would play a softening role in the mechanical properties.

From Table 3-1, the C_{ij} are reduced due to the weaker M-X bonding, as the concentration of N vacancies is increased. In the hexagonal lattice, the C_{11} is the in-plane elastic response, which is larger than C_{33} derived by the out-of-plane distortion, indicating the average bonding along the in-plane is stronger than the out-of-plane. It is indeed true, as determined by the layered structure. However, with higher N deficiency, these two constants become similar as the MAX lattice becomes more isotropic. When C_{33} is close to or smaller than C_{11}, it might be feasible to break the M−A−M bonds or significantly damage the M−X−M bonds[21, 22]. This would open a new route to obtaining the derivative 2D MXenes with clean surfaces by means of mechanical exfoliation, instead of the currently used chemical etching processes that lead to complicated surface terminal structures and compositions.

While the shear, bulk and Young's moduli are steadily suppressed with the increasing N vacancy concentration, the three moduli show different magnitudes of responses of 13.1%, 7.3%, and 11.7%, respectively. Experimentally, for pristine Ti_2AlN, the Young's modulus was found to be 278 ± 10 GPa, which is in very good agreement with the result obtained by Resonant Ultrasound Spectroscopy (RUS) on a Ti_2AlN bulk polycrystalline sample (E~277 GPa[5]) and 270 ± 20 GPa in another independent measurement by nanoindentation[23]. Note that the calculated E of Ti_2AlN with varying N vacancies are all falling into the regime between 258.2 and 293.1 GPa, which is in the line with the above measurements. We concluded that the perturbation of the various mechanical properties by N vacancies are different, and the incompressibility is the least affected.

3.2.4. Vacancy effects on electronic localization and Density of states

As discussed above, the combination of metallic and ceramic characteristics in MAX phases provides us with opportunities in many applications, where the formation of defects, their dynamics, and the consequences for the mechanical properties are critical. The formation energy for the varying N vacancies E_f was defined as $E_f = (E_v + n\mu_N - E_p)/16$, where E_v denotes the total energy of Ti_2AlN phase with N vacancies, μ_N is the chemical potential for a single N atom as of the $\frac{1}{2}N_2$ gas molecule, E_p stands for the total energy of the pristine Ti_2AlN, and n is the number of N vacancies in the supercell. Here, we consider the formation energy per unit cell by the division over the size of the supercell, 16. The formation energies

Table 3-1. The calculated elastic constants C_{ij} and the derived shear moduli, G, bulk moduli, B, Young's moduli, E and hardness, H (GPa).

MAX	C_{11}	C_{12}	C_{13}	C_{33}	C_{44}	G	B	E	$H_{v,Chen}$	$H_{v,Tian}$
$Ti_2AlN_{0.88}$	277.1	71.8	84.7	277.1	119.1	107.1	145.9	258.2	18.4	17.7
$Ti_2AlN_{0.91}$	272.1	74.0	84.9	283.6	121.1	107.8	146.1	259.7	18.6	17.9
$Ti_2AlN_{0.94}$	306.9	72.6	85.1	295.3	126.7	117.1	154.9	280.6	20.3	19.5
Ti_2AlN	310.7	68.9	88.3	286.8	127.7	119.4	155.4	285.2	21.1	21.0

of N vacancy in Ti_2AlN are positive, which is similar to the finding of N vacancy in Ti_4AlN_3.[24] It is thus demonstrated that the N vacancies are energetically costly. Moreover, the formation energy of N vacancies in the lower densities is higher than for higher densities.

Having the energetics of the N vacancy formation, we continue to elucidate the mechanical properties and the N vacancies induced changes. Here, we employed two widely used hardness models, $H_{v,Chen}$ [25] and H_v [26] to analyze both defect-free and the deficient Ti_2AlN. Note that Pugh's modulus ratio (k) defined as G/B, used as the indicator of a material's brittleness, is usually taken into account, and the above two models are expressed as:

$$H_{v,Chen} = 2(k^2G)^{0.585} - 3 \quad (3-1)$$

$$H_{v,Tian} = 0.92k^{1.137}G^{0.708} \quad (3-2)$$

We find that in the above two models the hardness is ~20 GPa and decreases monotonically with greater N deficiency. The reduction magnitude of $H_{v,Chen}$ and $H_{v,Tian}$ are respectively approximately 16% and 15% from the pristine to the highest N deficient MAX phase. In Eqns. (3-1) and (3-2), the exponential of k, G is the key to deducing the different slopes of the change, but the overview of the moduli and hardness of nitride MAX provides a clear insight into the role of the N deficiency. Overall, the reduction in hardness by introducing the N deficiency does not exhibit a dramatic change, in contrast to that found in binary nitrides.

It is well known that the bonding in the MAX phases is a combination of covalent, ionic and metallic bonding. To quantify the chemical bonding characters of Ti_2AlN, we compare the ELF in both the N defect-free and deficient ($N_{0.90}$) MAX phases in Fig. 3-5. In Fig. 3-5 (a), the predominate Ti-N bond shows a mixture of covalency (the blue bridge feature) and ionicity (the red spheres on N that gain extra electrons from Ti). For the Ti-Al bond, there is no evident covalent bonding, but near the Ti surface, a red triangle-shaped electronic cloud appears and represents the Ti-Al bonding. This strong localized feature illustrates that the Ti-Al bonding is a more ionic feature, and neither covalent (showing shared electrons) nor metallic (the level of localization would be about 0.5). Moreover, in Fig. 3-5 (b), the two N vacancies, marked by black circles, bring about the expansion of the Ti-N block because of the lack of chemical bonding. We could also observe a slight change within the interlayer spacing where the arrow is pointed. It is thus found that the Ti-N block is suppressed in the N-poor regime, and the interlayer interactions are also weakened by N vacancies.

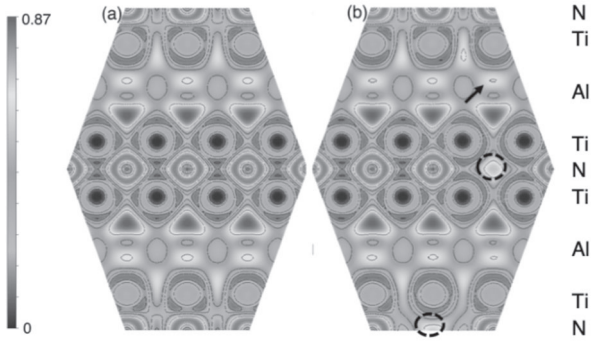

Fig. 3-5: 2D cut of the electronic localization function of (a) pristine Ti_2AlN in the miller indices (-1101), (b) 2D cut of ELF of $Ti_2AlN_{0.90}$. The view with the miller indices of (-1110) for capturing the defects (marked by spheres) and the changes in the interlayer spacing is marked by the arrow. Note that the color bar on the left represents the level of localization.

We unravel the physical origin behind the electronic properties based on the two series of bonding: Ti(3*d*)-N(2*p*) and Ti(3*d*)-Al(3*p*). First of all, the primary characteristics of the chemical bonding could be deduced from the vacancy free MAX phase: i) the Fermi energy is dominated by Ti(3*d*) states, and the valley shaped DOS near the vicinity of Fermi energy is present. ii) The strong covalent bond is on the Ti(3*d*)-N(2*p*) hybridization and is primarily situated between [-6, -4] eV with a pseudo-gap about -4.8 eV, as a result of the band splitting. iii) The hybridization of Ti(3*d*)-Al(3*p*) states occurred around -1.4 eV, is weaker in intensity and also higher in energy than those of Ti(3*d*)-N(2*p*). In general, for N deficient MAX, the Ti(3*d*)-N(2*p*) hybridization states are become more broadened in contrast to the pristine MAX, due to the band splitting originating from the symmetry breaking. Moreover, the splitting width between [-4, 5] eV, as highlighted by the arrow in Fig. 3-6, is experiencing a decrease with introducing more N vacancies, indicating the weakened Ti-N bonds. For Ti-Al, although weak, a similar tendency is also observed, where the hybridization primarily centered at -1 eV does experience a broadening. We therefore suggest that MAX phases are a unique class of ceramic, able to tolerate N deficiency, supporting the fact of slightly weakened Ti(3*d*)-N(2*p*) hybridization and the slowly decreased moduli. The methodology of synthesizing the controllable N concentration of MAX phases would stimulate the development of nitrides MAX and MXenes in substoichiometry. Our results show that N deficiency in ternary MAX phases leads to a slow reduction of the bond lengths and mechanical properties, particularly the

hardness, resulting in smaller changes than the binary TiN_y [18, 20].

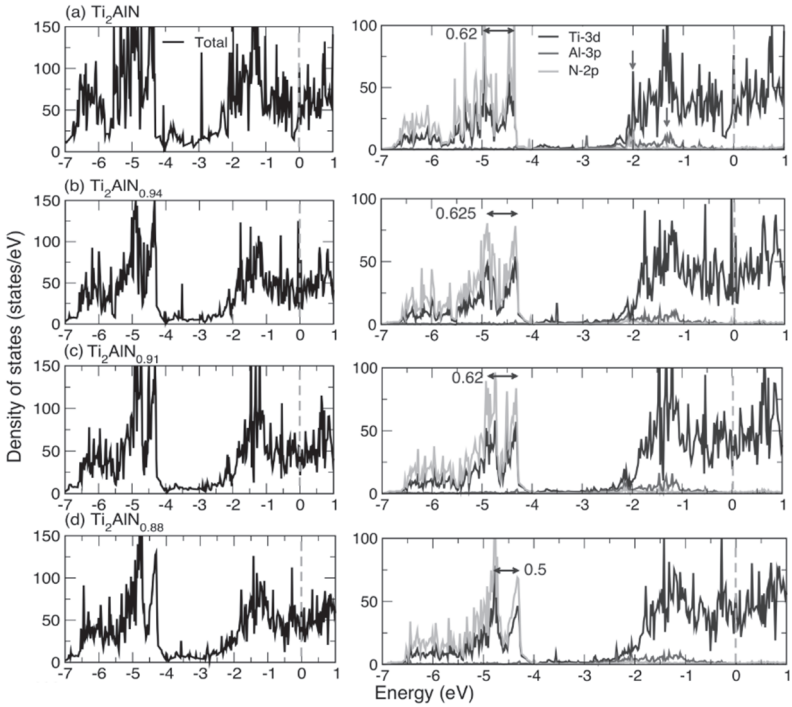

Fig. 3-6 The total and projected DOS of Ti_2AlN and N deficient MAX phases: (a) Ti_2AlN, (b) $Ti_2AlN_{0.94}$, (c) $Ti_2AlN_{0.91}$, (d) $Ti_2AlN_{0.88}$. The total DOS (left side) is represented by black curves, and the projected DOS (right side) for Ti (3*d*), Al (3*p*), and N (2*p*) states are shown in blue, red and orange, respectively.

3.3. Transport properties of $Ti_2Al(C_xN_y)$ solid solutions

3.3.1. Electronic structure and local order

The C-K and N-K edges recorded for the different solid solutions and related end-members are plotted in Fig. 3-7. The Feff simulations corresponding to Ti_2AlC and Ti_2AlN are also given (gray dashed and dotted lines). For the sake of comparison, the spectra were aligned and normalized on the most intense peak (B). It is worth noting that, as mentioned in the experimental details section, the C and N-K edges were recorded on grains oriented close to the [0001] zone axis. In these

conditions, the momentum transfer from the electron beam to the sample is mainly oriented within the basal plane of the structure: this could raise questions concerning the effect of the anisotropy of the unit cell on the recorded signal. However, contrary to the low loss spectra of MAX phases which exhibit a significant anisotropy related to the anisotropy of the dielectric response of these materials[27-30], the anisotropy observed at the X element K edge by EELS in the MAX phases is weak. This is evidenced in Fig. 3-7 where the C-K edge recorded on a Ti_2AlC thin film prepared in cross section is also given (dashed black lines). This last spectrum is clearly similar to that obtained on the bulk sample: the main reason is that the X element in the MAX phase is an octahedral environment. This is in agreement with recent results obtained at the C-K edge in Cr_2AlC [31]. For this reason, we do not expect any major restriction related to anisotropy effects in the results that will be presented in the following section.

Focusing first on the carbon K edges (Fig. 3-7 (a)), one can see that the ELNES consist of 6 different peaks labeled A to F. These six structures are evidenced in all experimental spectra and confirmed by the simulations which reproduce nicely their relative intensities (except for peak A) and energy positions. Note that these spectra are in very good agreement with those previously published by Hug et al.[32], with a better resolution, thus allowing the identification of the A shoulder. Our calculation is also very consistent with the one presented in reference [32]. The comparison between the experimental and theoretical spectra calls for two comments: (i) the shoulder A is more intense in the simulations than in the experiments and (ii) the structures C and D are broadened in the experimental spectrum corresponding to $Ti_2AlC_{0.85}$. Concerning point (i), a slight inaccuracy in the calculation of the charge transfers between the X and M elements that would then modify the electronic levels filling could well explain this difference. That charge transfers are quite complex in MAX phases is now well documented: these materials exhibit covalent, ionic and metallic-like bonds. Another possibility is that a slight change in the carbon content (as is obviously the case in $Ti_2AlC_{0.85}$) could also change the intensity of peak A since, as will be detailed below, this structure is representative of the carbon sites surrounding the excited carbon atom. Concerning point (ii), this broadening could be a consequence of some disorder induced by the 15% vacancies measured on the X site. Such an observation is in line with the previously mentioned broadening of ELNES observed in many materials when increasing disorder. This argument is also consistent with the fact that reducing the cluster size from 7.4 to 6.1 Å results in a broadening of these two structures (see the gray dotted line in Fig. 3-7 (a)) and that for vacancies-free systems ($Ti_2AlC_{0.25}N_{0.75}$, $Ti_2AlC_{0.5}N_{0.5}$ and

$Ti_2AlC_{0.75}N_{0.25}$), structures C and D recorded experimentally are very close to the calculations.

From the comparisons between experiments and calculations, one can safely assume that the C-K edge is sensitive to the local order up to approximately c/2 around the excited carbon atom since theoretical spectra are converged for cluster radii of approximately 7 Å. Considering the three main criteria showing the influence of solid solutions on the ELNES, the C-K edges presented here evidence a rather weak impact on the carbon atoms DOS. There is no significant energy shift, weak broadening and weak changes in the relative intensities of the different peaks. Still, having a closer look at the data, one can see a slight broadening of peaks A and B for the $C_{0.5}N_{0.5}$ sample (this is evidenced in the inset of Fig. 3-7 (a)). This broadening goes together with the fact that slight ELNES intensity variations were observed in the same sample when focusing on different grains. As an example, the blue dotted curve is a spectrum recorded on another grain of the sample. Interestingly this particular edge becomes very close to that recorded for the nitrogen atoms in the same sample (see the blue curve in Fig. 3-7 (b)): these changes could thus arise from the fact that for $C_{0.5}N_{0.5}$ the C and N atoms adopt almost identical surroundings which in turn gives identical ELNES at these two edges.

Focusing now on the N-K edges and the corresponding calculations, one can draw conclusions rather similar to those related to the C-K edges. One can hardly observe any change in the experimental fine structures of the different compounds (as evidenced in the inset and contrary to the C-K edge, peak B is unaffected by solid solution effects). From the ELNES point of view, the weak perturbation observed on the carbon atoms is thus confirmed for nitrogen atoms. Concerning the comparison with the calculations, it is worth mentioning that the agreement is less satisfactory than for the C-K edges. In particular, peaks A and B, which are clearly resolved in the calculations, are not separated experimentally. This is in complete agreement with the results published by Hug et al.[32] Apart from this point, the different structures C', C, D, E and F are observed. Here again, given the cluster size considered in the calculations to reproduce all these structures, the N-K edges are shown to probe the local order around the N atoms up to approximately c/2. It is important to compare our results to those Calmels et al. obtained for the TiC_xN_y system. In these last systems, solid solution effects induce peak broadening, energy shifts and variations of the relative intensities of the ELNES features[33]. From this point of view, the electronic structure of the MAX phase is clearly less perturbed by solid solution effects than the corresponding binary compounds.

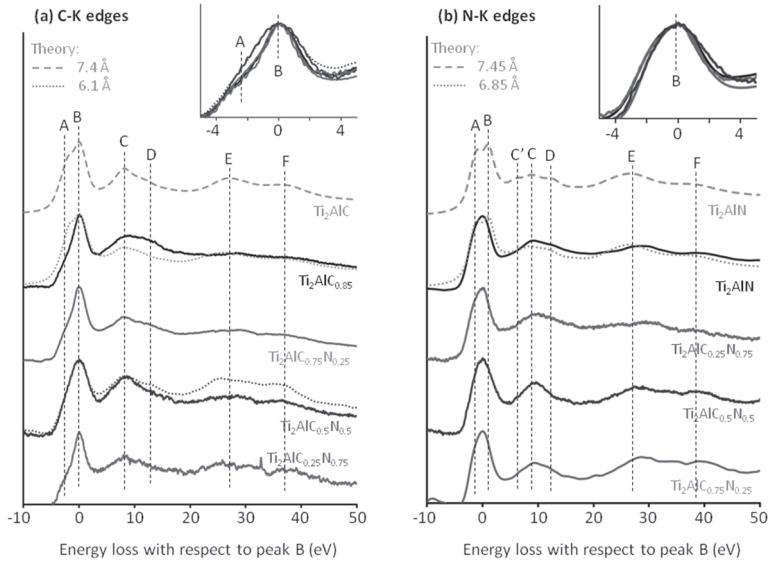

Fig. 3-7: (a) C-K edges and (b) N-K edges recorded for the different solid solutions: $C_{0.75}N_{0.25}$ (green lines), $C_{0.5}N_{0.5}$ (blue full and dotted lines), $C_{0.25}N_{0.75}$ (red lines). These spectra are compared to those obtained on the end-members of the series - $Ti_2AlC_{0.85}$ or Ti_2AlN and the corresponding Feff calculations obtained considering different cluster sizes (gray dashed and dotted lines). For the $Ti_2AlC_{0.85}$ sample, a spectrum recorded on a thin film prepared in cross section (i.e. [1-210] zone axis) is also shown for comparison (thin dashed black lines). The energy range corresponding to the peaks A and B is enlarged in the insets.

In order to gain more insight into the sensitivity of the ELNES on the local order in the $Ti_2AlC_xN_{1-x}$ systems, one can look at their decomposition among the different coordination shells around the excited atom. This is given in Fig. 3-8. For the sake of clarity, we only focus on the C-K edge decomposition since it is equivalent to the N-K edge. The sensitivity of the ELNES to the different coordination shells is quite obvious from Fig. 3-8: the energy position of peak B changes as a function of the number of coordination shells considered in the calculation: it is only stabilized when considering more than five coordination shells (the fifth coordination shell being comprised of 12 titanium atoms). Peak A is due to the presence of the tenth coordination shell made of 6 carbon atoms that confirms the possible dependence of its intensity on the carbon content in the material. The splitting of the C-D structures occurs at the ninth shell built

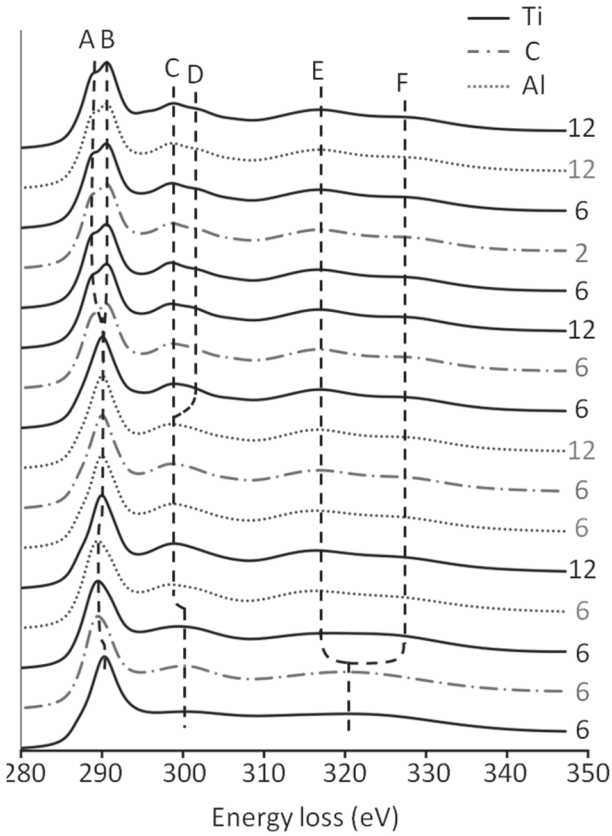

Fig. 3-8: Decomposition of the C-K fine structures in Ti_2AlC among the different coordination shells around the excited atom. Full black lines correspond to a Ti shell, the red dotted-dashed line to a carbon shell and the blue dotted line to an aluminum shell. The numbers on the right give the multiplicity of the atom in the considered coordination shell. Vertical dashed lines are guides for the eye.

on 6 titanium atoms whereas the E-F double structure already appears at the third coordination shell. These different features thus give information on the local order at different distances from the carbon site. More interestingly, except for the fourth coordination shell which slightly shifts the C-D peaks, the aluminum atoms do not participate in the ELNES: the C-K edge (and the N-K edge as well) is thus characteristic of the electronic density within the MX octahedra layers. This is important in terms of transport properties since these states are precisely those mainly

involved in the transport properties of the MAX phase as evidenced by the densities of states discussed in the next section. Although a direct comparison between EELS results and transport properties is not straightforward since the energy ranges investigated are not the same, one can expect from the EELS results that the solid solution effects are of the second order when considering the band structure part of the transport properties (e.g., ignoring the relaxation mechanisms). This is discussed in detail in the following section.

3.3.2. Resistivity vs temperature measurements

Fig. 3-9 shows the $Ti_2AlC_xN_y$ resistivity variations as a function of temperature. In the 100-300 K temperature range, there is a linear dependence of ρ as a function of temperature as generally observed for MAX phases compounds[1, 34-36]. This typical metal-like behavior simply results from the large density of states at the Fermi level[9, 37, 38].

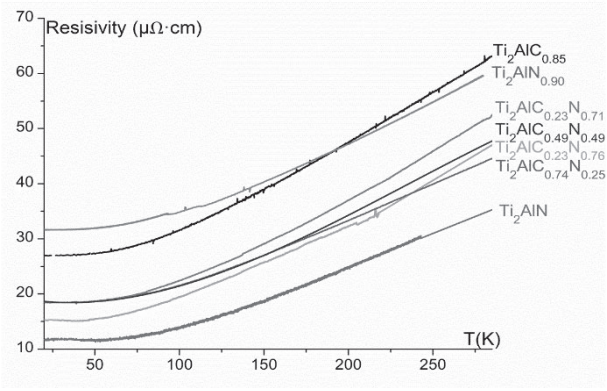

Fig. 3-9: Resistivity of $Ti_2AlC_xN_y$ solid solutions as a function of temperature.

To investigate the effect of grain size and grain boundaries on transport properties, two highly pure $Ti_2AlC_{0.85}$ samples, with the same carbon stoichiometry but with different grain sizes, have been synthesized (see Fig. 3-10). The residual resistivity (i.e., the low temperature resistivity) of the different samples has been extracted to investigate the vacancy and solid solution effects (see Fig. 3-11 (a) and (b)). Fig. 3-11 (a) shows the residual resistivity variation as a function of the vacancy content in the $Ti_2AlC_xN_y$ solid solutions. It can be noticed that the coarse-grained and fine-grained $Ti_2AlC_{0.85}$ samples have almost the same residual resistivity.

Such a small variation implies that the main defects that contribute to the residual resistivity are not grain boundaries. One can also notice that the residual resistivity monotonically increases with vacancy content. Such a result is related to electron scattering by vacancies as reported in the 1960s for titanium carbide[7]. It confirms that, as in binary carbides, vacancies are important electron scattering centers. Fig. 3-11 (b) shows residual resistivity variation as a function of the carbon content in the $Ti_2AlC_xN_{1-x}$ stoichiometric solid solutions. It demonstrates that the substitution of X element leads to an increase in electron scattering. Such an effect likely results from the increase of disorder when substituting carbon by nitrogen or nitrogen by carbon as previously observed for M substitution in $(Ti_{0.5}Nb_{0.5})_2AlC$[32].

Fig. 3-11 (b) also shows that the residual resistivity only varies between 6 and 18 $\mu\Omega$ cm^{-1} in the entire composition range. Such a variation is very small compared to the one measured, for example, on $Ti_{1-x}Al_x$ disordered alloys. In such an alloy, resistivity is vertically shifted by about 1 order of magnitude for x ranging from 0 to 0.06[39]; even higher variations are found in highly pure Al/Ag/Cd or Mg metals[40]. This difference indicates that making solid solutions in the $Ti_2AlC_xN_{1-x}$ system only induces a small disorder in the MAX phase structure. However, the variation is more important in systems with vacancies. For example, the residual resistivity of Ti_2AlN_y increases from 12 to 32 $\mu\Omega$ cm^{-1} when 10% of vacancy is introduced on the N site (see Fig. 3-11).

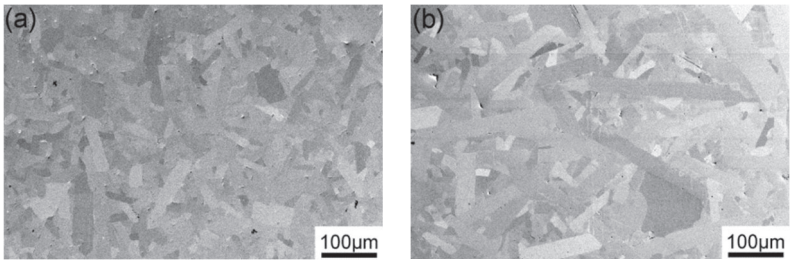

Fig. 3-10**:** SEM micrographs (back-scattered electrons) of polished sections of HIPed $Ti_2AlC_{0.85}$ samples (a) fine-grained sample (mean grain size W: 20 µm: L: 80 µm), (b) coarse-grained sample (mean grain size W: 35 µm: L: 150-200 µm).

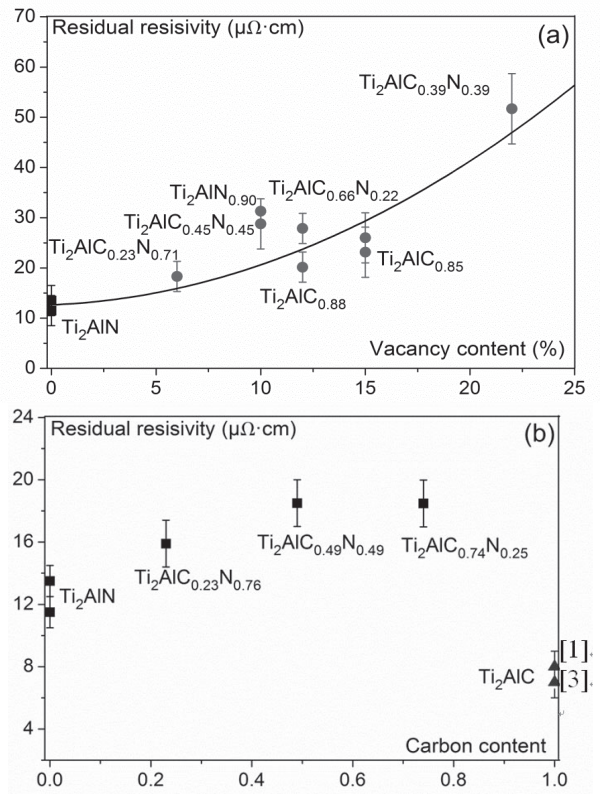

Fig. 3-11: Variation of the residual resistivity (a) as a function of the vacancy content in substoichiometric $Ti_2AlC_xN_y$ MAX phase solid solutions, (b) as a function of the carbon content in stoichiometric $Ti_2AlC_xN_{(1-x)}$ MAX phase solid solutions.

As defect and impurity contents slightly differ in the different samples and as ρ varies linearly with temperature in the 100–300 K range, one can calculate the slope of the linear variation (see Fig. 3-12) and the ideal resistivity which is the difference between the resistivity at the temperature T and the residual resistivity. The slope ($d\rho/dT$) and the ideal resistivity are representative of the intrinsic transport properties of the solid solutions and do not depend, in a first approximation, on defect and impurity contents. For Ti_2AlN samples, one can notice that the RT ideal resistivity (22 μΩ cm^{-1}) and slope of the linear variation (0.1 μΩ cm^{-1} K^{-1}), given the experimental errors, are the same whatever the Ti_2AlN sample. Such a result is not surprising, as ideal resistivity and electron scattering

mechanisms are the same for the same compound. It also means that the different Ti_2AlN synthesized in the literature[2, 41-44] likely has the same nitrogen stoichiometry. Moreover, experimental characterization of Ti_2AlN compounds indicates that the *a*-parameter standard deviation is small, which likely results from the small variation of the N stoichiometry in the different Ti_2AlN_y synthesized samples[2, 41-44]. Furthermore, the RT ideal resistivity (32 μΩ cm^{-1}) and slope of the linear variation (0.15 μΩ cm^{-1} K^{-1}) of $Ti_2AlN_{0.90}$ unambiguously demonstrates that vacancies lead to an increase of the intrinsic resistivity. Such a result is also significant for Ti_2AlC_x samples provided that Ti_2AlC discussed in references [1], [2] and [3] are considered as stoichiometric samples, although their chemical compositions have not been determined. Furthermore, we focus on our experimental results, as demonstrated from WDS experiments and transport measurements, the slope of the ρ(T) variation (0.10, 0.13, and 0.18 μΩ cm^{-1} K^{-1} for Ti_2AlC, $Ti_2AlC_{0.88}$ and $Ti_2AlC_{0.85}$ respectively) increases with the vacancy content. These results mainly differ from the ones obtained on substoichiometric TiC_x for which the slope of the ρ(T) variation decreases with the increase of the vacancy content[45]. Our results demonstrate that vacancies, as static defects, not only increase the residual resistivity but also the intrinsic resistivity. Furthermore, the results obtained on fine-grained and coarse-grained $Ti_2AlC_{0.85}$ samples show that the grain boundaries play a minor role in ρ and dρ/dT.

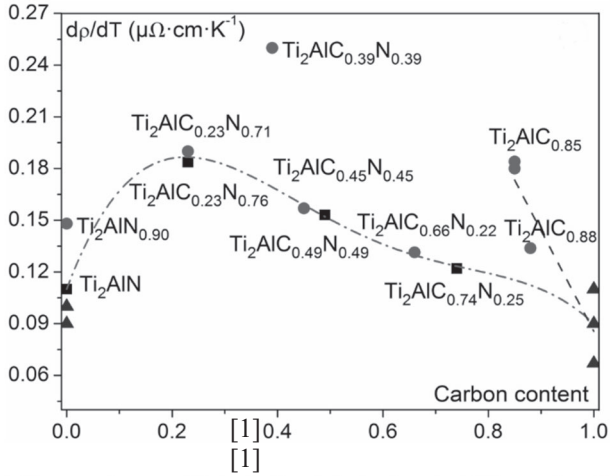

[1]
[1]

Fig. 3-12: Temperature coefficient of resistivity ($\alpha = d\rho/dT$) as a function of the carbon content in stoichiometric (black rectangles) and substoichiometric (red circles) $Ti_2AlC_xN_y$ solid solutions. Red and blue dotted lines are guides for the eye.

3.3.3. Effect of solid solution on the resistivity of stoichiometric $Ti_2AlC_xN_{1-x}$ MAX phases

Fig. 3-12 also shows that the slope of ρ(T) is larger for solid solutions than for the Ti_2AlN and Ti_2AlC end-members. In a single-band model, such a slope is given by $d\rho/dT = m_e^* / ne^2[d(1/\tau)/dT]$ where m_e^* is the electron effective mass, n is the charge carrier density and τ is the relaxation time. For a two-band model and a compensated conductor for which n = p, such a slope is given by $d\rho/dT = 1/ne^2[d(m_e^* \cdot m_h^*/(m_e^* \tau_e + m_h^* \tau_h)/dT]$ where m_e^*, m_h^*, τ_e and τ_h are the electron and hole effective mass and relaxation time, respectively; n is the charge carrier density. From these equations, such a slope depends on the charge carrier density, on the carrier effective mass and on the derivative of the inverse of the relaxation time. To clarify these points, the results of ab initio calculations are discussed in the next section.

In principle, the theoretical investigation of solid solution effects should be performed using approaches that are more complex than the VCA: either Special Quasi Random Structures (SQRS) or Cluster Expansion methods (CE). These methods have been used by Arroyave et al.[14]. They are much more time consuming and according to the results given in Fig. 3-14, the VCA gives a reasonable description of the DOS near the Fermi level compared to CE calculations[14]. As Ti *d* states dominate the TDOS near the Fermi level (see Fig. 3-14 (b) and 3-14 (c)), a modification of the X atom potential only acts to the second order on the DOS shape near E_F. In addition, both EELS[46] and resistivity data (see Fig. 3-11 (b)) show that the substitution does not induce major disorder (in particular, the Ti_6C/N octahedra are weakly deformed). From the DOS computed for the different solid solutions (see Fig. 3-13 (a)), it is demonstrated that modifying the composition thus only acts as a 0.5 eV rigid shift of the Fermi energy. It is worth noticing that the shift observed on the state lying below the Ti *d* bands (in the range -3 to -2 eV) is more important (these low lying states disappear from the considered energy range for x = 0.5). This can be understood form the fact that these states, which are shaded in Fig. 3-7 (a) and (b), correspond to Ti-X hybridizations which are probably more sensitive to an accurate description of the X atom potential.

These band structures were used as inputs for the calculation of σ/τ. The obtained σ/τ values are given in Table 3-2. In the whole composition range, the maximum relative variation is 10%, a value well below the relative resistivity variation observed experimentally (~50%). These weak variations are consistent with the fact that the rigid shift observed in the

electronic structure is within a flat part of the DOS. As the charge carrier density and the TDOS at E_F are related ($n = 1/3\pi^2(2mE_F/\hbar^2)^{3/2}$ in the free electron model), the charge carrier density should follow the same qualitative variation. Therefore, there are only weak changes in the charge carrier density in the different stoichiometric samples. Most of the variations of the slope of the stoichiometric $Ti_2AlC_xN_{1-x}$ solid solution's resistivity can thus be attributed to changes in the relaxation time which itself mainly results from the changes of electron-phonon relaxation time.

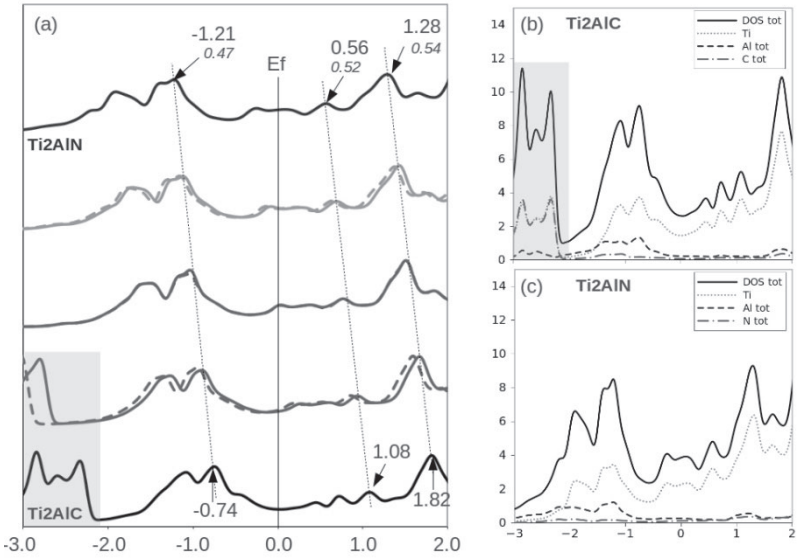

Fig. 3-13: (a) Density of states computed for the different solid solutions (Ti_2AlC (black line), $Ti_2AlC_{0.75}N_{0.25}$ (red line), $Ti_2AlC_{0.5}N_{0.5}$ (green line), $Ti_2AlC_{0.25}N_{0.75}$ (red line), (orange line) and Ti_2AlN (blue line)) in the VCA. (b) Ti_2AlC and (c) Ti_2AlN density of states.

Table 3-2: Ratio of the conductivity by the relaxation time obtained from the ab initio calculations for the different solid solutions.

Composition	Ti_2AlN	$N_{0.75}C_{0.25}$	$N_{0.5}C_{0.5}$	$N_{0.25}C_{0.75}$	Ti_2AlC
σ/τ ($1/(\Omega\ m^{-1}\ s^{-1})$)	$2.80\ 10^{20}$	$2.63\ 10^{20}$	$2.54\ 10^{20}$	$2.70\ 10^{20}$	$2.94\ 10^{20}$

3.4. Conclusions

Nanoindentation has been used to measure intrinsic hardness and elastic modulus of substoichiometric $Ti_2Al(C_xN_y)$ solid solutions and $Ti_2AlC_{0.85}$, Ti_2AlN_y (y = 0.9 and 1) related end-members. It has been shown that intrinsic hardness and elastic modulus of $Ti_2Al(C_xN_y)$ solid solutions are respectively in the 8-11 GPa and in the 220-280 GPa range. It is demonstrated that substitution and substoichiometry lead to antagonist effects on the mechanical properties. The former leads to an increase of the elastic modulus and intrinsic hardness, the latter leading to a deterioration of such mechanical properties.

The elastic modulus and intrinsic hardness of substoichiometric $Ti_2AlN_{0.9}$ (268 GPa and 8.1 GPa respectively) are shown to be smaller than that of Ti_2AlN (278 GPa and 9.7 GPa respectively). Overall the variation of moduli and hardness with up to 10% N deficiency is small in magnitude compared to the stoichiometric materials both experimentally and theoretically, confirming that the Ti_2AlN exhibits a great potential for tolerating N defects. Ab initio calculations demonstrate that both Ti-N and Ti-Al bonding exhibit only a slight weakening by the N deficiency.

Transport properties have been studied by four-point probe measurements in the temperature range 15-300 K. It is demonstrated that vacancies are strong scattering centers of electrons and lead to an increase of the residual resistivity; results also unambiguously demonstrated that the presence of vacancies leads to an increase of $d\rho/dT$.

It is also demonstrated that the solid solution effect leads to a weak variation of residual resistivity, but it induces some modifications of the intrinsic resistivity. The residual resistivity variation is much smaller than the one measured on $Ti_{1-x}Al_x$ disordered alloys[39], and highly pure Al/Ag/Cd or Mg metals[40]. Such a result suggests that substitution leads to a small variation of the local order on the X site not the region near the A-planes by the substitution, which has been recently demonstrated by V. Mauchamp from EELS experiments[46]. Furthermore, the rigid shift observed in the electronic structure is within a flat part of the DOS which allows the conclusion that there are weak changes in the charge carrier density. The maximum relative variation of the calculated σ/τ is 10%, which is well below the relative variation of the experimentally measured resistivity in the whole stoichiometric solid solution samples. Therefore, the relative variation of resistivity in solid solution samples mainly results from the variation of the electron-phonon relaxation time.

References

[1] T. Scabarozi, A. Ganguly, J. Hettinger, S. Lofland, S. Amini, P. Finkel, T. El-Raghy, M. Barsoum, Electronic and thermal properties of $Ti_3Al(C_{0.5}, N_{0.5})_2$, $Ti_2Al(C_{0.5}, N_{0.5})$ and Ti_2AlN, Journal of applied physics 104 (2008) 073713.
[2] M. Barsoum, T. El-Raghy, M. Ali, Processing and Characterization of Ti_2AlC, Ti_2AlN, and $Ti_2AlC_{0.5}N_{0.5}$, Metallurgical and Materials Transactions A 31(7) (2000) 1857-1865.
[3] X. Wang, Y. Zhou, Solid-liquid reaction synthesis and simultaneous densification of polycrystalline Ti_2AlC, Zeitschrift für Metallkunde 93(1) (2002) 66-71.
[4] P. Wang, B.-c. Mei, X.-l. Hong, W.-b. Zhou, Synthesis of Ti_2AlC by hot pressing and its mechanical and electrical properties, Transactions of Nonferrous Metals Society of China 17(5) (2007) 1001-1004.
[5] M. Radovic, A. Ganguly, M. Barsoum, Elastic properties and phonon conductivities of $Ti_3Al(C_{0.5},N_{0.5})_2$ and $Ti_2Al(C_{0.5},N_{0.5})$ solid solutions, Journal of Materials Research 23(6) (2008) 1517.
[6] Y. Du, Z. Sun, H. Hashimoto, M. Barsoum, Theoretical investigations on the elastic and thermodynamic properties of $Ti_2AlC_{0.5}N_{0.5}$ solid solution, Physics Letters A 374(1) (2009) 78-82.
[7] W.S. Williams, Scattering of electrons by vacancies in nonstoichiometric crystals of titanium carbide, Physical Review 135(2A) (1964) A505.
[8] L.W. Shacklette, W.S. Williams, Scattering of Electrons by Vacancies through an Order-Disorder Transition in Vanadium Carbide, Journal of applied physics 42(12) (1971) 4698-4703.
[9] S. Lofland, J. Hettinger, K. Harrell, P. Finkel, S. Gupta, M. Barsoum, G. Hug, Elastic and electronic properties of select M_2AX phases, Applied physics letters 84(4) (2004) 508-510.
[10] A.C. Fischer-Cripps, Nanoindentation, Springer 2011.
[11] C. Tromas, N. Ouabadi, V. Gauthier-Brunet, M. Jaouen, S. Dubois, Mechanical Properties of Nanolaminate Ti_3SnC_2 Carbide Determined by Nanohardness Cartography, Journal of the American Ceramic Society 93(2) (2010) 330-333.
[12] G. Bei, V. Gauthier-Brunet, C. Tromas, S. Dubois, Synthesis, Characterization, and Intrinsic Hardness of Layered Nanolaminate Ti_3AlC_2 and $Ti_3Al_{0.8}Sn_{0.2}C_2$ Solid Solution, Journal of the American Ceramic Society 95(1) (2011) 102-107.
[13] W.D. Nix, H. Gao, Indentation size effects in crystalline materials: a law for strain gradient plasticity, Journal of the Mechanics and Physics of Solids 46(3) (1998) 411-425.

[14] R. Arróyave, M. Radovic, Ab initio investigation of $Ti_2Al(C, N)$ solid solutions, Physical Review B 84(13) (2011) 134112.
[15] M. Magnuson, M. Mattesini, S. Li, C. Höglund, M. Beckers, L. Hultman, O. Eriksson, Bonding mechanism in the nitrides Ti_2AlN and TiN: An experimental and theoretical investigation, Physical Review B 76(19) (2007) 195127.
[16] M.W. Barsoum, and T. El-Raghy, Processing and characterization of Ti_2AlC, Ti_2AlN and $Ti_2AlC_{0.5}N_{0.5}$, Metallurgical and Materials Transactions A 31(7) (2000) 1857-1865.
[17] H.O. Pierson, Handbook of Refractory Carbides & Nitrides: Properties, Characteristics, Processing and Apps, William Andrew1996.
[18] S.H. Jhi, S.G. Louie, M.L. Cohen, J. Ihm, Vacancy hardening and softening in transition metal carbides and nitrides, Physical review letters 86(15) (2001) 3348-51.
[19] M. Magnuson, M. Mattesini, S. Li, C. Höglund, M. Beckers, L. Hultman, O. Eriksson, Bonding mechanism in the nitrides Ti_2AlN and TiN: an experimental and theoretical investigation, Physical Review B 76(19) (2007) 195127.
[20] X. Jiang, M. Wang, K. Schmidt, E. Dunlop, J. Haupt, W. Gissler, Elastic constants and hardness of ion-beam-sputtered TiN_x films measured by Brillouin scattering and depth-sensing indentation, Journal of applied physics 69(5) (1991) 3053-3057.
[21] M. Khazaei, M. Arai, T. Sasaki, M. Estili, Y. Sakka, Trends in electronic structures and structural properties of MAX phases: a first-principles study on M_2AlC (M = Sc, Ti, Cr, Zr, Nb, Mo, Hf, or Ta), M_2AlN, and hypothetical M_2AlB phases, Journal of Physics: Condensed Matter 26(50) (2014) 505503.
[22] M. Khazaei, M. Arai, T. Sasaki, M. Estili, Y. Sakka, The effect of the interlayer element on the exfoliation of layered Mo_2AC (A = Al, Si, P, Ga, Ge, As or In) MAX phases into two-dimensional Mo_2C nanosheets, Science & Technology of Advanced Materials 15(1) (2014) 1-7.
[23] T. Joelsson, A. Horling, J. Birch, L. Hultman, Single-crystal Ti_2AlN thin films, Applied physics letters 86(11) (2005) 111913-111913-3.
[24] D. Music, R. Ahuja, J.M. Schneider, Theoretical study of nitrogen vacancies in Ti_4AlN_3, 86(3) (2005) 235108.
[25] X.Q. Chen, H. Niu, D. Li, Y. Li, Modeling hardness of polycrystalline materials and bulk metallic glasses, Intermetallics 19(9) (2011) 1275-1281.
[26] Y. Tian, X. Bo, Z. Zhao, Microscopic theory of hardness and design of novel superhard crystals, International Journal of Refractory Metals & Hard Materials 33(33) (2012) 93-106.

[27] V. Mauchamp, G. Hug, M. Bugnet, T. Cabioc'h, M. Jaouen, Anisotropy of Ti_2AlN dielectric response investigated by ab initio calculations and electron energy-loss spectroscopy, Physical Review B 81(3) (2010) 035109.
[28] M. Magnuson, M. Mattesini, N. Van Nong, P. Eklund, L. Hultman, Electronic-structure origin of the anisotropic thermopower of nanolaminated Ti_3SiC_2 determined by polarized x-ray spectroscopy and Seebeck measurements, Physical Review B 85(19) (2012) 195134.
[29] G. Hug, P. Eklund, A. Orchowski, Orientation dependence of electron energy loss spectra and dielectric functions of Ti_3SiC_2 and Ti_3AlC_2, Ultramicroscopy 110(8) (2010) 1054-1058.
[30] N. Haddad, E. Garcia-Caurel, L. Hultman, M.W. Barsoum, G. Hug, Dielectric properties of TiAlC and TiAlN MAX phases: The conductivity anisotropy, Journal of applied physics 104 (2008) 023531.
[31] M.Bugnet, Synthèse, structure électronique et comportement sous irradiation aux ions de films minces de phases MAX (2014). Thèse de doctorat Milieux denses, matériaux et composants Poitiers http://www.theses.fr/2011POIT2318/document
[32] G. Hug, M. Jaouen, M. Barsoum, X-ray absorption spectroscopy, EELS, and full-potential augmented plane wave study of the electronic structure of Ti_2AlC, Ti_2AlN, Nb_2AlC, and $(Ti_{0.5}Nb_{0.5})_2AlC$, Physical Review B - Condensed Matter and Materials Physics 71(2) (2005) 024105-1-024105-12.
[33] L. Calmels, C. Mirguet, Y. Kihn, Evidence of alloying effects in TiC_xN_{1-x} compounds from calculated and experimental electron energy loss spectra, Physical Review B 73(2) (2006) 024207.
[34] J. Hettinger, S. Lofland, P. Finkel, T. Meehan, J. Palma, K. Harrell, S. Gupta, A. Ganguly, T. El-Raghy, M. Barsoum, Electrical transport, thermal transport, and elastic properties of M_2AlC (M= Ti, Cr, Nb, and V), Physical Review B 72(11) (2005) 115120.
[35] P. Finkel, B. Seaman, K. Harrell, J. Palma, J. Hettinger, S. Lofland, A. Ganguly, M. Barsoum, Z. Sun, S. Li, Electronic, thermal, and elastic properties of $Ti_3Si_{1-x}Ge_xC_2$ solid solutions, Physical Review B 70(8) (2004) 085104.
[36] P. Finkel, J. Hettinger, S. Lofland, M. Barsoum, T. El-Raghy, Magnetotransport properties of the ternary carbide Ti_3SiC_2: Hall effect, magnetoresistance, and magnetic susceptibility, Physical Review B 65(3) (2001) 035113.
[37] Z. Sun, Y. Zhou, Ab initio calculation of titanium silicon carbide, Physical Review B 60(3) (1999) 1441.

[38] G. Hug, Electronic structures of and composition gaps among the ternary carbides Ti_2MC, Physical Review B 74(18) (2006) 184113.
[39] J. Mooij, Electrical conduction in concentrated disordered transition metal alloys, Physica status solidi (a) 17(2) (1973) 521-530.
[40] R. Seth, S. Woods, Electrical resistivity and deviations from Matthiessen's rule in dilute alloys of aluminum, cadmium, silver, and magnesium, Physical Review B 2(8) (1970) 2961.
[41] T. Cabioch, P. Eklund, V. Mauchamp, M. Jaouen, Structural investigation of substoichiometry and solid solution effects in $Ti_2Al(C_x, N_{1-x})_y$ compounds, Journal of the European Ceramic Society 32(8) (2012) 1803-1811.
[42] M.W. Barsoum, D. Brodkin, T. El-Raghy, Layered machinable ceramics for high temperature applications, Scripta Materialia 36(5) (1997) 535-541.
[43] Z. Lin, M. Zhuo, M. Li, J. Wang, Y. Zhou, Synthesis and microstructure of layered-ternary Ti_2AlN ceramic, Scripta Materialia 56(12) (2007) 1115-1118.
[44] B. Manoun, F. Zhang, S. Saxena, T. El-Raghy, M. Barsoum, X-ray high-pressure study of Ti_2AlN and Ti_2AlC, Journal of Physics and Chemistry of Solids 67(9-10) (2006) 2091-2094.
[45] S. Otani, T. Tanaka, Y. Ishizawa, Electrical resistivities in single crystals of TiC_x and VC_x, Journal of materials science 21(3) (1986) 1011-1014.
[46] W. Yu, V. Mauchamp, L. Gence, L. Piraux, T. Cabioc'h, and S. Dubois, Solid solution effects in the $Ti_2Al(C_xN_y)$ MAX phases: synthesis and transport properties, Acta Materilia 80 (2014) 421-434.

CHAPTER 4

ANISOTROPIC TRANSPORT PROPERTIES OF Ti_2AlC AND Ti_3SiC_2

4.1 Introduction

4.1.1. Electronic transport properties in the framework of the two-band model

M. W. Barsoum and co-workers[1-6] used the two-band model to determine electron-like and hole-like mobilities; in a first approximation they also assumed that n = p or $\mu_n = \mu_p$. One can notice that such an assumption implies that RH = 0. Nevertheless, it seems not difficult to adjust μn and μp to yield the correct values and signs for RH. Moreover, the mobility values are relatively close to each other as stated by equations 4-6 shown in chapter 1 and by the low value of the Hall coefficients.

Table 4-1 summarizes electrical transport parameters of some MAX phases that have been calculated from the above equations with the assumption of n = p. It seems that MAX phases can be considered as compensated conductors with n = p and electron-like and hole-like mobilities in the same range. A two-band model also seems to give account of their electronic properties.

Table 4-1 also allows some main conclusions found in the framework of the two-band model to be drawn:

- The density of charge carriers are typically in the range 0.3-3.10^{+27} m^{-3}. n and p are not functions of temperature.
- The low temperature mobility is inversely proportional to the TDOS at the Fermi level[7]. Since the main contribution to the conduction of MAX phases comes from d states of M atoms, it is quite reasonable to obtain such a result which is in good agreement with Mott approximation in transition metals.
- Averaging n and p listed in Table 4-1 allows correlation of the charge carrier density and the TDOS at the Fermi level.

Table 4-1: Summary of electrical transport parameters of some MAX phases that have been calculated from equations 1-4-1-6 shown in chapter 1 and assuming that n=p, with reference to [6].

Composition	T (K)	ρ μΩ cm^{-1}	$d\rho/dT$ μΩ cm^{-1} K^{-1}	R_H (10^{11}) (m^3/C)	$\alpha(T^{-2})$ 10^{-5} ($m^4/V^{-2}s^{-2}$)	$n = p$ (10^{27} m^{-3})	$\mu_n(5k)=\mu_p$ (5k) (10^{-3} $m^2V^{-1}s^{-1}$)	Ref.
211 Phases								
Ti_2AlC	300	36	0.11	-27	8.3	0.95	9	[1]
	4	7.3		-8	200	0.95	45	
Ti_2AlC	300	36		-28	20	0.65	14	[8]
$Ti_2AlC_{0.5}N_{0.5}$	300	43	0.12	45.6	3.5	1.47	5.9	[1]
	4	16.7		60	22	1.67	15	
Ti_2AlN-a	300	25	0.10	-3.9	17	0.95	13	[1]
	4	2.9		6.1	687	1.3	83	
Ti_2AlN-b	300	34.3	0.09	-7	4.8	1.32	6.9	[1]
	4	12.3		16	20	1.80	14	
Ti_2GeC	300	30	0.084	27	5	1.47	7.1	[3]
	4	9.4		16	73	1.23	27	
Ti_2SC	300	52	0.14	-160	23	0.39	15	[9]
	4	23		-149	120	0.39	35	
Cr_2GeC	300	72	0.27	-24.3	2	0.97	4.5	[10]
	4	6.4		0	50	2.18	22	
Cr_2AlC	300	74	0.27	15	0.73	1.56	2.7	[8]
	4	15		0	5	2.95	7	
V_2AlC	300	25	0.10	-10	2	2.8	4.5	[8]
	4	4		-6.5	37	4.05	19	
312 Phases								
Ti_3SiC_2	300	22		38	2.9	2.65	5.4	[11]
	4	3		30	206	2.3	45	
Ti_3AlC_2	300	35.3		-1.2	3.7	1.41	6.3	[2]
	4	18.1		1.0	11	1.71	10	
Ti_3AlCN	300	40		17.4	0.65	3.07	2.5	[2]
	4	27		33	3.3	2.07	5.7	
Ti_3GeC_2	300	28		-18	15	0.9	12	[11]
	4	5		-2.5	200	1.4	45	
413 Phases								
$Ti_4AlN_{2.9}$	300	261		90	0.03	3.5	0.55	[12]
	300	261		90±5	0.03	7.0	0.34	

4.1.2 Contradiction in transport properties

A large number of theoretical papers[13-16] have predicted strong anisotropic electronic conductivity. There is no gap between the valence band and the conduction band. As a result, MAX phases should present metal-like conductivity, as indeed is demonstrated experimentally. As shown in Fig. 4-1, the calculated band structure and Fermi surface of Ti_2AlC given by the band structure show strong anisotropic features:

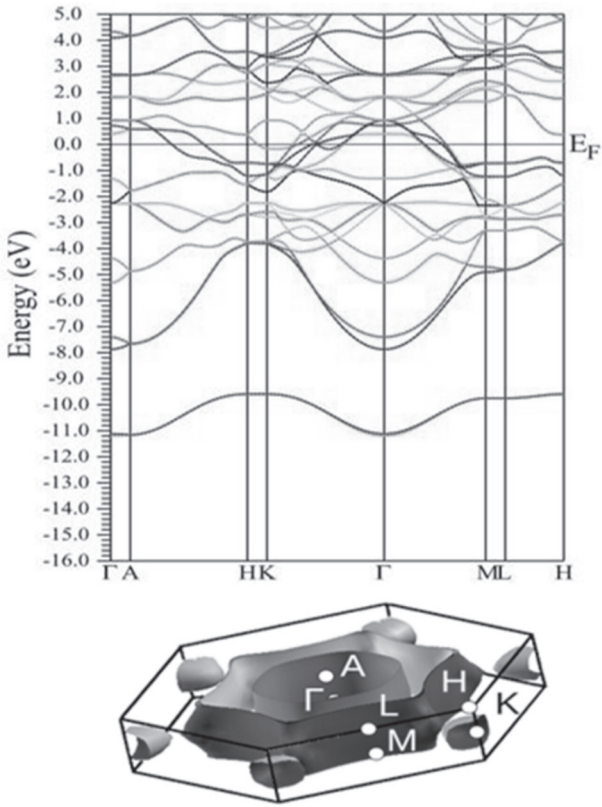

Fig. 4-1: Calculated band structure of Ti_2AlC accompanied with the distribution of the Ti_2AlC Fermi surface in the first Brillouin zone, computed with Xcrysden software.

a. A single band crosses the Fermi level along the K-H direction (i.e., along the c-axis) whereas more than one band cross the Fermi level along

the Γ-M direction (i.e., along the basal plane).

b. The bands are much less dispersive along the c-axis (i.e., along the Γ-A, H-K and M-L directions) than along the basal plane (i.e., along the Γ-K and Γ-M directions). The Fermi velocity ($\partial E/\partial k$) should be higher along the basal plane than along the c-axis which would also result in very different conductivities in the basal plane and out of the basal plane.

Conductivity along the basal planes is thus typically predicted to be higher (even one order of magnitude higher) in the basal plane than normal to it. Nevertheless, a few very recent experimental results have suggested that the anisotropy in the conductivity is rather limited. Furthermore, some experimental studies actually suggest that the c-axis conductivity of Ti_2AlN[17] and Nb_2AlC[18] might be higher than the in-plane conductivity. These suggestions are counterintuitive and contradict the theoretical band structure.

These key contradictions in the literature show that MAX phases electronic properties, and especially the anisotropy resulting from the nanolaminated crystal structure, are not satisfactorily understood. In order to clarify the anisotropic transport porperties of MAX phases, Ti_2AlC and Ti_3SiC_2 in the forms of epitaxial (000l) thin films and bulks were chosen for the typical representatives in the following section.

4.2. Ti_2AlC transport properties anisotropy

4.2.1. Hall effect

The (000l)-oriented film thickness of 140 nm was obtained by ultrahigh vacuum (UHV) magnetron sputtering[19], whereas the polycrystalline after chemomechanical polishing bulk sample was 26.5 µm thick. Wavelength Dispersive x-ray Spectroscopy (WDS) was used to determine the carbon stoichiometry in the two different samples. Carbon stoichiometry are respectively 0.82 and 0.85, with a standard deviation of 0.05, for the Ti_2AlC (000l)-oriented film and the Ti_2AlC polycrystalline bulk sample. The Hall resistivity recorded as a function of the magnetic field at 25 K, 150 K and RT on the $Ti_2AlC_{0.82}$ (000l)-oriented thin film and at RT on the bulk sample is shown in Fig. 4-2. Only RT measurements could be performed on the bulk sample since the Hall voltage is very weak (typically two orders of magnitude smaller than that for the (000ℓ)-oriented film), so that even small temperature variations led to important fluctuations in Hall voltage. In all cases, the variation of the Hall resistivity is linear, whereas its sign depends on the relative orientation of the current and the Ti_2AlC crystal. For the current flowing in the Ti_2AlC

basal plane, the Hall resistivity is definitely positive whereas it is negative for a current flowing in the Ti_2AlC bulk sample; such a result is in compatible agreement with band structure calculations and dE/dk signs. These two opposite signs of the Hall coefficient justify the interpretation of MAX phase transport properties in terms of a two-band model, with electron-like and hole-like states respectively along the c-axis and in the basal plane. It is also consistent with the results obtained by L.Chaput et al.[7] [20] in M_3AX_2 phases.

The Hall constants extracted from these curves are -3.4×10^{-10} and $+2.2\times10^{-10}$ m^3 C^{-1} for the bulk sample and the (000l)-oriented thin film respectively. The experimental value measured on the bulk polycrystalline sample is moreover in good agreement with the one measured by Scabarozi et al.[1] on a similar sample: -2.8×10^{-10} m^3 C^{-1} with very weak variations with the temperature.

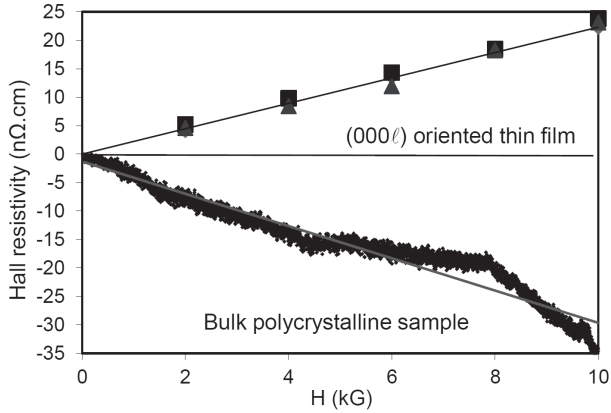

Fig. 4-2: Hall resistivity recorded as a function of the magnetic field at 25K (black squares), 150K (blue triangles) and RT(red diamonds) on the Ti_2AlC (000ℓ)-oriented thin film and at RT on the bulk polycrystalline sample.

Furthermore, the temperature independent positive Hall constant measured along the basal plane allows it to be assumed that:

- a single-band model can be applied to give account of the basal plane transport properties,
- hole-like electron states are involved in transport properties.

In the low field limit of the single-band model, the following equations apply:

$$R_H = {}^{1}/_{pe} \qquad (4-1)$$

$$\sigma = ep\mu_p \qquad (4-2)$$

where p is hole-like carrier density and μ_p is the charge carrier mobility.

From relation (4-1) and the measured Hall constant, hole-like carrier density (p) can be estimated to be $2.8\times10^{+28}\,m^{-3}$. This value is in good agreement with results deduced from heat capacity measurements ($\approx 3.8\times10^{+28}\,m^{-3}$)[2, 21]. The charge carrier mobility deduced from relation (4-2) and resistivity measurement in the basal plane, is thus, at RT, μ_p = 1.1×10^{-3} m^2 V^{-1} s^{-1}.

Table 4-2 summarizes electrical transport parameters calculated in this work with those obtained by Scabarozi et al.[1] who assumes a two-band model and $\mu_n=\mu_p$. One can notice that our values are one order of magnitude higher for the hole-like concentration and five times smaller for the mobility. Such a discrepancy can be ascribed to their assumption of $\mu_n = \mu_p$, which is questionable with the important band dispersion anisotropy evidenced in Fig. 4-1.

The R_H value obtained from ab initio calculation confirms that hole-like electron states dominate transport properties along the Ti_2AlC basal plane. Moreover, the negative value of the R_H trace, in good agreement with the experimental value measured on the polycrystalline sample, suggests that electron-like states dominate transport properties along the c-axis. Nevertheless, the relative error between the experimental and calculated R_H values in the thin film is much higher than for the bulk sample: 50% and 10%, respectively. One possible explanation is the failure of the isotropic relaxation time approximation used for the transport properties calculations. The very good agreement obtained for the bulk sample can result from the cancelation of errors between the different components of the Hall tensor when computing the trace. Such an explanation is in qualitative agreement with results obtained on the Seebeck coefficient of Ti_3SiC_2[22]. It has been shown that the in-plane component obtained with similar calculations is 25% lower than the experimental value at room temperature. However, the trace of the Seebeck coefficient is in very good agreement with experimental data obtained on a Ti_3SiC_2 polycrystalline sample[7].

Table 4-2: Ti_2AlC temperature dependent Hall constants (R_H), room temperature ideal resistivity (ρ_i) and slopes of the $\rho(T)$ curves measured on the bulk sample and the (000l)-oriented thin film. The Hall constants obtained from ab initio calculations are also given for comparison. The RT ideal resistivity along the c-axis is deduced from the effective medium (EM) approach considering elongated spheroids with an aspect ratio of 2.5. Results obtained by Scabarozi et al., deduced from a two-band model and $\mu_n=\mu_p$, are given at RT and 4K.

Sample	Measured R_H 10^{-10} (m^3 C^{-1})	Calculated R_H 10^{-10} (m^3 C^{-1})	density 10^{+28} (m^{-3})	mobility 10^{-3} (m^2 V^{-1} s^{-1})	RT ideal resistivity ($\mu\Omega$ cm^{-1})	$d\rho/dT$ ($\mu\Omega$ cm^{-1} K^{-1})	Ref.
Bulk	RT: - 3.4	- 3.7			37	0.18	[23]
(0001)-oriented thin film	25K,150K and RT: + 2.2	+ 1.0	p = 2.8	$\mu_p = 1.1$	20	0.10	
c-axis (deduced from E.M.)					347	1.75	
bulk	RT: - 2.7		n = 0.139 p = 0.12	$\mu_n = 5.1$ $\mu_p = 5.1$	30		[1]
	4K: - 0.8		n=0.21 p=0.19	$\mu_n = 21$ $\mu_p = 21$			

4.2.2 Resistivity vs temperature measurements

Fig. 4-3 (a) shows bulk and thin film Ti_2AlC resistivity variations as a function of temperature. In the 100-300 K temperature range, there is a linear dependence of ρ as a function of T as generally observed for MAX phases compounds [1, 2] [24]. This typical metal-like behavior simply results from the large density of states at the Fermi level [16, 25, 26].

The RT and residual resistivities are 36 μΩ cm^{-1} and 16 μΩ cm^{-1} for the (000l)-oriented thin film and 65 μΩ.cm and 27 μΩ.cm for the bulk sample, respectively. The RT and residual resistivities of the (000l)-oriented thin film are in the same range as those determined on the bulk samples by Hettinger et al. and very close to those reported for a thin film by Magnuson et al. (40 μΩ cm^{-1})[27, 28]. The values obtained on the bulk sample are larger. This implies that defects limit the mean free path at low temperatures; electron scattering by vacancies can explain the higher resistivity values (see chapter 3). Using Mathiessen's rule, one can extract the ideal resistivity (ρ_i) which is given by

$$\rho_i(T) = \rho(T) - \rho_{imp} \qquad (4-3)$$

where ρ(T) is the total resistivity of a crystalline material, $\rho_i(T)$ is the ideal resistivity which only depends on the electron-scattering mechanisms and is thus an intrinsic characteristic of the compound under study, ρ_{imp} is the residual resistivity (resistivity of the material at low temperature) which only depends on electron scattering by defects and impurities.

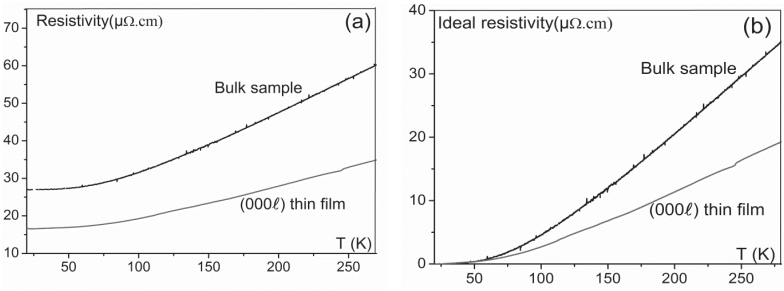

Fig. 4-3: Resistivity vs temperature: (a) raw data obtained on the (000ℓ)-oriented thin film and on the bulk polycrystalline sample; (b) corresponding ideal resistivities.

The ideal resistivity is shown in Fig. 4-3 (b). At RT, the ideal resistivities are 20 and 37 μΩ. cm for the (000l)-oriented thin film and the bulk sample respectively (the bulk sample resistivity is in excellent agreement with that reported by Scabarozi et al.[1]) These values, summarized in Table 4-2, give evidence for the resistivity anisotropy of this nanolaminated compound. As usually observed in MAX phases, ρ_i varies linearly with the temperature in the range 150-300 K and one can calculate the slope of the linear variation. The slopes are 0.10 and 0.18 μΩ cm^{-1} K^{-1} for the (000l)-oriented thin film and the bulk polycrystalline sample respectively.

The thin film resistivity is in good agreement with measurements carried out on other Ti_2AlC samples for which $d\rho/dT$ are in the range 0.067-0.1 μΩ cm^{-1} K^{-1}. However, it is clear that the slope obtained for the bulk sample is higher than all previously reported values. Such behavior can be ascribed to the presence of vacancies and the disorder that they induce in the structure. Indeed, vacancies are known to be strong scatterers of electrons in binary transition carbides [29, 30] and this is supported, in our study, by the high residual resistivity that we find, 27 μΩ. cm, compared to that reported by Scabarozi et al., 7 μΩ cm^{-1}. Although the details of the scattering mechanism are unknown, an equivalent increase of the ρ(T) slope with disorder or vacancies concentration is also observed in metals or semi-metals exhibiting the same linear ρ(T) tendency as that observed in MAX phases[31, 32].

Considering that the thin film and the bulk sample exhibit very similar compositions (as demonstrated with WDS measurements), one can extract the c-axis resistivity, ρ_{zz}, from these two curves. As Scabarozzi et al.[3] did for Ti_2GeC; an effective medium (EM) approach, assuming spherical grains, was used:

$$\frac{(\sigma_b - \sigma_{xx})}{2\sigma_b/_3 + \sigma_{xx}/_3} + \frac{(\sigma_b - \sigma_{zz})}{2\sigma_b/_3 + \sigma_{zz}/_3} = 0 \qquad (4-4)$$

where σ_b and σ_{xx} are the bulk and thin film conductivities, respectively. The corresponding curve is plotted in Fig. 4-4.

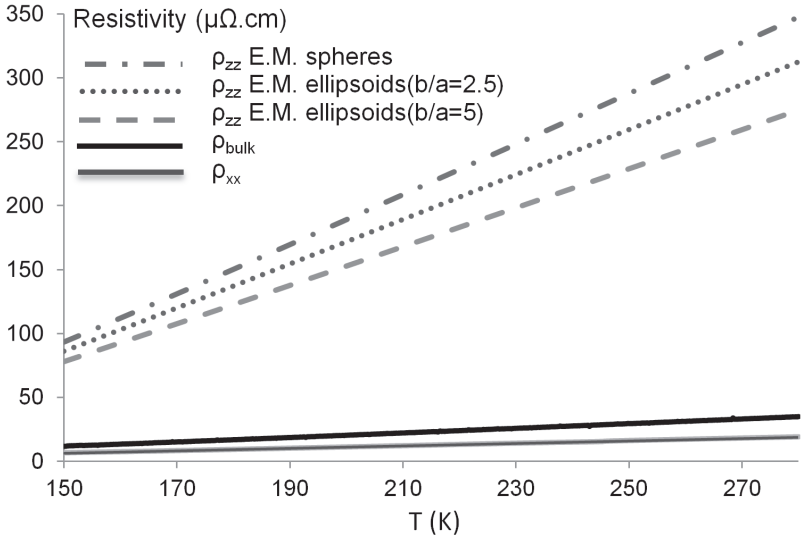

Fig. 4-4: ρ_{zz} obtained from the effective medium approach considering spherical grains (blue dotted-dashed line), spheroids with an aspect ratio a/b = 2.5 (red dots) and a/b = 5 (green dashed line). For comparison, ρ_{xx} and ρ_{bulk} are also given: gray and black curves respectively.

Contrary to what is observed for Ti_2GeC, the E.M. approach evidences a very important anisotropy of the resistivity. Indeed, at RT, ρ_{zz} is more than 20 times higher than ρ_{xx}. This value most probably overestimates the anisotropy because of the assumption of spherical grains, which is not realistic considering the shape of MAX phase grains (see chapter 3 and corresponding SEM images). In order to investigate the influence of the grain shape, ρ_{zz} has been extracted from an E.M. approach considering elongated spheroid grains with an aspect ratio a/b = 2.5 or 5, systems much closer to the true configuration. In such cases, the equation fulfilled by σ_{xx}, σ_{zz} and σ_b is:

$$p\left[\frac{\sigma_{xx}-\sigma_b}{\sigma_b+g_{//}(\sigma_{xx}-\sigma_b)}+\frac{2(\sigma_{xx}-\sigma_b)}{\sigma_b+g_{\perp}(\sigma_{xx}-\sigma_b)}\right]+(1-p)\left[\frac{\sigma_{zz}-\sigma_b}{\sigma_b+g_{//}(\sigma_{zz}-\sigma_b)}+\frac{2(\sigma_{zz}-\sigma_b)}{\sigma_b+g_{\perp}(\sigma_{zz}-\sigma_b)}\right]=0 \qquad (4-5)$$

where

- p is the volume fraction of grains oriented along the basal plane. Supposing that the grain orientation is averaged in the bulk sample, which, according to the results obtained on the trace of the Hall constant, seems to be a reasonable approximation, we

took $p = 2/3$.

- $g_{//}$ and $g_{\perp}$ are the depolarization factors corresponding to the major axis and the transverse direction of the spheroid. These factors can be found in reference [33].

For the particular case of spherical grains, $g_{//} = g_{\perp} = 1/3$ and equation 4-5 is transformed into equation 4-4. The ρ_{zz} values deduced from equation 4-10 for aspect ratios a/b=2.5 and 5 are compared to the E.M. with spherical grains in Fig. 4-5. Although ρ_{zz} is reduced when considering elongated grains, it is still much more important that the basal plane resistivity with RT resistivities ranging from 347 to 290 μΩ.cm depending on the aspect ratio considered in the effective model. Compared to ρ_{xx} the deduced resistivity is more than one order of magnitude larger. The slope of $\rho_{zz}(T)$ is also very important compared to the one obtained along the basal plane. The values vary from 1.97 $\mu\Omega.\,\mathrm{cm}.\,\mathrm{K}^{-1}$ for the model with spherical grains to 1.51 $\mu\Omega.\,\mathrm{cm}.\,\mathrm{K}^{-1}$ for the spheroids with a/b=5. These values are here again much higher than those obtained on the thin film (0.10 $\mu\Omega.\,\mathrm{cm}.\,\mathrm{K}^{-1}$).

Although our E.M. approach can only give a crude estimate of the anisotropy, the obtained results are in reasonable agreement with the RT optical conductivities deduced from ellipsometry[34]. In these experiments performed in reflection, the signal retrieved from the polycrystalline sample is the average between the basal plane and c-axis response: $\rho_{bulk} = \frac{1}{3}(2\rho_{xx} + \rho_{zz})$. This is a big difference with transport measurements where the current flow is influenced by the respective resistivity of the different grains and explains why the resistivity deduced from ellipsometry is generally higher than the one obtained from four points probe measurements in MAX phases. Taking the ρ_{xx} and ρ_{zz} values deduced from our models, we obtain an average resistivity of 130 μΩ cm^{-1} taking an aspect ratio a/b = 2.5 and 110 μΩ cm^{-1} taking an aspect ratio a/b = 5. These values are in reasonable agreement with the ellipsometry data: 84 μΩ cm^{-1} [34]. Here again, the higher value that we obtain can be explained by the disorder induced by the vacancies. This phenomenon has already been observed in niobium carbides for instance where the optical conductivity is reduced by almost a factor of three for 13% of vacancies on the carbon site when compared to the stoichiometric compound[35].

In order to gain more insight into Ti_2AlC resistivity anisotropy, the ρ_{zz}/ρ_{xx} ratio is plotted as a function of the temperature in Fig. 4-5 and compared to the anisotropy of the Fermi surface velocities distribution as deduced from the ratio $\varepsilon_{xx}/\varepsilon_{zz}$. It appears clear that ρ_{zz}/ρ_{xx} is large,

between 14 and 18, and weakly dependent on the temperature in the 150-300 K temperature range. This anisotropy is a combination of the Fermi surface anisotropy (see Fig. 4-1) and the anisotropy of the scattering mechanisms.

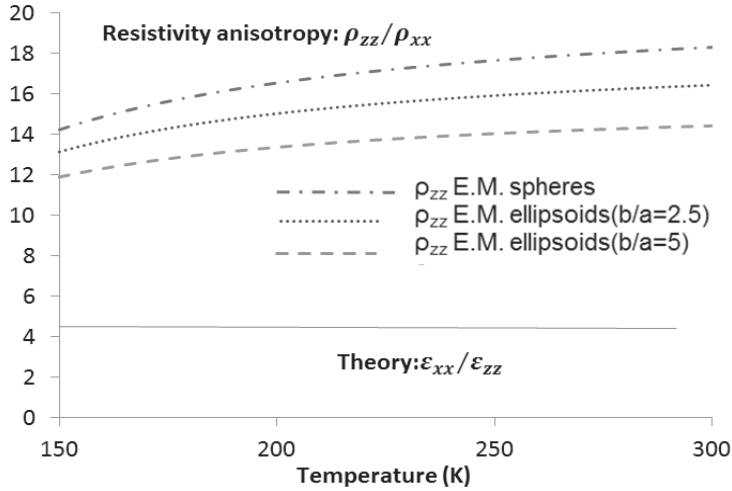

Fig. 4-5: Experimental resistivity anisotropy, ρ_{zz}/ρ_{xx}, deduced from the curves shown in Fig. 4-3 compared to the anisotropy $\varepsilon_{xx}/\varepsilon_{zz}$ resulting from the Fermi surface anisotropy.

From the electronic structure point of view, Ti_2AlC already evidences important resistivity anisotropy since the $\varepsilon_{xx}/\varepsilon_{zz}$ ratio gives a resistivity almost five times higher along the c-axis than within the basal plane. This anisotropy is drastically increased by more than one order of magnitude by the scattering mechanisms which, from the linear dependence of the $\rho(T)$, are most probably dominated by electron-phonon interactions. These results reveal a stronger electron-phonon interaction along the c-axis than within the basal plane of the MAX phases as previously observed in Cr_2GeC[36]. They also evidence the important interplay between electronic structure and scattering mechanisms in MAX phases transport properties. Note that in other materials such as elemental zinc, the electron-phonon interaction tends to compensate the Fermi surface anisotropy so that this material exhibits very weak resistivity anisotropy[37].

4.2.3. Discussion and summary

The anisotropy of Ti_2AlC transport properties has been investigated focusing on a (000l)-oriented $Ti_2AlC_{0.85}$ thin film, giving access to the basal plane response of the MAX phase, and a bulk highly pure polycrystalline sample of similar composition. Both temperature dependent Hall effect and resistivity measurements were performed and interpreted thanks to ab initio calculations.

Concerning Hall effect measurements, the anisotropy of the Fermi surface resulting from the nanolaminated structure is evidenced through a change of the charge carriers' sign with the crystallographic orientation. Given Hall constants of both samples are weakly temperature dependent and of the opposite sign, our results justify the interpretation of MAX phases polycrystalline bulk samples transport properties in terms of a two-band model, one describing the electron-like behavior along the c-axis and the other reporting hole-like behavior along the basal plane. This behavior is moreover consistent with that observed in 312 MAX phases[7, 20]. Considering a single-band model and hole-like state to account for the basal plane Hall constant, the charge carrier density is found to be $2.8\times10^{+28}$ m^{-3}, a value in good agreement with others deduced from heat capacity measurement[2, 21]. The charge carrier mobility is found to be $\mu_p = 1.1 \times 10^{-3} m^2\ V^{-1}\ s^{-1}$, a value five times lower than that reported by others[1] who assumed a two-band model and $\mu_n=\mu_p= 5.1 \times 10^{-3} m^2\ V^{-1}\ s^{-1}$ at RT. However, a careful analysis of either the Fermi surface or the band structure reveals an important band velocity anisotropy when focusing on reciprocal directions corresponding to the basal plane (hole-like states) and the c-axis (electron-like states). As a consequence, it is unlikely that electron-like and hole-like state mobilities are equal.

The calculations qualitatively reproduce the experimental results: the charge carrier signs are confirmed for both the thin film and the bulk sample. The agreement on the absolute value of the Hall constant is however dependent on the crystallographic orientation. It is in very good agreement for the bulk sample but the discrepancy is much more pronounced for the $R_H$xyz component corresponding to the thin film data (the relative error is worse than 50%). This discrepancy is understood in terms of a failure of the isotropic relaxation time approximation used in our calculations, which would be canceled in the calculation of the Hall tensor trace. This explanation is coherent with Ti_3SiC_2 Seebeck coefficient data which were recently published[22].

The resistivity measurements also clearly evidence a strong anisotropy of Ti_2AlC electronic properties. According to the effective medium

approach, it is shown that the ratio ρ_{zz}/ρ_{xx} is above 10. The slope of the $\rho(T)$ curves confirm such an anisotropy, $\frac{d\rho_{zz}}{d(T)} = 1.75\ \mu\Omega \bullet \text{cm} \bullet \text{K}^{-1}$, whereas $\frac{d\rho_{xx}}{d(T)} = 0.1\ \mu\Omega \bullet \text{cm} \bullet \text{K}^{-1}$. Comparison of the experimental data with the anisotropy of the Fermi surface deduced from the ab initio calculations reveals that the observed anisotropy is a cumulated effect of the band structure anisotropy and of the anisotropy of the electron-phonon interaction. This behavior is significantly different from that evidenced in Ti_2GeC with a similar approach where the resistivity was found to be almost isotropic[3]. These results evidence the crucial role of the chemical composition on the transport properties in MAX phase family. Since, in Ti_2GeC, the electron-phonon interaction is found to be weaker along the c-axis than within the basal plane, it can be an explanation for the reduced anisotropy observed in this sample. A similar effect was observed in elemental zinc[37].

4.3. Ti_3SiC_2 transport properties anisotropy

4.3.1. Resistivity and Hall coefficient measurements

Ti_3SiC_2 film (thickness = 40 nm) growth was conducted in the PPRIME Institute on two α-SiC substrates by magnetron sputtering of pure Al and Ti targets in a high vacuum system[38]: (1) n-type (000l) 4H-SiC single crystal with a mirror-polished surface supplied by CREE Research Inc., (2) n-type $(11\bar{2}0)$-4H-SiC single crystal with a mirror-polished surface supplied by CREE Research Inc. Two parallelepiped specimens were cut along (000l) and $(11\bar{2}0)$ orientations from the same $(11\bar{2}0)$-oriented thin film, which allowed us to compare the resistivity in the basal plane and along the c-axis using the same sample. Ti_3SiC_2 single crystal was synthesized by Thierry Ouisse et al. in LMGP (Laboratoire des Matériaux et du Génie Physique, Grenoble) from high-temperature solution growth[39]. The Ti_3SiC_2 polycrystalline sample was synthesized, in the PPRIME Institute, by HIPing under 1400 °C/4 h/80MPa. The Ti_3SiC_2 polycrystalline thick film (thickness = 26 μm) was prepared by TEM polishing.

Fig. 4-6 (a) shows the temperature dependence of the resistivity measured with current flowing in the (000l) direction and in the basal plane of the same Ti_3SiC_2 $(11\bar{2}0)$-oriented thin film. The resistivities of a Ti_3SiC_2 single crystal and of a polycrystalline sample are also plotted as a function of temperature.

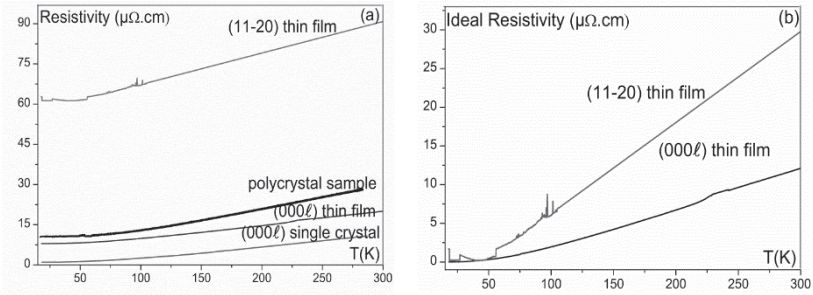

Fig. 4-6: (a) Resistivity versus temperature for several Ti_3SiC_2 samples (single crystal, polycrystal, thin films with current flowing in two different directions and cut from the same sample). (b) Ideal resistivity of the thin films with current flowing in two different directions.

The RT resistivity of the Ti_3SiC_2 polycrystal is about 30 μΩ cm^{-1} which is slightly higher than was determined by Barsoum et al. (RT resistivity in the range 21-25 μΩ cm^{-1}). However, the dρ/dT value (0.09 μΩ cm^{-1} K^{-1}), in the temperature range 150-300 K, is in very good agreement with previously determined values[40-42]. The $d\rho/dT$ value is an intrinsic property of the material and it thus has to be the same for the same compound. The RT resistivities of the Ti_3SiC_2 single crystal and of the (000l)-oriented Ti_3SiC_2 thin film are respectively 11 and 20 μΩ cm^{-1} whereas the $d\rho/dT$ values, in the temperature range 150-300 K, are respectively 0.048 and 0.049 μΩ cm^{-1} K^{-1}. Such a result confirms that the Ti_3SiC_2 $(11\bar{2}0)$-oriented thin film is of good enough quality to get intrinsic transport properties of the material. Thus, one can calculate the intrinsic RT anisotropy (ρ^i_{zz}/ρ^i_{xx} ~ 3) by dividing the RT ideal resistivity along the c-axis by the RT ideal resistivity in the basal plane. The ideal resistivities (ρ^i_{zz} and ρ^i_{xx}), calculated by subtracting the residual resistivity (resistivity at low temperature) to the measured RT resistivity, are plotted versus temperature in Fig. 4-6 (b). For temperatures in the range 150-300K, the $d\rho/dT$ value, calculated in the case of the current flowing in the c-axis direction, is 0.118 μΩ cm^{-1} K^{-1}. Such a value is more than twice the value measured in the case of the current flowing in the basal plane. This result suggests that charge carrier mobility more strongly varies with temperature along the c-axis than along the basal plane. Assuming Ti-3d hole-like states and Ti-3d electron-like states respectively dominate transport properties in the basal plane and along the c-axis, as demonstrated by L. Chaput et al.[7], one can assess that electron-like over hole-like mobility's ratio varies with temperature. It has also been

demonstrated that the near-zero thermopower in polycrystals is a direct effect of anisotropy in the electronic structure[6]; the density of states in the Ti_3SiC_2 basal plane being much larger than that along the c-axis for the Ti 3d and the C 2p states. Such a result can also contribute to an increase of the ρ(T) slope by decreasing the charge carrier density.

Fig. 4-7 shows the Hall resistivity, measured versus magnetic field, at different temperatures (5 K, 35 K, 70 K, 130 K and 200 K) for the Ti_3SiC_2 (000ℓ)-oriented thin film (a) and for the Ti_3SiC_2 polycrystalline thick film (b). For both samples, Hall resistivity varies linearly with magnetic field, whatever the temperature is. These results indicate that the systems are in the magneto-transport low field limit.

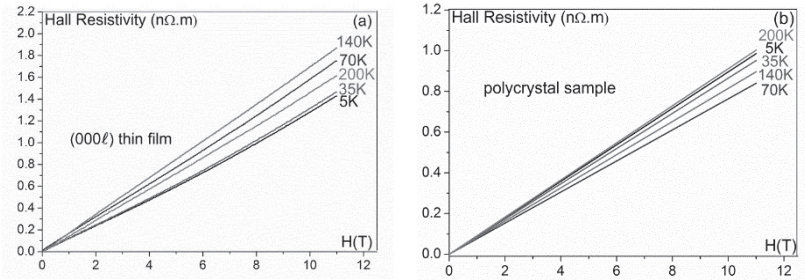

Fig. 4-7: (a) Hall resistivity versus magnetic field measured at different temperatures (4 K, 35K, 70 K, 130 K and 200 K) for the Ti_3SiC_2 (000ℓ)-oriented thin film (a) and for the Ti_3SiC_2 polycrystalline thick film (b).

Fig. 4-8 shows the variation of the Hall coefficient (R_H) as a function of temperature. Whatever the temperature, the Hall coefficient values are weak and can be considered as constant. Furthermore, one can notice that the Hall coefficient value measured on the bulk polycrystalline thick film is smaller than the one measured on the (000l)-oriented thin film. Such a result can be ascribed to the averaging of basal plane (hole-like behavior) and c-axis (electron-like behavior) transport properties in the bulk polycrystalline sample. Such hole-like and electron-like behaviors, respectively in the basal plane and out of the basal plane, have been demonstrated by L. Chaput through calculations of the c-axis and basal plane components of the Ti_3SiC_2 thermoelectric tensor[7, 43].

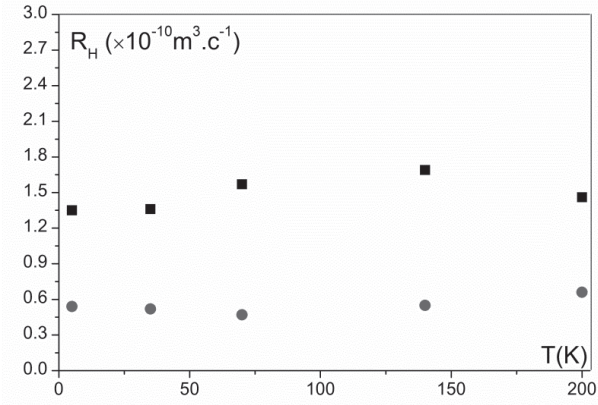

Fig.4-8: Hall coefficient (R_H) calculated at different temperatures for the (000l)-oriented thin film (black squares) and Ti_3SiC_2 polycrystalline thick film (red circles).

Furthermore, one can find, in Table 4-3, a relatively strong discrepancy between R_H values determined on different samples. Taking into account the opposite influence of electron-like states (along the c-axis), and hole-like states (in the basal plane) on the Hall constant, it has to be noticed that R_H values of bulk polycrystalline samples depend on the grain orientations. More specifically, it means that the trace of the Hall tensor corresponds to the experimental value if the grains are randomly oriented in the polycrystalline sample. The Hall constants obtained by Barsoum et al.[44] are almost zero in a Ti_3SiC_2 polycrystalline sample without preferred grain orientations. Such a value is in quite good agreement with our result (0.5×10^{-10} m^3 C^{-1}) also obtained on a polycrystalline sample. On the other hand, a positive Hall constant ($R_H = 3\times10^{-10}$ m^3 C^{-1}) has been measured[41] on a Ti_3SiC_2 polycrystalline sample which contains extra-large (1-2 mm) (000l)-oriented grains[45]. Thus, the R_H value of such a sample should correspond to the one obtained on Ti_3SiC_2 (000l)-oriented thin film. One can notice that the R_H value obtained on our Ti_3SiC_2 (000l)-oriented thin film (1.5×10^{-10} m^3 C^{-1}) is only in qualitative agreement with the one of Finkel et al.[41]

Table 4-3: Summary of the Ti_3SiC_2 transport properties.

Composition	T (K)	ρ $\mu\Omega$ m^{-1}	$\partial\rho/\partial T$ $\mu\Omega$ cm^{-1} K^{-1}	R_H (10^{-10}) m^3 C^{-1}	Two bands				Ref.
					$\alpha(T^{-2})$ 10^{-5}	$\mu_n = \mu_p$ 10^{-3} (m^{2}Vs)	n 10^{28} (m^{-3})	p 10^{28} (m^{-3})	
Ti_3SiC_2 Bulk Forging oriented grains	300 4	22 3	0.071	3.8 3	2.9 206	6 45	0.6 0.6	0.6 0.6	[41]
Ti_3SiC_2 Bulk	300	22.7	0.089						[40]
Ti_3SiC_2 Bulk	300	22.2	0.075	0		0.06-0.1	14-24	14-24	[44]
Ti_3SiC_2 Bulk	300 20	30.6 10.6	0.09	0.5					[23]
Ti_3SiC_2 $(11\bar{2}0)$-oriented thin film	300 20	90.8 61.2	0.118						
Ti_3SiC_2 (000l)-oriented thin film	300 20	19.8 7.9	0.049	1.5 (4-200K)	One hole-like band $p = 4.2\ 10^{28}$ m^{-3}				
Ti_3SiC_2) (000l)-oriented single crystal	300 20	10.9 1.1	0.048						

As in the case of the Ti_2AlC (000l)-oriented thin film, the weak temperature dependence of the basal plane Hall constant obtained on the Ti_3SiC_2 (000l)-oriented thin film, justifies the interpretation of basal plane MAX phase transport properties in terms of a single-band model. It is thus possible to extract the charge carriers' density from the basal plane Hall constant measurement. In this model, hole-like carrier density (p) can be estimated from the relation $R_H = 1/pe$ which leads to a hole-like carrier density $p = 4.2\times10^{28}$ m^{-3}. One can notice that this value is one order of magnitude higher than the hole-like carrier density obtained assuming equal electron-like and hole-like mobilities. This equality is questionable given the important band dispersion anisotropy, and questionable with our MR results discussed in the next section[15].

4.3.2. Magnetoresistance measurements

Fig. 4-9 shows the Ti_3SiC_2 (000l)-oriented thin film and the Ti_3SiC_2 polycrystalline sample magnetoresistance as a function of the magnetic field (from 0 to 11 Tesla). For a magnetic field lower than 5T, the experimental results can be fitted with the relation $MR = |\mu_n u_p| B^2$. Such an equation has been extensively used by Barsoum et al.[41] to determine the charge carrier mobility. However, Fig. 4-9 demonstrates that, in the range 5-11T, the magnetoresistance is not a quadratic function of the magnetic field.

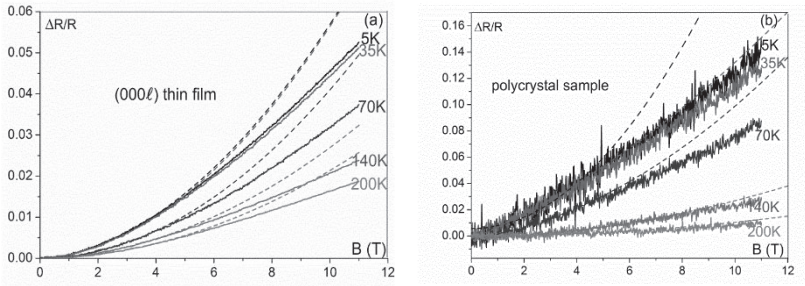

Fig. 4-9: Magnetoresistance of a Ti_3SiC_2 (000ℓ)-oriented thin film (a) and of a Ti_3SiC_2 polycrystalline sample (b). Dotted lines correspond to quadratic fits of the magnetoresistance variation.

Fig. 4-10 shows the MR variation with temperature at a magnetic field of 11T. One can notice that MR rapidly decreases with increasing temperature, such a decrease being faster in the polycrystalline sample.

Usually, the MR effect may be weakened by mixing the transport components along different directions of the crystallographic axes[46]. However, the opposite is observed in Fig. 4-11 (the MR effect is larger in the polycrystalline sample than in the (000ℓ)-oriented thin film). Such a difference unambiguously demonstrates that the variation of the charge carrier mobility with temperature is higher along the c-axis than in the basal plane, as suggested by the ρ(T) slope measured along the c-axis (0.118 μΩ cm $^{-1}$ K^{-1}) and in the basal plane (0.049 μΩ cm^{-1} K^{-1}). Such a difference in mobility variation with temperature may be attributed to the anisotropic electron-phonon interactions in the two crystallographic directions. Neutron diffraction experiments performed on Ti_3SiC_2 have shown that the Si atoms act as "rattlers" and vibrate with an anisotropic elliptical thermal motion with the highest amplitudes in the basal plane simultaneously coupled with the Ti_{II} atoms[47]. More recently, the anisotropic electron-phonon interactions have been evidenced by Magnusson et al. [48]. Rattling of Si atoms implies substantial anisotropy between the in-plane and out-of-plane orbitals that need to be included in theoretical modeling.

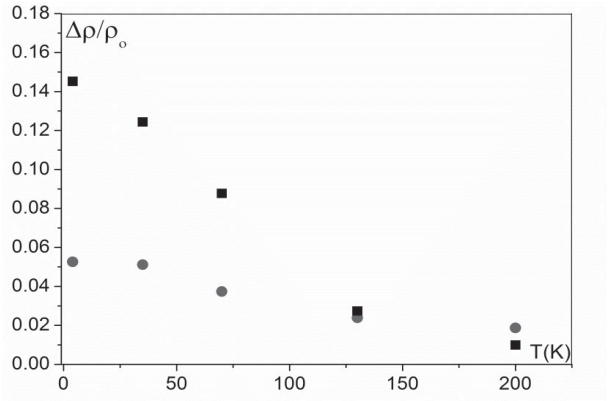

Fig. 4-10: Variation, with temperature, of the magnetoresistance at 11T. Ti_3SiC_2 (000l)-oriented thin film (red circles) and Ti_3SiC_2 polycrystalline sample (black rectangles).

For many metallic materials with a symmetric Fermi surface, Kohler's law is normally obeyed. According to Kohler's law[49], MR, at different temperatures and whatever the impurity content, can be scaled by the expression:

$$\left(\frac{\Delta\rho}{\rho_0}\right) = f(H\tau) = F\left(\frac{H}{\rho}\right) \qquad (4-6)$$

with the assumption that scattering time $1/\tau(T) \propto \rho(T)$, f and F are unknown functions. Generally, the function F has a power-law form[41].

As originally stated, this rule is applicable to single-band metals for which the number of carriers does not vary with temperature. Thus, ρ variations are a measure of the inverse mobility of the carriers. The concept of scaling is based on the fact that if Kohler's rule is applicable, then temperature dependent changes in magnetoresistance are due entirely to mobility variation. Such a law has been generalized to the case of a semi-metal or semi-conductor for which the galvanomagnetic coefficients (ρ_{xx} and ρ_{xy}) can be described in the framework of the two-band model. The MR can be written as:

$$MR = \frac{\Delta\rho}{\rho_0} = \frac{\frac{npb(1+b)^2}{(n+pb)^2}\,\mu^2\,B^2}{1+\left[\frac{n-p}{n+bp}\right]^2 b^2\mu^2\,B^2} \qquad (4-7)$$

where n and p are respectively the electron-like and hole-like carrier density, μ is the electron mobility and b is the ratio of hole to electron mobility.

Such an equation does not satisfy Kohler's rule due to the n, p, b dependence. Thus, the two-band magnetoresistance cannot generally be scaled to obtain mobilities. However, for compensated conductors with n=p, then Kohler's rule is applicable and MR reduces to:

$$\left(\frac{\Delta\rho}{\rho_0}\right) = b\mu(H)^2 = (\overline{\mu}H)^2 \qquad (4-8)$$

Fig. 4-11 is a log-log plot of the MR versus H/C(T) obtained at different temperatures on the Ti_3SiC_2 (000ℓ)-oriented thin film (a) and on the Ti_3SiC_2 polycrystalline sample (b). At the lowest temperature, the constant C(5K) has been fixed to the low temperature resistivity (ρ(5K)) whereas the constant C(T) has been adjusted to try to get a single curve whatever the temperature and magnetic field. It can be noticed that a single curve can be obtained for the (000ℓ)-oriented thin film. However, it is not possible to get a single curve for the Ti_3SiC_2 polycrystalline sample and the MR variation is not a quadratic function of the magnetic field (as shown also in Fig. 4-9 (b)). These results illustrate that a single-band model can be used to account for the transport properties in the basal plane of MAX phases. However, Fig. 4-11 (b) shows that the assumption n = p is likely not verified. Such a result is also supported by a recent study which showed that the density of states in the basal plane is much larger than that along the c-axis for the Ti 3d and the C 2p states[41]. Another

possible explanation may be that more than two bands have to be considered to account for the transport properties of polycrystalline samples. Indeed, a large number of bands cross the Fermi level in the Ti_3SiC_2 band structure[15]. It now seems necessary to perform Hall effect and MR measurements on $(11\bar{2}0)$-oriented thin film MAX phase. It should demonstrate that a single electron-like band can account for the transport properties along the c-axis.

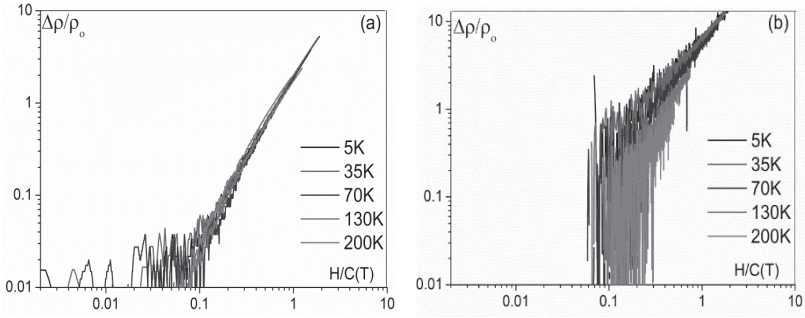

Fig. 4-11: Log-log plot of the magnetoresistance versus H/C(T) obtained at different temperatures on the Ti_3SiC_2 (000ℓ)-oriented thin film (a) and on the polycrystalline sample (b).

The single curve of Fig. 4-11 (a) can be well fitted with the following equation:

$$\frac{\Delta\rho}{\rho_0} = 2.75 * x^{1.68} = 2.75 * \left(\frac{H}{\rho}\right)^{1.68} = 2.75 * \left(peu_pH\right)^{1.68} \qquad (4-9)$$

Where: $x = \frac{H}{\rho}$ represents the ratio between magnetic field (H) and corresponding resistivity ρ when H=0.

From such an equation, one can get the mobility variation with magnetic field and temperature provided that the hole-like carrier density is known. By using the hole-like carrier density determined from the Hall constant, the hole-like mobility has been calculated at different temperatures (4K, 35K, 70k, 140k and 200K) and zero magnetic field. The results, with those obtained directly from resistivity and Hall constant measurements, are summarized in Table 4-4. One can notice that the different mobility values are in very good agreement. Such an agreement demonstrates that Kohler's rule is well verified for the (000ℓ)-oriented thin film (i.e., the constant C(T) determined to get a single curve corresponds well to ρ(T)). It also demonstrates that a single-band model can be used to give an account of the basal plane transport properties of Ti_3SiC_2 MAX

phases.

Table 4-4: Summary of the mobilities calculated, at different temperatures, from Kohler's law and from resistivity and Hall constant assuming a single-band model.

Temperature	4 K	35 K	70 K	140 K	200 K
p (10^{28}) m^{-3}	4.2				
μ_p($10^{-3}m^2/Vs$) by Kohler's Rule	2.0	2.0	1.6	1.3	1.1
μ_p($10^{-3}m^2/Vs$) by $\rho = \frac{R_H}{\mu_p}$	1.9	1.9	1.7	1.3	1

The results given in Table 4-4 can be compared with the ones obtained by Finkel et al.[41]. In polycrystalline MAX phases, Finkel et al.[2, 5, 8, 9, 11] have used equation (4-8) and the assumption n=p to determine the electron-like and hole-like mobilities. Our values are one order of magnitude higher for the hole-like carrier density and also about one order of magnitude lower for the charge carrier mobility. Such a discrepancy can be ascribed to their assumption n = p which is likely not valid as evidenced by Magnusson et al.[41]. Moreover, the variation of the polycrystalline sample MR does not seem to vary as expected from equation (4-8) (see Fig. 4-9b).

4.3.3. Summary and conclusions

The anisotropy of Ti_3SiC_2 transport properties has been evidenced by direct measurement of the resistivity along the basal plane (ρ_{xx}) and out of the basal plane (ρ_{zz}). Such measurements have been performed using Ti_3SiC_2 $(11\bar{2}0)$-oriented thin film. The resistivity anisotropy (ρ_{zz}/ρ_{xx}) is of the order of 3 at room temperature. Moreover, the $d\rho/dT$ value along the c-axis direction is 0.118 μΩ cm^{-1} K^{-1} which is more than twice the value measured in the case of the current flowing along the basal plane direction (0.049 μΩ cm^{-1} K^{-1}). In addition, the MR measured on the polycrystalline sample is larger than the one measured along the basal plane. These two results suggest that charge carrier mobility more strongly varies with temperature along the c-axis than along the basal plane. The $d\rho/dT$ variation can also be partly explained by the hole-like density of states (in the basal plane) which has been shown to be higher than the electron-like density of states (along the c-axis)[6]. From MR and Hall

effect measurements, it has been demonstrated that basal plane transport properties may be understood using a single-band model and hole-like states. The Hall constant does not depend on temperature and allows extracting charge carrier density. The variation of the MR with magnetic field and temperature is in good agreement with Kohler's rule and MR measurements allow determination of the mobility variation with magnetic field and temperature.

References

[1] T. Scabarozi, A. Ganguly, J. Hettinger, S. Lofland, S. Amini, P. Finkel, T. El-Raghy, M. Barsoum, Electronic and thermal properties of $Ti_3Al(C_{0.5}, N_{0.5})_2$, $Ti_2Al(C_{0.5}, N_{0.5})$ and Ti_2AlN, Journal of applied physics 104 (2008) 073713.
[2] S. Lofland, J. Hettinger, K. Harrell, P. Finkel, S. Gupta, M. Barsoum, G. Hug, Elastic and electronic properties of select M_2AX phases, Applied physics letters 84(4) (2004) 508-510.
[3] T.H. Scabarozi, P. Eklund, J. Emmerlich, H. Hogberg, T. Meehan, P. Finkel, M.W. Barsoum, J.D. Hettinger, L. Hultman, S.E. Lofland, Weak electronic anisotropy in the layered nanolaminate Ti_2GeC, Solid State Communications 146 (2008) 498-501.
[4] M.W. Barsoum, I. Salama, T. El-Raghy, J. Golczewski, W.D. Porter, H. Wang, H. Siefert, F. Aldinger, Thermal and electrical properties of Nb_2AlC, $(Ti, Nb)_2AlC$ and Ti_2AlC, Metallurgical and Materials Transactions 33a (2002) 2779.
[5] S.E. Lofland, J.D. Hettinger, T. Meehan, A. Bryan, P. Finkel, G. Hug, M.W. Barsoum, Electron-Phonon Coupling in MAX Phase Carbides, Phys. Rev. B 74 (2006) 174501.
[6] M.W. Barsoum, MAX Phases: Properties of Machinable Ternary Carbides and Nitrides, John Wiley & Sons 2013.
[7] L. Chaput, G. Hug, P. Pécheur, H. Scherrer, Anisotropy and thermopower in Ti_3SiC_2, Physical Review B 71(12) (2005) 121104.
[8] J.D. Hettinger, S.E. Lofland, P. Finkel, J. Palma, K. Harrell, S. Gupta, A. Ganguly, T. El-Raghy, M.W. Barsoum, Electrical Transport, Thermal Transport and Elastic Properties of M_2AlC (M = Ti, Cr, Nb and V) Phases, Phys. Rev. B 72 (2005) 115120.
[9] T.H. Scabarozi, S. Amini, P. Finkel, M.W. Barsoum, W.M. Tambussi, J.D. Hettinger, S.E. Lofland, Electrical, Thermal, and Elastic Properties of the MAX Phase Ti_2SC, J. Appl. Phys 104 (2008) 033502.
[10] M.W. Barsoum, T.H. Scabarozi, S. Amini, J.D. Hettinger, S.E. Lofland, Electrical and Thermal Properties of Cr_2GeC, Journal of the

American Ceramic Society 94(12) (2011) 4123-4126.
[11] P. Finkel, B. Seaman, K. Harrell, J. Palma, J. Hettinger, S. Lofland, A. Ganguly, M. Barsoum, Z. Sun, S. Li, Electronic, thermal, and elastic properties of $Ti_3Si_{1-x}Ge_xC_2$ solid solutions, Physical Review B 70(8) (2004) 085104.
[12] P. Finkel, M. Barsoum, J. Hettinger, S. Lofland, H. Yoo, Low-temperature transport properties of nanolaminates Ti_3AlC_2 and Ti_4AlN_3, Physical Review B 67(23) (2003) 235108.
[13] Y. Zhou, Z. Sun, Electronic structure and bonding properties of layered machinable Ti_2AlC and Ti_2AlN ceramics, Physical Review B 61(19) (2000) 12570.
[14] Z. Sun, Y. Zhou, Electronic structure and structural properties of Ti_4AlN_3 investigated by ab initio calculations, Journal of the Physical Society of Japan 71(5) (2002) 1313-1317.
[15] Y. Zhou, Z. Sun, Electronic structure and bonding properties in layered ternary carbide Ti_3SiC_2, Journal of Physics: Condensed Matter 12(28) (2000) L457.
[16] G. Hug, E. Fries, Full-potential electronic structure of Ti_2AlC and Ti_2AlN, Physical Review B 65(11) (2002) 113104.
[17] N. Haddad, E. Garcia-Caurel, L. Hultman, M.W. Barsoum, G. Hug, Dielectric properties of Ti_2AlC and Ti_2AlN MAX phases: The conductivity anisotropy, Journal of applied physics 104 (2008) 023531.
[18] T. Scabarozi, J. Roche, A. Rosenfeld, S. Lim, L. Salamanca-Riba, G. Yong, I. Takeuchi, M. Barsoum, J. Hettinger, S. Lofland, Synthesis and characterization of Nb_2AlC thin films, Thin Solid Films 517(9) (2009) 2920-2923.
[19] H. Högberg, L. Hultman, J. Emmerlich, T. Joelsson, P. Eklund, J.M. Molina-Aldareguia, J. Palmquist, O. Wilhelmsson, U. Jansson, Growth and characterization of MAX-phase thin films, Surface and Coatings Technology 193(1) (2005) 6-10.
[20] L. Chaput, G. Hug, P. Pécheur, H. Scherrer, Thermopower of the 312 MAX phases Ti_3SiC_2, Ti_3GeC_2, and Ti_3AlC_2, Physical Review B 75(3) (2007) 035107.
[21] M.K. Drulis, H. Drulis, S. Gupta, M. Barsoum, T. El-Raghy, On the heat capacities of M_2AlC (M= Ti, V, Cr) ternary carbides, Journal of applied physics 99 (2006) 093502.
[22] M. Magnuson, M. Mattesini, N. Van Nong, P. Eklund, L. Hultman, Electronic structure origin of the anisotropic thermopower of nanolaminated Ti_3SiC_2 determined by polarized x-ray spectroscopy and Seebeck measurements, Physical Review B 85(19) (2012) 195134.
[23] V. Mauchamp, W. Yu, L. Gence, L. Piraux, T. Cabioc'h, V. Gauthier,

P. Eklund, S. Dubois, Anisotropy of the resistivity and charge-carrier sign in nanolaminated Ti_2AlC: Experiment and ab initio calculations, Physical Review B 87(23) (2013) 235105.
[24] C. Hu, L. He, J. Zhang, Y. Bao, J. Wang, M. Li, Y. Zhou, Microstructure and Properties of Bulk Ta_2AlC Ceramic Synthesized by an in situ Reaction/hot Pressing Method, J. Europ. Ceram. Soc. 28 (2008) 1679-1685.
[25] Y. Zhou, X. Wang, Z. Sun, S. Chen, Electronic and structural properties of the layered ternary carbide Ti_3AlC_2, Journal of Materials Chemistry 11(9) (2001) 2335-2339.
[26] C. Hu, J. Zhang, J. Wang, F. Li, J. Wang, Y. Zhou, Crystal Structure of V_4AlC_3: A New Layered Ternary Carbide, Journal of the American Ceramic Society 91(2) (2008) 636-639.
[27] J. Hettinger, S. Lofland, P. Finkel, T. Meehan, J. Palma, K. Harrell, S. Gupta, A. Ganguly, T. El-Raghy, M. Barsoum, Electrical transport, thermal transport, and elastic properties of M_2AlC (M= Ti, Cr, Nb, and V), Physical Review B 72(11) (2005) 115120.
[28] M. Magnuson, M. Mattesini, O. Wilhelmsson, J. Emmerlich, J.P. Palmquist, S. Li, R. Ahuja, L. Hultman, O. Eriksson, U. Jansson, Electronic structure and chemical bonding in Ti_4SiC_3 investigated by soft x-ray emission spectroscopy and first-principles theory, Physical Review B 74(20) (2006) 205102.
[29] W.S. Williams, Scattering of electrons by vacancies in nonstoichiometric crystals of titanium carbide, Physical Review 135(2A) (1964) A505.
[30] L.W. Shacklette, W.S. Williams, Scattering of Electrons by Vacancies through an Order Disorder Transition in Vanadium Carbide, Journal of applied physics 42(12) (1971) 4698-4703.
[31] M. Cutler, J. Leavy, R. Fitzpatrick, Electronic transport in semimetallic cerium sulfide, Physical Review 133(4A) (1964) A1143.
[32] G. Herranz, V. Laukhin, F. Sánchez, P. Levy, C. Ferrater, M. García-Cuenca, M. Varela, J. Fontcuberta, Effect of disorder on the temperature dependence of the resistivity of $SrRuO_3$, Physical Review B 77(16) (2008) 165114.
[33] L.D. Landau, E.M. Lifšic, J.B. Sykes, J.S. Bell, M. Kearsley, L.P. Pitaevskii, Electrodynamics of continuous media, Pergamon press Oxford 1960.
[34] A. Mendoza-Galvan, M. Rybka, K. Järrendahl, H. Arwin, M. Magnuson, L. Hultman, M. Barsoum, Spectroscopic ellipsometry study on the dielectric function of bulk Ti_2AlN, Ti_2AlC, $Nb_2AlC(Ti_{0.5}, Nb_{0.5})_2AlC$, and Ti_3GeC_2 MAX phases, Journal of applied physics 109 (2011) 013530.

[35] F. Modine, M. Foegelle, C. Finch, C. Allison, Electrical properties of transition-metal carbides of group IV, Physical Review B 40(14) (1989) 9558.
[36] P. Eklund, M. Bugnet, V. Mauchamp, S. Dubois, C. Tromas, J. Jensen, L. Piraux, L. Gence, M. Jaouen, T. Cabioc'h, Epitaxial growth and electrical transport properties of Cr_2GeC thin films, Physical Review B 84(7) (2011) 075424.
[37] L. Chaput, P. Pécheur, H. Scherrer, Thermopower, Hall tensor, and relaxation time approximation for elemental zinc, Physical Review B 75(4) (2007) 045116.
[38] A. Drevin-Bazin, J. Barbot, M. Alkazaz, T. Cabioch, M. Beaufort, Epitaxial growth of Ti_3SiC_2 thin films with basal planes parallel or orthogonal to the surface on α-SiC, Applied physics letters 101(2) (2012) 021606.
[39] F. Mercier, T. Ouisse, D. Chaussende, Morphological instabilities induced by foreign particles and Ehrlich Schwoebel effect during the two-dimensional growth of crystalline Ti_3SiC_2, Physical Review B 83(7) (2011) 075411.
[40] M. Barsoum, T. El-Raghy, A progress report on Ti_3SiC_2, Ti_3GeC_2, and the H-phases, M_2BX, Journal of Materials Synthesis and Processing 5(3) (1997) 197-216.
[41] P. Finkel, J. Hettinger, S. Lofland, M. Barsoum, T. El-Raghy, Magnetotransport properties of the ternary carbide Ti_3SiC_2: Hall effect, magnetoresistance, and magnetic susceptibility, Physical Review B 65(3) (2001) 035113.
[42] J. Li, F. Sato, R. Watanabe, Synthesis of Ti_3SiC_2 polycrystals by hot-isostatic pressing of the elemental powders, Journal of materials science letters 18(19) (1999) 1595-1597.
[43] L. Chaput, Calcul des proprietes de transport de materiaux thermoelectriques, Institut National Polytechnique de Lorraine-INPL, 2006.
[44] M. Barsoum, H.I. Yoo, I. Polushina, V.Y. Rud, T. El-Raghy, Electrical conductivity, thermopower, and Hall effect of Ti_3AlC_2, Ti_4AlN_3, and Ti_3SiC_2, Physical Review B 62(15) (2000) 10194.
[45] M. Barsoum, T. El-Raghy, Room-temperature ductile carbides, Metallurgical and Materials Transactions A 30(2) (1999) 363-369.
[46] P. Cheng, H. Yang, Y. Jia, L. Fang, X. Zhu, G. Mu, H. Wen, Hall effect and magnetoresistance in single crystals of $NdFeAsO_{1-x}F_x$ (x= 0 and 0.18), Physical Review B 78(13) (2008) 134508.
[47] M. Barsoum, T. El-Raghy, C. Rawn, W. Porter, H. Wang, E. Payzant, C. Hubbard, Thermal properties of Ti_3SiC_2, Journal of Physics and

Chemistry of Solids 60(4) (1999) 429-439.
[48] A. Togo, L. Chaput, I. Tanaka, G. Hug, First-principles phonon calculations of thermal expansion in Ti_3SiC_2, Ti_3AlC_2, and Ti_3GeC_2, Physical Review B 81(17) (2010) 174301.
[49] J. Zinman, Electrons and Phonons (Classics Series), Oxford: Oxford University Press, 2001.

CHAPTER 5

GRAIN SIZE EFFECT ON OXIDATION BEHAVIOR OF Ti_2AlC AND ATOMIC LEVEL REACTION BEHAVIOR BETWEEN Ti_2AlC AND Cu

5.1. Grain size effect in Ti_2AlC oxidation behavior

5.1.1. Introduction

Ti_2AlC, as a typical representant of these so-called MAX phases, is characterized by Ti_6C octahedra interleaved with Al layers[1]. This inherent nanolayered structure provides a unique combination of metal-like and ceramic-like properties: machinability, good electrical and thermal conductivity, high thermal shock resistance and stiffness at high temperatures, which opens the way to diverse potential applications [2-4]. Being a ceramic, these materials exhibit self-healing capabilities when they are exposed to an oxidizing environment at high temperatures [5-9]. In Ti_2AlC, the outward diffusion of the weakly bonded Al atoms is much faster than that of the more covalently bonded Ti atoms in the Ti_2AlC structure[10-12]. As a consequence, the self-healing of Ti-Al-C MAX phase ceramic proceeds by oxidation, whereby cracks, gaps or notches are filled by α-Al_2O_3 and rutile-TiO_2 through oxidation[13].

For application at high temperatures, oxidation resistance in air is required and the oxidation kinetics of Ti_2AlC and Ti_3AlC_2 have been investigated. Their weight gain vs. time data are documented by cubic[14, 15] and parabolic[15, 16] kinetics in the temperature range 800-1300 °C, as presented by equations (5-1) and (5-2). In both cases, a rapid out-diffusion of Al atoms first occurs during oxidation and Al_2O_3 forms. Then, Ti atoms diffuse out along the Al_2O_3 grain boundary and form TiO_2[14, 31]. If a dense and continuous Al_2O_3 layer is formed with TiO_2 islands above, a cubic oxidation kinetics is observed and samples exhibit excellent oxidation resistance. Otherwise, a thick rutile-TiO_2 layer is formed on top of the discontinuous α-Al_2O_3 layer and parabolic kinetics is obeyed.[14]

$$\left(\frac{\Delta W}{S}\right)^3 = k_c t \qquad (5-1)$$

$$\left(\frac{\Delta W}{S}\right)^2 = k_p t \qquad (5-2)$$

where ($\Delta W/S$), k_c or k_p, and t are the weight gain per unit surface area, the cubic or parabolic rate constant, and oxidation time, respectively.

Until now, the oxidation mechanisms of CG and FG Ti_2AlC bulk samples have been unclear. For clarifying this effect, fine-grained (FG) and coarse-grained (CG) Ti_2AlC bulk samples were synthesized and oxidized at 800, 900, 1000 and 1100 °C in air. Their oxidation kinetics were characterized and compared. Furthermore, the crystallographic evolution of partially oxidized CG-Ti_2AlC was investigated by TEM and the oxidation mechanism is discussed.

5.1.2. Microstructure of FG and CG-Ti_2AlC bulks

Fig. 5-1 (a) illustrates that the FG-Ti_2AlC contains some Al_2O_3 traces (black round-shaped areas). As found in the literature, the introduction of oxygen results from the milling process of green Ti_2AlC into fine powders after pressureless sintering.[17, 18] The XRD patterns given in Fig. 5-1 (d) show that no impurities except Ti_2AlC peaks are observed. From Rietveld refinements of the XRD data using the MAUD software, the Al_2O_3 content determined in FG-Ti_2AlC is about 6.3 vol.%. MAX phases generally exhibit an anisotropic microstructure with grains being strongly elongated in the basal plane direction, especially when MAX particles size becomes bigger. Herein, a stronger (002) peak was found in CG-Ti_2AlC. Fig. 5-1 (b) and (c) reveal obvious grain size differences in these two bulks. By measuring 50 grains, we obtained the average dimensions of Ti_2AlC grains, given in Table 5.1. FG-Ti_2AlC grain lamellae are situated in the range of 2-5 μm in length and 1-3 μm in width. While CG-Ti_2AlC grain lamellae are an order of magnitude larger. Their size ranges from 50-150 μm in length and 15-40 μm in width. These differences indicate that CG-Ti_2AlC grains are strongly elongated in the basal plane direction. As FG-Ti_2AlC is not directly fabricated through HP, there is no different orientation in the axial and radial planes. For CG-Ti_2AlC, the compressed direction is uniform in the HIP method. Therefore, no artificial textures in FG and CG-Ti_2AlC bulks were introduced in this work.

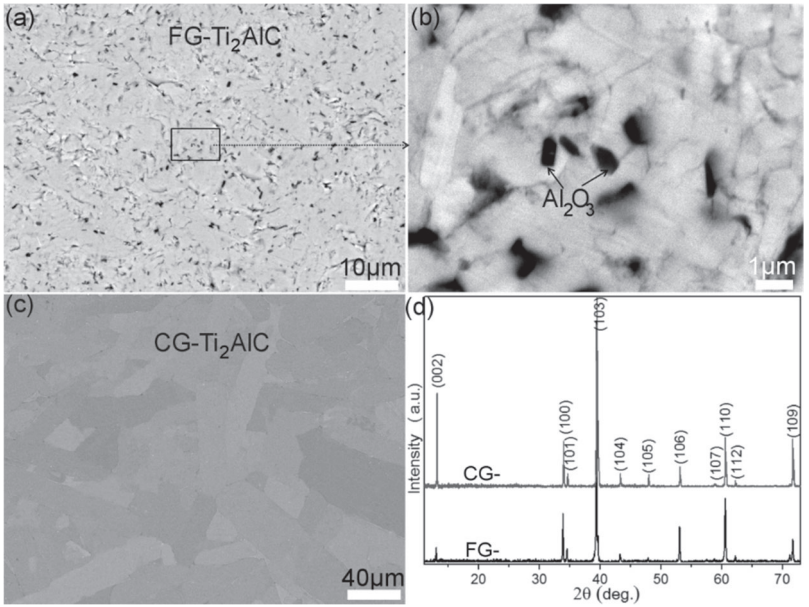

Fig. 5-1: Back-scattered electron (BSE) images of (a and b) FG and (c) CG-Ti_2AlC bulks, (d) X-ray diffraction patterns of FG and CG-Ti_2AlC bulks.

Table 5-1: Summary of sintering conditions, phase composition volumes, densities and grain sizes of FG-Ti_2AlC and CG-Ti_2AlC.

Samples	Processing Method	Phase composition (volume)	Density (g cm^{-3})	Grain size (μm)
FG-Ti_2AlC	Pressureless sintering at 1400 °C / 30 mins+ HP 1400 °C/30 MPa /30 mins in Ar	Ti_2AlC (93.7%) Al_2O_3 (6.3%)	3.99	W:1-3 L:2-5
CG-Ti_2AlC	HIP 1400 °C/4 h/80 MPa in Ar	Ti_2AlC (100%)	4.01	W:15-40 L:50-150

5.1.3. Oxidation behavior and phase evolution

Figs. 5-2 (a) and (c) show the weight gain per unit surface area of the FG and CG-Ti_2AlC samples oxidized at 800, 900, 1000 and 1100 ℃ in air as a function of time. Whatever the temperature is, the weight gain per unit surface area of CG-Ti_2AlC is two orders of magnitude higher than that of FG-Ti_2AlC. As shown in Fig. 5-2 (b) and (d), cubic[14, 15] and parabolic[15, 16] kinetics can be respectively used to fit the FG and CG-Ti_2AlC weight gain data. The goodness of fit of the experimental data (R^2 = 0.98–0.99) confirms that the coarse-grained and fine-grained Ti_2AlC bulk samples are characterized with parabolic and cubic oxidation kinetics, respectively. Table 5-2 summarizes oxidation data determined in this work and the literature. The oxidation kinetics of FG-Ti_2AlC are in good agreement with other published results, good oxidation resistance is observed when Ti_2AlC grain size is below 10 μm[14-16]. Otherwise, poor oxidation resistance occurred when Ti_2AlC grain size is above 20 μm. As in our CG-Ti_2AlC bulk samples, Barsoum et al. have observed parabolic oxidation kinetics in Ti_2AlC bulk samples composed of grain sizes of about 20 μm. These results strongly indicate that grain size plays an important role in the oxidation behavior of MAX phases.

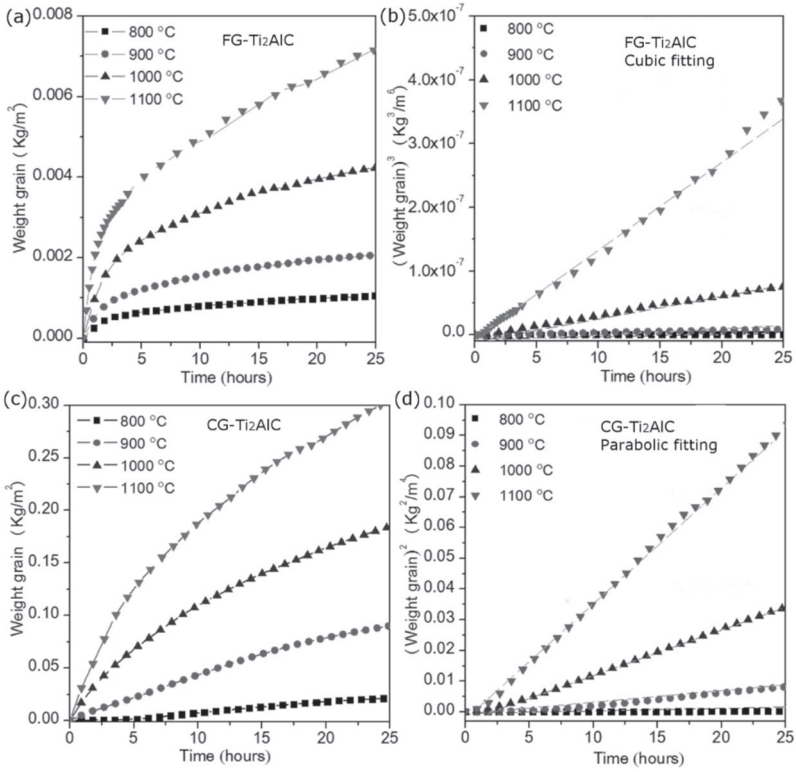

Fig. 5-2: Weight gain per unit surface area of Ti_2AlC as a function of oxidation time at 800, 900, 1000 and 1100 ℃ for oxidation in air of (a) FG-Ti_2AlC bulk samples and (c) CG-Ti_2AlC bulk samples and respective fitting (b) and (d).

Table 5-2. Summary of k_c (cubic, $kg^3\ m^{-6}\ s^{-1}$) and k_p (parabolic, $kg^2\ m^{-4}\ s^{-1}$) values for the oxidation of Ti_2AlC.

Phase	Grain size (μm)	800 ℃	900 ℃	1000 ℃	1100 ℃	Oxidation behavior	Comments and references
Ti_2AlC				3.2×10^{-13}	1.1×10^{-12}	Cubic	[14, 19]
Ti_2AlC	W: 4-7 L:5-10			3.3×10^{-13}	1.9×10^{-12}	Cubic	Air [20]
Ti_2AlC	W: 4-7 L:5-10			5.6×10^{-13}	2.0×10^{-12}	Cubic	100% H_2O [20]
Ti_2AlC	W: 1-3 L: 2-5	1.2×10^{-14}	1.0×10^{-13}	8.3×10^{-13}	3.3×10^{-12}	Cubic	This work
Ti_2AlC	W:15-40 L:50-150	5.7×10^{-9}	1.2×10^{-7}	4.0×10^{-7}	1.0×10^{-6}	Parabolic	This work
Ti_2AlC	≈23					Parabolic	[21, 22]

Fig. 5-3 shows typical SEM back-scattered electron (BSE) micrographs of the oxidized scales formed on the surfaces of FG-Ti_2AlC and CG-Ti_2AlC after oxidation at 1000 °C during 25 h in air. The excellent oxidation resistance behavior found in our FG-Ti_2AlC is similar to that previously reported[23]. Fig. 5-3 (a) and (c) show that a dark gray inner dense Al_2O_3 layer with a thickness of 1 μm formed between the bright TiO_2 nodules and Ti_2AlC matrix. Due to the depletion of Al atoms, an intermediate Ti-rich layer is observed between the α-Al_2O_3 inner scale and Ti_2AlC matrix. In the case of CG-Ti_2AlC, Fig. 5-3 (b) reveals a thick rutile-TiO_2 layer formed above the discontinuous α-Al_2O_3 layer at the surface of CG-Ti_2AlC. Underneath the Al_2O_3 layer, some very small Al_2O_3 crystallites are formed together with (TiO_2+Al_2O_3)-mixed agglomerates. This phenomenon is also reported by Barsoum et al.[21, 22] in $Ti_{n+1}AlC_n$ (n=1 and 2) with grain size in the range of 23-30 μm and by Lee et al.[24] in Ti_3AlC_2 with lamellar grains whose dimensions are ~58 μm in length and ~14 μm in thickness. Furthermore, in Fig. 5-3 (d), two contrasts were found in one Ti_2AlC grain under BSE mode, which were named poor and rich-Al areas. The different contrasts imply that Al atoms outwards diffused at different rates. At lower magnification, as given in Fig. 5-5 (a), Ti_2AlC grains were partially oxide with different degrees (area I). By first-principles investigation, Dr. Wang reported that Ti_2AlC is still stable when the content of aluminum is above 0.5[25]. To go deeper, an area II appeared where Al atoms out-diffused from Ti_2AlC into the grain boundary, followed by an area III containing intact grains (III). In addition, Fig. 5-3 (d) also indicates that some dotted lines appeared in the poor-Al area, which means crystal structure or volume possibly changed in Ti_2AlC during the outwards diffusion of Al atoms.

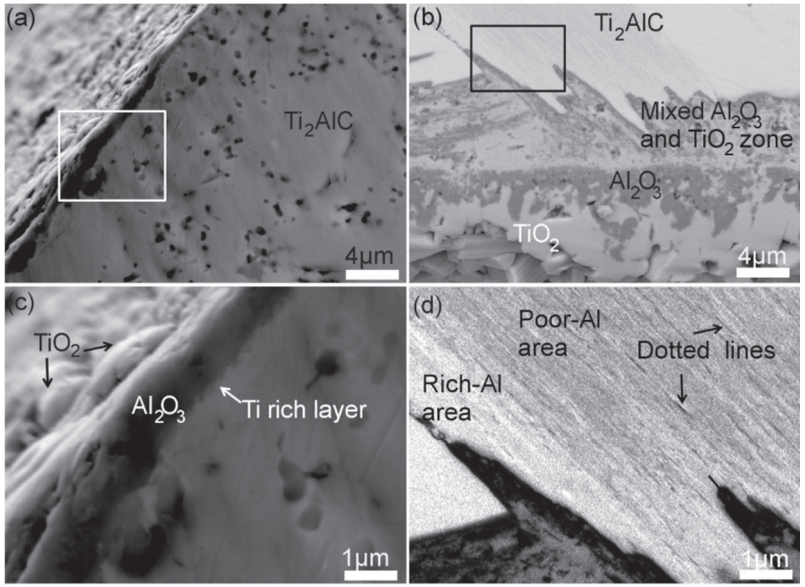

Fig. 5-3: BSE-SEM micrographs of the oxidized surface of FG-Ti_2AlC (a) and (c) and CG-Ti_2AlC (b) and (d). The oxidation was performed at 1000℃ for 25 h in air.

Fig. 5-4 shows typical SEM back-scattered electron (BSE) micrographs of the oxidized scales formed on the surfaces of FG-Ti_2AlC and CG-Ti_2AlC after oxidation at 1100 °C for 25h in air, respectively. Fig. 5-4 (a) reveals that after oxidation at 1100 °C, the TiO_2 nodules observed at 1000 °C are now transformed into TiO_2 clusters; nodules are connected to each other on top of Al_2O_3 layer. At 1100 °C, Ti atoms diffused out, along the Al_2O_3 grain boundaries, more easily than at 1000 °C which results in the presence of a higher number of TiO_2 nodules on top of the alumina layer. Even though some cavities formed at the Al_2O_3 and TiO_2 (rutile) interface, the FG-Ti_2AlC sample exhibits excellent oxidation resistance. These observations suggest that the inner Al_2O_3 layer remains intact and blocks the inward oxygen diffusion. Fig. 5-4 (b) shows that the outside TiO_2 and Al_2O_3 layers are detached from the bulk matrix. As observed in Fig. 5-5 (a), cracks appeared in the oxidation layer of CG-Ti_2AlC bulk oxidized at 1000 °C for 25h. This phenomenon could be ascribed to several reasons. Firstly, as the volume expansion between TiO_2 and Al_2O_3 are mismatched, the stress concentration increases during their mixed growth and gives rise to the spallation of protective layers.[15] The thermal expansion coefficient (TEC) of these different phases are: rutile

TiO_2 ($\alpha_a = 9.2\times10^{-6}\ K^{-1}$, $\alpha_c = 7.1\times10^{-6}\ K^{-1}$), Al_2O_3 ($\alpha_a = 7.9\times10^{-6}\ K^{-1}$, $\alpha_c = 8.8\times10^{-6}\ K^{-1}$), TiC ($\alpha_a = 7.0\times10^{-6}\ K^{-1}$), Ti_2AlC ($\alpha_a = 7.1\times10^{-6}\ K^{-1}$, $\alpha_c = 10\times10^{-6}\ K^{-1}$). The stress between Al_2O_3 and TiO_2 is estimated to be about 0.3 GPa through the equation of $\sigma = \alpha\Delta TE$ if the temperature range is 1000 ℃ and Young's modulus of the matrix is 260 GPa. Secondly, large volume (Δ59.0%) changes are associated with the oxidation of Ti_2AlC into TiO_2 and Al_2O_3, which promotes crack propagation.[15] Fig. 5-4 (c) and (d) are secondary and back-scattered micrographs of the enlarged area shown in Fig. 5-4 (b). It is shown that, inside Ti_2AlC grains, Al atoms preferentially diffused along basal planes as TiC lines appeared along Ti_2AlC basal planes (see Fig. 5-4 (c) and confirmed by EDX). This result indicates that the transformation of Ti_2AlC into TiC has already started from the interior of the Ti_2AlC grain. Al atoms thus react with oxygen at the extremity of the basal planes to form alumina particles (see Fig. 5-4 (d)). It also suggests a faster oxidation rate along the basal plane than along the c-axis. Such a conclusion is in good agreement with Xu et al.; they demonstrated that, at 1200 °C, the basal planes had a weight gain which was 45 times larger than that on the traverse plane.[17]

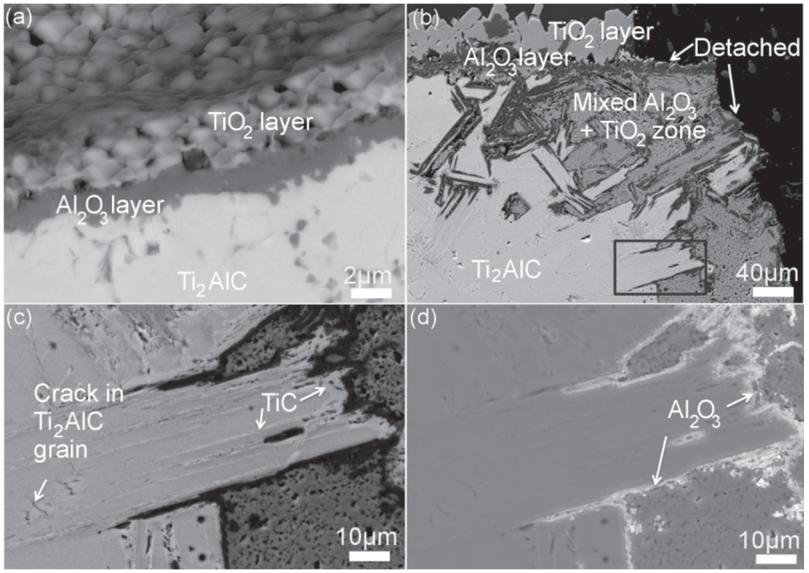

Fig. 5-4: BSE-SEM micrographs of the oxidized surface of FG (a) and CG-Ti_2AlC (b); the oxidation is performed at 1100 °C for 25 h in air. Secondary (c) and back-scattered (d) electron micrographs of the enlarged rectangular area marked in (b).

In CG-Ti_2AlC, Al atoms diffuse through both grain boundaries and basal planes. Al atoms have to travel much longer to cover the longitudinal surface of CG-Ti_2AlC. For example, Xu et al. found the obvious anisotropic oxidation resistance on the textured Ti_3AlC_2 and reported the basal planes had a weight gain which was 45 times larger than on the traverse plane at 1200 ℃.[17] Herein, a non-uniform Al_2O_3 layer is formed in CG-Ti_2AlC whereas a uniform and protective alumina layer is formed in the case of FG-Ti_2AlC. This inhomogeneous oxide scale was also reported by Rao et al. in the oxidation study of bulk Ti_2AlC with grain sizes whose dimensions were about 100 μm in length and 20 μm in width.[23] Subsequently, compared with FG-Ti_2AlC, much more Ti atoms passed through the uncontinuous Al_2O_3 layer and lead to the TiO_2 formation in CG-Ti_2AlC. For this stage, the oxidation of Ti_2AlC occurs via the reported and following reaction[15]:

$$Ti_2AlC + O_2 \rightarrow 2TiO_2 + \frac{1}{2}Al_2O_3 + CO_2 \qquad (5-3)$$

5.1.4. FIB-TEM investigations

To determine the origin of contrasts within grains far away from the surface, the grain microstructural evolution of the CG-Ti_2AlC was investigated. Fig. 5-5 (b) is a zoomed back-scattered image of the CG-Ti_2AlC grain marked by the rectangle in Fig. 5-5 (a). The image was taken 200 μm away from the interface between the Ti_2AlC and the Al_2O_3 layers. As can be seen, parallel straight lines are clearly visible within each grain. A TEM lamella was then prepared to be normal to these lines (i.e., along the c-axis of the Ti_2AlC unit cell), as indicated by the rectangle in Fig. 5-5 (b). Fig. 5-5 (c) and (d) show the bright field TEM images of the microstructure in the depth of the selected grain shown in Fig. 5-5 (b). A band shape-like structure with some delamination is equally observed close to the surface and in depth. Some bands show no contrasts and no defects from the top to the bottom of the TEM lamella, while others are full of inclusions. Depending on the bands, inclusions are either thin and straight or large and facetted (see Fig. 5-5 (d)). In addition, the length of the delamination bands is a few micrometers and the delamination bands are accompanied by elongated holes that are sometimes filled with matter. These in-depth observations of the microstructure thus suggest that straight lines observed previously by SEM are evidence of a significant in-depth change of the microstructure in the region called the bulk Ti_2AlC area. These changes may be evidence of the presence of oxygen deep inside the Ti_2AlC volume, suggesting an oxidation front far above the

Ti_2AlC/Al_2O_3 interface. Moreover, such oxidation far from the interface could explain the formation of elongated holes in the structures. Indeed, holes may be the result of the transformation between the Ti_2AlC and TiC. It was previously reported that the transformation of Ti_3AlC_2 and Ti_3SiC_2 in TiC_x induces 21% and 15% volume shrinkages, respectively.[26, 27] As the density of Ti_2AlC (4.067 g cm^{-3}) is lower than that of Ti_3AlC_2 (4.247 g cm^{-3}), a more severe volume shrinkage should happen during the transformation of Ti_2AlC in TiC_x (4.933 g cm^{-3}).

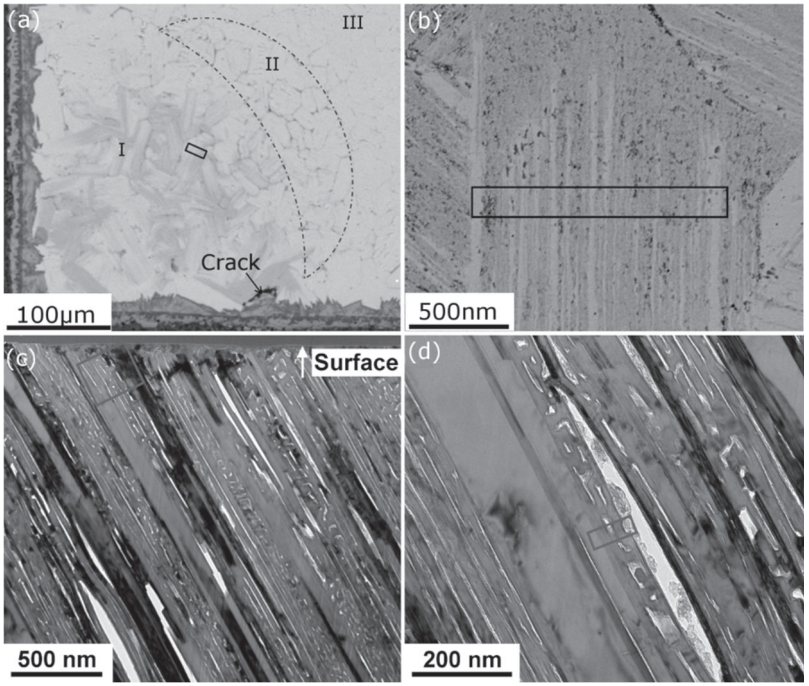

Fig. 5-5: BSE-SEM of the bulk CG-Ti_2AlC oxidized at 1000 °C for 25 h in air at two different magnifications (a) and (b). The rectangle in (b) shows where the FIB lamella was performed. Bright field TEM images of the in-depth microstructure (c) and (d). Rectangles in (c) and (d) show the area where EDX map and HRTEM images were performed.

EDX maps were performed to determine the chemical composition of the different phases observed in the sample. Due to the carbon content uncertainties, only the ratio between elements will be considered in the following. Values are averaged on different areas from different maps.

Fig. 5-6 shows a BFTEM image taken close to the surface of the sample (see Fig. 5-5 (c)), the corresponding elemental maps of Ti, Al, O and C, as well as the Ti-Al combined map. As can be seen, the different contrasts observed on the BFTEM reflect a huge change in the chemical composition. Maps of C and Ti exhibit identical distribution while maps of Al and O show important similarities. Three areas can be clearly distinguished by looking at the Ti-Al map: inclusions that are rich in Al (in green), the matrix surrounded inclusion that is rich in Ti (in red) and a homogeneous band on the right side of the image that is rich in both Al and Ti (in yellow). Note that areas in black in the Ti-Al map are holes. Concerning inclusions and the surrounding area, two different compositions are clearly identified. Around inclusions, only Ti and C atoms are detected, suggesting the formation of a TiC matrix. In inclusions, all elements are detected but levels of Al and O are the highest measured in the sample, while the concentration of Ti significantly drops. Indeed, the Ti/Al ratio is about 0.8 while the O/Al ratio varies from 1 to 2. These high contents of O and Al in inclusions may result from the formation of Al_2O_3 inclusions inside the TiC matrix. In the yellow area that is rich in Ti and Al, the situation is different. The Ti/Al ratio varies from 2 to 2.5 depending on the area in the sample. Such a ratio suggests the presence of MAX phases such as Ti_2AlC or Ti_3AlC_2. Note that no evidence of the presence of Ti-O complexes such as TiO_2 was observed in the sample.

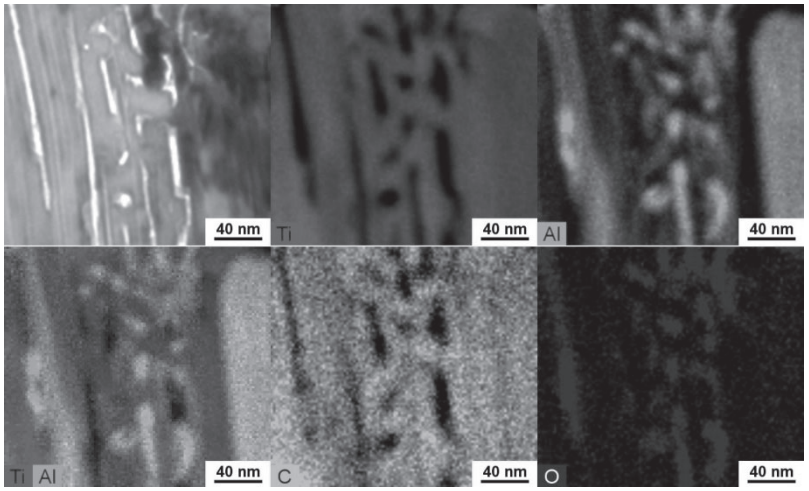

Fig. 5-6: BFTEM image of an area close to the surface (red rectangle in Fig. 5 ©) and the corresponding EDX maps.

5.1.5. The oxidation mechanism at the atomic level

HRTEM was then performed to determine the structure of the different phases in the sample. Fig. 5-7 shows representative images of the different phases and their relative interfaces. The Al-rich phase is polycrystalline and composed of small grains (of a few nanometers). In the enlarged area (green rectangle in Fig. 5-7), a periodicity of 2.2 Å was measured. According to chemical EDX results that showed a high concentration of Al and O, this value matches with the $(2\bar{1}\bar{1}0)$ of α-Al_2O_3 phase (2.2 Å).[28] Between or around the polycrystalline Al_2O_3, the Ti-rich matrix oppositely exhibits a long monocrystalline phase that extends from the surface to the bottom of the TEM lamella with a periodicity of 2.5 Å. Such a value is in good agreement with the theoretical value of the (111) TiC planes (2.5 Å) and thus confirms EDX results.[29] Far from the Al_2O_3 phase and close to TiC phases, the measured periodicities of the Ti-Al rich are about 6.8 Å and 9.3 Å. These values are in good agreement with the expected values of 6.8 Å and 9.4 Å for the (0001) Ti_2AlC and Ti_3AlC_2 planes, respectively.[2, 30] This sequence, (i.e., Ti_2AlC//Ti_3AlC_2//TiC) was observed everywhere in the sample. Furthermore, the HAADF image of the area marked by the white rectangle confirms the formation of Ti_3AlC_2 phase with a thickness of 11 atomic planes. The bright Ti atoms spots indicate that the stacking sequence is (0001) Ti_2AlC // (0001) Ti_3AlC_2 // (111) TiC. This strongly suggests that, in the presence of oxygen, Ti_2AlC decomposes in TiC by forming an intermediate phase of Ti_3AlC_2. At the same time, Al_2O_3 phases form close to the TiC phase as an additional result of the decomposition of Ti_2AlC into TiC.

This transformation is accompanied by a significant increase of density from 4.1 g. cm^{-3} (Ti_2AlC) to 4.93 g. cm^{-3} (TiC). This change of density for the same volume results in the formation of long and elongated holes near TiC grains. For clarification, equation 5-4 summarizes this process. As the Al_2O_3 layer could prohibit the inward diffusion of oxygen into the Ti_2AlC grain, a much lower oxygen partial pressure is created in these holes. Subsequently, as given in equation 5-5, the out-diffusion of Al atoms from Ti_3AlC_2 favors the formation of α-Al_2O_3 and filled the holes accompanied with the in situ formed TiC. During this process, no TiO_2 formed.

$$Ti_2AlC + O_2 \rightarrow xTi_3AlC_2 + (2-3x)TiC + \frac{1-x}{2}Al_2O_3 \quad (5-4)$$

$$xTi_3AlC_2 + O_2 \rightarrow 3xTiC + \frac{x}{2}Al_2O_3 \quad (5-5)$$

Where, as the carbon and oxygen content cannot be measured, only Ti and Al contents are balanced on both sides of the equations.

It should be pointed out that during the decomposition of Ti_2AlC into

TiC and Al_2O_3, the elongated holes form throughout the sample and weaken the entire material. These holes probably act as precursors to cracks due to their micrometer length. Moreover, the thermal expansion coefficients between the TiO_2 and Al_2O_3 formed on the surface are mismatched.[15] Both of these factors caused the crack and split of the oxidation layer on the surface of the CG-Ti_2AlC sample, finally leading to the poor oxidation resistance of the CG-Ti_2AlC sample.

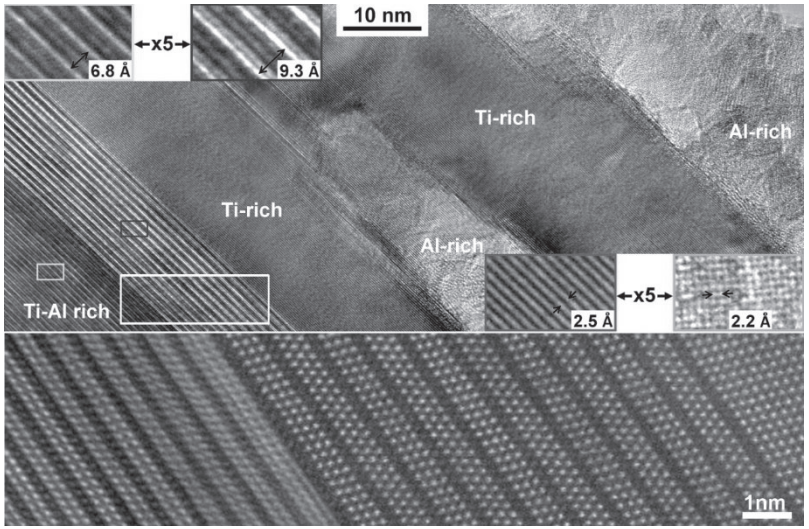

Fig. 5-7: HRTEM images of the different phases observed in the enlarged area marked in Fig. 5-5 (d) (far from the Ti_2AlC/Al_2O_3 interface), the HAADF image was obtained on Ti_2AlC- Ti_3AlC_2-TiC area marked in the white rectangle.

5.2. Reaction behavior with Cu at the atomic level

5.2.1. Introduction

Copper is one of the most used metals essentially because of its very high electrical conductivity. However, its poor mechanical and wear properties result in the premature failure of components, especially in extreme conditions. One possible route for overcoming this drawback is to introduce MAX phases, such as Ti_2AlC. Measurements of lattice parameters with numerous methods reveal that MAX phases exhibit elevated high crystalline anisotropy. The c/a ratio is generally higher than 4. This class of nanolaminated materials combine properties of both

ceramics (refractory, high stiffness, low density – 4.5 g cm^{-3} for Ti_3SiC_2, low ductility at room temperature) and metals (high thermal and electric conductivity, thermal shock resistance, low hardness, mechanical resistance). The deformation mechanism of MAX phases is based on dislocations[31]. From energy considerations, only basal dislocations play a role in their plastic behavior: due to the anisotropy and the lamellar lattice, nucleation of dislocations is supposed to occur only in the basal plane[31-34]. Moreover, at high temperatures out-of-basal plane dislocations are not just anecdotal events and cross-slip plays a key role[35]. Therefore, the challenge is to add MAX phase into Cu in order to enhance the mechanical properties without much loss of conductivity. However, no mechanism is proposed.

In the framework of MAX-Cu composites, Ti-based MAX phases including Ti_3AlC_2, Ti_2AlC and Ti_2AlN have been used[36]. Zhang et al. suggested that the de-intercalation of Al along basal planes induces the formation of Ti_xC platelets in Ti_3AlC_2-reinforced Cu composites[37]. The solid solution $(Ti_{1-\varepsilon}Cu_\varepsilon)_3(Al,Cu)C_2$ has been reported in sintered Ti_3AlC_2-Cu powders in which the presence of Cu is mainly located on the Al sites of the MAX phases [38] [39, 40]. These studies emphasize that the diffusion mechanisms between Ti-based MAX phases and Cu are strongly related to temperature. However, the different steps of this mechanism have not yet been observed, including the formation and decomposition of Ti_3AlCuC_2, Ti_2AlCuN or Ti_2AlCuC solid solutions.

With the aforementioned layered microstructure and unique set of properties, MAX phases are excellent candidates for the design of novel materials with tailored properties. In particular, this work aims to provide a comprehensive picture of structural changes caused by the diffusion of Cu in the Ti_2AlC MAX phase.

5.2.2. Diffusion and distribution of Cu and Al atoms

Fig. 5-8 shows the junction between Ti_2AlC and Cu at two magnifications. Fully dense Ti_2AlC was prepared by Hot Isostatic Pressing (HIP). Powders of Ti (150-250 µm, 99.5% purity), Al (45-150 µm, 99.5% purity) and TiC (<45 µm, 98% purity) were mixed in stoichiometric proportions and placed into a hot isostatic press where the powder compact was heated up to 1400 °C under a pressure of 80 MPa. Then pure Cu foil (99.9%, 50 µm thick) and the bulk Ti_2AlC were mechanically pressed under Ar atmosphere at a pressure of 10 MPa and a soaking temperature of 750 °C.

Fig. 5-8 (a) was acquired with the Secondary Electron (SE) detector, while Fig. 5-8 (b) was acquired with the BacScattered Electron (BSE) detector of the Scanning Electron Microscope (SEM). A thin foil was prepared perpendicular to the joining interface by Focused Ion Beam (FIB) milling with a ThermoFisher Helios Nanolab Dual Beam.

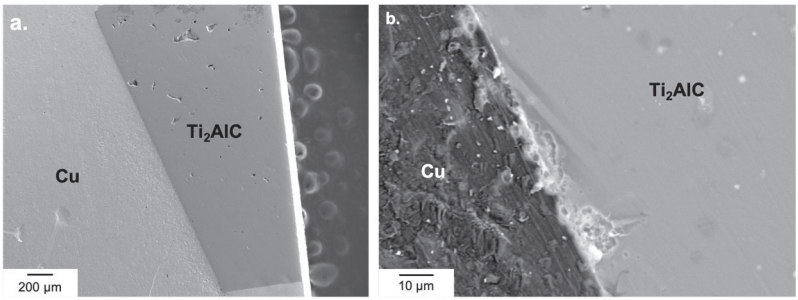

Fig. 5-8: SEM micrographs of the specimen near the Cu/Ti_2AlC boundary acquired with the SE detector (a), and with the BSE detector (b).

Fig. 5-9 (a) shows a STEM micrograph in High-Angle Annular Dark Field (HAADF) mode at low magnification. Three regions with different contrasts are easily distinguished in the Ti_2AlC area and they are labeled as RA, RB and RC (Fig. 5-9 (a)). Region RB appears as a bright band parallel to $(0\ 0\ 0\ 1)$ basal planes. The HAADF detector senses a greater signal from atoms with a higher atomic number Z, causing them to appear brighter in the resulting image. The mean Z of the region RB is thus expected to be higher than in region RA and region RC. The EDS line profile on both sides of the region RB (Fig. 5-9 (b)) combined with the EDS maps (

Fig. 5-9 (c-e)) confirm this observation: the atomic ratio of Al (Z=13) drops from ~33% to ~23% when crossing the boundary between regions RA and RB and it stays stable at ~23% in region RB. It then goes back to ~33% when crossing the other boundary from RB to RC. Meanwhile, the atomic ratio of Cu (Z=29) increases from ~2% to ~15% inside the region RB. Concerning Ti (Z = 22), the atomic ratio remains quite stable at ~62%. Note that several cracks along basal planes are observed close to the Cu/Ti_2AlC junction.

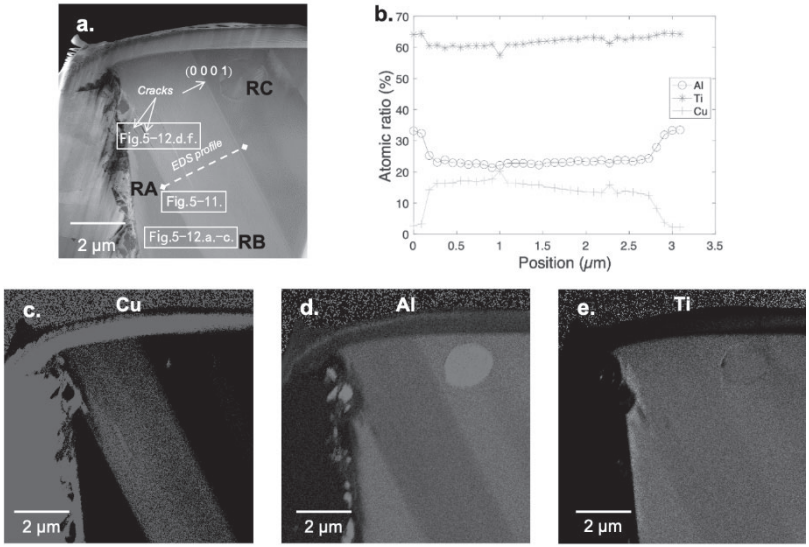

Fig. 5-9: chemical characterization of the Cu-MAX phase composite. (a) HAADF-STEM micrograph at low magnification of the thin foil. Three regions labeled RA, RB and RC are distinguished. The basal plane direction (0 0 0 1) is also shown. Several cracks are observed in the vicinity of the Cu/Ti_2AlC junction. (b) EDS line profile taken along the dotted line in (a). (c), (d) and (e) are EDS maps of Cu, Al and Ti respectively.
White rectangles in (a) localize where Fig. and Fig. were taken.

The HAADF-STEM micrographs were captured at the interface between region RA and region RB, as shown in Fig. 5-10 (b-c). The observed crystallographic lattice is consistent with the expected one of the 211-MAX phase projected along [1 1 $\bar{2}$ 0]: zigzag stacking (Fig. a, black lines) of two TiC planes followed by one Al plane, the Al plane being the axis of symmetry of the zigzag. Here again, region RB appears brighter than region RA. More precisely, the change of contrast mainly comes from A-planes that are located between two adjacent Ti planes that appear brighter. EELS maps of Fig. 5-10 (d-f) clearly evidence that Cu atoms replace Al in the crystallographic lattice. Combining the EDS (Fig. 5-9) and EELS results (Fig. 5-10), one expects that solid solutions are formed in region RA and region RB with the average formula $Ti_2Al_{1.1}Cu_{0.06}C$ and $Ti_2Al_{0.74}Cu_{0.49}C$, respectively.

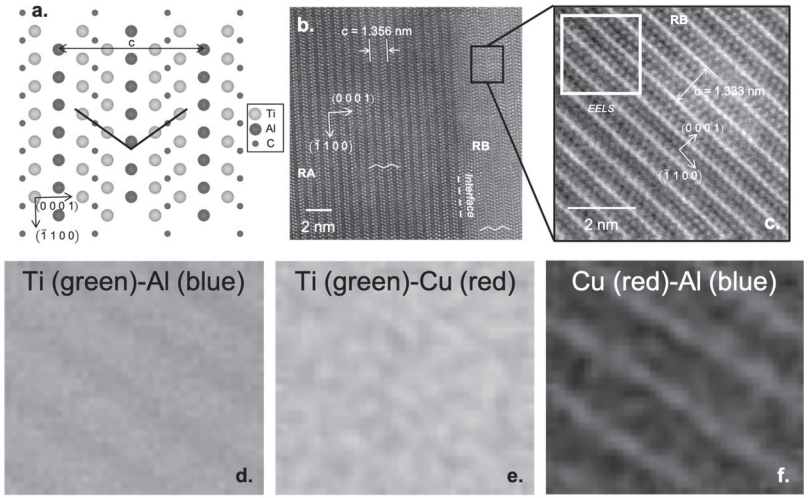

Fig. 5-10: Atomic EELS characterization. (a) Crystallographic structure of Ti_2AlC projected along [1 1 $\bar{2}$ 0] (b), (c) HR-STEM HAADF of the interface between region A (RA) and region B (RB). The electron beam is along [1 1 $\bar{2}$ 0]. The white square in (c) localizes the area in region B where the EELS maps were acquired ((d), (e) and (f)). Zigzag lines in (a) and (b) highlight the stacking of TiC planes, characteristic of the crystallography of a 211 MAX phase family.

5.2.3. The formation of Ti_2C platelets

Fig. 5-11 depicts some steps in the formation of Ti_2C platelets. Fig. 5-11 (a-c) first show the intercalation of Cu in A-planes along basal planes of Ti_2AlC. Yellow arrows localize bright "atomic channels" along basal planes. This change of contrast can be attributed to a localized increase of the atomic number Z due to the insertion of Cu atoms in A-planes of Ti_2AlC. Fig. 5-11 (c) shows the interface between region RA and region RB where the solid solution $Ti_2Al_{0.74}Cu_{0.49}C$ is formed. Moreover, this interface is abrupt. Both observations indicate a fast diffusion of Cu along basal planes. Close to the Cu source, i.e., close to the Cu/Ti_2AlC junction (

Fig. 5-11 (d)), A-planes de-intercalate (Fig. 5-11 (e)) forming a partial dislocation lying in the basal plane (Fig. 5-11 (e)) with a Burgers vector clearly along [0 0 0 1]. In Fig. 5-11 (f), two sorts of Ti_2C-platelets are distinguishable: perfect connection of the adjacent Ti planes (Fig. 5-11 (f), yellow arrows) and unperfect connection (Fig. 5-11 (f), white arrows) associated with a slide of ~0.26 nm along ⟨1 $\bar{1}$ 0 0⟩. This sliding direction

was already reported in the case of stacking faults with the insertion of MX planes[41]. From the crystallographic point of view of Ti_2C-platelets, both connections between adjacent Ti planes in MAX phases can be seen as Twin Boundary (TB) and are either perfect (Fig. 5-11 (f), yellow arrows) or shifted (Fig. 5-11 (f), white arrows)[42]. Note that in the Ti_2AlC point of view, they are seen as stacking faults where one A-plane was removed. Another description indicates that Ti_2C platelets localized by yellow arrows in Fig. 5-11 (f) can be seen as hexagonal Ti_2C as well. The TB description will be used in the following.

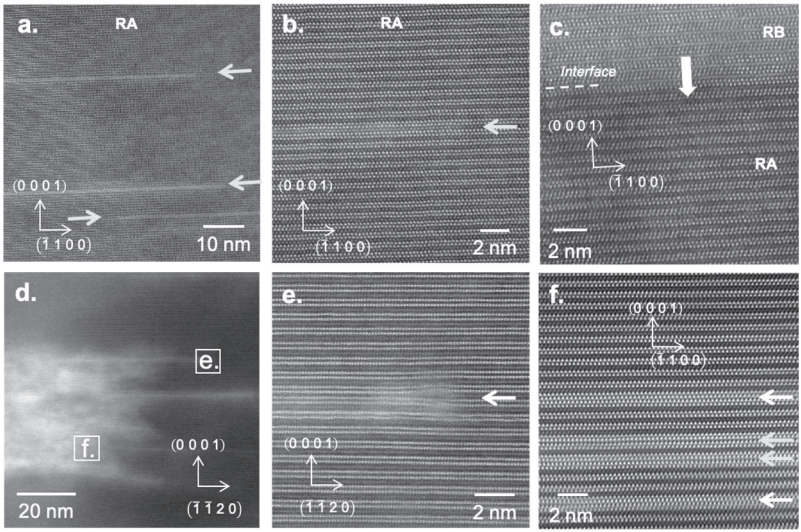

Fig. 5-11: Observations of several steps of the diffusion of Cu. (a)-(e) HR-STEM HAADF micrographs far away ((a)-(c)) and in the vicinity ((d)-(e)) of the Cu/Ti_2AlC junction. For (a)-(c) and (f), the electron beam is along [1 1 $\bar{2}$ 0] while it is along [$\bar{1}$ 1 0 0] for (d) and (e). (d) is a low-magnification micrograph which enables localization of where micrographs (e) and (f) were taken. The Cu/Ti_2AlC junction is localized on the left. (f) shows Ti_2C platelets (white and yellow arrows).

We investigated further the atomistic features that were observed by means of molecular static simulations. As no interaction model is available to model the Ti_2AlC MAX phase, we employed the Ti_2Al phase as a surrogate for a structure with A-element layers that intercalates within double Ti layers. Fig. 5-12 (a-d) show the atomistic configuration of the ground state of a basal dislocation formed by the removal of an A-element half-plane. Fig. 5-12 (a) and (b) show a sliced view of the dislocation

along the dislocation line [$\bar{1}$ 1 0 0] colored by chemical species (gray, Ti; blue, Al) and local crystallographic structure. Fig. 5-12 (b) in particular evidences the core (gray) and the stacking fault (green) of the partial dislocation. The elastic strain field generated by the dislocation is primarily directed along the Z-[0 0 0 1] direction as illustrated in Fig. 5-12 (c): only the shear component ε_{xz} is significant while the components ε_{xy} and ε_{yz} remain negligible. Fig. 5-12 (d) presents a magnified view of the dislocation core structure and illustrates the Burgers circuit. In our simulation, the Burgers vector is $\vec{b}=\frac{c}{6}$[0 0 0 1] with a norm measured at 2.3 Å. Fig. 5-12 (e) shows the critical stress required to reconstruct the perfect TB into a shifted TB or a disordered phase, as a function of the remaining non-diffused A-element. The diffusion of A atoms within an A-interlayer is characterized by the ratio $\frac{A}{A_0}$ of the number of atoms remaining in the interlayer after diffusion (A) with the number of atoms initially forming the interlayer (A_0). The critical stress shows a moderate increase for medium A concentration ($0.0<\frac{A}{A_0}<0.8$) and a steep increase in the concentration of A close to the dense interlayer ($\frac{A}{A_0}>0.8$). Note that a large concentration of A associated with very high critical stress leads to the formation of locally disordered Ti – A-element phase instead of a shifted TB. Fig. 5-12 (f) shows an example of the ground states of the TB formed after the diffusion of an A-element interlayer. In a stress-free environment, the TB exhibits a perfect structure independently on $\frac{A}{A_0}$ (

Fig. 5-12(f), $\sigma_{[0001]}=0$). As the stress normal to the TB plane reaches the critical value, the TB becomes shifted (Fig. 5-12 (f), $\sigma_{[0001]}>0$).

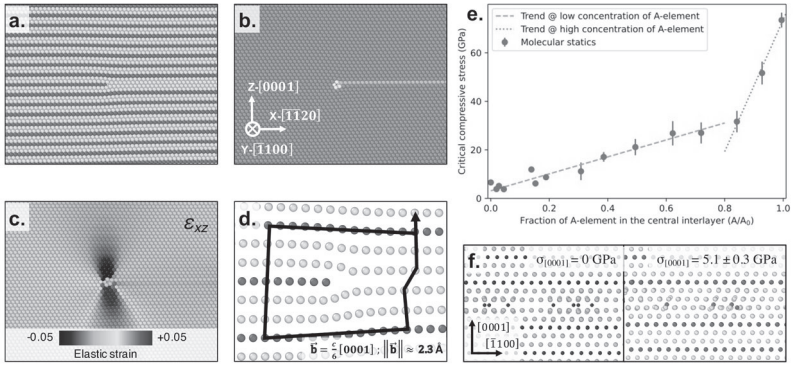

Fig. 5-12: Molecular static simulations of a de-intercalated A-element plane. (a)-(d) sliced views of the Frank partial dislocation along the dislocation line $[\bar{1}\ 1\ 0\ 0]$ formed by the removal of an A-element half-plane, (a) chemical representation: atoms in gray and blue represent Ti and A-element, respectively, (b) structural representation: atoms in red, gray and green represent hexagonal bulk, dislocation core and stacking fault structures, respectively, (c) atomic elastic strain shear component (εxz), (d) Burgers circuit and Burgers vector of the Frank partial dislocation on the magnified dislocation core structure, (e) critical stress required to reconstruct the perfect twin boundary into n shifted twin boundary or a disordered phase, as a function of the fraction $^{A}/_{A_0}$ of remaining de-intercalated A-element, (f) stable configurations of a twin boundary with $^{A}/_{A_0} = 0.04$ at zero stress and critical stress. The trend lines in (e) are guides for the eye.

Based on our experimental and numerical results, we propose a comprehensive description of the formation of Ti_2C platelets, as illustrated in Fig. 5-13. In the presence of Cu and at 700 °C, Al de-intercalate along basal planes of Ti_2AlC while Cu atoms diffuse progressively and replace Al atoms in the lattice (Fig. 5-13 (a)-(b)). This creates "atomic channels." The diffusion of Cu continues until the channel is filled, thus forming the solid solution $Ti_2Al_{0.74}Cu_{0.49}C$ (Fig. 5-13 (b)). The interface between both areas with high and low concentrations of Cu will diffuse by the successive addition of filled channels (Fig. 5-13 (c), white thick arrow). Then, atoms in A-planes de-intercalate (Fig. 5-13 (c)), thus forming a Frank partial dislocation with a Burgers vector $\vec{b}=\frac{c}{6}[0\ 0\ 0\ 1]$. The de-intercalation will propagate along $[1\ 1\ \bar{2}\ 0]$ by climbing of this *c*-dislocation. The nucleation of Frank partial dislocations causes a volume shrinkage along the *c*-axis (Fig. 5-13 (d)) i.e., the 2nd and the 3rd Ti planes move closer to each other and form a perfect TB. Note that this volume

shrinkage can lead to the initiation of cracks in (0 0 0 1) planes, as observed in Fig. 5-9 (a). To minimize the electrostatic repulsion between the adjacent Ti planes on both sides of the platelet, the perfect TB reconstructs into a perfect TB by sliding along $\langle 1\ \bar{1}\ 0\ 0 \rangle$ (Fig. 5-13 (e)). Our simulations tend to indicate that experimentally observed shifted twin boundaries might effectively contain a low but significant concentration of A -element that cannot be visible given the limitation of the TEM resolution.

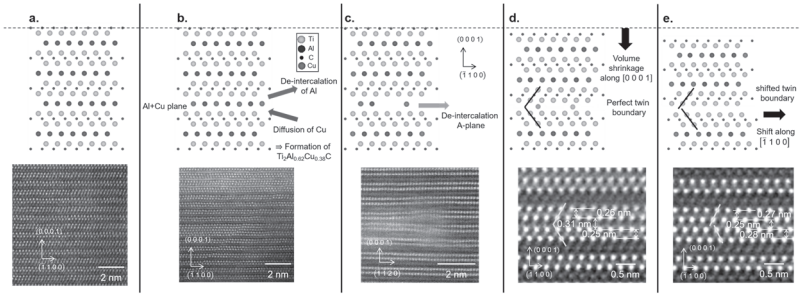

Fig. 5-13: Formation of Ti2C platelets. Here the projection axis of the crystallographic structures is $[1\ 1\ \bar{2}\ 0]$. As an illustration of each step of the mechanism, HR-STEM pictures are zoomed in on interesting areas. (a) initial step: the perfect crystal of Ti_2AlC. (b) de-intercalation of Al and diffusion of Cu for forming an atomic channel of $Ti_2Al_{0.62}Cu_{0.38}C$ solid solution. (c) de-intercalation of one A-plane. (d) volume shrinkage along the c-axis and formation of one Ti_2C platelet. (e) shift along $[\bar{1}\ 1\ 0\ 0]$ of one part of the platelet.

5.3. Conclusions

The results allow demonstration that grain size strongly influences the oxidation rate and oxidation mechanisms of Ti_2AlC MAX phase. The oxidation rate can be well fitted with cubic and parabolic kinetics, respectively. Ti_2AlC simultaneously transformed into Ti_3AlC_2 and TiC phases instead of directly transforming into TiC phase. The crystallographic orientation relationship can be summarized with the following sandwich-like form: (0001) Ti_2AlC // (0001) Ti_3AlC_2 // (111) TiC. Areas of TiC were scattered with the fully or partially filled elongated holes with polycrystalline α-Al_2O_3. Volume shrinkage resulting from the Ti_2AlC to TiC transformation induces cracks and stresses. Moreover, mismatched volume expansions between TiO_2 and Al_2O_3 during their mixed growth lead to an increase in the stress concentration.[24] Both these factors

provoke the cracking and splitting of the oxide layer on the surface of CG-Ti_2AlC samples, finally leading to the poor oxidation resistance of CG-Ti_2AlC samples.

By combining atomically resolved experiments and simulations, we propose a step-by-step scenario for the diffusion of Cu in Ti_2AlC MAX phase: (*i*) Replacement of Al by Cu diffusion, leading to the formation of atomic channels of solid solution, (*ii*) A-planes de-intercalation, leading to the formation of Frank partial dislocations, (*iii*) Volume shrinkage along the c-axis, leading to the formation of perfect TB in Ti_2C platelets, (*iv*) Minimization of the energy by a slide, leading to the formation of shifted TB in Ti_2C platelets. The formation of the Frank partial dislocation is of particular importance. At high temperatures, *a*-dislocations cross-slip onto non-basal glide planes and are of prime importance in the plasticity of MAX phases, particularly as an origin of their brittle-to-ductile transition[35]. To date, *c* and *a*+*c* dislocations have been considered as impossible dislocation types for energetic reasons[43, 44]. These results surprisingly evidenced the formation of *c* dislocations within the basal planes. Such sessile *c* dislocations confined in the basal plane will hinder the motion of *a*-type dislocations that are responsible for the plasticity, more precisely for the formation of kink bands.

References

[1] M. Shamma, E.I.N. Caspi, B. Anasori, B. Clausen, D.W. Brown, S.C. Vogel, V. Presser, S. Amini, O. Yeheskel, M.W. Barsoum, In situ neutron diffraction evidence for fully reversible dislocation motion in highly textured polycrystalline Ti_2AlC samples, Acta Materialia 98 (2015) 51-63.
[2] V. Mauchamp, W. Yu, L. Gence, L. Piraux, T. Cabioc'h, V. Gauthier, P. Eklund, S. Dubois, Anisotropy of the resistivity and charge-carrier sign in nanolaminated Ti_2AlC: Experiment and ab initio calculations, Physical Review B 87(23) (2013) 235105.
[3] A. Zhou, M.W. Barsoum, S. Basu, S.R. Kalidindi, T. El-Raghy, Incipient and regular kink bands in fully dense and 10 vol.% porous Ti_2AlC, Acta Materialia 54(6) (2006) 1631-1639.
[4] M. Radovic, M.W. Barsoum, A. Ganguly, T. Zhen, P. Finkel, S.R. Kalidindi, E. Lara-Curzio, On the elastic properties and mechanical damping of Ti_3SiC_2, Ti_3GeC_2, $Ti_3Si_{0.5}Al_{0.5}C_2$ and Ti_2AlC in the 300-1573K temperature range, Acta Materialia 54(10) (2006) 2757-2767.
[5] H. Yang, Y. Pei, J. Rao, J.T.M. De Hosson, S.B. Li, G.M. Song, High temperature healing of Ti_2AlC: On the origin of inhomogeneous oxide scale, Scripta Materialia 65(2) (2011) 135-138.

[6] H. Yang, Y. Pei, J.T.M. De Hosson, Oxide-scale growth on Cr_2AlC ceramic and its consequence for self-healing, Scripta Materialia 69(2) (2013) 203-206.
[7] S. Li, G. Song, K. Kwakernaak, S. van der Zwaag, W.G. Sloof, Multiple crack healing of a Ti_2AlC ceramic, Journal of the European Ceramic Society 32(8) (2012) 1813-1820.
[8] A.S. Farle, C. Kwakernaak, S. van der Zwaag, W.G. Sloof, A conceptual study into the potential of $M_{n+1}AX_n$ phase ceramics for self-healing of crack damage, Journal of the European Ceramic Society 35(1) (2015) 37-45.
[9] W.G. Sloof, R. Pei, S.A. Mcdonald, J.L. Fife, L. Shen, L. Boatemaa, A.S. Farle, K. Yan, X. Zhang, S.V.D. Zwaag, Repeated crack healing in MAX-phase ceramics revealed by 4D in situ synchrotron X-ray tomographic microscopy, Sci Rep 6 (2016) 23040.
[10] H.J. Yang, Y.T. Pei, G.M. Song, J.T.M. De Hosson, Healing performance of Ti_2AlC ceramic studied with in situ microcantilever bending, Journal of the European Ceramic Society 33(2) (2013) 383-391.
[11] M.W. Barsoum, M. Radovic, Elastic and Mechanical Properties of the MAX Phases, Annual Review of Materials Research 41(41) (2011) 195-227.
[12] A. Ganguly, M.W. Barsoum, R.D. Doherty, Interdiffusion Between Ti_3SiC_2-Ti_3GeC_2 and Ti_2 AlC-Nb_2AlC Diffusion Couples, Journal of the American Ceramic Society 90(7) (2007) 2200-2204.
[13] H.J. Yang, Y.T. Pei, J.C. Rao, J.T.M. De Hosson, Self-healing performance of Ti_2AlC ceramic, Journal of Materials Chemistry 22(17) (2012) 8304-8313.
[14] D.J. Tallman, B. Anasori, M.W. Barsoum, A Critical Review of the Oxidation of Ti_2AlC, $Ti_3AlC_2$and Cr_2AlC in Air, Materials Research Letters 1(3) (2013) 115-125.
[15] B. Cui, D.D. Jayaseelan, W.E. Lee, Microstructural evolution during high temperature oxidation of Ti_2AlC ceramics, Acta Materialia 59(10) (2011) 4116-4125.
[16] X.Wang, Y.C.Zhou, Layered Machinable and Electrically Conductive Ti_2AlC and Ti_3AlC_2 Ceramics a Review, Journal of materials science and technology 26(5) (2010) 385-416.
[17] L. Xu, D. Zhu, Y. Liu, T.S. Suzuki, B.n. Kim, Y. Sakka, S. Grasso, C. Hu, Effect of texture on oxidation resistance of Ti_3AlC_2, Journal of the European Ceramic Society 38(10) (2018) 3417-3423.
[18] H.B. Zhang, C.F. Hu, K. Sato, S. Grasso, M. Estili, S.Q. Guo, K. Morita, H. Yoshida, T. Nishimura, T.S. Suzuki, M.W. Barsoum, B.N. Kim, Y. Sakka, Tailoring Ti_3AlC_2 ceramic with high anisotropic physical

and mechanical properties, Journal of the European Ceramic Society 35(1) (2015) 393-397.
[19] X.H. Wang, Y.C. Zhou, High Temperature Oxidation Behavior of Ti_2AlC in Air, Journal of Materials Research 17(11) (2002) 2974-2981.
[20] S. Basu, N. Obando, A. Gowdy, I. Karaman, M. Radovic, Long-Term Oxidation of Ti_2AlC in Air and Water Vapor at 1000-1300 °C Temperature Range, Journal of the Electrochemical Society 159(5) (2012) S9.
[21] BARSOUM, W. M, Oxidation of $Ti_{n+1}AlX_n$ (n = 1-3 and X = C, N). I. Model, Journal of the Electrochemical Society 148(8) (2001) B234-B239.
[22] M. Barsoum, N. Tzenov, A. Procopio, T. El-Raghy, M. Ali, Oxidation of $Ti_{n+1}AlX_n$ (n= 1-3 and X= C, N). II. Experimental Results, Journal of The Electrochemical Society 148(8) (2001) C551-C562.
[23] J.C. Rao, Y.T. Pei, H.J. Yang, G.M. Song, S.B. Li, J.T.M. De Hosson, TEM study of the initial oxide scales of Ti_2AlC, Acta Materialia 59(13) (2011) 5216-5223.
[24] D.B. Lee, S.W. Park, High-temperature oxidation of Ti_3AlC_2 between 1173 and 1473K in air, Materials Science and Engineering: A 434(1-2) (2006) 147-154.
[25] J. Wang, Y. Zhou, T. Liao, J. Zhang, Z. Lin, A first-principles investigation of the phase stability of Ti_2AlC with Al vacancies, Scripta Materialia 58(3) (2008) 227-230.
[26] M.W. Barsoum, The $M_{n+1}AX_n$ phases: A new class of solids: Thermodynamically stable nanolaminates, Progress in Solid State Chemistry 28(1) (2000) 201-281.
[27] J. Zhang, J.Y. Wang, Y.C. Zhou, Structure stability of Ti_3AlC_2 in Cu and microstructure evolution of $CuTi_3AlC_2$ composites, Acta Materialia 55(13) (2007) 4381-4390.
[28] S.B. Lee, Y.M. Kim, Direct observation of in-plane ordering in the liquid at a liquid Al/α-Al_2O_3 interface, Acta Materialia 59(4) (2011) 1383-1388.
[29] M. Dahlqvist, B. Alling, I.A. Abrikosov, J. Rosen, Phase Stability of Ti_2AlC Upon Oxygen Incorporation: A First-Principles Investigation, Physical Review B 81(2) (2010) 024111.
[30] Z.J. Lin, M.J. Zhuo, Y.C. Zhou, M.S. Li, J.Y. Wang, Microstructural characterization of layered ternary Ti_2AlC, Acta Materialia 54(4) (2006) 1009-1015.
[31] A. Guitton, A. Joulain, L. Thilly, C. Tromas, Dislocation analysis of Ti_2AlN deformed at room temperature under confining pressure, Philos. Mag 92(36) (2012) 4536-4546.

[32] G.P. Bei, A. Guitton, A. Joulain, V. Brunet, S. Dubois, L. Thilly, C. Tromas, Pressure enforced plasticity in MAX phases: from single grain to polycrystal investigation., Philos. Mag 92(36) (2012) 4536-4546.
[33] K. Gouriet, P. Carrez, P. Cordier, A. Guitton, A. Joulain, L. Thilly, C. Tromas, Dislocations modelling in Ti_2AlN MAX phase based on the Pierls Nabarro model, Philos. Mag. 95(23) (2015) 2539-2552.
[34] A. Guitton, S. Van Petegem, C. Tromas, A. Joulain, H. Van Swygenhoven, L. Thilly, Effect of microstructure anisotropy on the deformation of MAX polycrystals studied by in situ compression combined with neutron diffraction, Appl. Phys. Lett. 104(241910) (2014).
[35] A. Guitton, A. Joulain, L. Thilly, C. Tromas, Evidence of dislocation cross-slip in MAX phase deformed at high temperature, Sci. Rep. 4(6358) (2014).
[36] Y. Zhang, G.C. Wang, Y.M. He, Y. Sun, X.D. He, Effect of joining temperature and holding time on microstructure and shear strength of Ti_2AlC/Cu joints brazed using Ag-Cu filler alloy, Materials Science and Engineering: A 567 (2013) 58-64.
[37] J. Zhang, J.Y. Wang, Y.C. Zhou, Structure stability of Ti_3AlC_2 in Cu and microstructure evolution of $CuTi_3AlC_2$ composites, Acta Materialia 55 (2007) 4381-4390.
[38] M. Nechiche, V. Gauthier-Brunet, V. Mauchamp, A. Joulain, T. Cabioc'h, X. Milhet, P. Chartier, S. Dubois, Synthesis and characterization of a new $(Ti_{1-e},Cu_e)_3(Al,Cu)C_2$ MAX phase solid solution., Journal of the European Ceramic Society 37 (2017) 459-466.
[39] Y. Li, M. Li, J. Lu, B. Ma, Z. Wang, L.Z. Cheong, K. Luo, X. Zha, K. Chen, P.O.A. Persson, L. Hultman, P. Eklund, C. Shen, Q. Wang, J. Xue, S. Du, Z. Huang, Z. Chai, Q. Huang, Single-Atom-Thick Active Layers Realized in Nanolaminated $Ti_3(Al_xCu_{1-x})C_2$ and Its Artificial Enzyme Behavior, ACS Nano 13 (2019) 9198-9205.
[40] H. Ding, Y. Li, J. Lu, K. Luo, K. Chen, M. Li, P.O.A. Persson, L. Hultman, P. Eklund, S. Du, Z. Huang, Z. Chai, H. Wang, P. Huang, Q. Huang, Synthesis of MAX phases Nb_2CuC and $Ti_2(Al_{0.1}Cu_{0.9})N$ by A-site replacement reaction in molten salts, Materials Research Letters 7 (2019) 510-516.
[41] A. Joulain, L. Thilly, J. Rabier, Revisiting the defect structure of MAX phases: the case of Ti_4AlN_3, Philosophical Magazine 88 (2008) 1307-1320.
[42] L. Priester, Grain boundaries, From theory to engineering, Springer 2013.

[43] M.W. Barsoum, T. El-Raghy, The MAX Phases: Unique New Carbide and Nitride Materials: Ternary ceramics turn out to be surprisingly soft and machinable, yet also heat-tolerant, strong and lightweight, American Scientist 89 (2001) 334-343.
[44] M.W. Barsoum, T. Zhen, S.R. Kalidindi, M.W. Radovic, A. Murugaiah, Fully reversible, dislocation based compressive deformation of Ti_3SiC_2 to 1 GPa, Nature Materials 2 (2003) 107-111.

CHAPTER 6

MECHANICAL PROPERTIES OF MG COMPOSITES REINFORCED BY Ti_2AlC AND Ti_3SiC_2

6.1. Introduction

Magnesium alloy matrix composites (MMCs) are characterized by a low density, high specific strength and stiffness from room temperature to high temperatures, a superior wear resistance and damping capacity.[1, 2] The requirement of these high performance materials in aerospace and automobile industries has led to extensive investigations on MMCs, as well as cost-effective fabrication technologies.[3]

To date, apart from the traditionally ceramic particles (such as TiC[4, 5], SiC[6, 7] and AlN[8]), kinking nonlinear elastic (KNE) ternary Ti_2AlC and Ti_3SiC_2 MAX phases[9, 10] are scarcely used as MMCs reinforcement [11-13]. In previous reports, MAX phases have been introduced into different metal matrices to optimize their mechanical properties, e.g., Ti_3AlC_2–Cu[14], Ti_2AlC–Cr[15] and Ti_3AlC_2–Al[16] composites. Recently, Anasori et al. have reported that the fabricated Ti_2AlC/Mg composites are not only machinable, stiff and light, but also exhibit higher damping capabilities.[11, 17] In comparison with TiC reinforced Mg composites, the stronger interfacial bonding endows Ti_2AlC/Mg with better mechanical properties than TiC/Mg[11].

MAX phases contain more than 70 different species and A elements are easily out-diffused from MAX unit cell. For example, migration energy of Si in Ti_3SiC_2 (0.9 eV)[18, 19] is higher than that of Al in Ti_2AlC (0.83 eV). This means that it is possible to regulate the interfacial structure of MAX-Mg by replacing Ti_2AlC with Ti_3SiC_2. Furthermore, the formed nano Mg grains did not coarsen in Ti_2AlC-Mg composite under heating three times to 700 °C, while this phenomenon is not found in Ti_3SiC_2-Mg composite[20].

As the growth normal to the basal planes is about an order of magnitude smaller than that parallel to these planes, the configuration of MAX phases is generally characterized with different aspect ratios.[16]

Therefore, it is possible to regulate Ti_2AlC orientation by hot extrusion. For example, the elongated particles are perfectly oriented in magnesium and aluminum composites after the hot extrusion, such as SiC particles (aspect ratio = 2).[17,18] To date, no relevant results about texturing MAX reinforced metal composites have been reported. Only pure MAX phases were textured and characterized with exceptional anisotropic mechanical and physical properties. [19-22]

Concerning the Ti_2AlC/Mg MMCs fabrication methods, only melt infiltration and powder metallurgy methods have been reported for 50 vol.% Ti_2AlC/pure Mg or Mg alloy and 5-20 vol.% Ti_2AlC/pure Mg composites, respectively.[11] In comparison, stir casting is much more adaptable and economically applicable due to its low processing cost and high production rate. This process enables near-net-shape formation.[8, 21] In addition, the possible hypothesis is that the mechanical and physical properties of Ti_2AlC-Mg composite should be anisotropic if the Ti_2AlC orientation was textured in the Mg matrix.

6.2. As-cast Ti_2AlC/Mg and Ti_3SiC_2/Mg composites

6.2.1. Microstructural characterization

Fig. 6-1 (a)-(d) shows the SEM images of four composites with different Ti_2AlC volume fractions. The composites containing 5% and 10% Ti_2AlC show uniform particle distribution. However, with the increasing volume of reinforced particles, the agglomeration of Ti_2AlC particles appears in composites containing 15% and 20% Ti_2AlC, especially in 20%. Fig. 6-1 (e)-(f) reveals the morphologies of cast AZ91D and A10 under BSE mode. Fig. 6-1 (e) depicts distinguishable primary α-Mg and primary β-$Mg_{17}Al_{12}$ phases along the grain boundaries, and another high Al content eutectic α-Mg in primary β-$Mg_{17}Al_{12}$ phases.[22] Like the distribution of $Mg_{17}Al_{12}$, Fig. 6-1 (f) indicates that Ti_2AlC particles distribute along the primary α-Mg grain boundaries. Furthermore, the enlarged area in Fig. 6-1 (f) reveals that Ti_2AlC and $Mg_{17}Al_{12}$ could coexist together. The sharp and clear interface indicates no reaction between Ti_2AlC and $Mg_{17}Al_{12}$.

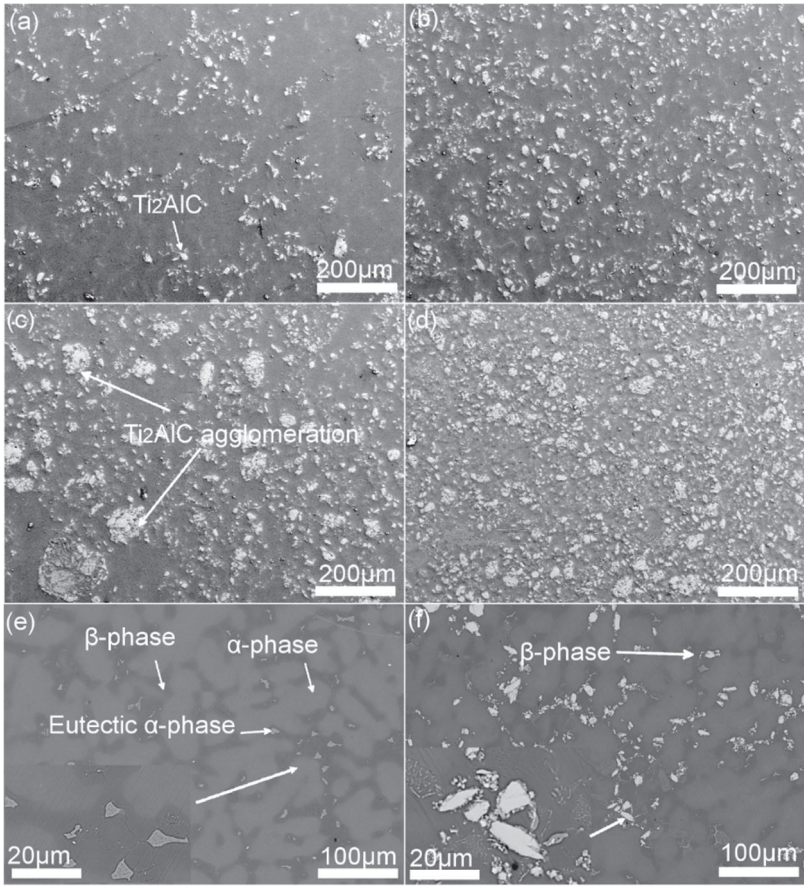

Fig. 6-1: The SEM images of the composites with different Ti_2AlC fractions (a) 5%, (b) 10%, (c) 15% and (d) 20% in SE mode; (e) cast AZ91D alloy and (f) 5% in BSE mode.

Fig. 6-2 shows the microstructure of the as-cast AZ91D alloy and composites reinforced with different MAX phases. As found in Fig. 6-2 (a)-(c), despite the introduction of Ti_3SiC_2 or Ti_2AlC, the composites present similar microstructures. MAX phases particles distribute along grain boundaries of the primary α-Mg phase and coexist with eutectic α (Mg) and β ($Mg_{17}Al_{12}$) phases. As previously observed on Ti_2AlC-AZ91D composite[23], when the introduction of Ti_3SiC_2 particles increased from 5

vol.% to 15 vol.%, the agglomeration of Ti_3SiC_2 particles appeared (Fig. 6-2 (d)).

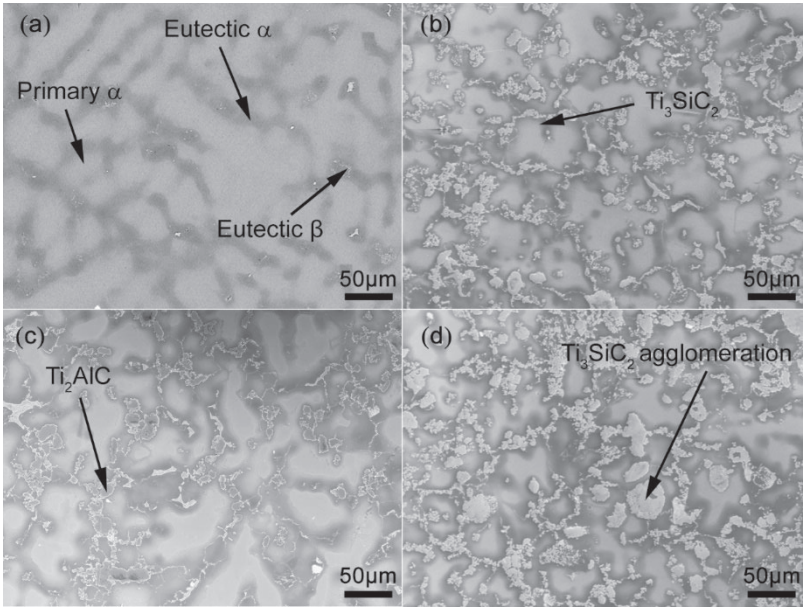

Fig. 6-2: Back-scattered electron (BSE) micrographs of (a) as-cast AZ91D alloy and the composites reinforced with (b) 5 vol.% Ti_3SiC_2, (c) 5 vol.% Ti_2AlC and (d) 15 vol.% Ti_3SiC_2.

The XRD analysis corresponding to Fig. 6-1 is given in Fig. 6-3 (b). It reveals that there is no detectable trace of impurities except Z91D (α-phase and β-phase) and Ti_2AlC. Furthermore, a region wherein Mg penetrated a pre-existing crack in a Ti_2AlC particle in a Mg-Ti_2AlC composite was imaged in the TEM (Fig. 6-7). This shows that Mg could penetrate into the submicron cracks among Ti_2AlC particles. The backscatter electron STEM micrograph (Fig. 6-8) confirms that no chemical reaction happens between Ti_2AlC and AZ91D. In addition, the enlarged area in Fig. 6-3 (b) indicates that the Mg peak shifted to a higher angle with increasing Ti_2AlC content in composites. Ti_2AlC particles segregated within dendritic α-Mg intergranular regions due to the "push" effect of the solidification front. During the solidification of MMS composites by stir casting, most particles are segregated in the intergranular regions during impingement with other growing grains.[24, 25] As no chemical reaction happens, the shift

of the Mg peak could be ascribed to the compressive force resulting from the restriction of dendritic α-Mg growth because of intergranular dispersed Ti_2AlC particles. Furthermore, the zone shown in Fig. 6-7 (c) was milled and the corresponding TEM images are given in Fig. 6-8. It reveals that the molten AZ91D can wet the Ti_2AlC. This result is similar to the previous report, where the molten Mg can wet the Ti_2AlC, especially in Mg-Al alloy.[12] In addition, submicron Mg grains were found among the Ti_2AlC particles, this was also found by the melt infiltration method.[12]

Fig. 6-3 shows the XRD diffractograms of Ti_3SiC_2-AZ91D and Ti_2AlC-AZ91D composites. No impurities were detected in either of the composites. The shift of Mg peak appeared for all of the Mg peaks. For example, it is clear that the Mg peak (103) at around 2θ of 48° continuously shifts with the increasing content of Ti_2AlC particles in Ti_2AlC-AZ91D composite, while it is much less clear in Ti_3SiC_2-AZ91D composite. During solidification, as most particles are segregated in the intergranular regions during impingement with other growing grains[24, 25], the growth of dendritic α-Mg is restricted and produces a compressive force. The difference between these two composites suggests that much higher compressive force formed around Mg grains with the increasing Ti_2AlC volume in Ti_2AlC-AZ91D composite.

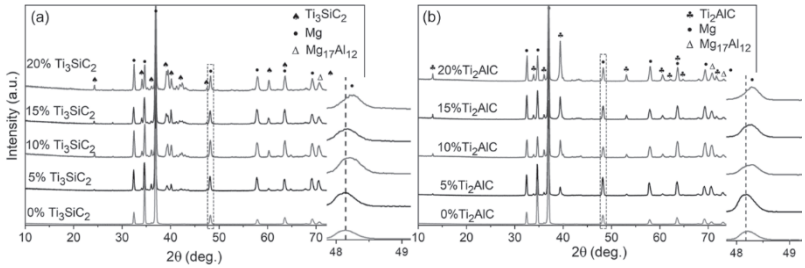

Fig. 6-3: XRD diffractograms of as-cast (a) Ti_3SiC_2-AZ91D and (b) Ti_2AlC-AZ91D[23] composites.

6.2.2. Different tensile fracture between Ti_2AlC/Mg and Ti_3SiC_2/Mg

Fig. 6-4 plots the room temperature tensile stress-strain curves of as-cast AZ91D and its composites reinforced by Ti_2AlC and Ti_3SiC_2. With the introduction of more MAX particles, the ductility of composites strongly decreased, especially for Ti_3SiC_2-AZ91D composites. The

composites reinforced with 15 vol.% and 20 vol.% Ti_3SiC_2 particles did not even reach the summit of yield strength before fracture. Table 6-1 summarizes the elastic moduli (E), tensile yield strength (YS), and ultimate tensile strength (UTS) values of the different specimens. For clarity, E and UTS values of the two composites are plotted as a function of reinforcement volume fraction (Fig. 6-5). E of both composites were continuously enhanced with the increasing content of reinforcement, especially in the case of Ti_3SiC_2. Such a result is considered to be the difference in E between Ti_2AlC (277 GPa)[26] and Ti_3SiC_2 (343 GPa)[27]. Regarding UTS, the UTS of AZ91D alloy is enhanced when 5 vol.% of Ti_2AlC or Ti_3SiC_2 MAX phase is introduced into magnesium alloy. Similar to the results found in Ti_2AlC-AZ91D composite[23], the addition of Ti_3SiC_2 could refine the grains of α-Mg and produce the Hall-Petch effect. The UTS of Ti_2AlC-AZ91D composites increases with the introduction of Ti_2AlC from 5 vol.% to 10 vol.%, then decreases with more introduction of Ti_2AlC. However, the UTS of Ti_3SiC_2-AZ91D continuously decreases with the increasing content of Ti_3SiC_2 volume fraction. In addition, the UTS of Ti_2AlC-AZ91D composite is higher than that of Ti_3SiC_2-AZ91D for each volume fraction. This phenomenon was also reported by Anasori et al.[28] who studied the MAX phases particles (50 vol.%) reinforced Mg composites fabricated by the pressureless melt infiltration method. In order to clarify this difference, the tensile fracture surface and interfacial evolution in these two composites were further explored in the following section.

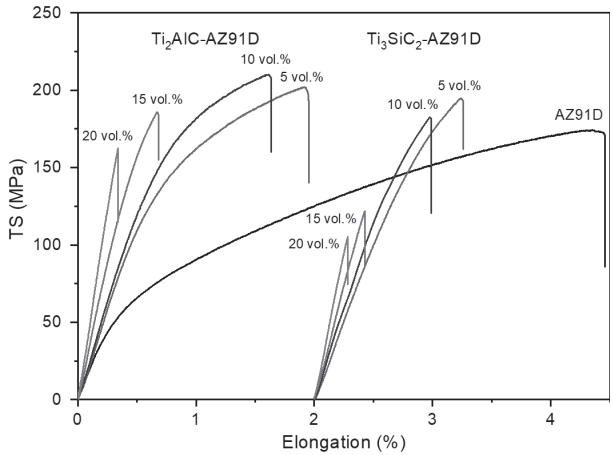

Fig. 6-4: The room temperature tensile stress-strain curves of the as-cast AZ91D and its composites reinforced by Ti_2AlC and Ti_3SiC_2.

Table 6-2: Mechanical properties of the as-cast AZ91D alloy and its composites reinforced by Ti_2AlC and Ti_3SiC_2, including Elasticity moduli (E), 0.2% yield strengths (YS), ultimate tensile strengths (UTS).

Materials	E (GPa)	YS (MPa)	UTS (MPa)	Reference
AZ91D	40 ± 1	70 ± 2	175 ± 5	this work
5 vol.% Ti_3SiC_2-AZ91D	46 ± 1	178 ± 3	195 ± 6	this work
10 vol.% Ti_3SiC_2-AZ91D	55 ± 1	173 ± 3	180 ± 6	this work
15 vol.% Ti_3SiC_2-AZ91D	66 ± 2	-	120 ± 4	this work
20 vol.% Ti_3SiC_2-AZ91D	76 ± 2	-	105 ± 4	this work
5 vol.%Ti_2AlC-AZ91D	52	108	200	[23]
10 vol.% Ti_2AlC-AZ91D	56	135	215	[23]
15 vol.%Ti_2AlC-AZ91D	62	145	185	[23]
20 vol.%Ti_2AlC-AZ91D	69	160	165	[23]

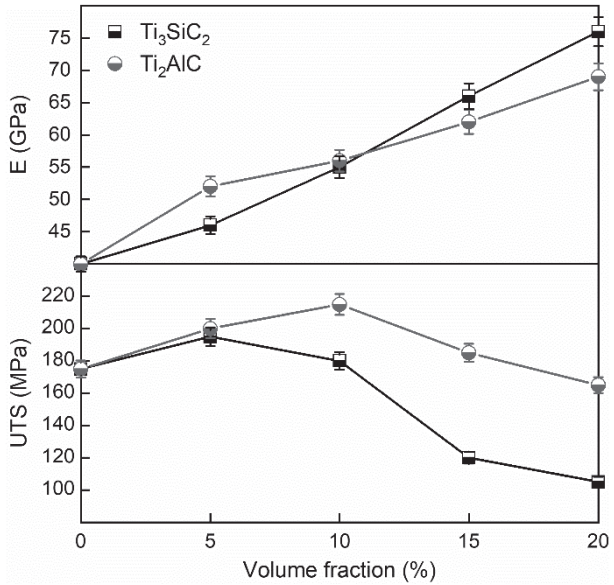

Fig. 6-5: Elasticity moduli (E) and ultimate tensile strengths (UTS) of Ti_3SiC_2-AZ91D and Ti_2AlC-AZ91D composites as a function of the reinforcement volume fraction.

Fig. 6-6 (a) and (b) show the tensile fracture morphologies of AZ91D composites reinforced by 5 vol.% and 15 vol.% Ti_3SiC_2. Tear edges in the Mg matrix are strongly reduced with the increasing content of Ti_3SiC_2 particles in the composites. However, as found in Fig. 6-6 (b) and (c), Ti_3SiC_2 and Ti_2AlC particles exhibit different fracture behaviors in MAX particles. The enlarged area shown in Fig. 6-6 (d) indicates that Ti_3SiC_2 particles are detached from the Mg matrix due to interfacial decohesion. However, no interfacial decohesion was observed in Ti_2AlC-AZ91D composite. In Fig. 6-6 (c), the clean and flat fracture surface of Ti_2AlC indicates that delamination occurred in Ti_2AlC particles.

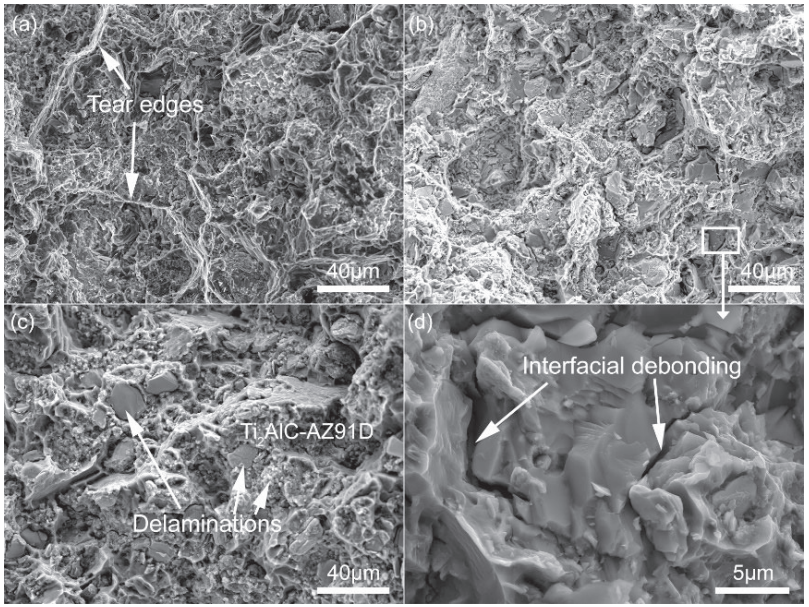

Fig. 6-6: Tensile fracture surfaces of the AZ91D composite reinforced with (a) 5 vol.% Ti_3SiC_2, (b, d) 15 vol.% Ti_3SiC_2 and (c) 15 vol.% Ti_2AlC.

6.2.3. Effects of A-site atoms in Ti_2AlC and Ti_3SiC_2 reinforced Mg composites

Fig. 6-7 presents the high-angle annular dark field (HAADF) micrographs of Ti_3SiC_2-AZ91D and Ti_2AlC-AZ91D interfaces. As shown in Fig. 6-7 (a) and (b), no nanometric Mg grains were found in the vicinity of Ti_3SiC_2 particles. However, Fig. 6-7 (c) and (d) reveal the formation of nanometric Mg grains among Ti_2AlC particles. This agrees with the results reported by Amini et al.[29]. In addition, different contrasts can be observed in the Mg matrix among Ti_2AlC particles. Fig. 6-8 shows the magnified area marked in Fig. 6-7 (c). Close to the interface, the nano Mg grains become smaller. The corresponding diffraction patterns of selected areas confirmed this phenomenon. The polycrystalline rings were found in regions 2 and 3, especially in region 2. This indicates that finer polycrystalline magnesium tends to form on the Ti_2AlC surface. As the formation of nano-sized Mg grains among Ti_2AlC particles could strongly strengthen the metal matrix due to the Hall-Petch effect[29-31], the UTS of Ti_2AlC-AZ91D composite is higher than that of Ti_3SiC_2-AZ91D for each volume fraction.

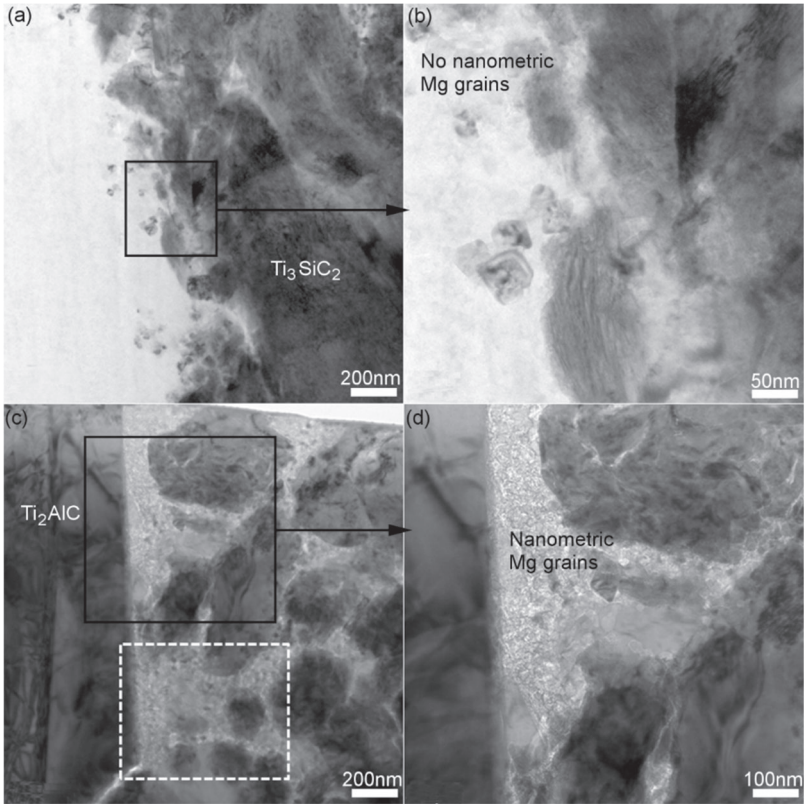

Fig. 6-7: HAADF micrographs of (a, b) Ti_3SiC_2-AZ91D and (c, d) Ti_2AlC-AZ91D interfaces.

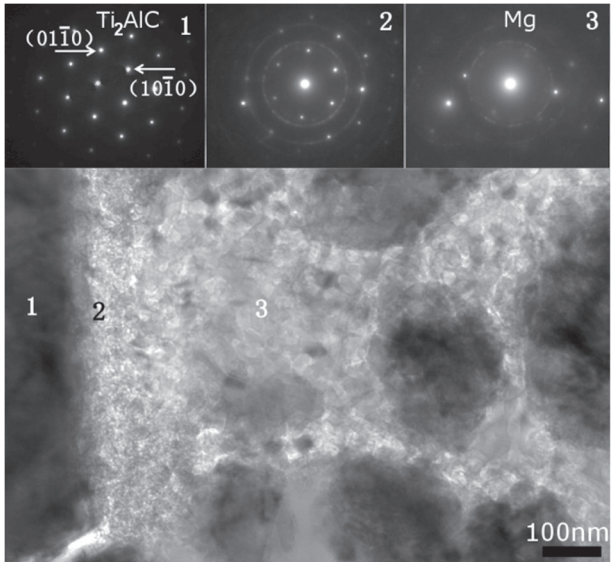

Fig. 6-8: Enlarged area marked with a dotted box in Fig. 6-7 (c) and Selected Area Electron Diffraction patterns of the zones marked as 1, 2 and 3.

Fig. 6-9 shows images taken close to the interfaces of the composites accompanied with the corresponding elemental EDX maps of Ti, Al and Si. Fig. 6-9 (b)-(c) show that maps of Ti and Si exhibit identical distribution in Ti_3SiC_2-AZ91D composite. However, Fig. 6-9 (f)-(g) indicate that the Al zone is much bigger than that of Ti in the Ti_2AlC-AZ91D composite. The Al distribution in Fig. 6-9 (g) suggests that Al atoms in Ti_2AlC outwards diffused into the AZ91D magnesium matrix. Finally, nano Mg grains formed among Ti_2AlC particles. In addition, the out-diffusion of Al atoms may result in the formation of a thin amorphous magnesium layer between Ti_2AlC and nano Mg grains. This robust amorphous layer was respectively found by Yu et al.[32] and Amini et al.[29]. Khoddam et al. pointed that the robust amorphous layer could reduce the interfacial energy of an incoherent interface due to large lattice mismatch and therefore promote the interfacial bonding strength[33]. Hence, interfacial decohesion happens in Ti_3SiC_2-AZ91D composite, while it is not found in Ti_2AlC-AZ91D composite.

This difference may be caused by the difference in solubility between Al and Si in the magnesium matrix or by the different migration energy between Al and Si in MAX phases. First-principles calculations show that the migration energy of Al in Ti_2AlC (0.83 eV) is lower than that of Si in

Ti_3SiC_2 (0.9 eV)[18, 19], which indicates that out-diffusion of Si from Ti_3SiC_2 is much harder than Al from Ti_2AlC under the same conditions. It has been experimentally proven that the ratio between Al and Si in $Ti_3(Si_{1-x}Al_x)C_2$ solid solution can be arbitrarily regulated[34]. This means that it could be possible to control the interface bonding strength between the Ti_3SiC_2 and Mg matrix with the formation of $Ti_3(Si_{1-x}Al_x)C_2$ solid solution.

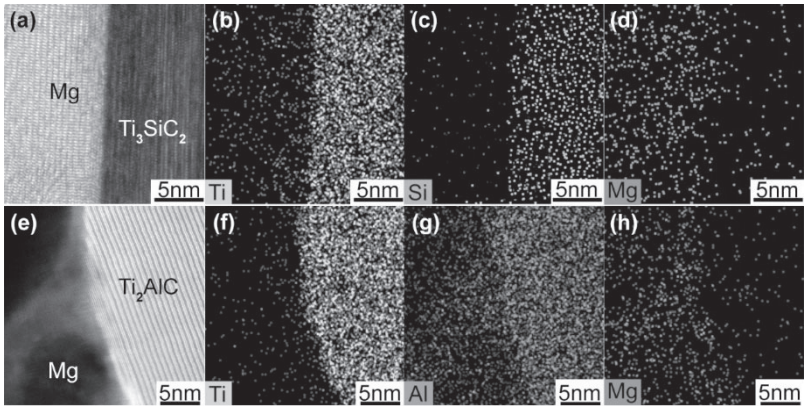

Fig. 6-9: HAADF-STEM images of the interfaces and the corresponding EDX maps of Ti_3SiC_2 (a-d) and Ti_2AlC (e-h) interfaces.

6.2.4. In situ tensile fracture behavior of as-cast Ti_2AlC/Mg

In order to compare the experimental results of the composites with the theoretical evaluations of elastic modulus, the means of the mixture rule expression (equation (6-1)), the Halpin-Tsai equation[35] (equation (6-2) and (6-3)) and the Hashin and Shtrickman equation (equation (6-4))[1] were adopted:

$$E_c = E_m V_m + E_r V_r \qquad (6-1)$$

$$E_c = \frac{E_m(1 + 2sqV_r)}{1 - qV_r} \qquad (6-2)$$

$$q = \frac{E_r/E_m - 1}{E_r/E_m + 2s} \qquad (6-3)$$

$$E_c = E_m * \frac{E_m V_m + E_r(V_r + 1)}{E_r V_m + E_m(V_r + 1)} \qquad (6-4)$$

where E_c = elastic modulus of composite (GPa), given the E of Ti_2AlC is

278 GPa[36]. V_m = % volumetric matrix, V_r = % volumetric reinforcement, E_m = matrix modulus (GPa), E_r = reinforcement modulus (GPa), s = aspect ratio.

The measurements of elastic modulus, as well as the values from mixture rules, Hashin–Shtrickman, and Halpin-Tsai equations for different aspect ratios are shown in Fig. 6-10. The mixture rule is generally used for continuous fiber-reinforced composites. Usually, the Halpin-Tsai model is a mathematical model for the prediction of elasticity of composite material based on the geometry and orientation of the reinforcement and the elastic properties of the reinforcement and matrix. Several aspect ratios were adopted in order to observe the effect of the aspect of the reinforcement. The best results were obtained for an aspect ratio of 3.

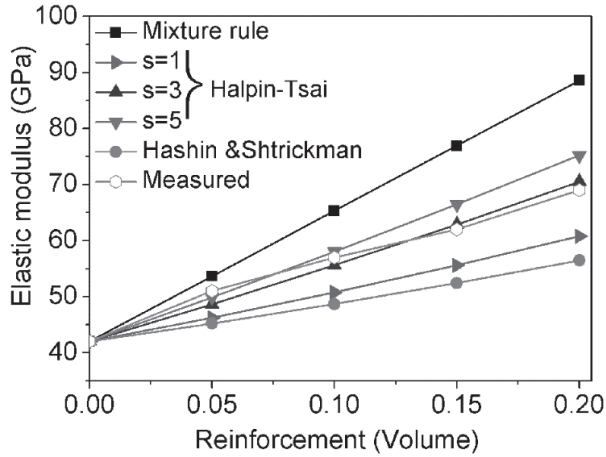

Fig. 6-10: Elastic modulus results as a function of the volume fraction of reinforcement.

Fig. 6-11 presents the curve of applied load as a function of displacement of the A5 composite. The aslant discontinuous tails of the line are related to the several interruptions performed during the mechanical test for the purpose of capturing the constantly changing morphology of the specimen.

Fig. 6-12 (a)-(h) represents the detailed deformation about crack initiation and propagation in Ti_2AlC reinforced AZ91D composite and corresponding to the interruption points of solid line indicated in Fig. 6-11. First, at the yielding point marked as “b”, no cracks were found. With increasing loads, one “spring curve” appears in tensile curve. Corresponding to the point “c-e” in Fig. 6-11, Fig. 6-12 (c)-(e) reveals some Ti_2AlC

particles broken into two parts. This may be caused by the shape and orientation of the Ti_2AlC particles. Meanwhile, no interfacial decohesion occurred between Ti_2AlC and AZ91D. After that, slipping bands appear in the vicinity of the Ti_2AlC-matrix interface. Due to the mismatch in CTE, some plastic deformation occurs in Mg-alloy matrices close to the interface leading to the nucleation of dislocations and concomitant strengthening.[11] As shown in Fig. 6-12 (g), the shearing deformation of the AZ91D matrix among the broken Ti_2AlC particles is clearly shown. Fig. 6-12 (h) reveals cracks propagated along grain boundaries where the $Mg_{17}Al_{12}$ (β-phase) exists, but not in the whole sheared Mg-alloy matrix interface. Finally, the tendency of the curve dropped at the end of the plateau because of the connection of cracks among the cracked Ti_2AlC particles. Contrary to SiC-Mg alloy where the interface decohesion was observed in SiC-Mg alloy[37, 38], here, the Ti_2AlC remains combined to the Mg matrix. It confirms that the Ti_2AlC and AZ91D have a strong interfacial bonding.

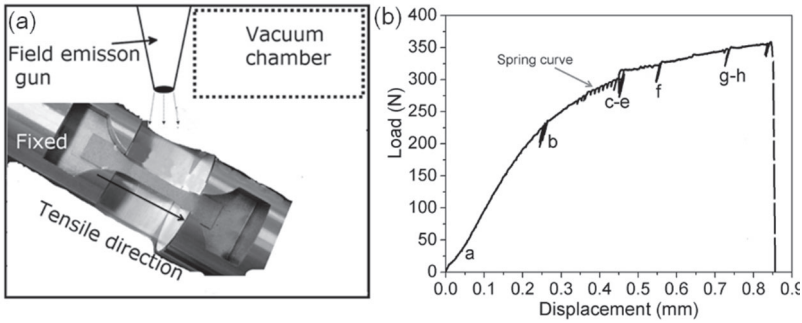

Fig. 6-11: (a) Configuration of in situ tensile test, (b) the typical tensile curves of 5%Ti_2AlC reinforced AZ91D.

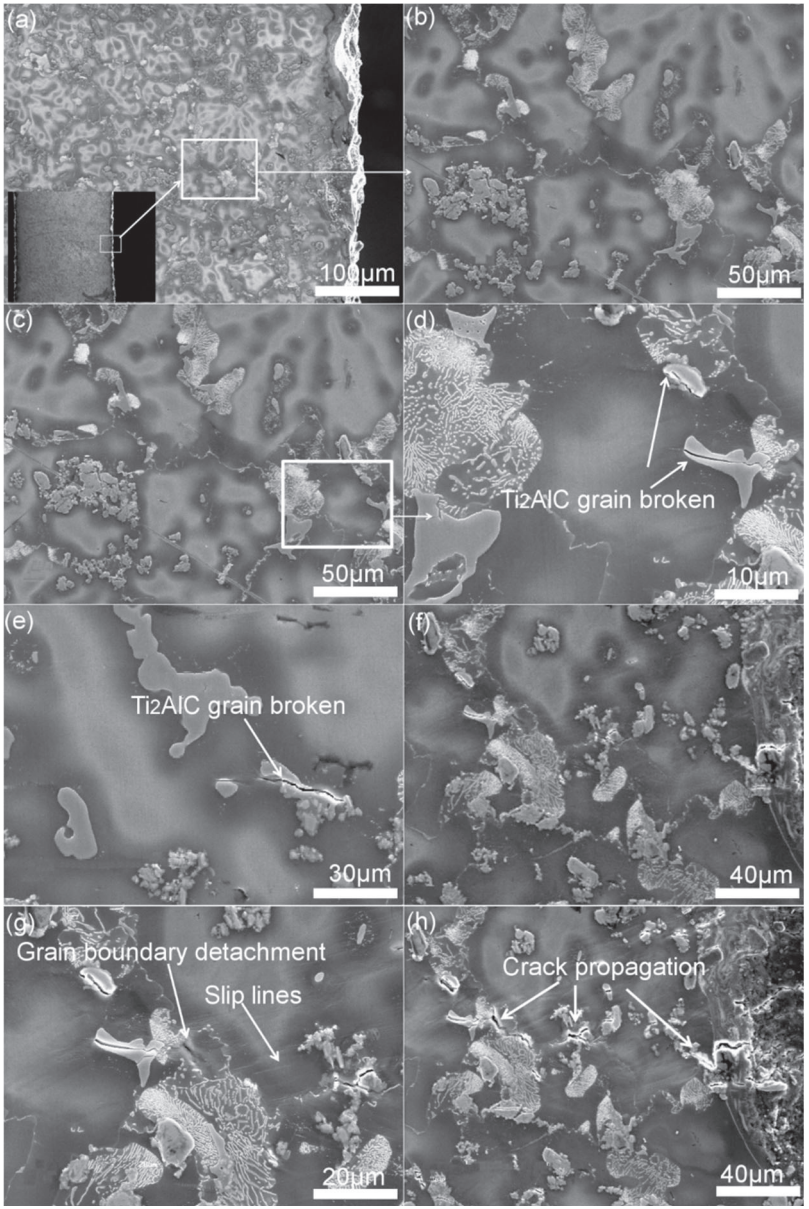

Fig. 6-12: (a-h) represents the detailed deformation morphologies of the specimen corresponding to the interruption noted on the solid line indicated in Fig. 6-11.

For the Ti_2AlC particles to fracture, they must be loaded to their fracture stress. This is achieved globally by the tensile stress and locally by shear loading through the interface. The extent of particle loading by the shear mechanism is dependent on the aspect ratio of the reinforcing particles. For the case of symmetrically packed particles in the metal matrix, the aspect ratio (S) for maximum loading is[39]:

$$S = \frac{\sigma_{Ti_2AlC}}{\tau_i} \qquad (6-5)$$

where σ_{Ti_2AlC} is the strength of the particle (above 1000MPa)[40] and τ_i is the interfacial shear strength.

With the aspect ratio (S=3) predicated by the Halpin-Tsai approach, we can predict the interfacial shear strength (about 330MPa). This value is higher than the UTS of fabricated composites (215MPa for A10), it is reasonable that no Ti_2AlC-AZ91D interface decohesion happened in this work. Finally, the cleaned delaminated Ti_2AlC surface was observed in Fig. 6-6.

6.2.5 Summary

Both Ti_3SiC_2 and Ti_2AlC (5, 10, 15, 20 vol.%) reinforced AZ91D magnesium composites were fabricated at 700 ℃ by the stir casting method and compared. As previously observed on Ti_2AlC-AZ91D composite[23], an agglomeration of particles occurred when the introduction of Ti_3SiC_2 particles is higher than 5 vol.%. A slight and continuous shift of the Mg peaks appears with the increasing content of Ti_2AlC particles due to the formation of nanometric Mg grains, while this phenomenon was not found in the case of Ti_3SiC_2-AZ91D composite.

Ti_3SiC_2 particles were detached from the Mg matrix due to the interfacial decohesion. However, no interfacial decohesion has been observed in the Ti_2AlC-AZ91D composite. Hence, the UTS of the Ti_3SiC_2-AZ91D composite is much lower than that of the Ti_2AlC-AZ91D composite. TEM analyses have revealed that the outwards diffusion of Al from Ti_2AlC into the Mg matrix aroused the formation of the thin amorphous magnesium and nano Mg grains among Ti_2AlC particles. In contrast, no outwards diffusion of Si from Ti_3SiC_2 into the Mg matrix was detected. This study suggests that it is possible to control the interface bonding strength between Ti_3SiC_2 and Mg matrix through the ratio design between Al and Si in $Ti_3(Si_{1-x}Al_x)C_2$ solid solution.

In situ observation reveals the cracks were initiated in Ti_2AlC particles and propagated along α-Mg grain boundaries. As the Ti_2AlC- AZ91D interfacial shear strength was predicated above 330MPa, no interfacial

decohesion occurred between Ti_2AlC and AZ91D. This behavior is different from the cases of SiC-AZ91D[37], SiC/Mg-6%Zn[38], TiC-Mg[11].

6.3. Hot extruded Ti_2AlC/Mg composites

6.3.1. Microstructural characterization

Fig. 6-13 represents the microstructure of the different specimens. In Fig. 6-13 (a), the as-cast Ti_2AlC-AZ91D composite consists of the white primary α-Mg phase, lamellar eutectic α phase, co-existed Ti_2AlC particles and gray β-$Mg_{17}Al_{12}$ phases distributed along the primaryα-Mg grain boundaries. After hot extrusion, from Fig. 6-13 (a) to Fig. 6-13 (e), the accumulated Ti_2AlCparticles along α-Mg grain boundaries are uniformly redistributed in the Mg matrix after hot extrusion. Some sub-micrometer Ti_2AlC particles even dispersed into the Mg grains. In addition, Fig. 6-13 (b)-(d) indicates that the small precipitates $Mg_{17}Al_{12}$ are distributed in α-Mg grains and at α-Mg grain boundaries for both parallel and perpendicular to the extruded axis. Generally, for AZ91D alloy, the eutectic α-Mg phase and β-$Mg_{17}Al_{12}$ phase disappear and the matrix transforms to supersaturated solid solution after solution treatment.[32] The non-coherent equilibrium phase $Mg_{17}Al_{12}$ would precipitate and is aligned parallel to the extruded axis after hot extrusion, as can be seen in Fig. 6-13 (e) and (f). This changed distribution of precipitates $Mg_{17}Al_{12}$ from extruded alloy to composite demonstrated that reinforced Ti_2AlC could strongly modify the $Mg_{17}Al_{12}$ precipitation and distribution during the hot extrusion process.

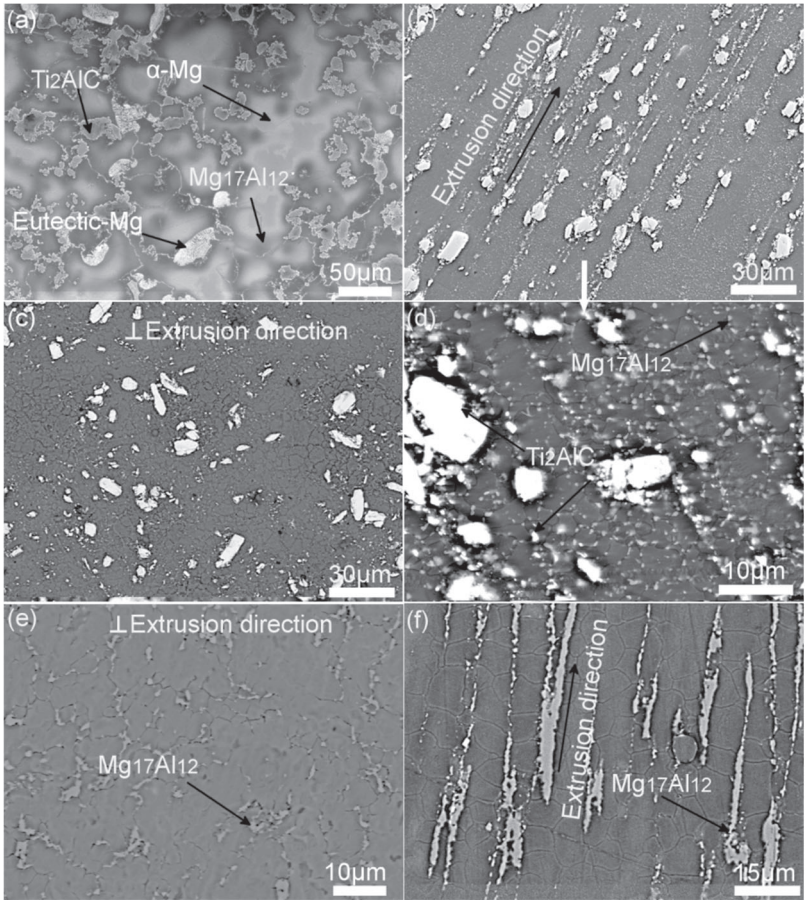

Fig. 6-13: The SEM images of 10 vol.% Ti_2AlC reinforced AZ91D composite: (a) as-cast and hot extruded (b) // ED and (c) ⊥ ED, hot extruded AZ91D alloy: (e) // ED and (f) ⊥ ED.

Fig. 6-14 (a) and (b) display the XRD analysis on AZ91D and Ti_2AlC-AZ91D composite before and after hot extrusion. Other phases except Ti_2AlC and AZ91D are not observed after hot extrusion, indicating that no chemical reaction happened. Like the extruded Mg or Mg-based composites[17], the changes in Mg diffraction peaks also indicate that a microstructural texture happened in AZ91D matrix during the hot extrusion process. This was also shown in microstructural morphologies

shown in Fig. 6-14 (c) and (d) of 3D-CT observations. Before extrusion, Ti_2AlC particles were randomly distributed in the AZ91D matrix without any preferential orientation. After extrusion, the Ti_2AlC particles were reoriented with their basal plane parallel to the extrusion direction.

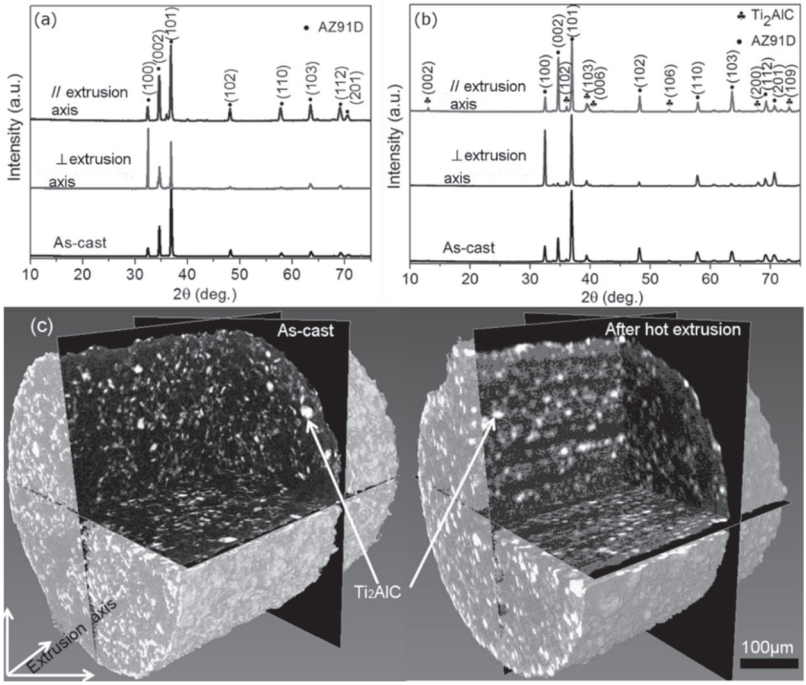

Fig. 6-14: (a) and (b) XRD pattern of AZ91D and 10%Ti_2AlC-AZ91D composite before and after hot extrusion; (c) and (d) CT observations on as-cast and textured Ti_2AlC-Mg composite.

6.3.2. Tensile properties

Fig. 6-15 plots the room temperature tensile stress-strain curves of the as-cast hot extruded composites (// ED axis). It is clear that hot extrusion could strongly optimize the tensile strength. Furthermore, distinctively different fracture surfaces of specimens after tensile test were found in Fig. 6-15 (b)-(c). Fig. 6-15 (b) reveals clear delamination of Ti_2AlC particles in the as-cast composite. However, // ED axis, Fig. 6-15 (c) indicates that Ti_2AlC-matrix interfacial decohesion occurred. This difference could be explained by the extent of particle loading related to the aspect ratio and

the reorientation of Ti_2AlC particles confirmed from our published XRD and 3-D reconstruction images[6]. Furthermore, due to the size and redistribution of $Mg_{17}Al_{12}$, some $Mg_{17}Al_{12}$ particles were found inside dimples in the fractured extruded composite while along grain boundaries in pure extruded AZ91D, as can be found in the inset of Fig. 6-15 (c) and Fig. 6-15 (d).

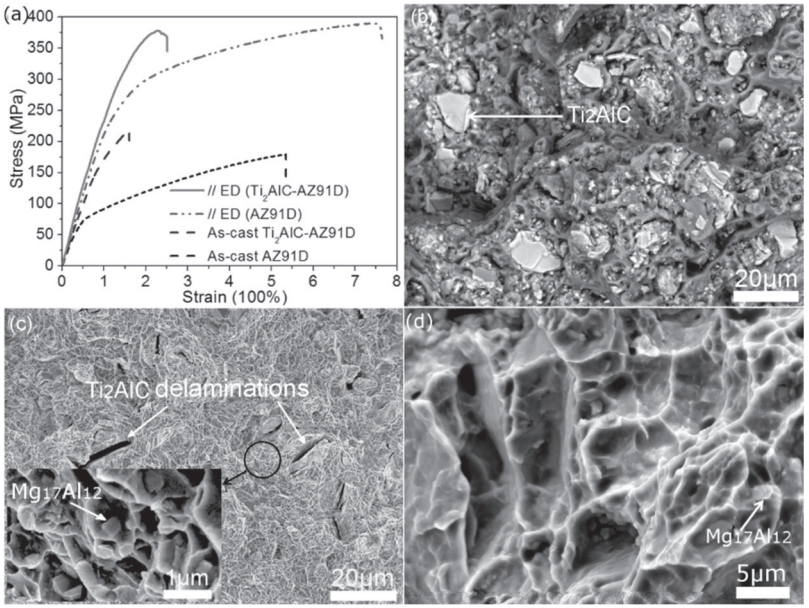

Fig. 6-15: (a) The room temperature tensile stress-strain curves of the specimens before and after hot extrusion; fracture surfaces: (b) as-cast and (c) extruded (// ED) of Ti_2AlC-AZ91D composite, (d) extruded AZ91D alloy (// ED).

The evolution of VH and YS is directly related to the capacity of the material to delay the dislocation motion. Three sources of dislocation mobility hindering are available[5]: the grain boundaries can be estimated through the Hall-Petch law(σ_{HP})[41], the presence of Ti_2AlC particles can be estimated from Orowan strengthening effect (σ_{Or}), and the thermal strain due to the mismatch of thermal coefficients (σ_{CTE}).

$$\sigma = \sigma_{\mathrm{Mg}} + \sigma_{Orowan} + \sigma_{\mathrm{Hall-petch}} + \sigma_{\mathrm{CTE}}$$
$$= \sigma_{\mathrm{Mg}} + M\frac{0.4Gb}{\pi\bar{\lambda}}\frac{Ln\left(\bar{d}/b\right)}{\sqrt{1-\nu_{Mg}}} + KD^{-0.5} + AMGb\left(\frac{12\sqrt{2}\Delta\alpha\Delta Tf}{bd(1-f)}\right)^{0.5} \qquad (6-5)$$

$$\bar{d} = d\sqrt{2/3} \qquad (6-6)$$

$$\bar{\lambda} = \bar{d}(\sqrt{\pi/4f} - 1) \qquad (6-7)$$

where, M is the mean orientation factor for Mg (6.5)[34], A is a constant of dislocation forest for Mg (0.2)[34], G is the shear modulus of Mg (17.3 GPa)[35], b is the Burgers vector of Mg (3.21×10^{-10} m), D is average matrix grain size. d is average particle size of Ti_2AlC, v_{Mg} is the Poisson's ratio of Mg (0.35)[1], f is the volume fraction of Ti_2AlC, ΔT is temperature change during matrix solidification (assumed to be 475 °C), K is the constant value of the material (K = 280 for AZ91). CTE ($7.1 \pm 0.3\times10^{-6}$ K^{-1} and $10.5 \pm 0.5 \times 10^{-6}$ K^{-1} for a- and c- directions in Ti_2AlC, 26×10^{-6} K^{-1} for Mg)[9].

The contribution of grain size effect in composite was found as 114MPa through the Hall-Petch formula. After hot extrusion, some submicron Ti_2AlC particles (800nm) and $Mg_{17}Al_{12}$ precipitates (200nm) were redistributed into the Mg matrix from the state of accumulation along Mg grain boundaries. Due to these redistributed particles, residual dislocation loops may be formed around each particulate which gives resistance to the dislocation movement and could lead to high work-hardening rates. This behavior was also confirmed from the $d\sigma/d\varepsilon - \varepsilon$ slope in the next compressive test. With the help of image plus software, the volume content of sub-micro Ti_2AlC and $Mg_{17}Al_{12}$ particles distributed in the Mg matrix was about 0.01and 0.03, respectively. Subsequently, the contribution of Ti_2AlC in σ_{Or} and σ_{CTE} was calculated respectively as 12MPa and 32MPa. The contribution of $Mg_{17}Al_{12}$ in σ_{Or} was calculated as 47 MPa. As can be seen from the plotted results in Fig. 6-16, the Hall-Petch strengthening effect is the most dominant. Furthermore, the effect of Orowan strengthening and mismatch thermal coefficient was also enhanced due to the optimized Ti_2AlC and $Mg_{17}Al_{12}$ redistribution through hot extrusion, especially for the Orowan strengthening effect. In the literature, it has been reported that Orowan strengthening is considered more favorable in the case of nanocomposites[36].

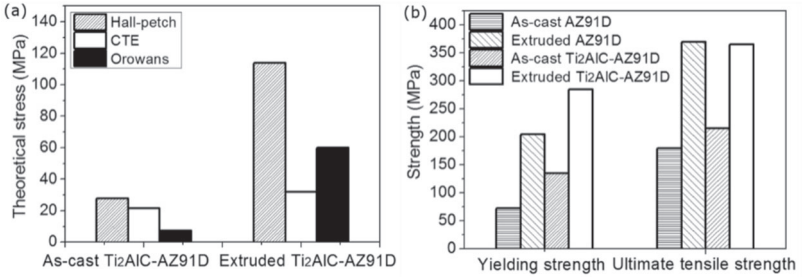

Fig. 6-16: As-cast and extruded 10 vol.% Ti_2AlC-AZ91D composite composites: (a) The calculated contribution of σ_{HP} σ_{CTE} and σ_{or} to the yield strength, (b) distribution of yield tensile strength and ultimate tensile strength.

6.3.3. Compressive properties

Fig. 6-17 (a) presents the compressive stress-strain curves obtained respectively from extruded AZ91D and Ti_2AlC-AZ91D composite. Like the previous report[37], hot extrusion could regulate the stress-strain behavior depending on the compressive axis, especially for extruded Ti_2AlC-AZ91D composites. In addition, the flow curves for C // ED specimens are characterized by a concave work-hardening region. Fig. 6-17 (b) shows the $d\sigma/d\varepsilon - \varepsilon$ slope relations derived from stress-strain curves. The Ti_2AlC-AZ91D specimen has a clearly higher strain hardening rate than the pure AZ91D specimen with respect to relevant directions. Due to the "pinning effect" of Ti_2AlC in the AZ9D matrix (grain boundaries and grains), the torn zone appeared above the Ti_2AlC in the glide direction, as shown in Fig. 6-17 (c), (d) and (e). The differences in fractographics indicate that the sub-micro Ti_2AlC particles appeared on shear bands in extruded specimens. This could highly strengthen the metal matrix and result in a higher strain hardening rate. Interestingly, in comparison with the other three cases, the $d\sigma/d\varepsilon - \varepsilon$ slope for C // ED Ti_2AlC-AZ91D characterized with a plateau once the strain hardening rate reached the peak. The differences between Fig. 6-17 (e) and (f) support the indications. The typical kink bands with very sharp radii of curvature and delamination of Ti_2AlC MAX phases were found in the C // ED specimen. In contrast, for the C $\perp$ ED specimen, some Ti_2AlC particles exhibited clear surfaces after the compression test.

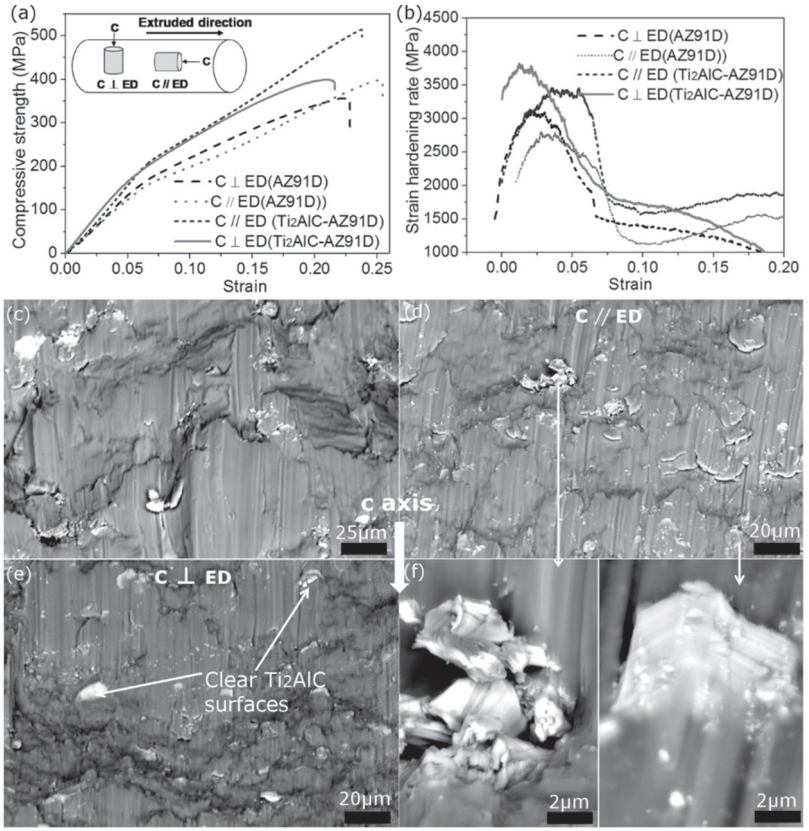

Fig. 6-17: (a) Compressive stress-strain curves obtained from four specimens at room temperature, (b) the $d\sigma/d\varepsilon - \varepsilon$ slope relations derived from stress-strain curves (a), (c), (d) and (e) fracture surfaces of the as-cast and hot extruded specimens.

To illustrate the different deformation behaviors of Ti_2AlC particles in // ED and ⊥ ED specimens, the crystal structure and orientation of Ti_2AlC MAX particles in regard to compressive force should be taken into consideration. As shown in Fig. 6-18 (a), in these so-called MAX phases, the $M_{n+1}X_n$ layers, characterized by mostly strong covalent M–X bonds, are interleaved with A layers through weaker M–A bonds. Due to their high c/a ratio and inherent nanolayered structure, the MAX phases are hugely plastically anisotropic in that dislocations are confined to the basal planes at all temperatures. Consequently, one of their more common

deformation modes is the formation of kink bands.[9,38-40] Fig. 6-18 (b) presents that the force distributed along the basal plane ($F \cdot \cos\theta$) is dependent on the angle between the compressive axis and the Ti_2AlC (0001) planes. In the case of the C // ED specimen, some Ti_2AlC particles with basal planes are inclined with compressive force, the slide happened among the basal planes, as shown in Fig. 6-18 (c). Differently, as Ti_2AlC basal planes were perfectly parallel with compressive force in the case of C ⊥ ED specimen, the plastic deformation in MAX phases occurs via delamination between basal planes and kink band formation.[9,10,41]

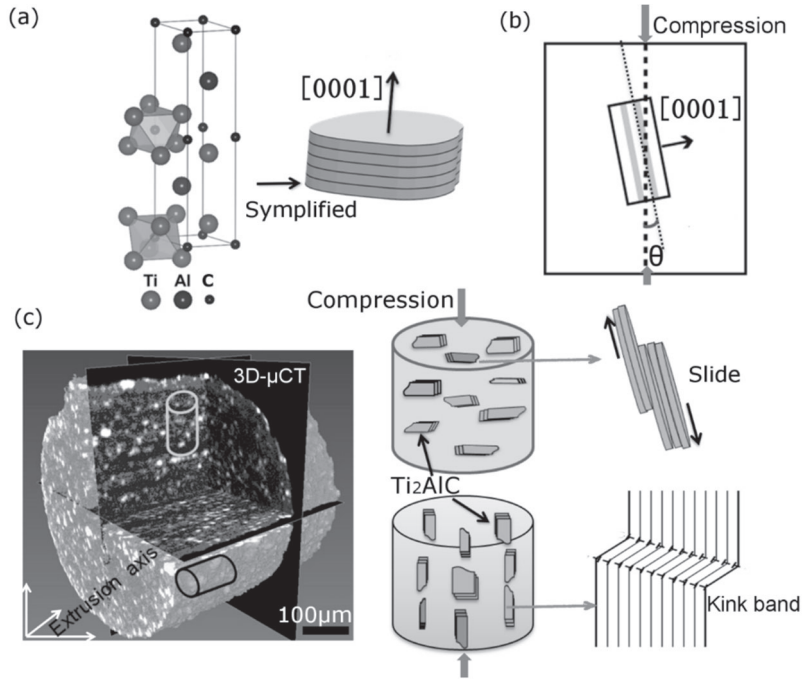

Fig. 6-18: (a) The reducible structure of Ti_2AlC particles, (b) the shear force in basal planes (0001) in regard to compressive force and the Ti_2AlC orientation, (c) schematic illustration of the deformation of Ti_2AlC particles in // ED and ⊥ ED specimens.

Table 6-2: The typical mechanical and physical properties of textured 10% Ti_2AlC-AZ91D and AZ91D.

Properties		10% Ti_2AlC-AZ91D		AZ91D	
		// ED axis	⊥ ED axis	// ED axis	⊥ ED axis
Yield tensile strength (MPa)		275±20	280±20	135±20	140±10
Ultimate tensile strength (MPa)		375±20	285±20	385±20	405±10
Ultimate compressive strength (MPa)		510±20	400±20	396±20	355±20
Electrical resistivity ($\mu\Omega$ cm^{-1} K^{-1})	300 K	21.18	22.25	18.21	17.68
	4K	0.19	0.39	0.85	1.4
RRR (R_{293K}/R_{77K})		5.75	5.33	7.16	6.08
$d\rho/dT$ ($\mu\Omega$ cm^{-1} K^{-1})		0.0796	0.0813	0.0695	0.0682
Thermal conductivity (W(m K^{-1})$^{-1}$)		70.08± 1.2	65.03± 1.2	72.21± 1.2	73.05± 1.2

6.3.4. Electrical resistivity

The resistivity variations as a function of temperature, ρ(T), for the different specimens is given in Fig. 6-19. By using Mathiessen's rule, one can extract the ideal resistivity (ρ_i) which is given by

$$\rho_i(T) = \rho(T) - \rho_0 \qquad (6-8)$$

where ρ(T) is the total resistivity of a crystalline material, $\rho_i(T)$ is the ideal resistivity which only depends on the electron-scattering mechanisms and is thus an intrinsic characteristic of the compound under study, ρ_0 is the residual resistivity (RR, resistivity of the material at low temperature) which only depends on electron scattering by defects and impurities.

It is clear that the extruded B10 composite has higher residual resistivity (RR) than the extruded AZ91D alloy. Fig. 6-1 evidences Mg grains became smaller with the introduction of Ti_2AlC in AZ91D alloy, which means the volume fraction of grain boundary increased. Furthermore, some nano Ti_2AlC and $Mg_{12}Al_{17}$ were found in the extruded composite, which could cause the large distortion of the Mg matrix and destroy the periodicity of the lattice. The grain boundary and distortion of the lattice were some of the scattering sources blocking the free movement of electrons. Therefore, the mean free path of electrons decreased and the residual resistivity increased.[42,43] Due to the reorientation of Ti_2AlC

particles, the cross section area fraction of Ti_2AlC along the ED axis is higher than that in the perpendicular direction to ED. In addition, the electrical conductivity of Ti_2AlC is lower than that of Mg. [23,25,43] Herein, like the results found in thermal conductivity, more electrical flux pass through Ti_2AlC phases and are retarded in ⊥ ED, rather than in the // ED axis.

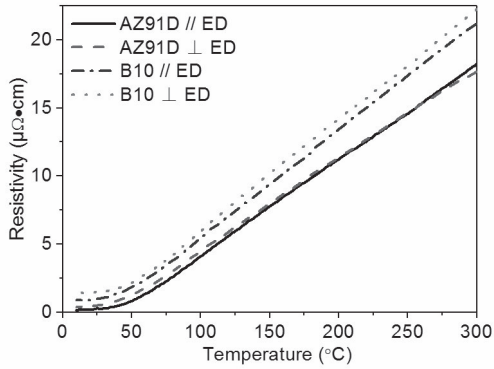

Fig. 6-19: Temperature dependence of the resistivity of extruded AZ91D alloy and 10% Ti_2AlC reinforced AZ91D composite (B10).

As ρ varies linearly with temperature in the range 100–300 K, one can calculate the slope of the ρ(T) curve (Table 6-2). Such a slope is representative of the intrinsic transport properties and should not depend on defects and impurity contents. In extruded AZ91D alloy, the slope of the ρ(T) curve in the direction parallel to the ED is higher than that perpendicular to ED. As most of the basal planes were parallel to the ED and atoms in the basal plane were the most close-packed in the Mg lattice, the electrons were more easily scattered in this direction by phonons.[42-44] In contrast, the slope of the ρ(T) curve in the direction parallel to the ED is lower than that perpendicular to the ED in the extruded composite. This difference can be explained by the same magnitude order in electrical resistivity between these two phases (Ti_2AlC and AZ91D alloy) and the anisotropy of Ti_2AlC MAX transport properties. The value of dρ/dT in the basal plane of Ti_2AlC is about 0.1 $\mu\Omega\ cm^{-1}\ K^{-1}$, whereas, the value perpendicular to the basal plane is 1.75 $\mu\Omega\ cm^{-1}\ K^{-1}$.[23] In addition, different from the values for no modification of RRR ($R293_K/R77_K$) found in the non-conductive alumina ceramic fibers reinforced AZ91D alloy[45], the changes in ratio RRR also proves that the introduction of Ti_2AlC into AZ91D alloy could modify its electrical properties.

6.4. Summary

With the introduction of Ti_2AlC particles in AZ91D alloy and hot extrusion, large scale dynamic recrystallization resulted in a fine matrix microstructure and nano-sized precipitates of $Mg_{17}Al_{12}$ dispersed in the composite. After tensile tests, clear delamination of Ti_2AlC particles was found in the ⊥ ED axis, while the Ti_2AlC-matrix interfacial decohesion occurred in the // ED axis. In the // ED axis, the values of yield tensile strength (YTS) and ultimate tensile strength (UTS) have been respectively enhanced by 103% and 74% in comparison with as-cast Ti_2AlC-AZ91D composites. The theoretical calculation on tensile yield strength reveals Hall-Petch strengthening and Orowan strengthening effects are predominant, followed by Forest strengthening. The Ultimate Compressive Strengths (UCS) of the composite were determined as 510 MPa (// ED axis) and 400 MPa (⊥ ED), whereas, the corresponding values were 396 MPa and 355 MPa for the extruded AZ91D alloy. Due to the Ti_2AlC orientation, the Ti_2AlC interlayer slide happened among the basal planes in C // ED specimen, while Ti_2AlC kink band behavior occured in the case of the C ⊥ ED specimen. As more thermal flux pass through Ti_2AlC phases and are retarded in the ⊥ ED, rather than in the // ED axis, the lower thermal conductivities of the composite were detected in the ⊥ ED specimen. Similar anisotropic phenomena were also found in electrical resistivity. Furthermore, in comparison with the extruded AZ91D alloy, the changes in $d\rho/dT$ and ratio RRR between // ED and ⊥ ED specimens confirm that Ti_2AlC does contribute to the AZ91 alloy to the scattering of the conductivity electrons.

References

[1] R. Couturier, D. Ducret, P. Merle, J. Disson, P. Joubert, Elaboration and characterization of a metal matrix composite: Al/AlN, Journal of the European Ceramic Society 17(15) (1997) 1861-1866.
[2] M. Mondet, E. Barraud, S. Lemonnier, J. Guyon, N. Allain, T. Grosdidier, Microstructure and mechanical properties of AZ91 magnesium alloy developed by Spark Plasma Sintering, Acta Materialia 119 (2016) 55-67.
[3] H. Friedrich, S. Schumann, Research for a “new age of magnesium” in the automotive industry, Journal of Materials Processing Technology 117(3) (2001) 276-281.
[4] L. Chen, Q. Dong, M. Zhao, J. Bi, N. Kanetake, Synthesis of TiC/Mg composites with interpenetrating networks by in situ reactive infiltration

process, Materials Science and Engineering: A 408(1) (2005) 125-130.
[5] G.K. Meenashisundaram, M. Gupta, Synthesis and characterization of high performance low volume fraction TiC reinforced Mg nanocomposites targeting biocompatible/structural applications, Materials Science and Engineering: A 627 (2015) 306-315.
[6] G. Cao, H. Konishi, X. Li, Mechanical properties and microstructure of SiC-reinforced Mg-(2, 4) Al-1Si nanocomposites fabricated by ultrasonic cavitation based solidification processing, Materials Science and Engineering: A 486(1) (2008) 357-362.
[7] K. Deng, K. Wu, Y. Wu, K. Nie, M. Zheng, Effect of submicron size SiC particulates on microstructure and mechanical properties of AZ91 magnesium matrix composites, Journal of Alloys and Compounds 504(2) (2010) 542-547.
[8] E. Bedolla, J. Lemus-Ruiz, A. Contreras, Synthesis and characterization of Mg-AZ91/AlN composites, Materials & Design 38 (2012) 91-98.
[9] M. Barsoum, T. Zhen, S. Kalidindi, M. Radovic, A. Murugaiah, Fully reversible, dislocation-based compressive deformation of Ti_3SiC_2 to 1 GPa, Nature Materials 2(2) (2003) 107-111.
[10] M.W. Barsoum, A. Murugaiah, S.R. Kalidindi, T. Zhen, Kinking nonlinear elastic solids, nanoindentations, and geology, Physical review letters 92(25) (2004) 255508.
[11] B. Anasori, E.a.N. Caspi, M.W. Barsoum, Fabrication and mechanical properties of pressureless melt infiltrated magnesium alloy composites reinforced with TiC and Ti_2AlC particles, Materials Science and Engineering: A 618 (2014) 511-522.
[12] S. Amini, C. Ni, M.W. Barsoum, Processing, microstructural characterization and mechanical properties of a Ti_2AlC/nanocrystalline Mg-matrix composite, Composites Science and Technology 69(3–4) (2009) 414-420.
[13] A. Kontsos, T. Loutas, V. Kostopoulos, K. Hazeli, B. Anasori, M.W. Barsoum, Nanocrystalline Mg–MAX composites: Mechanical behavior characterization via acoustic emission monitoring, Acta Materialia 59(14) (2011) 5716-5727.
[14] Z. Huang, J. Bonneville, H. Zhai, V. Gauthier-Brunet, S. Dubois, Microstructural characterization and compression properties of $TiC_{0.61}$/Cu (Al) composite synthesized from Cu and Ti_3AlC_2 powders, Journal of Alloys and Compounds 602 (2014) 53-57.
[15] S. Gupta, D. Filimonov, V. Zaitsev, T. Palanisamy, M.W. Barsoum, Ambient and 550 °C tribological behavior of select MAX phases against Ni-based superalloys, Wear 264(3–4) (2008) 270-278.

[16] W. Wang, V. Gauthier-Brunet, G. Bei, G. Laplanche, J. Bonneville, A. Joulain, S. Dubois, Powder metallurgy processing and compressive properties of Ti_3AlC_2/Al composites, Materials Science and Engineering: A 530 (2011) 168-173.
[17] B. Anasori, M.W. Barsoum, Energy damping in magnesium alloy composites reinforced with TiC or Ti_2AlC particles, Materials Science and Engineering: A 653 (2016) 53-62.
[18] J. Wang, Y. Zhou, T. Liao, J. Zhang, Z. Lin, A first-principles investigation of the phase stability of Ti_2AlC with Al vacancies, Scripta Materialia 58(3) (2008) 227-230.
[19] H. Wang, H. Han, G. Yin, C. Wang, Y. Hou, J. Tang, J. Dai, C. Ren, W. Zhang, P. Huai, First-Principles Study of Vacancies in Ti_3SiC_2 and Ti_3AlC_2, Materials (Basel, Switzerland) 10(2) (2017) 103.
[20] S. Amini, J.M. Córdoba Gallego, L. Daemen, A.R. McGhie, C. Ni, L. Hultman, M. Oden, M.W. Barsoum, On the stability of Mg nanograins to coarsening after repeated melting, Nano letters 9(8) (2009) 3082-3086.
[21] A. Martin, J. Llorca, Mechanical behaviour and failure mechanisms of a binary Mg-6%Zn alloy reinforced with SiC particulates, Materials Science and Engineering: A 201(1) (1995) 77-87.
[22] A.K. Dahle, Y.C. Lee, M.D. Nave, P.L. Schaffer, D.H. StJohn, Development of the as-cast microstructure in magnesium–aluminium alloys, Journal of light metals 1(1) (2001) 61-72.
[23] W. Yu, X. Wang, H. Zhao, C. Ding, Z. Huang, H. Zhai, Z. Guo, S. Xiong, Microstructure, mechanical properties and fracture mechanism of Ti_2AlC reinforced AZ91D composites fabricated by stir casting, Journal of Alloys and Compounds 702 (2017) 199-208.
[24] J. Hashim, L. Looney, M. Hashmi, Metal matrix composites: production by the stir casting method, Journal of Materials Processing Technology 92 (1999) 1-7.
[25] J. Hashim, L. Looney, M. Hashmi, Particle distribution in cast metal matrix composites—Part I, Journal of Materials Processing Technology 123(2) (2002) 251-257.
[26] M.W. Barsoum, M. Ali, T. El-Raghy, Processing and characterization of Ti_2AlC, Ti_2AlN and $Ti_2AlC_{0.5}N_{0.5}$, Metallurgical and Materials Transactions A 31 (2000) 1857-1865.
[27] M. Radovic, M.W. Barsoum, A. Ganguly, T. Zhen, P. Finkel, S.R. Kalidindi, E. Lara-Curzio, On the elastic properties and mechanical damping of Ti_3SiC_2, Ti_3GeC_2, $Ti_3Si_{0.5}Al_{0.5}C_2$ and Ti_2AlC in the 300–1573K temperature range, Acta Materialia 54(10) (2006) 2757-2767.
[28] B. Anasori, N.C. El'ad, M.W. Barsoum, Fabrication and mechanical properties of pressureless melt infiltrated magnesium alloy composites

reinforced with TiC and Ti_2AlC particles, Materials Science and Engineering: A 618 (2014) 511-522.
[29] S. Amini, C. Ni, M.W. Barsoum, Processing, microstructural characterization and mechanical properties of a Ti_2AlC/nanocrystalline Mg-matrix composite, Composites Science and Technology 69(3-4) (2009) 414-420.
[30] A. Sanaty-Zadeh, Comparison between current models for the strength of particulate-reinforced metal matrix nanocomposites with emphasis on consideration of Hall–Petch effect, Materials Science and Engineering: A 531 (2012) 112-118.
[31] L. Tian, L. Li, A Review on the Strengthening of Nanostructured Materials, International Journal of Current Engineering and Technology 8(2) (2018) 236-249.
[32] W. Yu, D. Chen, L. Tian, H. Zhao, X. Wang, Self-lubricate and anisotropic wear behavior of AZ91D magnesium alloy reinforced with ternary Ti_2AlC MAX phases, Journal of Materials Science & Technology 35(3) (2019) 275-284.
[33] S. Khoddam, L. Tian, T. Sapanathan, D. Hodgson Peter, A. Zarei-Hanzaki, Latest Developments in Modeling and Characterization of Joining Metal Based Hybrid Materials, Advanced Engineering Materials (2018).
[34] X. Xu, T.L. Ngai, Y. Li, Synthesis and characterization of quarternary $Ti_3Si_{(1-x)}Al_xC_2$ MAX phase materials, Ceramics International 41(6) (2015) 7626-7631.
[35] J.C. Halpin, Primer on Composite Materials: Analysis. Washington University, 1992.
[36] A.G. Zhou, M.W. Barsoum, S. Basu, S.R. Kalidindi, T. El-Raghy, Incipient and regular kink bands in fully dense and 10 vol.% porous Ti_2AlC, Acta Materialia 54(6) (2006) 1631-1639.
[37] X. Wang, K. Wu, W. Huang, H Zhang, M. Zheng, D. Peng, Study on fracture behavior of particulate reinforced magnesium matrix composite using in situ SEM, Composites Science and Technology 67(11–12) (2007) 2253-2260.
[38] B. Inem, G. Pollard, Interface structure and fractography of a magnesium-alloy, metal-matrix composite reinforced with SiC particles, Journal of Materials Science 28(16) (1993) 4427-4434.
[39] D.J. Lloyd, Aspects of fracture in particulate reinforced metal matrix composites, Acta Metallurgica et Materialia 39(1) (1991) 59-71.
[40] Y. Bai, X. He, C. Zhu, G. Chen, Microstructures, Electrical, Thermal, and Mechanical Properties of Bulk Ti_2AlC Synthesized by Self-Propagating High-Temperature Combustion Synthesis with Pseudo Hot

Isostatic Pressing, Journal of the American Ceramic Society 95(1) (2012) 358-364.
[41] M. Taya, R.J. Arsenault, Metal matrix composites: thermomechanical behavior. Pergamon Press, 1989.

CHAPTER 7

DAMPING BEHAVIOR AND TRIBOLOGICAL PROPERTIES OF Ti_2AlC/Mg COMPOSITES

7.1. Introduction

The vital demands for reducing weight and dissipating elastic strain energy under cyclic load or vibration have aroused great attention on lightweight metallic materials, especially in applications subjected to strong acceleration and high speed[1-3]. For example, lightweighting offers up to a 7% improvement in fuel economy for each 10% reduction in vehicle weight[4]. Among all structural materials, Mg alloys are regarded as the most attractive candidates for the reduction of vehicle weight owing to their low density[5, 6]. However, the disadvantage of their poor elevated temperature tensile strength restricts their wide utilization for applications[7, 8]. Hence, the development of new magnesium-based materials such as magnesium-based composites combining good mechanical properties and a high damping capacity has become a hot research topic in recent years[9, 10].

Some of the most widely adopted materials to reinforce the Mg matrix in terms of mechanical properties, wear resistance and damping capacities are SiC[11, 12], TiC[13] and graphite particulates[14-16]. Among these reinforcements, SiC particles have positive effects on the mechanical properties and wear resistance[17-19], while being detrimental to the damping capacities of magnesium composites[15]. With the introduction of graphite particulates, the damping capacities of magnesium composites are improved due to the high inherent damping properties of the graphite [15, 16]. Unfortunately, at temperatures higher than 300℃ and especially in an oxidizing environment, graphite particulates rapidly degrade, thereby eliminating any gain in damping capacities. Herein, relatively stable reinforcements with high damping capacity are crucially required in magnesium composites. Anasori et al. reported that Mg composites reinforced with Ti_2AlC MAX phases have a better damping capacity than those reinforced by the traditional binary ceramic particles such as TiC or

SiC[20-22]. These Mg composites reinforced with 20 vol.% Ti_2AlC could dissipate 30% mechanical energy during each compressive load at 250 MPa[20]. However, no study reports damping mechanisms in these new types of Mg composites composed with MAX phases.

Low wear and corrosion resistance restrict the utilization of pure Mg.[7, 23, 24] Such limitations can be overcome with the introduction of ceramic particles or alloying elements, especially ceramic particles including SiC[25], TiC[13], CaB_6[26] and B_4C[27]. However, the wear tests indicated that the easy pulling-out of hard ceramic particles caused severe grooves and scratches on the magnesium matrix surface.[25] To resolve this problem, self-lubricating graphene has been introduced into the magnesium composite to decrease the coefficient of friction, such as B_4C-Graphite/Mg[28] and SiC-Graphene/Mg[14]. Unfortunately, at temperatures above 350 ℃ and especially in oxidizing environments, the lubricants graphite and MoS_2 degrade rapidly. Hence, a relatively soft and self-lubricated ceramic owning high thermal stability is crucially required in the magnesium composite. It was found that Ti_2AlC exhibited self-lubricating behavior and low wear rate (1.8×10^{-6} mm/(N m^{-1})) during dry sliding against a steel disk[29].

Based on the above discussion, we propose to study damping mechanisms and tribological properties of Ti_2AlC/Mg composites in this chapter. In addition, the potential application of MAX/Mg composites is also presented.

7.2. Damping capacity

7.2.1. Strain amplitude dependence of damping capacities

Strain amplitude dependence of damping capacities in specimens containing different volumes of Ti_2AlC (0%, 5%, 10%, 15% and 20%, named A0, A5, A10, A15 and A20) are given in Fig. 7-1. As for other particle-reinforced metal matrix composites[15, 16, 30, 31], the strain amplitude dependence of damping capacities exhibits two regions[32]:

$$Q^{-1}(\varepsilon) = Q_0^{-1} + Q_H^{-1}(\varepsilon) \qquad (7-1)$$

Q_0^{-1} is the damping component independent of the strain amplitude. The Granato–Lucke theory explained this by the fact that matrix dislocations are pinned by strong pinning points (grain boundaries, reinforcing particles) and weak pinning points (solution atoms, vacancies)[33]. At low strain level, only weak pinning points can be dragged to dissipate energy, thus the damping from dislocations is consequently limited. Above a certain strain, the unpinning of the

dislocations from the weak pinning points occurs in the avalanche mode. Dislocation lines become long and comparatively free between strong pinning points. Therefore, the damping capacities increase rapidly with increasing strain amplitude[15, 33]. Furthermore, the strain amplitude component Q_H^{-1} is related to dislocations by the following equation derived from the Granato–Lucke (G–L) model[33, 34]:

$$\mathrm{Ln}(Q_H^{-1}(\varepsilon)) = \mathrm{Ln}C_1 - \frac{C_2}{\varepsilon} \qquad (7-2)$$

$$C_1 = \frac{\rho L_N^3 F_B}{6bEL_c^2}$$

$$C_2 = \frac{F_B}{bEL_c}$$

Where ε is the strain amplitude; C_1 and C_2 are material constants; ρ is the dislocation density; F_B is the binding force between dislocations and weak pinning points; E is the elastic modulus; $L_c$and L_N are the average dislocation distances between weak pinning points and strong pinning points, respectively; b is the Burger's vector.

From Eq. (7-2), the G–L plots should be straight lines, whose intercept and slope are the values of $\mathrm{Ln}C_1$ and $-C_2$, respectively. As shown in Fig. 7-1 (b), the Ti_2AlC/AZ91 composites satisfy the G–L model in this work, as already observed for graphite reinforced magnesium composites[16]. Therefore, factors such as intrinsic damping of Ti_2AlC particles, particles/matrix interface damping or grain boundary damping, also contribute to the damping capacities of Ti_2AlC/AZ91 composites[16].

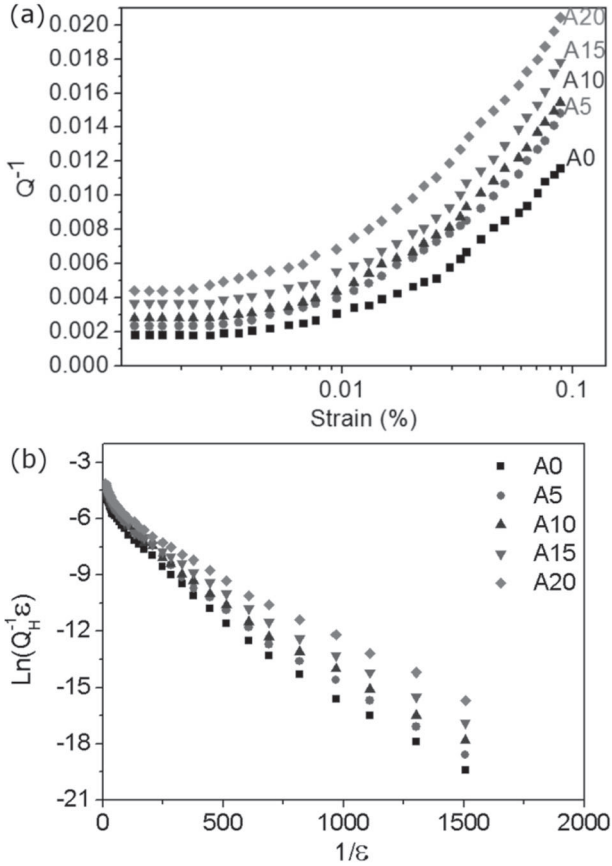

Fig. 7-1: (a) strain dependent damping capacities and (b) G-L plots of as-cast AZ91D and Ti_2AlC/AZ91D composites at RT with f = 1 Hz.

7.2.2. Temperature dependence of damping capacities

Temperature dependences of damping capacities in the Mg alloy (A0) and composites (A5 to A20) for different frequencies are given in Fig. 7-2. For all tested frequencies, damping capacities exhibit a roughly similar evolution with the temperature. Below 200 °C, there is almost no effect of the temperature on the damping capacities. But above this temperature, differences between Ti_2AlC-AZ91D composites significantly increase with the increasing temperature. This change of damping mechanism with the temperature was already observed in SiC reinforced metal composites[11,

[30] and was attributed to the sliding of grain boundaries and to interfaces between the matrix and particles. Furthermore, the damping capacities are higher in composites containing more Ti_2AlC particles at low and high temperatures that confirm an overall improvement of damping capacities with the volume fraction of Ti_2AlC particles. It has been pointed out that at low temperatures, the damping mechanisms are mainly due to intrinsic damping of each constituent[33, 34].

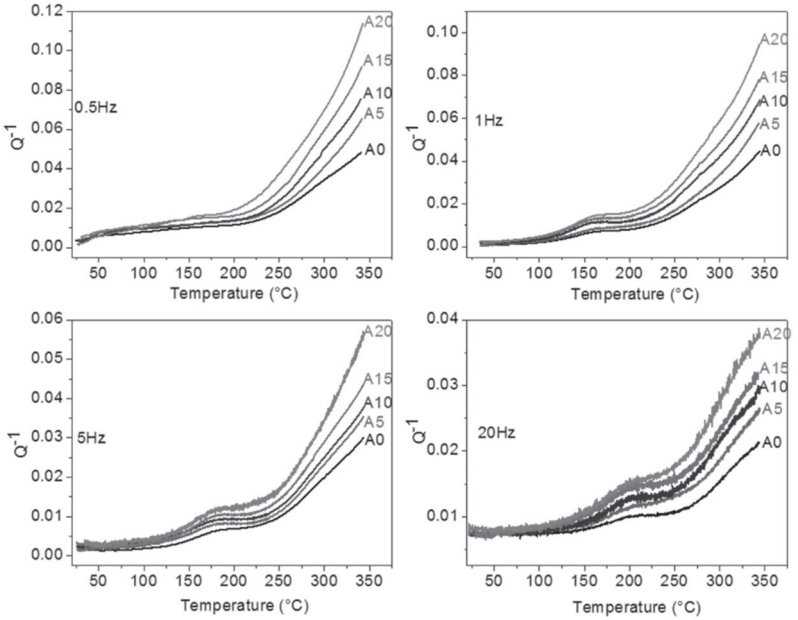

Fig. 7-2: Damping capacity as a function of temperature for unreinforced AZ91D and Ti_2AlC-AZ91D composites at different frequencies (0.5 Hz, 1 Hz, 5 Hz, 20 Hz).

7.2.3. Dynamic Young's modulus

The damping capacity was evaluated by using the following expression:

$$\tan\theta = E''/E' \qquad (7-3)$$

where θ is the phase lag angle between the applied strain and response stress. E'' is the loss modulus and E' corresponds to storage modulus. The dynamic Young's modulus (E) was also determined by using the Eq. (7-4)

[35]:

$$E = \sqrt{(E')^2 + (E'')^2} \qquad (7-4)$$

Fig. 7-3 shows the dynamic Young's modulus values extracted by Eq.(7-4) for unreinforced AZ91D (A0) and Ti_2AlC-AZ91D composites (A5 to A20) at different frequencies. The modulus curves show a similar trend, as the dynamic Young's modulus decreases with increasing temperature. For each frequency, it is clear that the addition of Ti_2AlC particles to the AZ91D matrix leads to an increase of dynamic Young's modulus due to the high intrinsic modulus of the Ti_2AlC. These measurements thus confirm results previously obtained in tensile tests[36]. Previous results have also shown that the better wetability of Mg on Ti_2AlC particles endows a stronger interfacial bonding strength in Ti_2AlC-AZ91D composites[36, 37]. Consequently, the stress transfer to the reinforcing particles is the most significant contributor to the elevation in the stiffness and strength of composites[38-41].

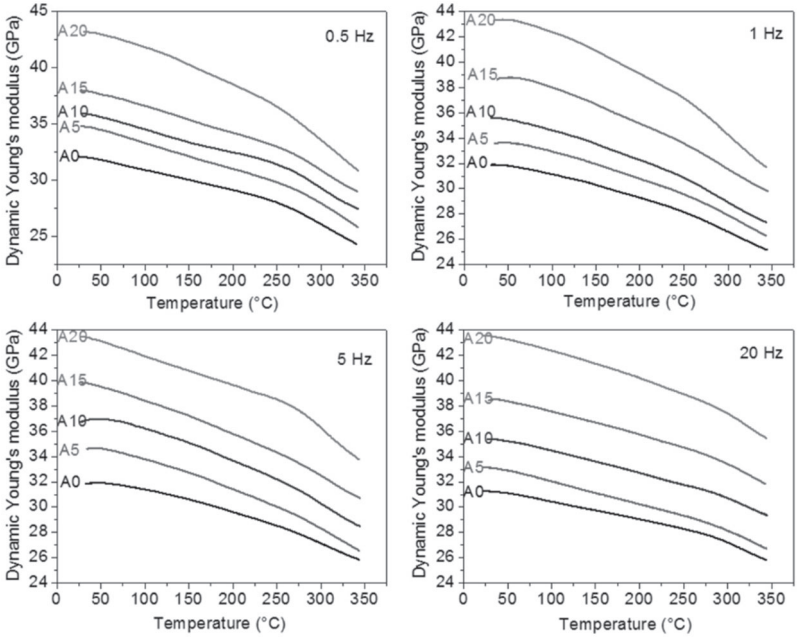

Fig. 7-3: Dynamic Young's modulus as a function of temperature for unreinforced AZ91D and different volume fractions of Ti_2AlC reinforced AZ91D composites at different frequencies (0.5 Hz, 1 Hz, 5 Hz, 20 Hz).

The dynamic Young's moduli of composites (Fig. 7-3) decrease faster than those of the AZ91D specimen (A0) with the increasing temperature. This phenomenon can be explained from different tensile fracture surfaces with the temperature as observed in the A10 composite (Fig. 7-4 (a) and (b)). At RT, a clear cleavage of Ti_2AlC without interfacial debonding dominates the fracture surface (Fig. 7-4 (a)). In contrast, at 200 ℃, the tensile fracture surface was characterized by the pulling-out and the debonding of Ti_2AlC particles (Fig. 7-4 (b)). This suggests that at high temperatures the Ti_2AlC-AZ91D interfacial bonding strength becomes weaker than the metallic Ti-Al bonds in basal planes of Ti_2AlC grains. This transformation to a tensile fracture regime suggests that the damping regime induced by dislocation gliding at low temperature is substituted when increasing the temperature by a new one controlled by interface gliding. This change in the damping mechanism should be responsible for the significant decrease of the dynamic Young's modulus of composites, compared to as-cast alloy, with increasing temperature.

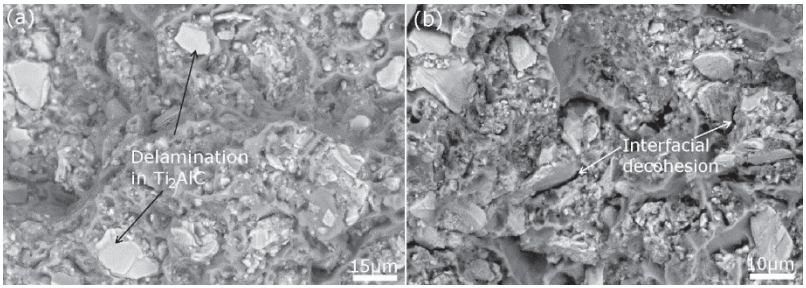

Fig. 7-4: SEM images of the 10 vol.%Ti_2AlC reinforced magnesium composite (A10) showing the tensile fracture surfaces at RT (a) and at 200 °C (b).

7.2.4. Damping mechanisms

Dislocation damping

As shown in Fig. 7-2, the damping capacities are independent or weakly dependent on temperature when the temperature is below about 220 ℃, while damping capacities exhibit a remarkable increase when the temperature is above 220 ℃, especially for the composites. This implies that different damping mechanisms dominate below and above 220 ℃. During the solidification of composites, dislocations are generated due to the difference of the thermal expansion coefficient ($\Delta\alpha$) between the

Ti_2AlC ($7.1\pm0.3\times10^{-6}$ K^{-1} and $10.5\pm0.5\times10^{-6}$ K^{-1} for the a- and c- direction respectively) and the AZ91D alloy (30.7×10^{-6} K) [42]. The generated interfacial dislocation density can be described by the following Eq. 7-5[43]:

$$\rho_{th} = \frac{B\Delta\alpha\Delta T V_f}{bt(1-V_f)} \qquad (7-5)$$

Where B is a geometrical constant, f is the volume fraction of Ti_2AlC, ΔT is temperature change, b is the Burgers vector of Mg (3.21×10^{-10} m)[44], t is the minimum dimension of reinforcement. From this equation, it is clear that the dislocation density increases with the increasing volume of Ti_2AlC particles in composites, which leads to the higher damping capacity of composites containing a higher content of Ti_2AlC particles.

Interface damping

The microstructure of Ti_2AlC-AZ91D composites was then investigated by TEM. Fig. 7-5 shows the interfacial area between the Mg matrix and Ti_2AlC at different scales. Similar to the findings in Ti_2AlN[45, 46], a large number of dislocation interactions were also observed between the numerous dislocation arrays produced inside the Ti_2AlC grain, as can be seen in Fig. 7-5 (a). It was suggested that the observed dislocation alignments along specific orientations could be a sign of an elevated lattice friction[45]. In this way, the movement of these dislocations could dissipate some energy and enhance the damping capacity. Fig. 7-5 (b) reveals many nano-sized Mg grains formed among Ti_2AlC particles. It is well known that decreasing grain size can strengthen the matrix due to the Hall-Petch effect[37, 47, 48]. The stiffness of composites are further enhanced. A typical interface was studied by HRTEM and shown in Fig. 7-5 (c). A thin amorphous magnesium layer was found between Ti_2AlC and submicron Mg grains. It was previously reported that this robust and amorphous layer could survive during the melting and solidification processes[49]. The formation of this robust amorphous Mg layer between the Ti_2AlC and the Mg matrix can reduce the interfacial energy of an incoherent interface due to large lattice mismatch and therefore, can promote the interfacial bonding strength[50]. Furthermore, in situ tensile tests at RT performed in a previous study revealed that cracks initiate in (0001) planes of Ti_2AlC particles rather than from the Ti_2AlC-Mg interfaces[51]. Based on these observations, it can be concluded that the interface damping effect does not happen due to a strong interfacial bonding strength at RT. On the contrary, at high temperatures, the interface sliding between reinforcement and matrix occurred due to a reduction in friction energy. Hence, the

increasing damping rate probably results from the sliding of grain boundaries at interfaces between the Mg and Ti_2AlC particles instead of pure dislocation damping[33, 34].

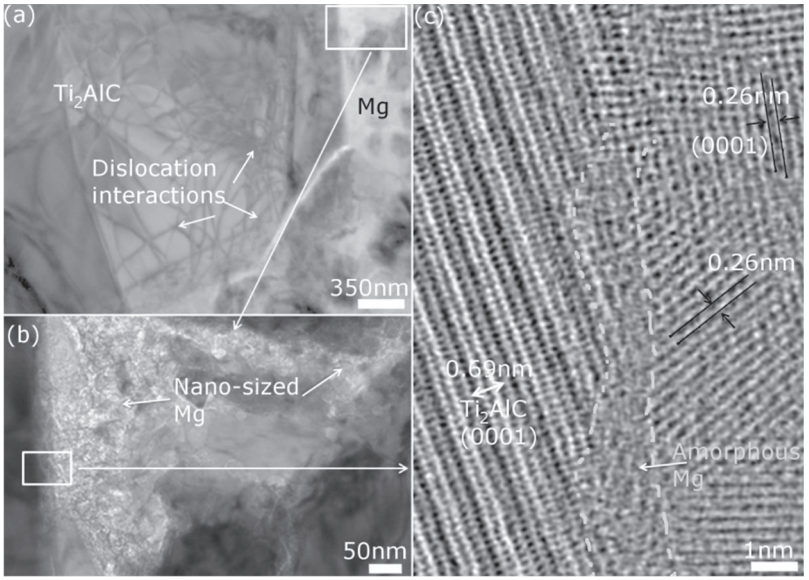

Fig. 7-5: TEM images of the Ti_2AlC-Mg Interface: (a) dark field image in which white arrows indicate dislocation interactions in a Ti_2AlC grain, (b) the presence and morphology of the nano-sized Mg particles among Ti_2AlC particles, (c) HRTEM image of an interface between Ti_2AlC and Mg with the electron beam parallel to the $[1\bar{2}10]$ direction of the Ti_2AlC.

According to Lederman's analysis, the increase of the damping component resulting from the interface slip can be approximately given by:[52]

$$\varphi_i = \frac{3\pi}{2}\frac{\mu\sigma_r(\varepsilon_0 - \varepsilon_{crit})}{\sigma_0^2/E_c}V_p \qquad (7-6)$$

Where μ is the coefficeint of friction between the ceramic particle and metal matrix; $\sigma_r$is the radial stress at the particle/matrix interface under the applied stress amplitude σ_0; ε_0 is the strain amplitude corresponding to σ_0, ε_{crit} is the critical interface strain corresponding to the critical interface shear stress at which the friction energy dissipation begins; E_c the elastic modulus of the composites; V_p the volume fraction of the particulates.

Above a certain temperature, interfacial slip occurred when the magnitude of the shear stress at the interface is sufficient to overcome friction resistance (i.e., $\varepsilon_\tau > \varepsilon_{crit}$). The friction energy loss resulting from interfacial slip is one of most important factors of generating damping[53]. As the frequency is the reciprocal of the stress cycle time, the interface slip can carry through more thoroughly at a low frequency rather than at a high frequency under the same stress level[31]. According to Zener's thermoelastic theory, damping capacities increase with increasing frequency for frequencies lower than the Zener frequency (160 Hz)[54]. However, our results shown in Fig. 7-2 suggest that damping capacities decrease with increasing frequencies over the tested temperature range, suggesting that there is no contribution of the thermoelastic damping mechanism to the damping capacity of these composites.

Damping peak analysis

Fig. 7-6 (a) presents that the damping peaks shift to the left with the introduction of Ti_2AlC in the magnesium matrix, especially with increasing frequencies. This change indicates that the modified microstructures of the composites would be responsible, especially the introduction of particle/matrix interfaces. It was reported that damping peaks are related to activation-relaxation processes, and some parameters such as relaxation strength and relaxation time.[55] At the peak of temperature (T_p),$w\tau = 1$ is satisfied and the Arrhenius equation[55] can be given as follows.

$$\log w + \log\tau_0 + \left(\frac{H}{2303k}\right)\left(\frac{1000}{T_p}\right) = 0 \qquad (7-7)$$

Where τ and τ_0 are the relaxation time and the inverse attempt frequency, W is the vibration angular frequency, H is the activation energy of the activation-relaxation process and k is the Boltzmann constant. Herein, the activation energy (H) can be calculated by the slope of $\log 2\pi f \sim 1000/T_p$ (f is the frequency) and is given in Fig. 7-6 (b).

Based on the temperature peaks at different frequencies, H values for AZ91D and 15 vol.% Ti_2AlC-AZ91D composite were calculated to 116 kJ mol^{-1} and 128 kJ mol^{-1}, respectively. These two values are between the grain boundary diffusion energy (82-105 kJ mol^{-1}) and the lattice self-diffusion (135kJ mol^{-1}) of magnesium[15]. Thus, the damping peak could be considered to be caused by boundary slip controlled by the grain boundary diffusion and the lattice self-diffusion, such as interface slip and grain boundary slip[11]. Furthermore, the calculated H value of Ti_2AlC reinforced AZ91D composites is higher than those of SiC or graphite

reinforced AZ91D composites (110 kJ mol^{-1} [12] and 123kJ mol^{-1} [16]). This can be attributed to a stronger interfacial bonding strength of Ti_2AlC reinforced AZ91D composites in comparison with SiC reinforced magnesium composite[36]. This trend is also observed in Cu-coated and uncoated SiC reinforced magnesium composites in which a higher damping activation energy has been found[31].

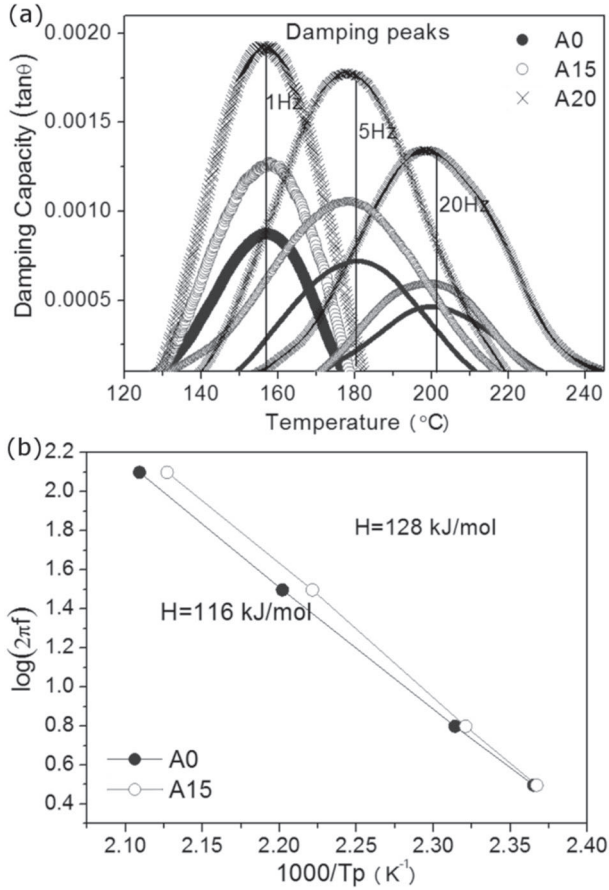

Fig. 7-6: (a) Variations of peak temperatures for as-cast AZ91D alloy and Ti_2AlC reinforced AZ91D composites for several frequencies, (b) the logarithmic plots of angular frequency vs reciprocal peak temperature for A0 and A15 samples.

7.2.5. Conclusions

The evolution with temperature of the damping capacities and dynamic Young's moduli of ternary Ti_2AlC particles reinforced AZ91D composites were investigated. This work has highlighted that Ti_2AlC significantly contributes to the damping capacity and to dynamic moduli of composites. With increasing temperature, especially above 200 ℃, the interfacial damping capacity becomes dominant and dynamic moduli of composites decrease. These trends were revealed from the transformed tensile fracture mechanisms. At room temperature, Ti_2AlC particles delaminated without any decohesion between Ti_2AlC particles and the Mg matrix. However, interfacial decohesion occured above 200 °C. One explanation of this change of decohesion mechanism could be ascribed to the inherent structure of the Ti_2AlC MAX phase and to the formation of a robust amorphous magnesium layer at the interface between Ti_2AlC and the magnesium matrix that was evidenced by HRTEM. This amorphous layer further gives rise to high activation energies (H) of damping peaks for composites, which was calculated as 128 kJ mol^{-1}. This value is higher than those calculated for SiC or graphite reinforced AZ91D composites (110 kJ mol^{-1} [12] and 123 kJ mol^{-1} [16]), which is due to the stronger interfacial bonding strength.

7.3. Tribological properties

7.3.1. Wear rate

Fig. 7-7 shows the volumetric wear rate variation against load at a speed of 0.5 m s^{-1} for the different specimens. As a general trend, the volumetric loss increased with the increasing loads for all specimens. In addition, at all the applied stresses, the addition of Ti_2AlC reinforcement brings an improvement in the wear resistance, as compared with the unreinforced alloy.

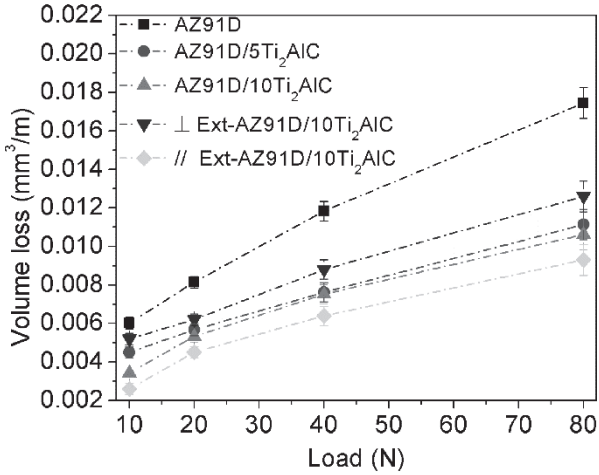

Fig. 7-7: Variation of volume loss with normal stress for as-cast AZ91D alloy and composites tested at a sliding speed of 0.5 m s^{-1}.

The results of the specific wear rate k ($mm^3/N\ m^{-1}$) are given in Fig. 7-8 as a function of the force applied. Based on the Archard's equation, the increased hardness improves the resistance of the materials against plastic deformation and decreases wear rate.[56] Herein, all composites exhibit better wear resistance than the AZ91D magnesium alloy, especially with the increasing Ti_2AlC content. However, in micro-sized SiCp reinforced magnesium composite, Lim et al. and Gracia et al. reported that the presence of SiCp is detrimental to the wear resistance at a speed of 0.5 m s^{-1} and load of 30-80 N.[17, 57] For example, at a load of 80 N and sliding speed of 0.5 m s^{-1}, 10% SiC-AZ91D and 5% SiC-AZ91D decreased the wear rates of AZ91D by about 25-35% and 10-15%, respectively. [17] In contrast, the specific wear rate of the Ti_2AlC reinforced magnesium composites is lower than that of pure as-cast AZ91D in our work. To clarify this difference, the modification in the surface of the monolithic alloy by the introduction of Ti_2AlC is given in the next section.

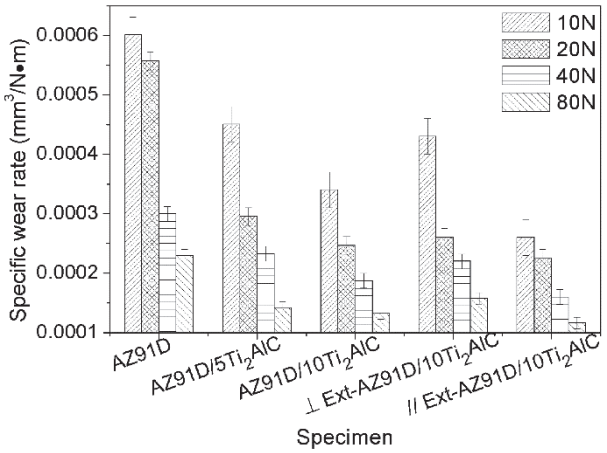

Fig. 7-8: Specific wear rate of investigated samples at different applied loads.

7.3.2. Worn surfaces and debris

The worn surfaces and wear debris provide valuable information about the mechanism of wear. As shown in Fig. 7-9, the typical fine grooves parallel to the sliding direction were found in most tested conditions. These lines are caused by hard zones of the counterbody surface that plow the soft surface of the magnesium pin. This wear mechanism caused the removal of material at the surface, especially for the AZ91D magnesium alloy due to its low hardness. As reported in the literature and also found in Fig. 7-9 (d), the abrasion mechanism is generally extensive in the composite due to the presence of detached and fractured SiC_p that become trapped in the sliding interface or embedded in the counterface, especially with the increasing amount of hard SiC_p particles.[17, 58]. In Fig. 7-9 (b) and (c), less abrasion and grooves were found in Ti_2AlC-Mg composite. This difference suggests that the reinforced Ti_2AlC particles could form an intensive interfacial bond with the magnesium matrix and avoid detachment during sliding, more evidence is given in the TEM images of Fig. 7-15.

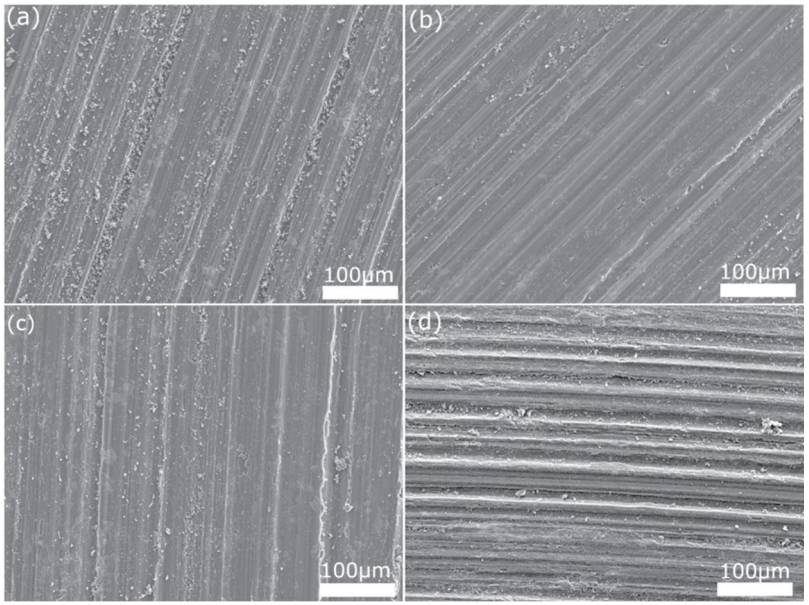

Fig. 7-9: SEM images of different samples at applied load 40N and sliding speed 0.5m/s: (a) as-cast AZ91D, (b) 5%Ti_2AlC-AZ91D, (c) 10%Ti_2AlC-AZ91D and (d) 10%SiC-AZ91D composite.

Fig. 7-10 presents the effect of different loads on worn surfaces of 10%Ti_2AlC-AZ91D magnesium composites. The SEM images (left column) showed that the grooves strongly decreased with the increasing load. In addition, the BSE images (right column) indicated that much finer Ti_2AlC particles dispersed into the magnesium matrix surface at higher loads. This phenomenon evidenced that the fractured Ti_2AlC particles were trapped and embedded in the sliding surface. Subsequently, this trapped self-lubricated Ti_2AlC reduced the wear rate of the reinforced composites. In addition, the corresponding SEM (left column) and BSE (right column) images showing counterbody surfaces are given in Fig. 7-11. This observation further confirmed that more fractured Ti_2AlC particles were trapped and conserved between the pin and disk with the increasing load.

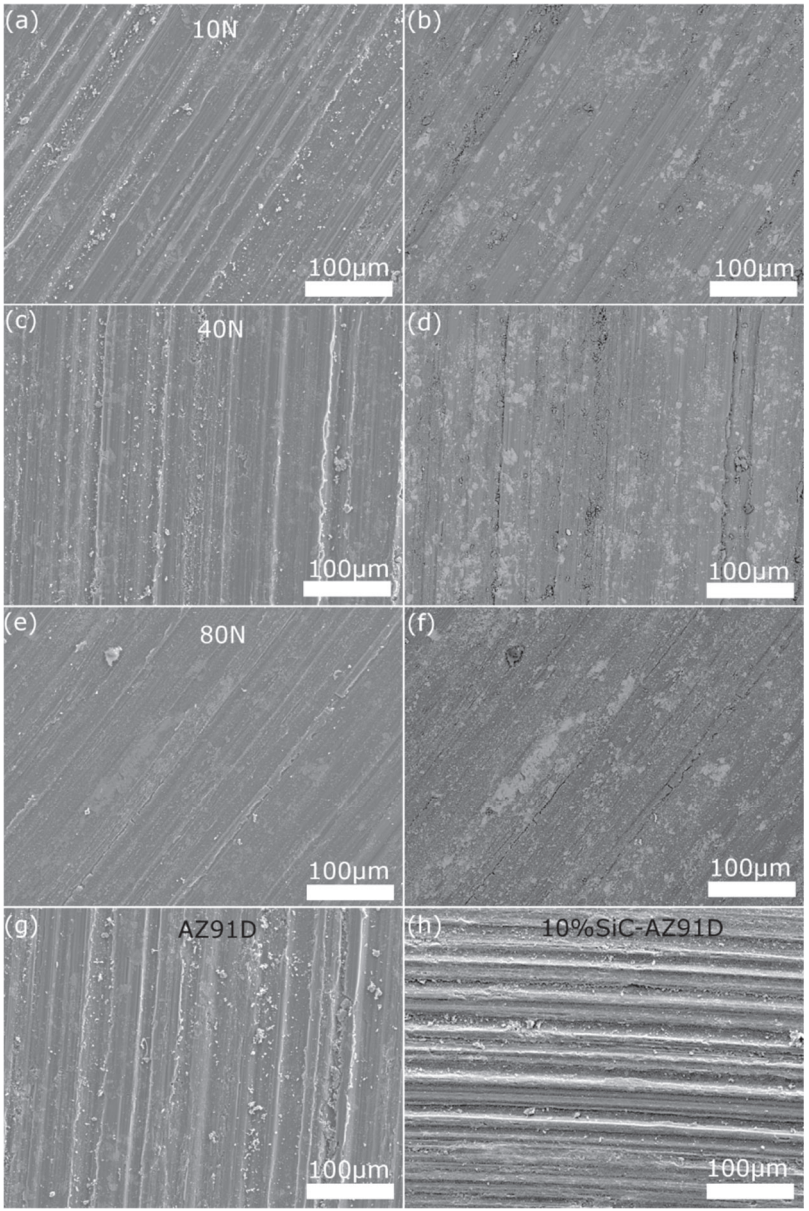

Fig. 7-10: (a-h) SEM (left) and BSM (right) images of 10% Ti_2AlC-AZ91D composite at different loads.

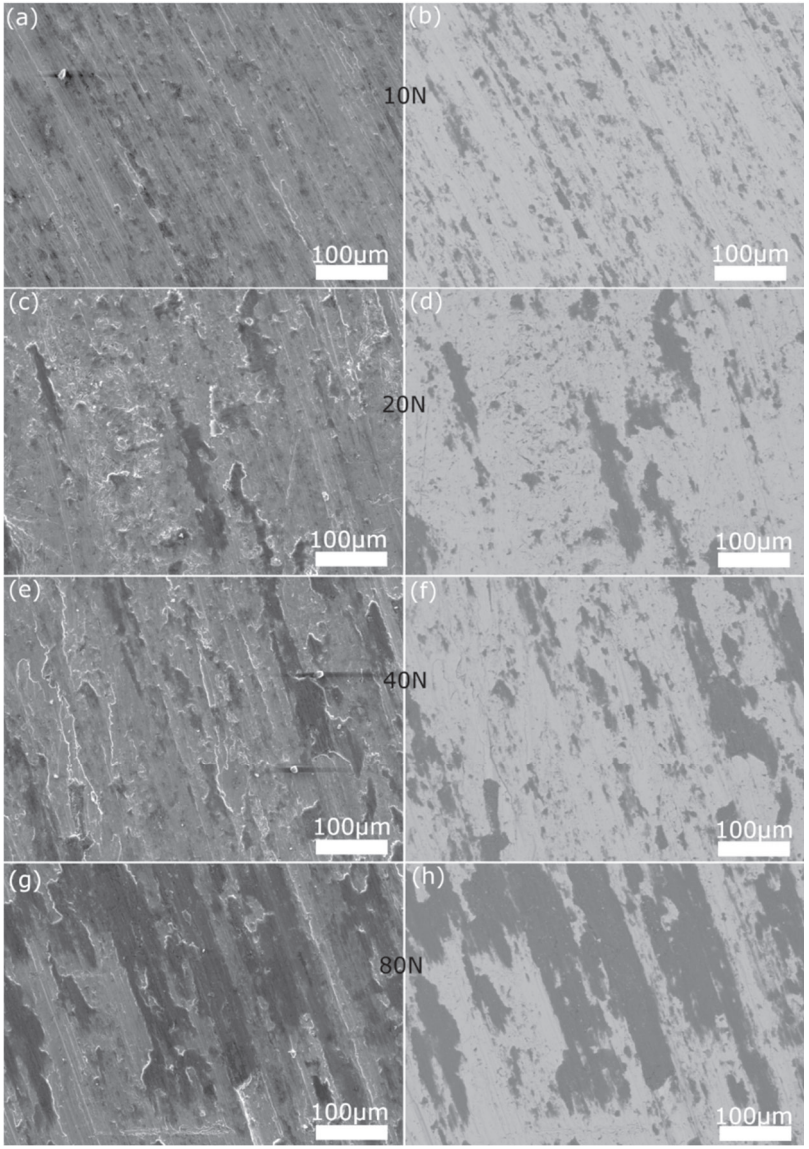

Fig. 7-11: (a-h) SEM (left) and BSM (right) images of disk (counterbody) surfaces against 10%Ti_2AlC-AZ91D composite at different loads.

Fig. 7-12 presents the EDS analysis of the debris collected at 80N and 0.5 m s^{-1} for 10% Ti_2AlC-AZ91D. In comparison with the Ti_2AlC particle size (about 10 μm) in the matrix, the smaller Ti_2AlC particles (about 2 μm) found in the debris suggested that the Ti_2AlC particles were fractured, rather than detached. In the literature, if the soft slip planes in MAX phase are oriented so that they are parallel to the loading axis, deformation can occur by kinking, where two dislocation walls are nucleated by the sequential breaking of individual crystal planes. Furthermore, classical node reactions between dislocations lying in the basal plane and dipole interactions were observed under confining pressure[45, 59, 60]. This behavior is different from the results found in SiC-AZ91D magnesium composite, whose SiC particles were detached from the magnesium matrix and found in the debris[17, 25].

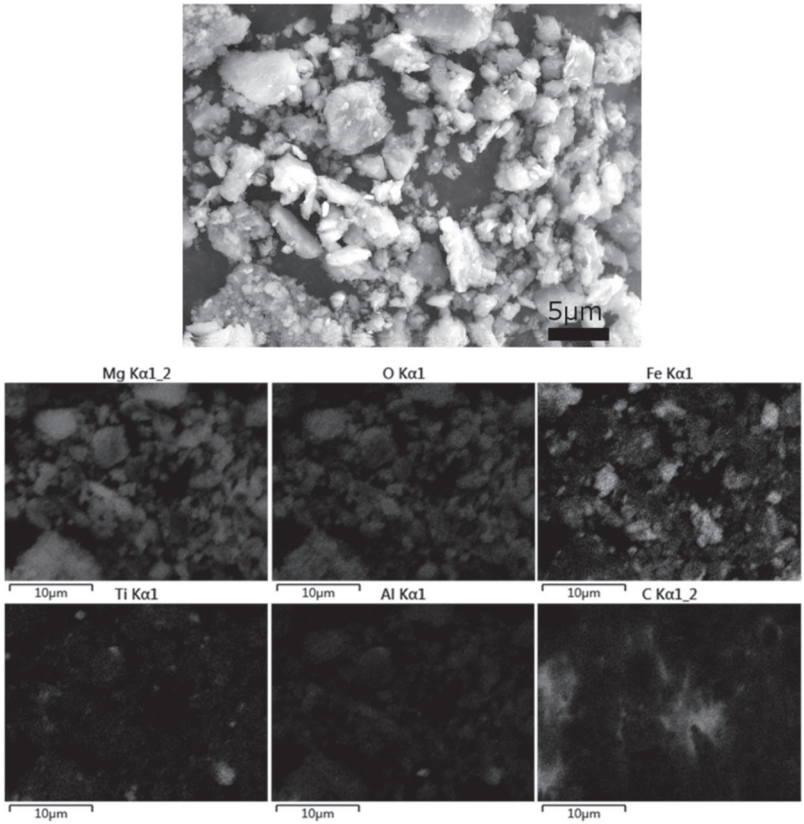

Fig. 7-12. EDS mapping for the wear debris collected for 10% Ti_2AlC-AZ91D composite at applied load 80 N and sliding speed 0.5m s^{-1}.

Furthermore, the worn surfaces of the corresponding AZ91D pin and steel disk were respectively analyzed by EDS mapping, as shown in Fig. 7-13 and Fig. 7-14. The oxidative wear surface was characterized by the formation of spots covering most of the surface of the Mg pin test. Combined with the strongly oxidized wear debris found in Fig. 7-12, it demonstrated that an oxidation layer continuously formed during the wear test. According to the previous report, this oxide layer hinders the contact between the pin and the conterbody and reduces the friction coefficient[17, 61, 62]. At the same time, the higher oxygen content was detected in the region where Ti_2AlC particles were found, as can be seen from the oxygen distribution in Fig. 7-12 and Fig. 7-13. In order to clarify this phenomenon, the cross-sectional lamina in Ti_2AlC/Mg interface was sliced with FIB and observed by TEM.

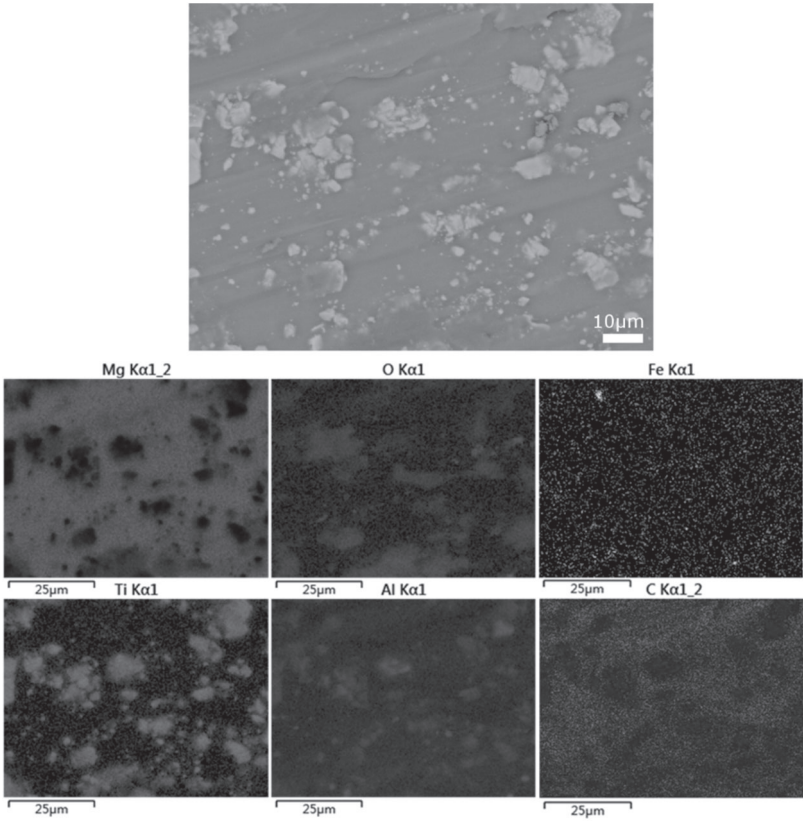

Fig. 7-13: EDS mapping for the counterpart surface at applied load 80 N and sliding speed 0.5 m s^{-1}.

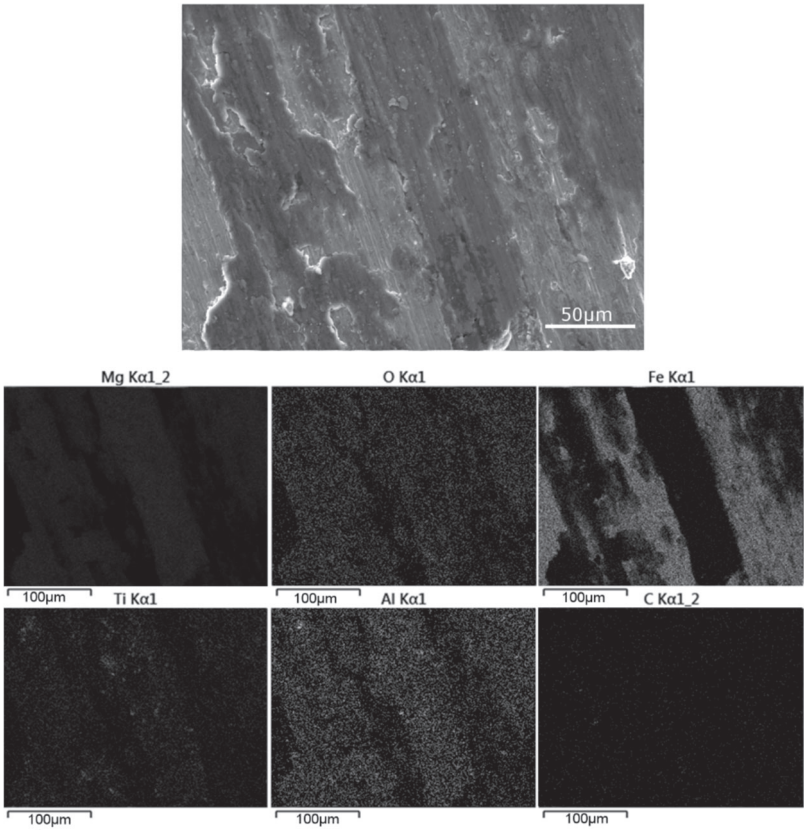

Fig. 7-14. EDS mapping for the disk surface of 10% Ti_2AlC-AZ91D composite at applied load 80 N and sliding speed 0.5 m s^{-1}.

Fig. 7-15 (a) indicates that the submicron Mg grains formed around the Ti_2AlC particle, which was also found in the literature.[63] As nano-sized Mg is much easier to be oxidized than micro-sized Mg, more oxygen tended to accumulate around the Ti_2AlC particles during the wear test. Herein, the higher oxygen content was detected in the region where Ti_2AlC particles were found, as shown in the EDS analysis. A HRTEM image of a Ti_2AlC/Mg interface was taken with the incident beam parallel to $[11\bar{2}0]$ of Ti_2AlC and Mg, as can be seen in Fig. 7-15 (b). A high coherency of the Ti_2AlC/Mg interface was found, which confirmed that the molten AZ91D could well wet the Ti_2AlC and strong Ti_2AlC/Mg interfacial bonding be formed. As found in the in situ SEM tensile test, the

cracks were initiated in Ti_2AlC particles instead of at the Ti_2AlC-Mg interface. This behavior is different from the cases of SiC-AZ91D[64], SiC/Mg-6%Zn[65], and TiC-Mg[66]. Due to the strong interfacial bonding strength, no Ti_2AlC decohesion occurred. Finally, unlike the extensive abrasions that were found in SiC reinforced magnesium composite caused by SiC detachment, less abrasion and fewer grooves were found in the Ti_2AlC-Mg composite.

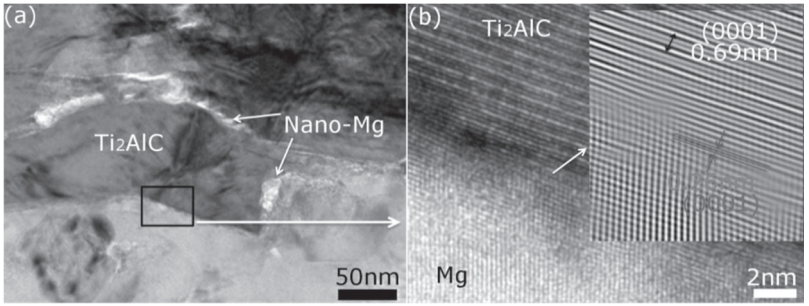

Fig. 7-15. (a) TEM micrographs of AZ91D-Ti_2AlC interface, (b) Lattice image of a Ti_2AlC/Mg interface recorded with the incident beam parallel to the <1120> direction of Ti_2AlC. The inset represents the corresponding fast Fourier transform diffractogram of Ti_2AlC/Mg interface.

7.3.3. The effect of Ti_2AlC orientation

Fig. 7-16 presents the SEM images of the surfaces of extruded composite containing 10 vol.% of Ti_2AlC particles worn at sliding directions parallel and perpendicular to the extrusion axis, respectively. Distinctive worn surface topographies were revealed in Fig. 7-16 (a) and (c). No scratches or grooves were found when the sliding direction was parallel to the extrusion axis, while some grooves, together with furrows, were found when the sliding direction was perpendicular to the extrusion axis. This difference should be ascribed to the Ti_2AlC orientation in the AZ91D matrix. The enlarged area, Fig. 7-16 (b), shows that some Ti_2AlC particles delaminated into layers, which indicated self-lubricating behavior. In Fig. 7-16 (d), the Ti_2AlC particles broke into pieces. According to the previous studies, in these MAX phases, the $M_{n+1}X_n$ layers with mostly strong covalent M–X bonds, are interleaved with A layers through weaker M–A bonds.[67-69] As interfacial shear strength along the Ti_2AlC basal planes is lower than the Ti_2AlC/Mg interfacial bonding strength, the slide could happen along the Ti_2AlC basal planes under the shear force.[38, 51]

Once the Ti_2AlC was broken into pieces, the lower interfacial bonding strength could not support the sliding shear strength. Subsequently, this caused the pulling-out of some Ti_2AlC particles from the matrix and resulted in the abrasive wear mechanism, as found in Fig.12 (c).

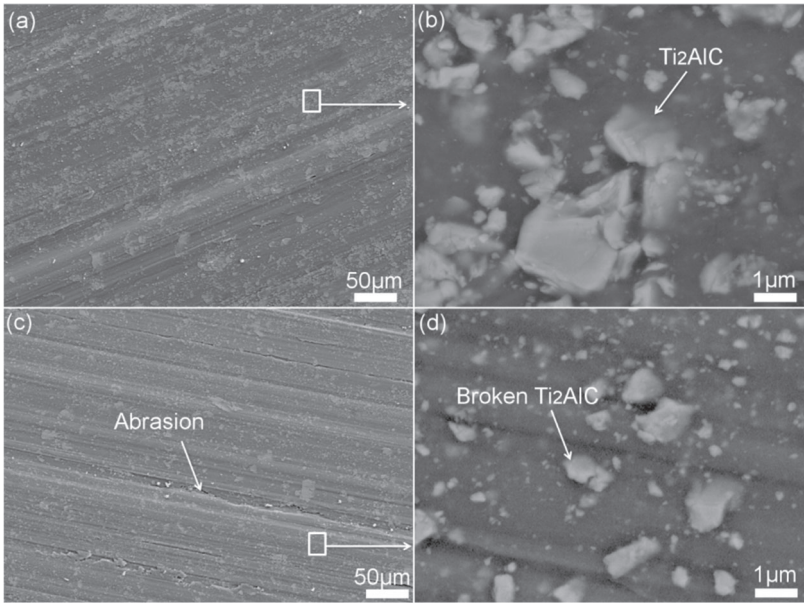

Fig. 7-16. SEM images of textured 10 vol.% Ti_2AlC-AZ91D composite at sliding speed 0.5 m s^{-1} and applied load 80 N, (a) and (b) sliding direction parallel to hot extrusion axis; (c) and (d) sliding direction perpendicular to hot extrusion axis.

Fig. 7-17 represents the variation of the average friction coefficient values of different samples as a function of the applied load during the wear tests. In all conditions, the friction coefficient is below 0.35. Concerning the as-cast specimens, the Ti_2AlC reinforced AZ91D composite had lower friction coefficients than the as-cast AZ91D. However, SiC-AZ91D has a higher friction coefficient than the as-cast AZ91D under the same experimental procedure, especially for 10% SiC/AZ91D at test loads above 40N, in which case severe abrasion was found due to the pulling of SiC particles.[17] In addition, the friction coefficient variations of extruded composites against load confirmed the anisotropic trobological properties at sliding directions parallel and perpendicular to the extrusion axis. Differently, at a load of 80 N, the

friction coefficient of extruded Ti_2AlC-AZ91D with sliding direction perpendicular to the extrusion axis became lower than that of as-cast AZ91D. This change can be ascribed to the reason that more self-lubricated Ti_2AlC particles were trapped and embedded in the sliding surface with increasing load.

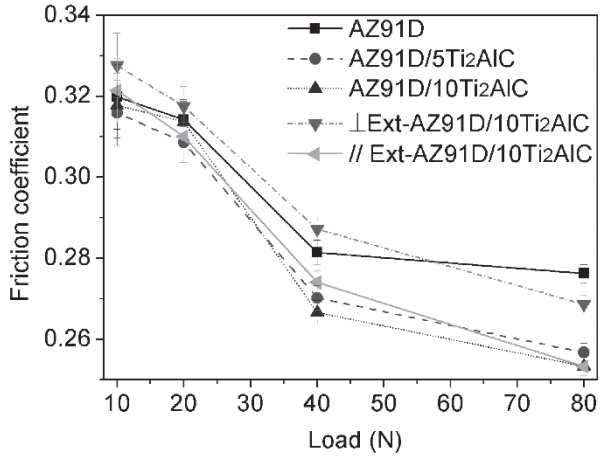

Fig. 7-17**.** Variation of friction coefficient with the applied load for as-cast AZ91D alloy and composites tested at sliding speed 0.5 m s^{-1}.

7.3.4. Conclusions

Pin-on-disk dry sliding wear tests with pins of Ti_2AlC reinforced AZ91 magnesium composites were investigated at a sliding velocity of 0.5 m s^{-1} under loads of 10, 20, 40 and 80 N against a Cr15 steel disk. Based on the results, the following major conclusions were obtained:

(1) The wear tests showed that the volumetric loss increased for all the samples with the increasing applied stress. At all the applied stresses, the addition of Ti_2AlC reinforcement brings an improvement in the wear resistance compared with the unreinforced alloy.

(2) SEM and EDS studies conducted on the worn surfaces and debris revealed a combination of oxidative and abrasive wear mechanisms at all applied stresses. The Ti_2AlC particles were surrounded by MgO in the debris and counterbody. With increasing applied stress, the abrasive wear mechanism became weaker due to the self-lubricating ability of reinforced Ti_2AlC particles.

(3) Unlike the extensive abrasions found in SiC reinforced magnesium

composite caused by SiC detachment, less abrasion and fewer grooves were found in Ti_2AlC-Mg composite due to the strong interfacial bonding between Ti_2AlC and magnesium matrix.

(4) The anisotropic tribological behavior happened in the textured composites fabricated by hot extrusion. The lowest friction coefficient of extruded composites was found in the sliding direction parallel to the extrusion axis.

7.4. Application of MAX/Mg composites

Due to their light weight, excellent dimensional stability and mechanical integrity, magnesium matrix composites are considered as possible candidates in aerospace, automotive and electronics applications for substituting traditional magnesium alloys and composites[70]. In the automotive industry, fuel consumption would be reduced by 7% if the weight could be reduced by 10%[71]. Generally, the engine cylinder block of a motorcycle is made of an aluminum cylinder and an iron cylinder liner. This structure produces low heat transfer efficiency because of the heterogeneous metal interface. The density of iron is 7.9g cm^{-3}, which is much higher than Ti_2AlC/Mg composite (1.9 g cm^{-3}). For resolving these problems and obtaining a new cylinder, as shown in Fig. 7-18, we designed and developed an integrated forming process, including powder metallurgy, semi-solid casting, hot extrusion and high pressure die casting. The Ti_2AlC/Mg billet was fabricated by the semi-solid stirring casting method with the introduction of Ti_2AlC particles into AZ91D alloy. Then, the cylinder liner was obtained by hot extrusion of semi-solid billet. Finally, the line was moved into the mold and was encapsulated by AZ91D alloy during high pressure die casting. As shown in Fig. 7-19, the weight of the original LPw200 motorcycle cylinder was reduced from 1.7 Kg to 1.25 Kg with a weight reduction of 26% in this method. This development can meet the requirements of energy saving and emission reduction in the transportation sector.

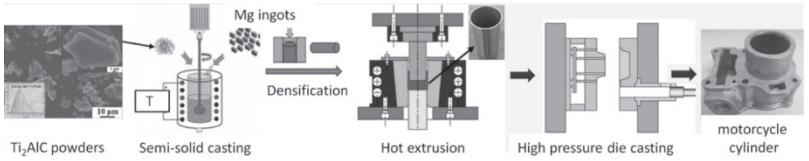

Fig. 7-18: The integrated forming process of Ti_2AlC reinforced magnesium matrix composite motorcycle cylinder.

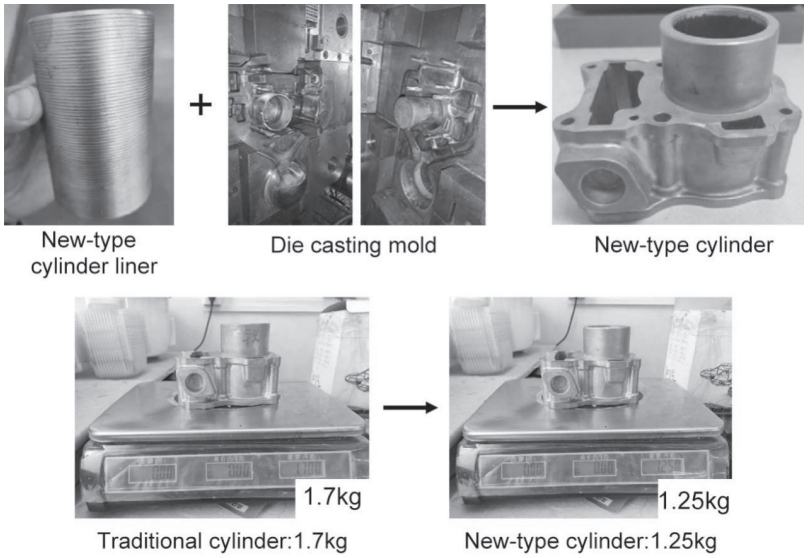

Fig. 7-19 Production and application of LP200 motorcycle cylinder block with magnesium matrix composite cylinder liner, and the weight compared with the traditional cylinder.

References

[1] P. Singh, H. Pungotra, N.S. Kalsi, On the characteristics of titanium alloys for the aircraft applications, Materials Today: Proceedings 4(8) (2017) 8971-8982.
[2] W.J. Joost, P.E. Krajewski, Towards magnesium alloys for high-volume automotive applications, Scripta Materialia 128(Supplement C) (2017) 107-112.
[3] L. Tian, A. Russell, T. Riedemann, S. Mueller, I. Anderson, A deformation-processed Al-matrix/Ca-nanofilamentary composite with low density, high strength, and high conductivity, Materials Science and Engineering: A 690 (2017) 348-354.
[4] W.J. Joost, Reducing Vehicle Weight and Improving U.S. Energy Efficiency Using Integrated Computational Materials Engineering, JOM 64(9) (2012) 1032-1038.
[5] M.P. Staiger, A.M. Pietak, J. Huadmai, G. Dias, Magnesium and its alloys as orthopedic biomaterials: A review, Biomaterials 27(9) (2006) 1728-1734.

[6] B. Song, N. Guo, T. Liu, Q. Yang, Improvement of formability and mechanical properties of magnesium alloys via pre-twinning: A review, Materials and Design (1980-2015) 62(Supplement C) (2014) 352-360.
[7] X. Wang, D. Xu, R. Wu, X. Chen, Q. Peng, L. Jin, Y. Xin, Z. Zhang, Y. Liu, X. Chen, G. Chen, K. Deng, H. Wang, What is going on in magnesium alloys?, Journal of Materials Science and Technology 34(2) (2018) 245-247.
[8] T.T.T. Trang, J.H. Zhang, J.H. Kim, A. Zargaran, J.H. Hwang, B.C. Suh, N.J. Kim, Designing a magnesium alloy with high strength and high formability, Nature Communications 9(1) (2018) 2522.
[9] H.Z. Ye, X.Y. Liu, Review of recent studies in magnesium matrix composites, Journal of Materials Science 39(20) (2004) 6153-6171.
[10] J. Umeda, K. Kondoh, H. Imai, Friction and wear behavior of sintered magnesium composite reinforced with CNT-Mg_2Si/MgO, Materials Science and Engineering: A 504(1) (2009) 157-162.
[11] C. Wang, K. Deng, W. Liang, High temperature damping behavior controlled by submicron SiCp in bimodal size particle reinforced magnesium matrix composite, Materials Science and Engineering: A 668 (2016) 55-58.
[12] K. Deng, J. Li, K. Nie, X. Wang, J. Fan, High temperature damping behavior of as-deformed Mg matrix influenced by micron and submicron SiCp, Materials Science and Engineering: A 624 (2015) 62-70.
[13] L. Falcon-Franco, E. Bedolla-Becerril, J. Lemus-Ruiz, J.G. Gonzalez-Rodríguez, R. Guardian, I. Rosales, Wear performance of TiC as reinforcement of a magnesium alloy matrix composite, Composites Part B: Engineering 42(2) (2011) 275-279.
[14] A. Das, S.P. Harimkar, Effect of Graphene Nanoplate and Silicon Carbide Nanoparticle Reinforcement on Mechanical and Tribological Properties of Spark Plasma Sintered Magnesium Matrix Composites, Journal of Materials Science and Technology 30(11) (2014) 1059-1070.
[15] Y. Wu, K. Wu, K. Nie, K. Deng, X. Hu, X. Wang, M. Zheng, Damping capacities and tensile properties in Grp/AZ91 and SiCp/Grp/AZ91 magnesium matrix composites, Materials Science and Engineering: A 527(29) (2010) 7873-7877.
[16] Y. Wu, K. Wu, K. Deng, K. Nie, X. Wang, X. Hu, M. Zheng, Damping capacities and tensile properties of magnesium matrix composites reinforced by graphite particles, Materials Science and Engineering: A 527(26) (2010) 6816-6821.
[17] S. García-Rodríguez, B. Torres, A. Maroto, A.J. López, E. Otero, J. Rams, Dry sliding wear behavior of globular AZ91 magnesium alloy and AZ91/SiCp composites, Wear 390-391(Supplement C) (2017) 1-10.

[18] S. Shang, K. Deng, K. Nie, J. Li, S. Zhou, F. Xu, J. Fan, Microstructure and mechanical properties of SiCp/Mg–Al–Zn composites containing $Mg_{17}Al_{12}$ phases processed by low-speed extrusion, Materials Science and Engineering: A 610 (2014) 243-249.
[19] P. Poddar, V. Srivastava, P. De, K. Sahoo, Processing and mechanical properties of SiC reinforced cast magnesium matrix composites by stir casting process, Materials Science and Engineering: A 460 (2007) 357-364.
[20] B. Anasori, S. Amini, V. Presser, M.W. Barsoum, Nanocrystalline Mg-Matrix Composites with Ultrahigh Damping Properties, in: W.H. Sillekens, S.R. Agnew, N.R. Neelameggham, S.N. Mathaudhu (Eds.), Magnesium Technology 2011, Springer International Publishing, Cham, 2016, pp. 463-468.
[21] B. Anasori, E.A.N. Caspi, M.W. Barsoum, Fabrication and mechanical properties of pressureless melt infiltrated magnesium alloy composites reinforced with TiC and Ti_2AlC particles, Materials Science and Engineering A 618 (2014) 511-522.
[22] X. Wang, N. Wang, L. Wang, X. Hu, K. Wu, Y. Wang, Y. Huang, Processing, microstructure and mechanical properties of micro-SiC particles reinforced magnesium matrix composites fabricated by stir casting assisted by ultrasonic treatment processing, Materials and Design 57 (2014) 638-645.
[23] X.B. Chen, N. Birbilis, T.B. Abbott, Review of Corrosion-Resistant Conversion Coatings for Magnesium and Its Alloys, CORROSION 67(3) (2011) 035005-1-035005-16.
[24] J. An, R.G. Li, Y. Lu, C.M. Chen, Y. Xu, X. Chen, L.M. Wang, Dry sliding wear behavior of magnesium alloys, Wear 265(1) (2008) 97-104.
[25] F. Labib, H.M. Ghasemi, R. Mahmudi, Dry tribological behavior of Mg/SiCp composites at room and elevated temperatures, Wear 348-349(Supplement C) (2016) 69-79.
[26] P. Seenuvasaperumal, A. Elayaperumal, R. Jayavel, Influence of calcium hexaboride reinforced magnesium composite for the mechanical and tribological behviour, Tribology International 111(Supplement C) (2017) 18-25.
[27] Y. Yao, L. Jiang, G. Fu, L. Chen, Wear behavior and mechanism of B_4C reinforced Mg-matrix composites fabricated by metal-assisted pressureless infiltration technique, Transactions of Nonferrous Metals Society of China 25(8) (2015) 2543-2548.
[28] I. Aatthisugan, A. Razal Rose, D. Selwyn Jebadurai, Mechanical and wear behaviour of AZ91D magnesium matrix hybrid composite reinforced with boron carbide and graphite, Journal of Magnesium and Alloys 5(1)

(2017) 20-25.
[29] L. Cai, Z. Huang, W. Hu, S. Hao, H. Zhai, Y. Zhou, Fabrication, mechanical properties, and tribological behaviors of Ti_2AlC and $Ti_2AlSn_{0.2}C$ solid solutions, Journal of Advanced Ceramics 6(2) (2017) 90-99.
[30] S. Madeira, G. Miranda, V.H. Carneiro, D. Soares, F.S. Silva, O. Carvalho, The effect of SiCp size on high temperature damping capacity and dynamic Young's modulus of hot-pressed AlSi–SiCp MMCs, Materials & Design 93 (2016) 409-417.
[31] J. Gu, X. Zhang, Y. Qiu, M. Gu, Damping behaviors of magnesium matrix composites reinforced with Cu-coated and uncoated SiC particulates, Composites Science and Technology 65(11) (2005) 1736-1742.
[32] X. Hu, Y. Zhang, M. Zheng, K. Wu, A study of damping capacities in pure Mg and Mg–Ni alloys, Scripta Materialia 52(11) (2005) 1141-1145.
[33] A. Granato, K. Lücke, Application of Dislocation Theory to Internal Friction Phenomena at High Frequencies, Journal of Applied Physics 27(7) (1956) 789-805.
[34] S. Asano, Theory of nonlinear damping due to dislocation hysteresis, Journal of the Physical Society of Japan 29(4) (1970) 952-963.
[35] J. Zhang, R.J. Perez, E.J. Lavernia, Documentation of damping capacity of metallic, ceramic and metal-matrix composite materials, Journal of Materials Science 28(9) (1993) 2395-2404.
[36] W. Yu, X. Wang, H. Zhao, C. Ding, Z. Huang, H. Zhai, Z. Guo, S. Xiong, Microstructure, mechanical properties and fracture mechanism of Ti_2AlC reinforced AZ91D composites fabricated by stir casting, Journal of Alloys and Compounds 702 (2017) 199-208.
[37] S. Amini, C. Ni, M.W. Barsoum, Processing, microstructural characterization and mechanical properties of a Ti_2AlC/nanocrystalline Mg-matrix composite, Composites Science and Technology 69(3) (2009) 414-420.
[38] W. Yu, H. Zhao, X. Hu, Anisotropic mechanical and physical properties in textured Ti_2AlC reinforced AZ91D magnesium composite, Journal of Alloys and Compounds 732 (2018) 894-901.
[39] W. Hu, Z. Huang, L. Cai, C. Lei, H. Zhai, S. Hao, W. Yu, Y. Zhou, Preparation and mechanical properties of TiC_x-Ni_3(Al, Ti)/Ni composites synthesized from Ni alloy and Ti_3AlC_2 powders, Materials Science and Engineering: A 697 (2017) 48-54.
[40] Z. Huang, J. Bonneville, H. Zhai, V. Gauthier-Brunet, S. Dubois, Microstructural characterization and compression properties of $TiC_{0.61}$/Cu(Al) composite synthesized from Cu and Ti_3AlC_2 powders, Journal of Alloys

and Compounds 602(4) (2014) 53-57.
[41] W. Yu, D. Chen, L. Tian, H. Zhao, X. Wang, Self-lubricate and anisotropic wear behavior of AZ91D magnesium alloy reinforced with ternary Ti_2AlC MAX phases, Journal of Materials Science and Technology (2018).
[42] J. Zhang, R. Perez, E. Lavernia, Dislocation-induced damping in metal matrix composites, Journal of Materials Science 28(3) (1993) 835-846.
[43] Z. Trojanová, W. Riehemann, H. Ferkel, P. Lukáč, Internal friction in microcrystalline magnesium reinforced by alumina particles, Journal of Alloys and Compounds 310(1) (2000) 396-399.
[44] M. Mondet, E. Barraud, S. Lemonnier, J. Guyon, N. Allain, T. Grosdidier, Microstructure and mechanical properties of AZ91 magnesium alloy developed by Spark Plasma Sintering, Acta Materialia 119 (2016) 55-67.
[45] A. Guitton, A. Joulain, L. Thilly, C. Tromas, Dislocation analysis of Ti_2AlN deformed at room temperature under confining pressure, Philosophical Magazine 92(36) (2012) 4536-4546.
[46] A. Guitton, A. Joulain, L. Thilly, C. Tromas, Evidence of dislocation cross-slip in MAX phase deformed at high temperature, Scientific Reports 4 (2014) 6358.
[47] A. Sanaty-Zadeh, Comparison between current models for the strength of particulate-reinforced metal matrix nanocomposites with emphasis on consideration of Hall–Petch effect, Materials Science and Engineering: A 531 (2012) 112-118.
[48] L. Tian, L. Li, A Review on the Strengthening of Nanostructured Materials, International Journal of Current Engineering and Technology 8(2) (2018) 236-249.
[49] S. Amini, J.M. Córdoba Gallego, L. Daemen, A.R. Mcghie, C. Ni, L. Hultman, M. Odén, M.W. Barsoum, On the Stability of Mg Nanograins to Coarsening after Repeated Melting, Nano Letters 9(8) (2009) 3082-3086.
[50] S. Khoddam, L. Tian, T. Sapanathan, D. Hodgson Peter, A. Zarei-Hanzaki, Latest Developments in Modeling and Characterization of Joining Metal Based Hybrid Materials, Advanced Engineering Materials 0(0) (2018).
[51] W. Yu, X. Wang, H. Zhao, C. Ding, Z. Huang, H. Zhai, Z. Guo, S. Xiong, Microstructure, mechanical properties and fracture mechanism of Ti_2AlC reinforced AZ91D composites fabricated by stir casting, Journal of Alloys and Compounds 702 (2017) 199-208.
[52] W.A. Lederman, The damping properties of composite materials, Wisconsin University., Milwaukee, WI (United States)1991.

[53] J. Zhang, R.J. Perez, E.J. Lavernia, Effect of SiC and graphite particulates on the damping behavior of metal matrix composites, Acta Metallurgica et Materialia 42(2) (1994) 395-409.
[54] G. Fan, L. Geng, Z. Zheng, G. Wang, The effect of an interfacial layer containing nanosized Pb particles on the damping behavior in $Al_{18}B_4O_{33}$/Al composite, Scripta Materialia 59(5) (2008) 534-537.
[55] J. Gu, X. Zhang, M. Gu, M. Gu, X. Wang, Internal friction peak and damping mechanism in high damping 6061Al/SiCp/Gr hybrid metal matrix composite, Journal of Alloys and Compounds 372(1) (2004) 304-308.
[56] M. Moazami-Goudarzi, F. Akhlaghi, Wear behavior of Al 5252 alloy reinforced with micrometric and nanometric SiC particles, Tribology International 102(Supplement C) (2016) 28-37.
[57] C. Lim, S. Lim, M. Gupta, Wear behaviour of SiC_p-reinforced magnesium matrix composites, Wear 255(1) (2003) 629-637.
[58] H.G.P. Kumar, M.A. Xavior, Assessment of Mechanical and Tribological Properties of Al 2024- SiC-Graphene Hybrid Composites, Procedia Engineering 174(Supplement C) (2017) 992-999.
[59] N.G. Jones, C. Humphrey, L.D. Connor, O. Wilhelmsson, L. Hultman, H.J. Stone, F. Giuliani, W.J. Clegg, On the relevance of kinking to reversible hysteresis in MAX phases, Acta Materialia 69 (2014) 149-161.
[60] A. Guitton, S. Van Petegem, C. Tromas, A. Joulain, H. Van Swygenhoven, L. Thilly, Effect of microstructure anisotropy on the deformation of MAX polycrystals studied by in-situ compression combined with neutron diffraction, Applied Physics Letters 104(24) (2014) 201.
[61] C. Taltavull, B. Torres, A.J. López, J. Rams, Dry sliding wear behavior of AM60B magnesium alloy, Wear 301(1) (2013) 615-625.
[62] J. Zhang, X. Zhang, Q. Liu, S. Yang, Z. Wang, Effects of Load on Dry Sliding Wear Behavior of Mg–Gd–Zn–Zr Alloys, Journal of Materials Science and Technology 33(7) (2017) 645-651.
[63] S. Amini, C. Ni, M.W. Barsoum, Processing, microstructural characterization and mechanical properties of a Ti_2AlC/nanocrystalline Mg-matrix composite, Composites Science and Technology 69(3–4) (2009) 414-420.
[64] X. Wang, K. Wu, W. Huang, H. Zhang, M. Zheng, D. Peng, Study on fracture behavior of particulate reinforced magnesium matrix composite using in situ SEM, Composites Science and Technology 67(11–12) (2007) 2253-2260.

[65] B. Inem, G. Pollard, Interface structure and fractography of a magnesium-alloy, metal-matrix composite reinforced with SiC particles, Journal of Materials Science 28(16) (1993) 4427-4434.
[66] B. Anasori, E.a.N. Caspi, M.W. Barsoum, Fabrication and mechanical properties of pressureless melt infiltrated magnesium alloy composites reinforced with TiC and Ti_2AlC particles, Materials Science and Engineering: A 618 (2014) 511-522.
[67] M.W. Barsoum, M. Radovic, Elastic and mechanical properties of the MAX phases, Annual review of materials research 41 (2011) 195-227.
[68] H. Li, S. Li, X. Du, P. Bao, Y. zhou, Thermal shock behavior of Cr_2AlC in different quenching media, Materials Letters 167(Supplement C) (2016) 131-133.
[69] G.P. Bei, G. Laplanche, V. Gauthier-Brunet, J. Bonneville, S. Dubois, Compressive Behavior of Ti_3AlC_2 and $Ti_3Al_{0.8}Sn_{0.2}C_2$ MAX Phases at Room Temperature, Journal of the American Ceramic Society 96(2) (2013) 567-576.
[70] M. Gupta, W. Wong, High Performance Magnesium Based Composites Containing Nano-Length Scale/Amorphous/Hollow Reinforcements, Materials ence Forum 879(PT.1) (2016) 642-647.
[71] W.J. Joost, P.E. Krajewski, Towards magnesium alloys for high-volume automotive applications, Scripta Materialia 128 (2016) 107-112.